Modélisation du comportement mécanique de la neige à partir d'images microtomographiques

Pascal Hagenmuller

UNIVERSITÉ DE GRENOBLE

THÈSE

Pour obtenir le grade de

DOCTEUR DE L'UNIVERSITÉ DE GRENOBLE

Spécialité : **Sciences de la Terre et Univers, Environnement**

Arrêté ministériel : 7 aout 2006

Présentée par

Pascal HAGENMULLER

Thèse dirigée par **Mohamed NAAIM**
et co-encadrée par **Guillaume CHAMBON**

préparée à **Irstea Grenoble & CNRM-GAME/CEN**
dans l'Ecole Doctorale **Terre, Univers, Environnement**

Modélisation du comportement mécanique de la neige à partir d'images microtomographiques

Thèse soutenue publiquement le **17/12/2014**,
devant le jury composé de :

M. Martin SCHNEEBELI
Directeur de recherche, WSL-SLF, Président
M. Edward ADAMS
Professeur, Montana State University, Rapporteur
M. Farhang RADJAÏ
Directeur de recherche, Université de Montpellier, Rapporteur
M. Henning LÖWE
Chargé de recherche, WSL-SLF, Examinateur
M. Samuel MORIN
Chargé de recherche IPEF, CEN, CNRM-GAME, Examinateur
M. Mohamed NAAIM
Directeur de recherche, IRSTEA, Directeur de thèse
M. Guillaume CHAMBON
Chargé de recherche, IRSTEA, Co-encadrant de thèse
M. Frédéric FLIN
Chargé de recherche, CEN, CNRM-GAME, Invité

Résumé

Caractériser les propriétés mécaniques de la neige est un défi majeur pour la prévision et la prédétermination du risque d'avalanche. Du fait du grand nombre de types de neige et de la difficulté à effectuer des mesures sur ce matériau très fragile, la compréhension de la relation entre la microstructure de la neige et ses propriétés mécaniques est encore incomplète. Cette thèse aborde ce problème par le biais d'une approche de modélisation mécanique basée sur la microstructure tridimensionnelle de neige obtenue par microtomographie aux rayons X. Tout d'abord, afin d'automatiser et améliorer la segmentation des images microtomographiques, un nouvel algorithme tirant profit de la minimisation de l'énergie de surface de la neige a été développé et évalué. L'image air-glace est ensuite utilisée comme entrée géométrique d'un modèle éléments finis où la glace est supposée élastique fragile. Ce modèle permet de reproduire le comportement fragile en traction et révèle le comportement pseudo-plastique apparent causé par l'endommagement microscopique, ainsi que la forte hétérogénéité des contraintes dans la matrice de glace. Pour reproduire les grandes déformations impliquant le ré-arrangement de grains, un modèle par éléments discrets a ensuite été développé. Les grains sont identifiés dans la microstructure en utilisant des critères géométriques dont la pertinence mécanique a été démontrée, et décrits dans le modèle par des blocs rigides de sphères. Le comportement simulé en compression est dominé par le rôle de la densité mais révèle également des différences liées au type de neige. Enfin, pour distinguer le degré de cohésion entre les types de neige, un indicateur microstructurel a été développé et s'est avéré être fortement corrélé aux propriétés mécaniques et physiques du matériau.

Abstract

Characterizing the complex microstructure of snow and its mechanics is a major challenge for avalanche forecasting and hazard mapping. While the effect of environmental conditions on the snow metamorphism, which leads to numerous snow types, is fairly known, the relation between snow microstructure and mechanical properties is poorly understood because of the very fragile nature of snow. In order to decipher this relation for dry snow, this thesis presents a modeling approach of snow mechanics based on the three-dimensional microstructure of snow captured by X-ray microtomography and the properties of ice. First, in order to automatically process the microtomographic data, we take advantage of the minimization of the snow surface energy through metamorphism to efficiently binary segment grayscale images. Second, assuming an elastic brittle behavior of the ice matrix, the tensile strength of snow is modeled via a finite element approach. The model reveals an apparent pseudo-plastic behavior caused by damage, and the highly heterogenous stress distribution in the ice matrix. Third, we develop a discrete element model, accounting for grain-rearrangements and the creation/failure of inter-granular contacts. The grains, geometric input of the model, are detected in the microstructure with mechanically-relevant criteria and described as rigid clumps of spheres. The model evidences that the compression behavior of snow is mainly controlled by density but that the first stage of deformation is also sensible to the snow type. Last, the inter-granular bonds, recognized to be critical for the mechanical properties, are characterized through a new microstructural indicator, which effectively highly correlates with the simulated mechanical and physical properties.

Remerciements

Le manuscrit est terminé, la thèse est soutenue mais le plus important reste à faire: remercier les personnes avec qui j'ai travaillé et échangé.

Tout d'abord je souhaite remercier mes encadrants de thèse. Merci Guillaume d'avoir toujours gardé ta porte ouverte et d'avoir compris instantanément mes questions scientifiques. Je pense que tu m'as guidé dans une bonne direction pour la thèse et la suite avec une réflexion profonde, précise et honnête. Merci Mohamed pour les discussions scientifiques mais aussi et surtout de tes conseils pour tout ce qui tourne autour de la science: la vie quotidienne, les gens et leur personnalité, les ficelles du corps des IPEF. Merci à "Microstructure" du CEN et surtout à Fred et Bernard. Ils ne sont pas sur la liste officielle des encadrants mais sans eux ma connaissance de la neige serait bien moins moindre. J'espère avoir la chance de continuer à travailler avec vous tous. Pour l'instant, c'est bien parti !

Je tiens également à remercier les membres de mon jury. Merci Martin pour la présidence de ce jury et une gestion parfaite du timing (une question pas facile de Farhang en moins!). C'est avec Martin et Thiemo Theile que j'ai découvert la microstructure de la neige en Master 2 à Davos. Merci Farhang et Edward pour votre lecture détaillée de mon manuscrit, votre intérêt pour mon travail et la pertinence de vos commentaires en mécanique. Merci également Edward pour avoir fait le déplacement depuis le Montana. Merci Henning pour avoir évalué ma soutenance et reviewé en profondeur bon nombre de mes articles. Merci Samuel pour tes retours toujours très efficaces et pour avoir soutenu, avec succès, ma candidature au CEN.

Merci à mes collègues de bureau. Merci Nejib pour ton humour décapant et les Bobines mémorables. Johan, j'espère qu'on sera bientôt collègues au CEN, on ferait une team d'enfer. Zhu, bon courage pour la suite. Gaetan (vu le temps que tu as passé dans mon bureau, je te compte parmi les collègues de bureau), merci pour les discussions enflammées avec Raphael sur les conditions de ski, la taille au patin et l'effet "mamie" pour relacher la pression. Faut que vous passiez dans mon bureau admirer la décoration chartrousine.

Mes remerciements vont également à l'équipe ETNA pour une ambiance de travail productive et dans la bonne humeur. Merci Evgeny pour nos discussions sur le matériau de neige dans un monde irstéen d'écoulement et de zonage. Merci aux doctorants avec qui j'ai partagé galères et bières. Merci Fred O. pour tes bons mots et nos échanges sur nos chevilles d'acier. Merci Manu, Hervé, Xavier pour me rappeler qu'après les modèles, il y a une réalité sur le terrain. Merci Christian pour ton humour et les conseils sur les vélos. Merci à Martine pour une gestion vraiment efficace des missions. Merci à Gwenola pour une gestion pas facile des travaux. Au passage, je ne remercie pas le concours de circonstance qui fait que j'ai pu profité, de A à Z, du marteau-piqueur et que j'observe un bâtiment tout neuf de ma fenêtre au CEN, sans y avoir jamais mis les pieds.

Merci à mes amis et à ma famille qui sont venus de loin pour assister à ce moment important et qui ont un peu fait de moi ce que je suis aujourd'hui (et qui m'ont bien aidé pour le pot). Trois docteurs pour débroussailler à la Chabreuye, papa serait

fier de nous, autant pour le diplôme que pour les choses simples. Mériem, merci pour ce qui est le plus important.

Contents

Chapter 1

Introduction

Contents

1.1 Context

1.1.1 Avalanche danger

An avalanche is a rapid gravity-driven flow of a significant snow mass on a mountainous slope. Every year, snow avalanches kill about one hundred people in the Alps and cause important material damage on human infrastructures.

Historical perspective. No attention would be paid to avalanches if nobody lived in the mountains. The first accidents are reported by military troops crossing the Alps to invade new territories behind this natural rampart. For instance, around 218 before Christ, Hannibal climbed into the Alps to attack Rome [Jenkins, 2000]. His troops had to face avalanches when they crossed high-altitude paths, as reported: "There where the path is intercepted by glistening slope, Hannibal pierces the resistant ice with his lance. Detached snow drags the men into the abyss and snow falling rapidly from the high summits engulfs the living squadrons" (Silius Italicus, [Jenkins, 2000]). As people settled in the remotest valleys of the European Alps in search of new living space (ex. Walser, Alemanni between the 12$^{\text{th}}$ and

Figure 1.1: Artist's view of avalanches in the 18th century (from "Neue und vollstaendige Topographie der Eydgnosschaft", David Herrliberger, 1754-1758).

14th century), death tolls began to rise. Avalanches were source of fear and thought as a fatality (Figure 1.1). However, progressively, people learned to live in secure places by continuously rebuilding the destroyed houses. In medieval times, people recognized that clearing of forest could significantly increase the avalanche danger. In consequence, for example in France, the administration ("Eaux et Forêts") set regulations of forest clearing in exposed areas (e.g. Barèges, Pyrénées in 1860) and, in 1899, started the "carnet d'avalanches" where avalanche events were systematically reported [de Crécy, 1965]. In Switzerland, which is proportionally much more exposed to avalanches than France, first experiments [e.g. Bader and Niggli, 1939] are conducted on snow in the 1930's and a laboratory (SLF) specifically dedicated to the study of snow is created in 1942. With the development of ski tourism and hydroelectricity, more knowledge on snow and avalanche is required and in the 1950's, experiments on snow are started at Col de Porte, Chartreuse, French Alps. In February 1970, the dramatic accidents of Val d'Isère[1] and Passy[2], stirred public opinion and highlighted the lack of the French avalanche risk management [Ancey, 1998]. Six months later, Saunier's commission proposed the creation of a national association for the study of snow and avalanches (ANENA), the establishment of the nivology division in the CERAFER (now Irstea) and the development of the activities of center for snow study (CEN, Météo-France) [Saunier, 1970].

Current costs of avalanches. Numerous defense structures have been built and successfully prevented from countless infrastructure damage. However, the catastrophic avalanche cycle of winter 1998-1999 in the European Alps[3] recalled that

[1] The 10th February 1970, 39 young people were killed by an avalanche in their chalet in Val d'Isère, France

[2] The 5th April 1970, a mudslide killed 77 people in a sanatorium in Passy, France

[3] 12 deaths in Montroc, France; 12 deaths in Evolene, Switzerland; 39 deaths in Galtür, Austria.

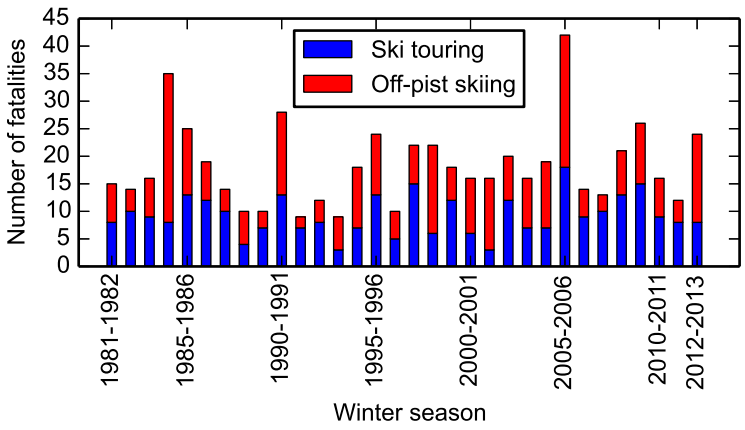

Figure 1.2: Avalanche fatalities of backcountry skiers in France during the period 1981-2013. Note that the fatalities in other outdoor sports, such as ice climbing or mountaineering, and due to avalanche are not taken into account in this figure. Data from http://www.anena.org.

avalanches are still threatening people and infrastructure in the Alps [Glass et al., 2000]. Besides death toll and infrastructure damage, the economy of mountainous area is deeply impacted by the avalanche hazard: non-constructible land, evacuation of people at risk[4], closing of highly frequented roads[5], etc. Nowadays avalanches are also threatening an increasing number of recreationists. An average of 30 fatalities per year in France are attributed to avalanches during outdoor hobbies including backcountry skiing (Figure 1.2).

Risk management. Two approaches of avalanche risk management can be distinguished: short-term forecast and long-term prevention (hazard mapping).

- *Short-term forecast:* Météo-France provides, on a daily basis during the winter season, an avalanche bulletin on a regional scale (Figure 1.3a). This bulletin consists in an estimation of the avalanche activity (frequency of release and size of the avalanche) and the stability of the snowpack. The avalanche danger is given on a international scale between 1 (low) and 5 (very high) and details on the avalanche type and on the most favorable conditions for a release are described. It is mainly intended for ski patrols, backcountry skiers but it also serves as warning system for local authorities in charge of infrastructure safety. The avalanche forecaster builds the bulletin with snowpack measurements, its own expertise and the results of a forecasting model (SAFRAN-CROCUS-MEPRA) which computes a stability index as a function of the past and modeled weather conditions [Durand et al., 1999]. The model helps

[4] e.g. in February 2012, 600 people were evacuated from Barèges, France because of high avalanche risk.

[5] e.g. the Mont-Blanc tunnel between France and Italy was closed the 31th December 2011 because of high avalanche risk

the forecaster in pointing out the range of elevations and aspects at which the snowpack undergoes processes affecting its stability [Durand et al., 1999]. However, the predictability of the avalanche danger is limited and relies on how the avalanche forecaster heuristically weights the influence of the diverse contributory factors as terrain, meteorological conditions, observations of the snowpack etc.

- *Long-term prevention:* Hazard mapping informs about the spatial extent of the risk and is used to regulate urbanism. This type of hazard map exists for industrial (explosion, leaking of chemical, etc.) and natural hazards (flooding, wildfire, avalanche, etc.). In France, the avalanche hazard map (PPRA) distinguishes four main zones (Figure 1.3b): (1) the red zone where all constructions are forbidden, (2) the dark blue zone where new constructions are forbidden but existing ones are allowed and should be protected, (3) the light blue zone where new constructions are allowed but under conditions that they support a certain mechanical load and (4) a green zone where the forest should be maintained because it has a protective role. This mapping results from a compromise between considering the maximum avalanche extent/intensity and the commitment of economical development in remote alpine valleys. The estimation of the intensity and the frequency of an avalanche for a given path is primarily based on historical data, as direct observations of avalanche deposition or indirect observations on the damage tracks left by the avalanche [de Crécy, 1980]. However, this kind of data is not available everywhere and on sufficiently long period to be representative of rare but very intense avalanche events. Therefore statistical models must be coupled with physically-based models to overcome the limitations of missing historical data [Gaume, 2013]. Risk management for long-term prevention still requires better understanding of the physics of the phenomenon even though it was already improved since the description of an avalanche as a "snow ball" (painting of Figure 1.1).

Even if, at present, the occurrence of a single avalanche event cannot be predicted in time and space, avalanches are not random events but result from a complex interaction of contributory factors. The release process can be studied and modeled to go toward better hazard mapping and short-term forecasting [Schweizer et al., 2003].

1.1.2 Avalanche formation

Understanding the processes at the origin of an avalanche release is critical for short-term forecasting but also for long-term prevention which requires the knowledge of snow rheological properties and the size of the released volume of snow. Snow avalanches result from the interplay between three elements: (1) snow properties (controlled by the weather conditions, vegetation, etc.), (2) topography (slope/gravity) and (3) a triggering element (physical: change in snow properties as temperature increase; mechanical: new falling snow, skier, explosive, earthquake) [Goetz, 2010].

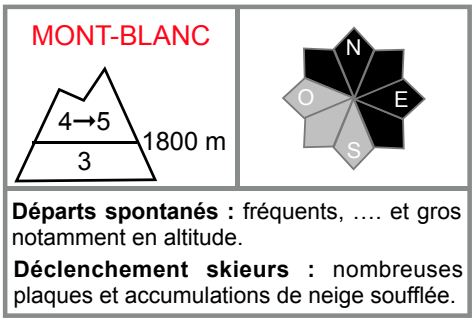

(a) Example of short-term avalanche forecasting for the Mont-Blanc massif, France. Adapted from www.meteofrance.com.

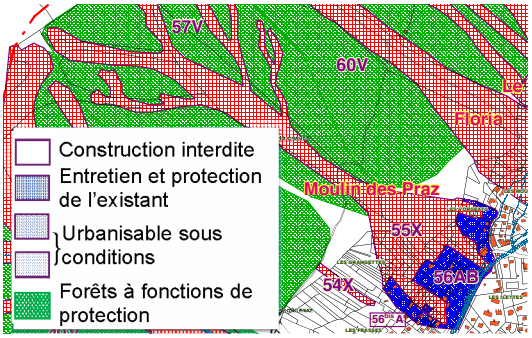

(b) Example of avalanche hazard mapping for urbanism (in french "Plan de Prevention du Risque Avalanche", PPRA). Adapted for readability purpose from PPRA of Chamonix.

Figure 1.3: Avalanche risk management: short-term forecast (a) and long-term prevention (b).

Two types of release are usually distinguished: loose snow avalanches and slab avalanches [Schweizer et al., 2003].

- Loose snow avalanches start at a single point at the snow surface. While the snow mass with low cohesion moves down the slope, the avalanche progressively spreads in a triangular shape and gains volume by eroding the snow surface. Their release can occur during a snowfall of very light and cold fresh snow or during a temperature increase which decreases the friction angle between snow grains or increases the water content. They can be artificially released by backcountry skiers but accidents can be avoided since the skier who triggered the avalanche is generally upstream the avalanche flow.

- Slab avalanches are the most dangerous because they involve much larger snow volumes. Moreover, Schweizer and Lütschg [2000] showed that fatalities of recreationists due to avalanches are nearly exclusively (99%) caused by slab avalanches. The snowpack is layered vertically. Each layer has its own properties determined by its history (snow fall, temperature, wind, etc.). When two successive layers are badly connected or because the thin layer in between is very weak (the weak layer), the upper layer(s) (the slab) can slide entirely on the lower layer (the basal layer) which creates a slab avalanche (Figure 1.4a). In details, the release of a slab avalanche involves two different failure processes (Figure 1.4b). First, the weak layer fails in shear and compression along a crack parallel to the slope (the basal crack). Then, the loss of shear cohesion between the slab and the basal layer creates tension in the slab which fails along a crown crack. Note that the basal crack can spread up and down the slope; the crown crack can thus be upslope of the triggering factor, as a skier. This explains why slab avalanches are more dangerous for skier than

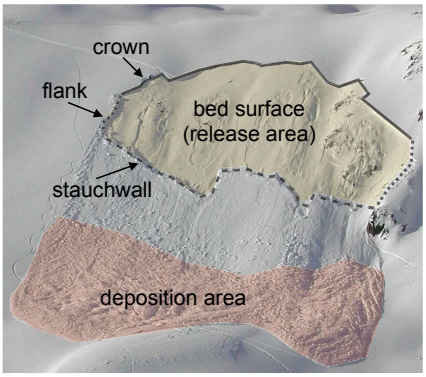

(a) Slab avalanche nomenclature. The nomenclature is as described by Perla [1977]. The background avalanche image is taken from [Sigrist, 2006].

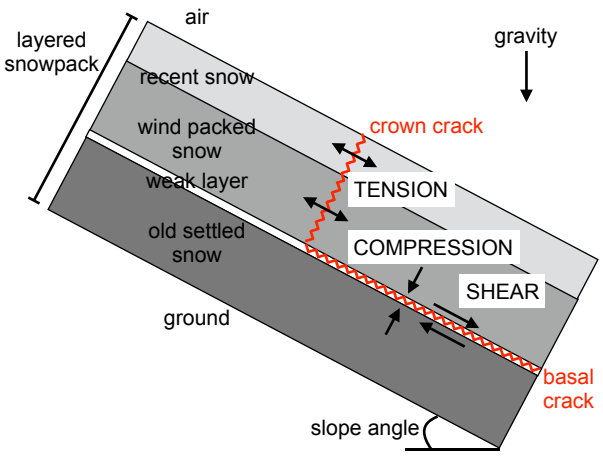

(b) Example of a slab configuration in the release area.

Figure 1.4: Slab avalanche release.

loose snow avalanches since the skier can be anywhere on the released slab.

1.1.3 Snow materials

Much about the avalanche release processes remains unknown because of the complexity and the variability of the snowpack [Schweizer et al., 2003]. To better understand the release mechanisms, there is clear need for comprehensive constitutive modeling of snow, which is currently missing [Shapiro et al., 1997]. One reason for this missing link in the avalanche knowledge might be the lack of industrial funding for research on snow mechanics. Indeed, compared to typical construction materials, snow is less valuable for commercial activities. Another reason is the existence of not only one snow material, but numerous snow materials characterized by a wide range of microstructural patterns. Besides, snow is a very fragile material, which makes experiments difficult to conduct.

Snow on the ground consists of snow crystals, which formed in the atmosphere by water vapor deposition on freezing nuclei. Atmospheric temperature and water supersaturation control the morphology of these snowflakes, which can thus have variable shapes and sizes (stellar dendrite, plate, column, etc.). Once on the ground, the snowflakes evolve rapidly with time (within hours and days), depending on environmental conditions like temperature, temperature gradient and forces applied to the snowpack. This process is called metamorphism. The different initial snowflake shapes and the various environmental conditions on the ground yield a wide range of microstructural patterns, variable in time and space. These different patterns are classified in snow types according to an international classification [Fierz et al., 2009]. Symbols and codes of the main snow types are shown in Figure 1.5. Snow metamorphism on the ground can be explained by three main processes:

- *Vapor transport:* Snow exists on the ground at homologous temperature above 0.9, i.e. its temperature is generally higher than 90% of its melting point using the Kelvin scale. Its density ranges roughly between 20 kg m^{-3} and 500 kg m^{-3}. The high homologous temperature and porosity promote intense water vapor exchanges (ice sublimation, vapor transport, vapor deposition) between ice zones, which modify the shape and the bounding of the ice matrix. The metamorphism primarily due to vapor exchanges is active on dry snow and is of two different types: equilibrium and kinetic. Equilibrium metamorphism occurs when there is almost no heat flux in the snowpack, i.e. when the temperature gradient ∇T is low ($\nabla T \leq 5$ K m^{-1}). It rounds the snow grains and thickens the ice matrix by promoting vapor transport from convex zones to concave zones [e.g. Flin et al., 2004, Vetter et al., 2010] (Figure 1.5). Therefore, it tends to stabilize the snowpack. Kinetic metamorphism is due to temperature gradients ($\nabla T > 5$ K m^{-1}), which induce vapor fluxes in the snow microstructure. It creates plane facets and sharp edges [e.g. Calonne et al., 2014, Schneebeli and Sokratov, 2004] (Figure 1.5). When the temperature gradient is very high ($\nabla T > 20$ K m^{-1}), depth hoar forms. In both cases, kinetic metamorphism tends to decrease the stability of the snowpack. Faceted crystals and depth hoar are of particular interest since theses types of snow are often involved in slab avalanche releases as the component of the weak layer [Duclos, 1998].

- *Melt:* The melting/refreezing cycle rounds the grains and increases their sizes [Colbeck, 1975]. The cohesion depends on the liquid water content: without any liquid water, the bonds are icy and very strong, if the water content is moderate, liquid water creates moderate capillary cohesion forces, if the water content is very high, liquid water plays the role of lubricant and decreases drastically snow cohesion.

- *Mechanical load:* Because of its high porosity, snow is a very fragile material. Because of its high homologous temperature and crystalline nature, it also exhibits a pronounced creep behavior. It is thus very sensitive to external mechanical stress. First, wind can break falling snowflakes or eroded snow grains into smaller parts [Fierz et al., 2009]. The small snow grains sinter easily together and form a cohesive layer often involved in avalanche release as a slab. Second, snow own weight can enhance its deformation [Chandel et al., 2007]. For instance, a deeply buried snow layer will densify and stabilize faster than the top layer. Lastly, numerous ski tracks or snow grooming also modifies the snow structure.

In summary, snow can be declined in numerous different materials characterized by a certain microstructure i.e. size, shape and spatial arrangement of grains. The microstructure evolves in time with metamorphism at a scale of the order of 10^{-4} m. The microstructure of snow and the ice properties control the snow properties including mechanical properties at the snowpack scale (10^{-1} m) relevant for avalanche

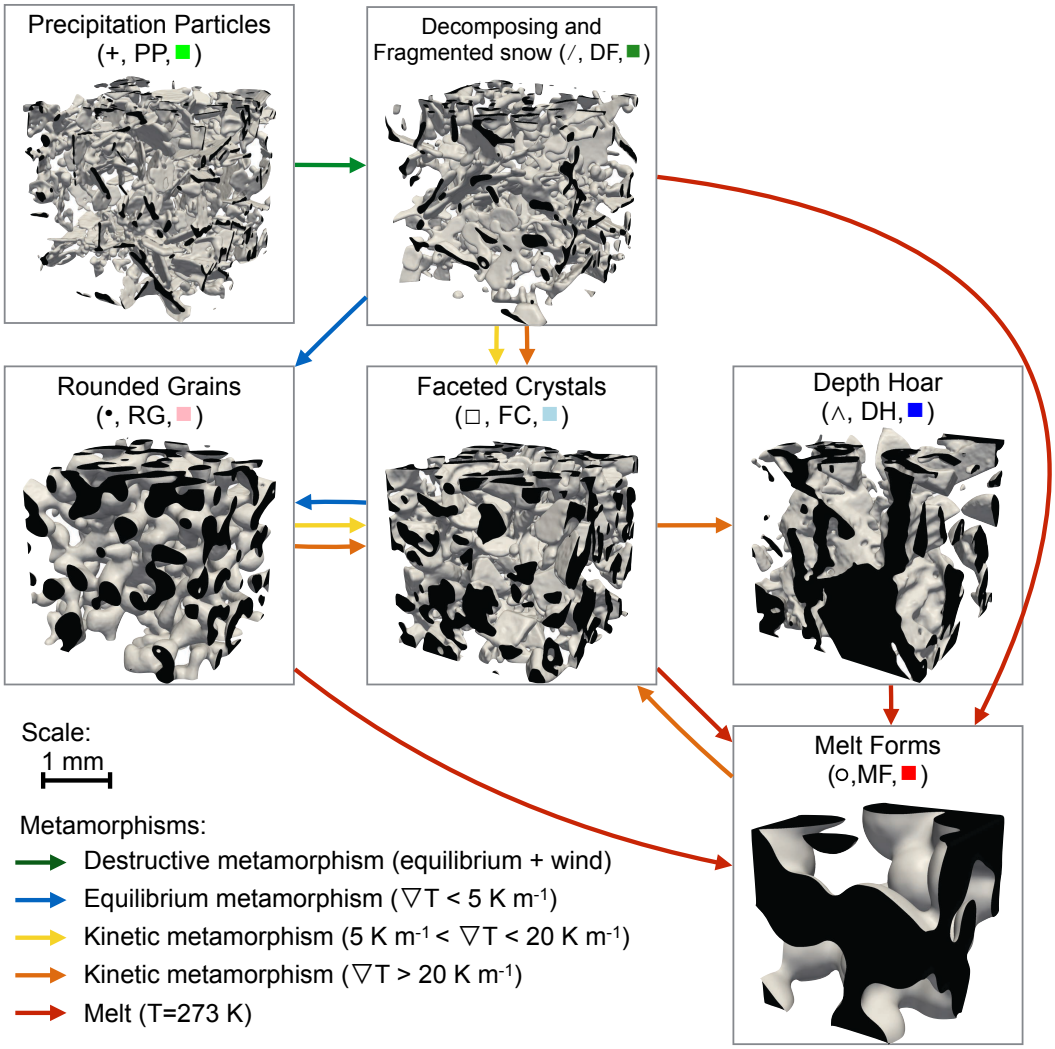

Figure 1.5: Metamorphism of snow induced by vapor transport and melt. The code and symbols for each snow type are indicated on top of each 3D image. The 3D images of the snow microstructure were obtained with X-ray microtomography.

release.

1.1.4 Snow mechanics

1.1.4.1 General points

Mellor [1975] defines snow mechanics in the following terms: "Narrowly defined, snow mechanics deals with forces and displacements in all forms of snow, i.e. with the kinematics, dynamics and energetics of snow in both condensed and dispersed states. More broadly defined, it also embraces the underlying physics of processes relevant to mechanical behavior, and the useful but disconnected empiricism associated with snow engineering, avalanche prediction, etc.". Let us focus on the narrow definition of snow mechanics and illustrates the aim of this science by two typical and simple questions:

- *What is the maximum force F_t a cylindrical sample can hold if one pull on it along its symmetry axis?* F_t defines the tensile maximum resistance force F of the sample, a variable that depends on the size of the sample. The material variable characteristic of the tested snow microstructure is the strength σ_t defined as the ratio $\sigma_t = F/S$ where S is the circular cross-section of the sample. By repeating this test several times on similar microstructure patterns, I can reasonably define the strength σ_t characteristics of the tested snow type. Being able to predict σ_t for different snow types is of great interest for avalanche forecasting since the tensile failure properties of snow control the opening of the crown crack. However, can I extrapolate the obtained strength to slab configuration? Do I obtain the same value if I pull on a bigger sample, in another direction and with a different speed? This raises the question of the effects of size, microstructural anisotropy and strain rate. Therefore, characterizing the tensile strength of a snow microstructural pattern is not only depending on the microstructure itself but on the chosen loading conditions (direction, strain rate) and the chosen scale.

- *How much the snow densifies because of its own weight?* Answering this question consists, in material science vocabulary, to determine the volumetric strain during a creep experiment. Does temperature have an effect on the deformation? Does the crystalline orientation (the fabric) of each individual ice crystals impact the overall behavior? This example points out that the mechanical behavior of snow is also a function of the environmental conditions, which drive the material properties of ice, and the complete snow microstructure including the crystalline fabric and not only the spatial arrangement of ice and pores.

In general, one goal of snow mechanics is to find a model (constitutive model), which links forces and displacements or stresses σ and strains ε. As mentioned before, the relations $\sigma = f(\varepsilon)$ or $\varepsilon = g(\sigma)$ (constitutive equations) might depend on the geometrical microstructure, the strain rate, temperature, the crystallographic

microstructure, the sample history, etc. The challenge of snow mechanics is to find as universal as possible relations and to know their range of validity. Given the wide range of possibilities for each contributing factor, this is a big challenge. To set the context of this PhD, let us focus on two of the main factors: strain rate and microstructure.

1.1.4.2 Effects of strain rate

Narita [1983] conducted one of the most comprehensive study on one type of load: tension. To investigate the behavior of snow under tensile stress, he performed several tests within a wide range of strain rates, temperatures, densities and examined whether the results obtained on small-sized specimens in laboratory were representative of the ones obtained at the scale of an avalanche slope in the field. Narita distinguished four types of deformations under tension according to the imposed constant tensile strain rate $\dot{\varepsilon}$ (Figure 1.6):

- Type (a) with $10^{-4}\ s^{-1} < \dot{\varepsilon}$. It corresponds to a visco-elastic regime characterized by a linear relation $\sigma = E \cdot \varepsilon$ between stress σ and strain ε with $E = E(\dot{\varepsilon})$ the Young's modulus. Note that the linear relation between stress and strain exists at small strains for the four described types of deformations, i.e. independently of the strain rate. Fracture occurs suddenly with a sharp failure surface. This type of regime is called "brittle" regime.

- Type (b) with $7.0 \times 10^{-5} < \dot{\varepsilon} < 2.4 \times 10^{-4}\ s^{-1}$. It corresponds to a visco-elastic and plastic behavior. Fracture occurs after the stress has reached a plateau and significant pseudo-plastic strain. The formation of micro-cracks around the final failure surface can be observed. This deformation regime is called "ductile" failure.

- Type (c) with $1.0 \times 10^{-6} < \dot{\varepsilon} < 7.0 \times 10^{-5}\ s^{-1}$. It is similar to the deformation regime observed on type (b) but there is no clear failure surface and the stress decreases smoothly to zero after reaching its maximum value. There is notable formation of micro-cracks throughout the sample.

- Type (d) with $\dot{\varepsilon} < 7.0 \times 10^{-6}\ s^{-1}$. The sample deforms continuously without the formation of micro-cracks even for large strain (up to 0.3). This deformation regime is called "creep".

The observations by Narita illustrate the effect of strain rate on the overall deformation regime. The different types of deformations are due to different mechanisms activated at the microstructural level such as elasticity, damage (micro-failure) or plasticity. Deciphering the macroscopic mechanical behavior of snow cannot be unlinked to the processes occurring at the microscopic level. These processes are governed by the microscopic ice properties which depend on temperature and crystal orientation, and the microscopic strain rate distribution which depends on the imposed macroscopic strain rate and the microstructure.

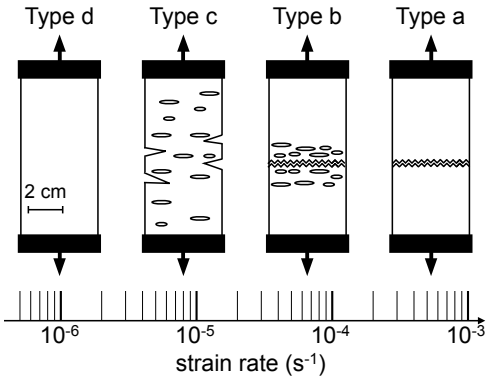

(a) Visual inspection of the deformed samples. The small ellipsoids represent micro-cracks.

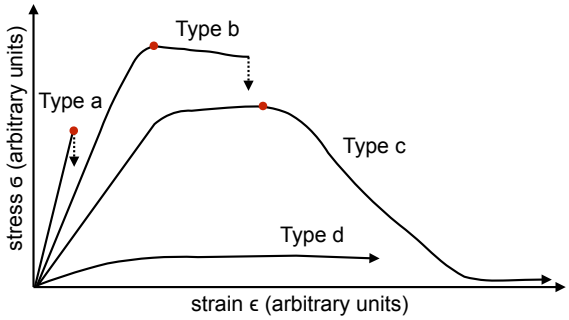

(b) Stress strain curves related to the deformation configurations shown in Figure 1.6a. Tensile strength is denoted with a red dot.

Figure 1.6: Qualitative description of four types of deformation and fracture of snow under uniaxial tensile strain. Adapted from [Narita, 1983].

1.1.4.3 Effects of microstructure and density

The tensile tests with different snow density and temperature conducted by Narita also show that strength tends to increase with density and decreases with temperature. He observed variations of strength with density in the range between 250 and 450 kg m^{-3}, of the same order of magnitude as those observed with strain rate in the range $\dot{\varepsilon} \in [10^{-6}, 10^{-3}]$ s^{-1}. Narita noted that "the structure of snow [...] i.e. diameter, length, orientation and number of ice bonds [..] is likely to have a predominant effect on the strength of snow rather than the density itself".

Mellor [1975], Shapiro et al. [1997] reviewed the most important results of snow mechanics. They recognized the importance of the microstructure in controlling snow's mechanical properties. However, in practice, a majority of the experimental studies determines the mechanical properties of snow and its density but give no further information of its microstructure. A few studies characterize the microstructure mainly in term of snow type in the international classification. However, the discrete classification in snow types does not account for the continuum between snow types and the bonding between snow grains expected to be a critical mechanical predictor. Therefore, the mechanical properties are usually plotted and fitted only against density [e.g. Mellor, 1975] (Figure 1.7). As shown for the Young's modulus and the tensile strength on Figure 1.7, the usual phenomenological mechanical parameterization based on density shows a large scatter for a fixed density. For instance, Keeler and Weeks [1968] showed that two snow samples with the same density but different microstructures may have strengths differing by as much as a factor of four. The scatter observed on Figure 1.7b is even bigger, about two orders of magnitude, and can be attributed to the effect of microstructure (other than density) and strain rate. This scatter decreases but remains important if the snow types are distinguished, indicating that the snow type classification is not sufficient

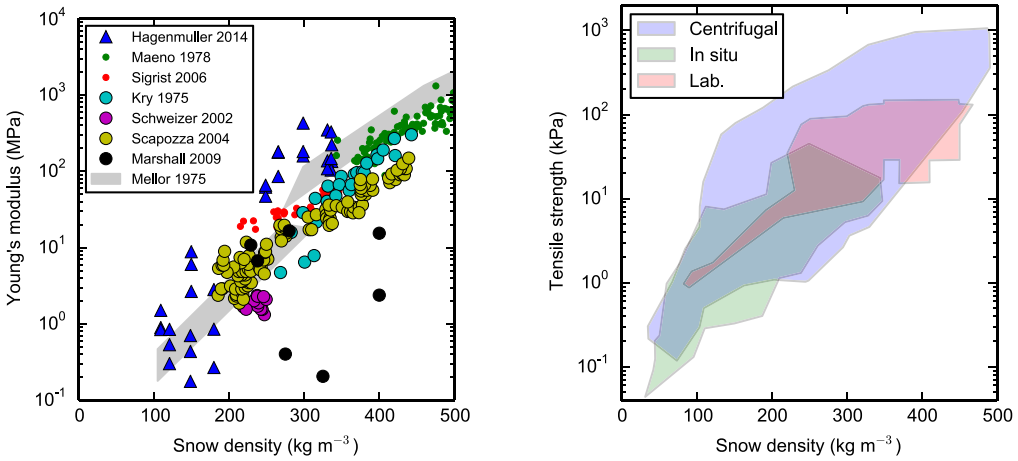

(a) Young's modulus E as function of snow density ρ. Compilation of microstructure based simulations and experimental data from [Hagenmuller et al., 2014a, Kry, 1975b, Maeno et al., 1978, Marshall and Johnson, 2009, Mellor, 1975, Scapozza, 2004, Schweizer and Camponovo, 2002, Sigrist, 2006].

(b) Domain of tensile strength σ_t as function of snow density ρ for different measurement procedures: centrifugal data (e.g. [Upadhyay et al., 2007]), in situ data (e.g. [McClung, 1979]) and other laboratory measurements (e.g. [Narita, 1983]). Taken from [Borstad, 2011] who compiled experimental data with over 2000 strengths tests from 20 different sources. See [Borstad, 2011] for details.

Figure 1.7: Young's modulus and tensile strength of snow as a function of snow density.

to describe the snow microstructure [e.g. Jamieson, 1988]. Therefore, there is a need to derive microstructural descriptors relevant for snow mechanics that go beyond the first order characterization by density. Since a similar status by Shapiro et al. ("developing a method of using microstructural properties as an indicator of deformational response to load still remains to be done" [Shapiro et al., 1997]), different approach linking microstructure and mechanical properties were proposed and are summarized in section 1.2.

1.1.5 General objective of the thesis

In summary, avalanches are still a major danger in mountainous area by threatening human infrastructures and activities. Therefore, there is a social need for short-term avalanche prediction and long-term prevention. However much about the release process remains unknown, which limits the predictability of an avalanche event. In practice, the forecasting of avalanche occurrence probabilities still relies on heuristic approach or on sparse historical data. One limiting point to understand the release mechanism is the complexity of snow and its mechanics. While the effect of meteo-

rological and environmental conditions on the snow metamorphism is fairly known, the relation between snow microstructure and mechanical properties is poorly understood. Strain rate controls the deformation mechanisms at the microstructural level and will be determinant to formulate a constitutive model of snow. The usual characterization of the snow microstructure only with density is not complete since it fails to describe the wide variety of microstructural patterns of snow.

The objective of this thesis is to better understand the mechanisms active at the microstructure scale when snow deforms and fracture to go toward a mechanical constitutive law accounting for microstructure in a more precise way. Given the wide range of deformation types, snow types, environmental conditions, etc. this challenge is too large for a single PhD. Therefore, I will limit this study to a certain range of possibilities and only consider:

- dry snow ($T < 0^oC$),
- relatively high strain rates ($10^{-4}\ s^{-1} < \dot{\varepsilon}$), relevant for slab avalanche releases,
- apparently homogeneous snow samples which evolve because of deformations and not "thermodynamic" metamorphism,
- small samples of volume on the order of 1 cm^3.

The present study aims to explore the link between the geometrical microstructure of snow and its bulk mechanical properties, assuming that ice behaves in a brittle regime. It is based on the current state of knowledge presented in the next section.

1.2 Present state of snow mechanics

In this section, we focus on the incorporation of microstructure indicators in constitutive modeling of snow mechanics. First, attention is paid to the description of the snowpack by avalanche forecasters and especially on how the snow microstructure is characterized in the mechanical module (MEPRA) of the French operational avalanche risk forecasting model (SAFRAN-CROCUS-MEPRA). Then the present state of academic research in this domain is summarized.

1.2.1 Operational avalanche forecasting

In many countries with snow-covered mountains, avalanche-forecasting services warn the public by issuing occurrence probabilities for a certain region [Schweizer et al., 2003]. We describe briefly here the avalanche forecasting conducted by Météo-France, which is similar to the ones conducted abroad. We especially pay attention on the characterization of the snow material.

Météo-France provides on a daily basis between December and May an avalanche bulletin (BRA) which estimates the type and intensity of the avalanche activity on a massif scale (about 150 km^2, ex. massif de la Chartreuse). The avalanche activity is detailed for different altitudes, exposures and time slots. As mentioned before, the

release of an avalanche results from the interplay of several contributing factors, some of which are poorly understood. Therefore, the avalanche risk cannot be predicted in a fully deterministic manner but its prediction results from a human expertise. The avalanche forecaster bases his analysis on: (1) field observations (atmospheric conditions, snow stratigraphy, record of past avalanche activity) and (2) the results of a snow mantle evolution model (SAFRAN-CROCUS-MEPRA).

1.2.1.1 Field observations

To follow and forecast the evolution of the snowpack and its stability, the snowpack is measured systematically during the winter season at different time/spatial resolution and level of details. This information is then gathered by Météo-France.

First, more than 100 sites mainly located between 1500 and 2000 m altitude throughout the Alps, Pyrenees and Corsica constitute an observation network ("réseau nivométéorologique", [Pahaut and Giraud, 1995]). This network comprises a majority of ski patrols. On each site, manual measurements are conducted twice a day (around 8h and 13h) to record cloud, temperature, wind, precipitation, total snow depth, new snow depth, blowing snow and past avalanche activity.

Second, in order to complete these first observations, detailed measurements of the snow profile from the ground to the surface are conducted on a large number of sites in the observation network. This measurement requires digging a snow pit and is therefore time-consuming. It is not done on a daily basis but at least once a week. To define the different snow layers, every change in snow characteristics is identified manually by detecting changes in snow "aspect" and hardness. Then the snow type, grain size, density, water content and hand hardness are measured for each layer according to a standard protocol described by Fierz et al. [2009] (Figure 1.8). The snow type and grain size are estimated under magnifying glasses (x10). The penetration resistance (or ram hardness) is also measured via a ramsonde [Bader and Niggli, 1939]. Ram and hand hardness are important mechanical measurements of the snowpack since they are linked to the cohesion of the snowpack and thus to its stability.

Last, about thirty automatic measurement stations "Nivose" covering the French massifs record air temperature, wind, snow height and humidity with a time resolution of about 1h [Lecorps and Sudul, 1991]. They are complementary to the observation network "réseau nivométéorologique", since they can be installed in places difficult to reach in winter and can cover a wider range of altitude and a finer time resolution.

1.2.1.2 MEPRA model

The avalanche forecaster has to synthesize the information provided by the observation network in order to provide an evaluation of the avalanche activity for the next day. However, given the variety of snow profiles and weather conditions at different locations, it is very difficult to capture the entire snowpack evolution and to point

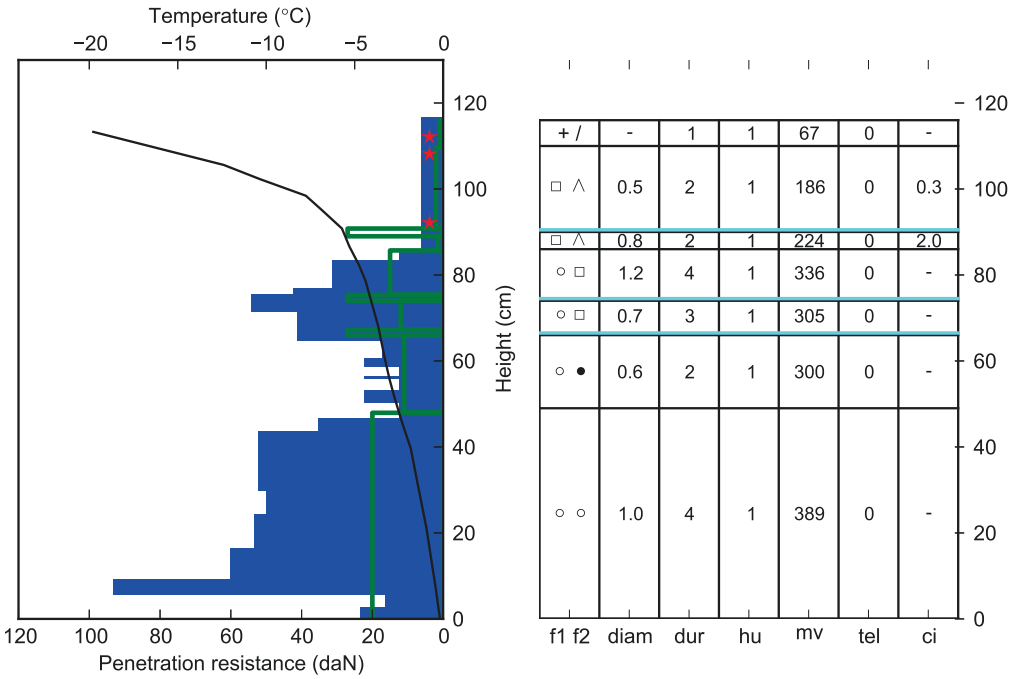

Figure 1.8: Measured snow profile at Col de Porte (Chartreuse, France) on the 13/02/2012. On the left, the blue bars represent the ram strength and the black line the temperature profile. The green horizontal bars represent the ram strength calculated by MEPRA (see below) based on the snow layer measurements (right). The red stars indicate the layers in which some samples were collected for microtomography. On the right, "f1 f2" denotes the primary and secondary snow types, "diam" the diameter of the grains, "dur" the hand hardness, "hu" the humidity of the layer, "tel" the liquid water content in % and "ci" the shear strength in kPa measured by a rotational vane. Ice layers are plotted in light blue.

out situations that can lead to instability [Pahaut and Giraud, 1995]. The hundred of measurement points are distributed throughout the Alps according to the altitude and exposure, the mesh network is thus very large and localized instability-prone conditions can be masked. In addition, the survey of the internal snow profile is only conducted once a week and; in case of very unstable weather conditions, the time resolution of this observation is thus insufficient to estimate snowpack changes [Pahaut and Giraud, 1995]. In order to help the forecaster, Météo-France developed in the 1990's, the automatic avalanche forecasting system SAFRAN-CROCUS-MEPRA (SCM) [Durand et al., 1999]. At present, this model is a secondary help for the avalanche forecaster but is intended in the future to provide a deterministic evaluation of the avalanche risk by progressively incorporating research results. SAFRAN estimates meteorological parameters affecting snowpack evolution. Based on the output of SAFRAN, CROCUS simulates the physical processes inside the snowpack to reproduce the evolution of the snowpack. MEPRA is an expert system which analyses the mechanics of the snowpack modeled by CROCUS to deduce natural and accidental avalanche risks. To describe the great variability of topographic situations, the system SCM simulates the snow-cover evolution and its stability for many typical slopes, elevations and aspects, representative of the different French massifs. In the following, we focus on the description in SCM of the snow microstructure and its link to mechanical properties.

In CROCUS, the microstructure of snow in each snow layer is described by density ρ, age A, liquid water content d_l and semi-quantitive descriptors of the microstructure morphology: dendricity d, sphericity s, historical variable h and grain size g_s [Brun et al., 1992, Vionnet et al., 2012]. In fact, the description of the snow microstructure is directly inspired from snow pit observations (Figure 1.9) and corresponds to a continuous parameterization of the discrete classification in snow type. Grain size g_s represents the diameter of grains observed in the field. Dendricity d characterizes freshly fallen snow and varies from 1 (recent snow) to 0 (no recent snow); it roughly represents the remaining initial geometry of snow crystals in the layer, and decreases over time in a given layer. Sphericity s ranges between 0 (angular grains) and 1 (rounded grains) and describes the ratio of rounded versus angular shapes. It is arbitrarily fixed at 0.5 for precipitation particles. The historical variable h records whether the snow layer had been in contact with liquid water or has undergone temperature gradient metamorphism. The variable h is discrete (1: has been angular, 2: has been in contact with liquid water but was never angular, 3: has been in contact with liquid water and has been angular, 4: has undergone several melt-freeze cycles and was never angular, 5: has undergone several melt-freeze cycles and has been angular, 0: all other cases). The snow type is a function of d, s, h and g_s (Figure 1.9). Note that semi-quantitative relations between dendricity d and sphericity s, on the one hand, and geometric quantities such as curvature κ, perimeter P and area a, on the other hand, can be derived from 2D images of snow grains [Bartlett et al., 2008, Lesaffre et al., 1998]. However, the evolution of the morphological variables was parameterized with (d,s) deduced from manual observations and linking (d,s) and (κ, P, a) requires additional adjustment

parameters. Recently, Carmagnola et al. [2014] rewrote the original equations of CROCUS formulated with d, s and g_s in terms of s and the optical diameter d_{opt} (details in [Warren, 1982]), which is a well-defined variable and measurable in the field: $d = \frac{d_{opt}-4+s}{s-3}$ and $g_s = (4 - s)$ with d_{opt} and g_s in mm. This is a first step toward a complete physical parameterization of CROCUS on variables unambiguously defined and measurable.

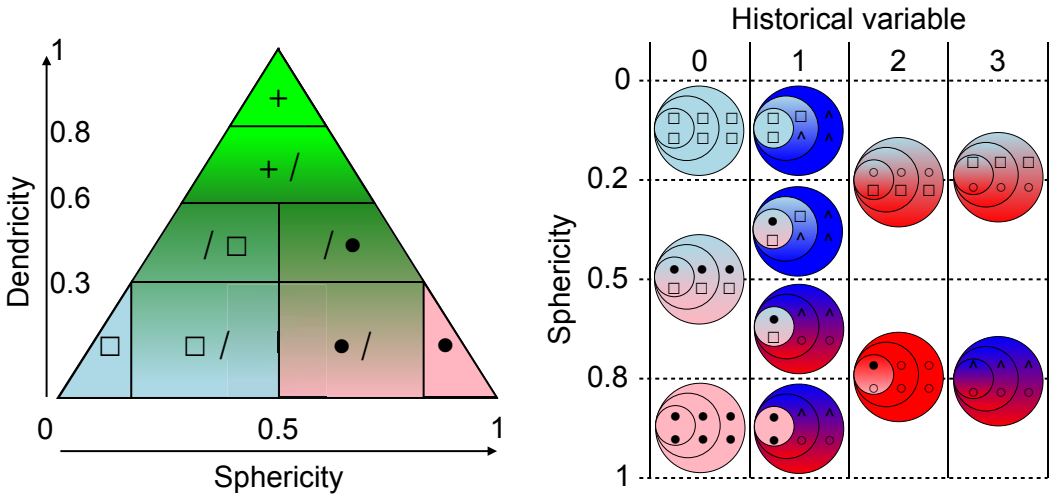

(a) Dendritic snow. Note that g_s is arbitrarily set to 0.3 mm for all dendritic snow ($d > 0$).

(b) Non dendritic snow. The size of the disk represents the grain size g_s (small disk $g_s < 0.5$ mm, intermediate $0.5 < g_s < 1.0$ mm, large 1.0 mm $< g_s$).

Figure 1.9: Recent snow is described in terms of dendricity and sphericity (a), and the "evolved" snow is defined by its grain size, sphericity and history (b). Color and symbol correspond to the international classification [Fierz et al., 2009]. If the snow type does not correspond to a unique type in the classification, it is described by two symbols. The first symbol (left or top) is the primary snow type, the second symbol (right or bottom) is the secondary snow type.

MEPRA [Giraud, 1992] deduces one risk level for natural avalanches and one for skier-triggered slab avalanches, based on the snowpack simulated by CROCUS. To compute these levels, MEPRA uses several "expert rules". For instance, if the snowpack stability increases from low to moderate, then the natural risk is relatively low since all potential avalanches should have already released. MEPRA is also based on a static stability index S computed for each layer and defined as:

$$S = \frac{\tau_{max}}{\tau_n + \tau_s}, \tag{1.1}$$

where τ_{max} is the shear strength of the layer, τ_n the shear stress due to the weight of snow and τ_s is a possible additional stress due to a skier. The value of S quantifies the level of instability for each layer. The risk level is computed with S but also with

the volume of snow above the potential failure layer, and additional expert rules not described here. The shear strength τ_{max} is a function of snow density ρ, type of grains (s, d, g_s, h) and the volumetric liquid-water content d_l. The relation between τ_{max} and the CROCUS output variables are empirical and obtained by adjustments on experimental data collected by J.-P. Navarre in the 1990's (unpublished work). This relation is of the general form:

$$\tau_{max} = C \cdot (10^{-4} \cdot \rho^2 - 0.6) + 0.12 \tag{1.2}$$

where C is a factor which depends on the snow type and the volumetric liquid water content:

$$C = C_{sph}(s,h) \cdot C_{den}(d) \cdot C_{mts}(g_s,d,s) \cdot C_{fe}(d_l,\rho) \cdot C_{fre}(d_l,\rho,h,s,C_{mts}). \tag{1.3}$$

The coefficients C_{sph}, C_{den}, C_{mts}, C_{fe}, C_{fre} respectively account for the effects of sphericity, dendricity, grain size, liquid water content and freeze-melt cycle on the shear strength. These coefficients are piecewise linear functions adjusted according experimental data and an expert analysis (see Appendix 1.A.1). Figure 1.10 shows the modeled τ_{max} as a function of density from dendritic snow. The parameterization of MEPRA is an "expert" parameterization also including qualitative knowledge on the influence of the morphology of grains on the bulk mechanical properties. Nevertheless, the complexity of the parameterization and the numerous cases distinguished on arbitrary threshold values tends to indicate that the current description of the microstructure might be not the most suited to characterize the mechanical properties of snow. The use of many adjustments variables in equations 1.2 and 1.3 also reveals our incomplete understanding of the link between microstructure and mechanical properties. Note that in order to evaluate MEPRA against snow mantle observations the ramsonde strength is also computed by MEPRA (G. Giraud, unpublished). The measured and modeled snow profiles are shown in Figure 1.8. The main structure of the measured ramsonde profile is fairly characterized by MEPRA and shows the absence of a dry slab structure (Figure 1.8). However, an important deviation from the measured penetration resistance is observed. Note that this deviation is partially due to the spatial variability of the snow mantle at the scale of a snow pit but it also reveals the difficulty to provide an accurate parameterization of the snow mechanical properties based on the current description of the snow morphology.

In summary, the formalism used to describe the snow microstructure in the system SCM is based on snow-pit observations. This provides a direct mean to compare simulations and observations. However, observations of the snow microstructure are mainly qualitative and restricted to a certain a number of classes (snow types in the international classification), whereas the mechanical properties are continuous. Moreover, the characterization of morphology (size and shape) of separated grains misses information about the connection between the snow grain which are determinant to estimate mechanical properties [Colbeck, 1997]. In consequence, the parameterization of mechanical properties in MEPRA requires many adjustment parameters.

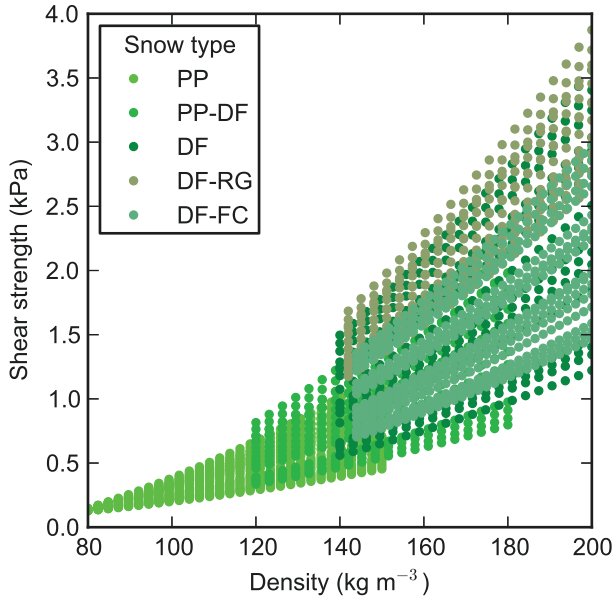

Figure 1.10: Shear strength computed by MEPRA as a function of density. For PP, $d \in [0.8, 1]$ and $s \in [0, 1]$. For PP-DF, $d \in [0.6, 0.8]$ and $s \in [0, 1]$. For DF, $d \in [0.4, 0.6]$ and $s \in [0, 1]$. For DF-RG, $d \in [0.0, 0.4]$ and $s \in [0.5, 1]$. For DF-FC, $d \in [0.0, 0.4]$ and $s \in [0, 0.5]$.

1.2.2 Research

The challenge of snow mechanics is to relate stress and strain with a parameterization taking into account strain rate, microstructure, temperature etc. Two main approaches to go toward constitutive modeling of snow can be distinguished: "descriptive" studies and "explicative" studies. In other words, these approaches are called "constitutive equations based on continuum theories" and "constitutive equations based on the structure" by Salm [1982] or "descriptive and experimental studies" and "microstructural studies" by Mellor [1975] and Theile [2010] or "correlation studies" and "causation studies" by Shertzer [2011]. The first approach consists in the measurement of mechanical properties under a certain range of experimental conditions and the formulation of an empirical model based on correlations between the observed properties and microstructural indicators or loading conditions. The second approach is intended to be explicative. A physical model is proposed based on assumptions of micro-mechanisms and on the microstructure geometry. Then, the model is compared against experimental data. If the agreement between the model predictions and experiments is good, the given assumptions are expected to be valid or, at least, to be relevant to predict the macroscopic behavior).

In the present state of the art, studies of both approaches will be presented with a more detailed focus on the second approach since this PhD work belongs to this explicative approach. Experimental methods to characterize the microstructure and to measure mechanical properties are prerequisite to both approaches and will be presented first.

1.2.2.1 Observations of the microstructure

The simplest and most common method to observe the snow microstructure in the field is by magnifying glasses (x10). A few individual grains are extracted from the snowpack and the grain size and grain shape are estimated visually. From these observations, a snow type is determined according to the international classification [Fierz et al., 2009]. The classification is not entirely deterministic since it relies on the interpretation of the observer based on limited information (size and shape). Moreover, fitting a continuum of microstructural patterns into a discrete classification inevitably requires arbitrary thresholds between types. For instance, endless discussions to choose between RG/FC (primary type is rounded grains, secondary type is faceted crystals) or FC/RG are common! To decrease variability due to various human observers, Lesaffre et al. [1998] automatized the evaluation of grain characteristics from digital grain images.

The observation of individual grains does not allow characterizing the bonding between grains. To overcome this limitation and in order to analyse the connectivity of the ice matrix, thin sections were rapidly used by snow scientists [e.g. Bader and Niggli, 1939]. A block of snow is slowly immersed in a liquid chemical with a negative melting point (e.g. acid diethyl ester [Kry, 1975a] or diethyl phthalate [Good, 1987]). The mixture is then frozen to obtain a solid block which is cut in thin slices. The thin slices reveal the geometry of the microstructure including the bonding system

in a certain plane. Under polarized light, the crystallographic structure can also be revealed [e.g. Quervain, 1983]. Arnaud et al. [1998] used preferential etching of the crystal boundaries to determine the crystallographic structure on thick sections. With stereological methods, 3D characteristics of the snow microstructure can be derived [e.g Kry, 1975a]. However, the assumptions used to convert measurements from 2D thin sections into 3D microstructural parameters are often overly simplified, e.g. the bonds are assumed to be planar and circular [Alley, 1986].

Good [1987] performed the first 3D reconstruction of a snow sample by combining a series of images of parallel thin sections. This method, called serial sectioning, is very time-consuming and rarely applied. The images of the successive slices are combined to create a 3D image of the microstructure. It allows deriving directly 3D properties which are difficult to extract from 2D data, especially properties linked to the connectivity of the ice matrix. A 3D image represents a huge amount of information. In the 1990's, the computing power was not able to efficiently analyse this wealth of data. Nowadays, computing power has tremendously increased and 3D imaging has become common. Theile and Schneebeli [2011] used serial sectioning and the preferential sublimation at grain boundaries [Arnaud et al., 1998] to detect crystallographic grain boundaries in a 3D sample. Serial sectioning remains the only method to obtain the 3D crystallographic structure with no limitations on the number of crystals.

Brzoska et al. [1999] conducted the first X-ray microcomputed tomography (μCT) on a snow sample. μCT uses back-projection algorithms to obtain 3D data from several radiographs recorded at different projection angles. μCT measures the 3D distribution of the X-ray attenuation coefficient, which differs between materials with different chemical composition and density. With this method, a snow sample can be imaged (e.g. a volume of 1000^3 voxels with a side-length of 10 μm) within one hour without any manual interactions. Moreover, μCT can be conducted without destroying the sample and therefore the time evolution of microstructure can be directly followed [Calonne et al., 2013, Schneebeli and Sokratov, 2004]. Very fragile and unstable samples collected in the field can be impregnated to avoid damage during transport and to block thermodynamic metamorphism [Flin, 2004, Heggli et al., 2009]. In this case, the imaging procedure is destructive since the impregnation product cannot be completely removed from the snow sample. Roscoat et al. [2011a] used X-ray diffraction contrast tomography (DCT) to reveal simultaneously the geometrical and crystallographic structure of snow. However, DCT is still under development and limited to about one hundred of different crystals, because of the difficulty to match each crystal to its diffraction spot.

1.2.2.2 Mechanical measurement techniques

The focus in this section is on the measurements of material properties of homogeneous snow. Many field tests exist to estimate the stability of a slope and to detect potential weak layers, such as the compression test, the extended column test, the Rutschblock or the saw test. Reiweger et al. [2010] also estimated the shear strength

of the weak layer - slab system in a cold laboratory. These measurements are essential to understand the release of an avalanche but from a material science point of view, they are already too complex to be able to understand the role of the microstructure on the overall behavior, because they characterize a system composed of different snow layers. I propose below an overview of measurements methods of homogeneous snow, an exhaustive list of which can be found in the reviews of Mellor [1975] and Shapiro et al. [1997].

Brittle failure properties To measure the mechanical hardness of a snowpack, Haefeli [Bader and Niggli, 1939] developed the ramsonde from penetrometers used in soil mechanics. The hardness is linked to the compression strength of snow at high strain rate. To improve the ability to detect thin layers in snow and to determine snow mechanical properties, Schneebeli and Johnson [1998] developed a new version of the ramsonde, a small diameter cone penetrometer called SMP. The small tip (5 mm diameter) of the SMP measures a highly variable force caused by the rupturing of microstructural elements in the snow. SMP force measurements are linked to the snowpack stability. However, exact interpretation of the SMP signal as a function of snow strength is not completely understood. For instance, Herwijnen [2013] showed that the compaction zone around the SMP tip is far from negligible and has to be accounted for when interpreting SMP force measurements.

The shear strength of alpine snow is an important parameter in avalanche stability evaluation. Several investigators have indexed the shear strength of alpine snow using in situ shear frames, in situ shear vanes, in situ rotary vanes or laboratory shear apparatus (see Perla et al. [1982] for references). Strong effects of apparatus geometry and loading rate are present in the shear indices. Barbero et al. [2013], Podolskiy et al. [2014] developed a new shear apparatus with a possible control of the normal pressure and shear strain rate.

Perla [1969] used cantilever beams to determine an index for tensile strength of snow. Kirchner et al. [2004] also used cantilever beams to measure snow strength and showed that there is no size dependence (at the scale around 0.1 m) of strength but that the measured strength distribution exhibits a very low Weibull modulus, which indicates that strength measurements can be contaminated with large statistical errors. Sigrist [2006] used cantilever beam tests and three-point bending tests to measure strength. He also used pre-cracked samples to measure toughness in mode I and II. Upadhyay et al. [2007] used a centrifugal machine to measure the tensile strength of snow. Note the excellent review of tensile strength measurements from Borstad [2011].

Elastic properties Elastic properties of snow are difficult to measure because elasticity is limited to very small strains and snow is very fragile. Nakaya [1959] measured the visco-elastic properties by a transversal vibration method. Sigrist [2006] used cyclic loading device (developed by F. Hempel) oscillating at 100 Hz. Camponovo and Schweizer [2001] performed dynamic torsional shear experiments

to measure the storage shear modulus and the dynamic viscosity. Scapozza [2004] conducted quasi-static compression tests and measured the Young's modulus. However, according to Kirchner et al. [2001], no reliable data for the elastic properties of snow exist.

Creep deformations Desrues et al. [1980] conducted tri-axial creep experiments on snow to formulate constitutive equations for low strain rate deformations. Chandel et al. [2007] performed numerous uniaxial unconfined constant stress experiments to fit a 4-parameters Burger's model on the creep behavior. Narita [1980] investigated the dependence of failure in tension on the strain rate. McClung [1977], Schweizer [1998] measured shear strength under varying conditions such as strain-rate. Recently, Schleef et al. [2014] used a new microcompression device for in situ microtomography measurements.

1.2.2.3 Correlation between microstructure indicators and mechanical properties

Mellor [1975] and Shapiro et al. [1997] concluded in their review that "it is necessary to characterize the microstructure along with determining the density in order to derive indicators of the mechanical properties of snow". Finding indicators of the microstructure that well correlate with mechanical properties is the goal of "descriptive studies". However, in practice, most studies determine mechanical properties and characterize the microstructure only with density. Moreover, it appears that most of the studies deal with only one type of snow, Rounded Grains (RG), which are the easiest to handle and to find in the field. Consequently most of the parameterizations of snow mechanical properties apply to these grains and are function of density ρ only, e.g.:

Young's modulus (Pa): $E(\rho) = 9.68 \times 10^8 \cdot (\rho/\rho_{ice})^{2.94}$ [Habermann et al., 2008]

Tensile strength (Pa): $\sigma_t(\rho) = (3.5 \pm 1.4) \times 10^5 \cdot (\rho/\rho_{ice})^{2.4\pm0.4}$ [Borstad, 2011]

Shear strength (Pa): $\sigma_s(\rho) = 2.075 \times 10^5 \cdot (\rho/\rho_{ice})^{2.91}$ [Yamanoi and Endo, 2002]

Toughness I (Pa$\sqrt{m}$): $K_I(\rho) = 6.30 \times 10^4 \cdot (\rho/\rho_{ice})^{2.76}$ [Sigrist, 2006]

As already shown on Figure 1.7, parameterization with density displays a great scatter, which confirms that other microstructural effects cannot be neglected. A few studies distinguish snow types on which systematic measurements are done. Jamieson and Johnston [1990] measured the tensile strength σ_t of snow samples of different types. They aggregated the different snow types in two groups: group I composed of PP, DF, RG and group II composed of FC, FC/RG. The parameterization of σ_t for group I is $\sigma_t(\rho) = 7.97 \times 10^5 \cdot (\rho/\rho_{ice})^{2.39}$ and for group II is $\sigma_t(\rho) = 5.83 \times 10^5 \cdot (\rho/\rho_{ice})^{2.65}$. This parameterization shows that grains presenting faceting (group II) are more fragile than the other snow types. However, a large scatter remains in each group and the parameterization is purely empirical and gives no clue on the physical mechanisms explaining how the presence of faceted grains affects strength.

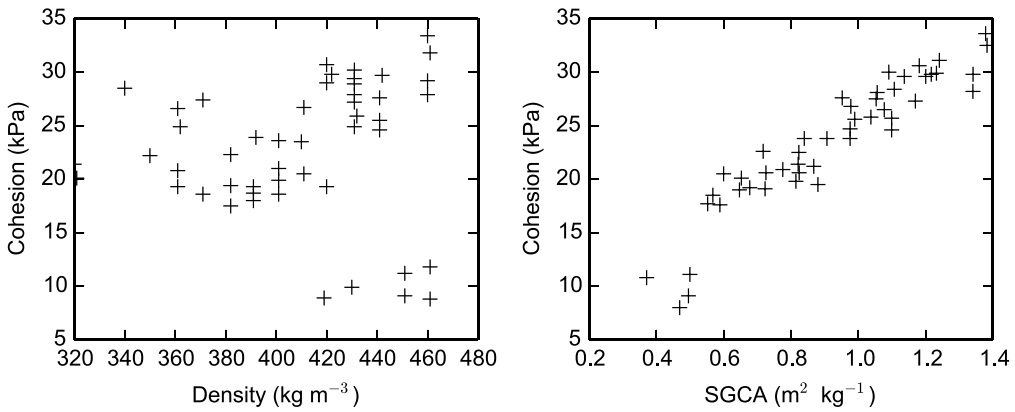

Figure 1.11: Cohesion strength vs. density or specific grain contact surface area (SGCA). Figure adapted from [Voitkovsky et al., 1975]. The procedure used to measure cohesion and SGCA is not detailed by Voitkovsky et al. [1975].

The bonding between snow grains has long been believed to be a reliable strength predictor. Voitkovsky et al. [1975] showed that the specific grain contact surface (cross-sectional area of the bonds per unit ice mass, SGCA) was a better cohesion predictor than density (Figure 1.11). However, Voitkovsky et al. [1975] do not give details on the measurement of cohesion strength and of the SGCA on thin sections, which can be ambiguous. Qualitatively, it is expected that the bonding plays a major role, but it is unclear whether the overall grain contact area is relevant to describe the bonding. Indeed, only a few bonds break during failure whereas the SGCA encompasses the entire set of bonds.

To conclude, the approach of descriptive studies is simple and provides, in practice, empirical constitutive models used for larger scale simulations [e.g. Gaume, 2013, Podolskiy et al., 2013]. However, experiments can be difficult to conduct because snow is a very fragile material. Moreover, the empirical models are valid only for the tested experimental conditions. Since they cannot be extrapolated, analysing the effects of the wide range of strain rate, temperature, density, snow grain morphology etc. requires an endless study. Lastly, since they are based on a priori correlation, the empirical models do not guide into a relevant parameterization of the microstructure. As stated by Salm [1982], "first we must understand what really happens when snow deforms and fractures".

1.2.2.4 Explicative studies

Studies based on observations and schematic microstructure Kry [1975b] first incorporated microstructure indicators (other than density) in constitutive models of snow. He developed constitutive relations with the concept of chains of grains, defined as series of stress-bearing grains. According to Kry [1975b], the

mechanical basic unit of snow structure is not the grain but a series of grains. Through this concept, the importance of individual bonds is combined with the connectivity of the bonding system between several grains. This concept contrasts with the usual description of snow as individual grains. Kry [1975b] formulated a quantitative model linking the Young's modulus of snow E under uniaxial strain to microstructural variables:

$$E = \left(\frac{M\lambda}{k}\right)\left(\frac{r_b}{L_g}\right)^2 L_g^2 \left(\frac{E_b}{a}\right) \tag{1.4}$$

where M is the number of chains per unit volume, λ is the mean length of chains in the direction of applied strain, k quantifies the orientation of individual bonds relatively to the direction of the overall chain orientation, r_b is the mean bond radius, L_g is the mean grain diameter, E_b is the bond Young's modulus and a depends on the form of the neck. The relation 1.4 involves many variables which are not measurable, and is thus not usable in practice. But with this relation, Kry [1975b] was able to explain observed changes in mechanical properties, which were not captured by the number and size of the bonds. For instance, the increase of the Young's modulus of an order of magnitude observed by Kry during the deformation of snow to a strain of 30% is accompanied by an increase of the total number of bonds by a factor of 1.5 only. In fact, the applied stresses are transmitted by only a fraction of the total number of grain bonds. Hence, it is the activation of new series of stress bearing grains, which mainly explains the stiffening of the snow sample and not solely the creation of new bonds.

After the pioneering work of Kry [1975a,b], different studies have attempted to incorporate state variables describing the bonding system into constitutive models. Hansen and Brown [1988] introduced internal state variables corresponding to mean intergranular slip-distance and mean grain size, and derived constitutive relations in the formal framework of thermodynamics. Mahajan and Brown [1993] developed a constitutive theory to describe the mechanical properties of snow in terms of the properties of the ice grains and the necks that interconnect them. They also incorporated different deformation mechanisms at the grain scale such as ice deformations at the bonds and inter-particle sliding. By considering only dislocation strains and not inter-particle sliding in their model, Bartelt and von Moos [2000] found a good agreement with low-strain rate triaxial experiments and concluded that the dislocations strains are the dominant deformation mechanisms in this regime. This emphasizes the "explicative" power of combined experiments and models. Reiweger [2009] used a fiber bundle model and the competition between fiber sintering (healing) and breaking to reproduce the ductile-to-brittle transition exhibited by snow with increasing strain rate. Nicot [2004] considered the directional arrangement of the microstructure through distribution functions of bond orientation. However, no clues are given to compute these distributions and, in practice, Nicot [2004] used an isotropic distribution of bonds orientation. Shertzer [2011] characterized the directional arrangement of bonds with 2D slices of μCT images and linked the textural arrangement of snow to material properties as strength or thermal conductivity. He

showed that the structural anisotropy due to vertical temperature gradient cannot be neglected to model the material properties of faceted snow types.

The mentioned studies [Bartelt and von Moos, 2000, Hansen and Brown, 1988, Mahajan and Brown, 1993, Nicot, 2004, Shertzer, 2011] use grains as the basic unit of the snow structure and do not consider chains of ice grains as done by Kry [1975b]. They assume that the effect of grain connectivity and directional arrangement at the grain scale dominates the one at the scale of chains. They recognize that this assumption is not valid for low-density snow. For moderate- and high-density snow, it remains to be proved whether the structure organizes only at the grain scale to support the load.

Johnson and Hopkins [2005] developed a discrete element model (DEM) for snow. They described the snow structure by randomly orienter cylinders of random length and hemispherical ends. They used a complex contact law incorporating bond deformation due to elasticity, plasticity, viscosity, friction and fracture, and bond growth due to sintering. The cylinders, i.e. the discrete elements, are rigid and the overall behavior is due to the relative displacement of the elements. The simulations account for all interactions between the cylinders and allow to follow microstructure changes during deformation. For instance, Johnson and Hopkins [2005] explained the dependence of viscosity on density by the simulated increase of the coordination number, the mean contact area and the viscosity at the contacts. Although the model was able to replicate the observed dependence of the snow bulk viscosity on density, the model assumptions are questionable. First, the DEM approach assumes that the dominant deformations are intergranular. This assumption is reasonable to model the brittle behavior of snow but this is not clear for the ductile behavior, as discussed by Meyssonnier et al. [2009] and Theile et al. [2011]. Second, the microstructure is represented by random cylinders. The relevance of this simplification is not evaluated by the authors. The distribution of the cylinder lengths can be chosen in the model to differentiate snow microstructures, but no direct link between this model parameter and observed snow types is proposed.

In summary, the presented models try to explain snow deformation by accounting for deformation processes at the microstructural level. Understanding the main processes active at the microstructural level and the influence of microstructure on the overall mechanical behavior is a necessary step to guide into a constitutive model for snow which is valid for a wide range of problems. In practice, this parameterization is still missing because of the over-simplification of the microstructure. First, the simplification of the microstructure inevitably introduces a bias in the model. It is thus difficult to assess if the agreement of the model with the experiments can be explained by the right choice for mechanical behavior at the microstructural level. For instance, as mentioned by Theile [2010], Nicot [2004] and Alley [1987] both found a good agreement of their model with experimental data obtained under the same conditions but Nicot [2004] considered only normal deformation at bonds whereas Alley [1987] considered only shear deformation. Second, these models rely on some variables describing the microstructure. However, it is sometimes hard to link the chosen variables to real snow. Indeed the modeled snow structure is often

too far from what can be observed, and the model variables cannot be unambiguously defined for all snow types.

Studies based on microstructure captured by μCT Owing to easier access to 3D imaging facilities and increasing computational capabilities, it is now possible to use the full 3D representation of microstructure as a direct input mechanical models.

Schneebeli [2004] used the voxel-based finite element (FE) programme developed by Rietbergen and Weinans [1996] to simulate the Young's modulus of snow. The mesh of the FE model is composed of hexagonal elements directly corresponding to the voxels of a 3D image. The material properties are set to isotropic elasticity with the Young's modulus (E_{ice} = 10 GPa) and the Poisson's ratio (ν_{ice} = 0.3) of ice. Schneebeli [2004] observed a decrease of the Young's modulus from 226 MPa to 62 MPa for a sample of rounded grains of density about 243 kg m^{-3} evolving toward faceted crystals with temperature gradient metamorphism. The computed moduli are 10-100 times larger than existing measurements [e.g. Mellor, 1975]. Schneebeli explained this difference by the effect of strain rate, not accounted for in the FE model. The observed stress concentrations in the microstructure also revealed that it is very difficult to deform snow elastically without damaging it. Comparably, Pieritz et al. [2004] presented a method to compute Young's modulus with tetrahedral FE but the obtained preliminary results were only qualitative.

Srivastava et al. [2010] used a similar approach with the voxel-based FE programme of Garboczi [1998]. They also simulated snow elastic properties of rounded grains (density of 350 kg m^{-3}) evolving toward depth hoar (density of 400 kg m^{-3}) with temperature gradient metamorphism. The Young's modulus in the direction parallel to the imposed temperature gradient increased from 0.5 GPa to 1 GPa, whereas in the directions perpendicular to the gradient, it remains constant equal to 0.5 GPa. Interestingly, Srivastava et al. [2010] showed that the anisotropy introduced by the temperature gradient is visible in the mechanical properties of snow. With the long-term objective of developing constitute models of snow, Srivastava et al. [2010] used the simulation results as "numerical experiments" to correlate geometrical characteristics (such as the mean intercept length) of the snow microstructure to mechanical properties, here the Young's modulus. Surprisingly, the observed trend, stiffening of the structure with temperature gradient, is opposite to the one observed by Schneebeli [2004]. This disagreement may be explained by the small size of the simulation volume, which might not be representative of the microstructure, regarding the mechanical properties. The simulated volume is $3.6 \times 3.6 \times 3.6$ mm^3 in Schneebeli's study and $2.6 \times 2.6 \times 2.6$ mm^3 in Srivastava's study. However, Srivastva et al. computed the elastic modulus of several sub volumes of the same image and obtained consistent values, indicating the representativeness of the simulation volume size.

Theile et al. [2011] simplified the full 3D microstructure captured by tomography into a 3D network of beams (Figure 1.12). This simplification reduces the number

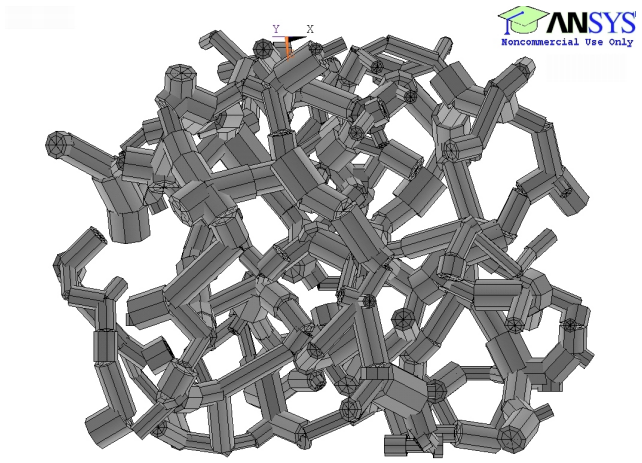

Figure 1.12: Simplification of the snow microstructure into a network of beams. The microstructure represents a cube of 2 mm side length of rounded grains. Figure taken from [Theile, 2010].

of degrees of freedom and enables to carry out creep simulation with FE. On the one hand, the use of a non linear constitutive equation for ice (here Glen's law with anisotropic ice properties, in contrast to isotropic elasticity in [Schneebeli, 2004, Srivastava et al., 2010]) significantly increases the complexity of the equations in the FE model. On the other hand, it is necessary to conduct simulations on sufficiently large volumes which are representative of the microstructure. In the model, each beam is supposed to correspond to a single crystal. The c-axis orientation of the crystals was randomly chosen in a uniform orientation distribution. The model does not take into account boundary sliding since only the beams deform. Theile et al. [2011] obtained a good agreement between the measured and modeled snow viscosity during the creep experiment. Their study points out that the contribution of single anisotropic grains cannot be averaged to a polycrystalline material since the displacement of the boundaries of ice crystals are not as constrained in snow as in ice. Moreover, Theile et al. showed that the increase of viscosity during creep is mainly explained by the creation of new bonds (topological change of the microstructure) and not by the increase of density. However, it is not possible to discern from the obtained results whether grain boundary sliding or intra-crystalline strain is the dominant deformation mechanism. The simplification of snow as a network of beams was applied to rounded grains snow. It is doubtful that this method could be used for different snow types such as depth hoar. Moreover, large FE cannot correctly reproduce the highly heterogeneous stress distribution created by a sudden load of the microstructure. In the case of creep, the stress distribution is "smoothed" by large strains and the beam representation might be therefore relevant in this case.

FE simulations are computationally very expensive which generally limits the simulations to small snow volumes of a few mm^3. To overcome this limitation and compute relevant mechanical properties from the snow microstructure, three main

approaches can be distinguished:

- *Simple basis equation.* Schneebeli [2004] was able to solve a FE problem composed of 5.4×10^6 elements (cubic snow sample of side-length 7.56 mm) on a computer with only 16 GB RAM because the material constitutive law was simple (isotropic linear elasticity) and all elements were of identical shape (cubes of side length equal to the image resolution). Linear elasticity enables to use "easy" matrix multiplication. Since all elements are identical in size and have the same orientation and material properties, all element stiffness matrices are the same. Thus, only one element stiffness matrix has to be stored, which enables fast solution algorithms that can compensate for a large number of elements [Rietbergen and Weinans, 1996].

- *Smart mesh.* The advantage of the voxel-based FE can also be a drawback. Zones of the ice matrix that are critical to model the mechanical behavior are described with the same resolution as the ones that do not contribute to the overall behavior. The voxel-based FE approach requires a large number of elements. The computing strategy of Theile et al. [2011] was to simplify the full 3D microstructure by keeping only the microstructural ingredients which are essential for the given application, i.e. to understand the role of the microstructure topology on snow viscosity.

- *Statistics on many sub-volumes.* Srivastava et al. [2010] computed the elastic modulus of snow on sub-volumes of the same 3D image. If the number of realizations is large enough, calculations can be done on relatively small volumes and averaged to obtain a value representative of the whole [Kanit et al., 2003]. The variance of computed apparent properties for each volume size can be used to define the precision of the estimation [Srivastava et al., 2010]. However, a systematic bias in the estimation of the effective properties can be observed if the sub-volumes are too small [Kanit et al., 2003].

In summary, micro-mechanical models for snow based on microtomographic data are very scarce. None of the existing models considered the brittle behavior of snow and re-arrangement of grains due to bond breakage. The main limitation of these models is their huge computing cost.

1.2.3 Scientific questions and approach

The principal objective of this PhD thesis is to investigate the link between snow microstructure and snow mechanical properties. Given the present state of knowledge, a constitutive model able to predict the mechanical properties for a wide range of loading conditions and snow types is still missing. During the last 30 years, efforts have been made to develop parameterizations of snow properties based on density and a discrete snow classification. This approach is still used in practice by avalanche forecasting services. The developed models are able to capture the first

order features of the snow mechanical behavior, but they are based on a schematic and oversimplified representation of the microstructure. Their link with "real" snow is thus difficult to assess and their extent of validity is limited.

Thanks to X-ray tomography, this limitation can now be overcome and full 3D images of the microstructure can be obtained with a resolution of a few microns. The main thrust of this thesis is to develop mechanical models of snow based on two fundamental ingredients: a realistic 3D geometry (1) composed of ice (2). The idea is to start from the most precise description of the snow microstructure available at present (microtomography) and the mechanical properties of ice, which are well-known compared to snow, in order to investigate the mechanical properties of snow. This approach was used by Pieritz et al. [2004], Schneebeli [2004], Srivastava et al. [2010], Theile [2010] to model the elastic and creep properties of snow. In this thesis, the focus is on rapid deformation of snow, including its brittle behavior and large deformations caused by grain re-arrangements. From our point of view, this constitutes an original contribution to snow mechanics.

Implementing this approach demands first a representation of the microstructure compatible with a mechanical model, and, second, a constitutive material for ice. In this thesis, the geometry of the ice matrix is extracted from X-ray microtomographic data and ice is supposed to be elastic brittle. The developed models are used to perform numerical experiments which help to follow and understand the deformation occurring in the ice matrix. Microtomography based models cannot be used in the daily forecast of snow avalanches for the whole Alps since tomography is time-consuming and limited to a few samples prepared and measured in a laboratory. However, the results of these models guide the parameterization of the mechanical properties of snow.

In this thesis, we have focused our efforts on the following scientific questions:

- How to get the maximum information out of microtomographic data? X-ray tomography provides an approximate representation of the spatial distribution of the attenuation coefficient to X-rays. Numerical processing is required to extract the position of pores and ice. We develop an algorithm enabling to process Gigabytes of tomographic data automatically and taking advantage of some specific properties of the scanned material (snow).

- How does failure in tension initiate in snow? In order to reproduce the brittle properties of snow, is it accurate to model snow as a "simple" structure of homogeneous brittle ice? To answer these questions, we develop a FE model accounting for the 3D geometry of the microstructure and the brittle failure of ice. The model does not account for the creation of new contacts, which are rare under tension. In parallel, the mechanical properties of the samples imaged by tomography and used as inputs of the model were also measured by an independent tensile test.

- How to compute large deformations of snow on representative volumes captured by microtomography, within the duration of one PhD thesis? A 3D

image represents a huge amount of data because the resolution must be small enough to capture essential structural details and the scanned volume must be large enough to be representative. Direct simulation of complex processes such as large deformations and the creation of new contacts is therefore extremely computationally intensive. It is necessary to simplify the representation of the microstructure and to evaluate the relevance of the simplification. We propose to consider snow as a cohesive granular material and develop a discrete element approach to model the mechanical behavior of snow.

- What makes certain snow so fragile? It is generally admitted that temperature gradient (TG) metamorphism tends to weaken snow, contrary to isothermal metamorphism. The presence of facets in the snow mantle is often used as a proxy of the action of TG metamorphism but does not explain why the sample is especially weaker. We propose a characterization of the bonding system, which reveals the very low connectivity of the ice matrix and the weakening effect of TG metamorphism.

1.3 Structure of the thesis

This thesis is a collection of articles which are either already published, submitted or under preparation. The work presented in the articles was done in collaboration with the co-authors but numerical developments, measurements, analysis and writing were mainly done by myself. All chapters can be read independently. As a consequence, the manuscript inevitably contains a few repetitions. The thesis is organized as follows.

Chapter 2 To allow a quantitative characterization of the microstructure, the output of the microtomograph, a three-dimensional grayscale image representing the X-ray attenuation coefficient, has to be segmented into a binary ice/pore image. This step, called binary segmentation, is crucial and affects all subsequent analysis and modelling. We developed a new binary segmentation algorithm based on the minimization of a segmentation energy. This energy is composed of a data fidelity term and a regularization term penalizing large interface area, which is of particular interest for snow where metamorphism naturally tends to reduce the surface energy. We evaluated the algorithm on synthetic images, whose ground truth is known, and on images of snow samples impregnated and conserved in 1-chloronapthalene, which constitute a three-phase material because of the unavoidable presence of residual air bubbles. The developed algorithm is shown to be accurate, robust and time-saving owing to reduced user interaction. It was used to prepare the images used in this thesis (except in Chapter 4).

This work was published as *Hagenmuller, P., G. Chambon, B. Lesaffre, F. Flin, and M. Naaim (2013), Energy-based binary segmentation of snow microtomographic images, J. Glaciol., 59(217), 859-873, doi:10.3189/2013JoG13J035.*

Chapter 3 The energy-based binary segmentation method was also applied to air-ice images obtained in the context of an international intercomparison workshop (Snow Grain Size Workshop, Grenoble-Davos-Reading, 2013-2014). One of the main objectives of the intercomparison is to discuss about the accuracy, comparability and quality of existing measurement methods to measure the specific surface area (SSA) of snow. I focused on the measurement of SSA from microtomographic data. SSA is not directly a mechanical indicator but the intercomparison provides a way to evaluate the binary segmentation method and the effective resolution of the images. The flexible energy-based segmentation method (Chapter 2) was adapted to two-phase images (air-ice) and applied to 38 images on which SSA measurements were conducted with independent instruments. Different algorithms to compute a surface of a binary object were also evaluated. It is shown that the variability of microstructure characteristics due to numerical processing can be limited to be of the same order as the one due to the spatial variability observed within one snow layer. However, certain techniques used to determine the segmentation threshold (local minimum) or the surface area on the binary image (marching cubes) introduce a systematic bias in the computation of density and specific surface area and are therefore not recommended.

The inter comparison is still undergoing. This study was presented during the workshop sessions (April 2013 in Grenoble, France; August 2014 in Reading, UK) and some of its results will be incorporated in a "workshop" article which summarizes the intercomparison study, and/or a specific paper devoted to the microtomographic method.

Chapter 4 The tensile strength of snow and microstructural failure processes were simulated based on a finite-element mesh of the ice matrix. Modeling procedures used only the elastic properties of ice with bond fracture assumptions as inputs. Combined measurements and simulations on rounded grains snow type showed that the model is able to predict tensile strength successfully. The model gives an insight on the deformation process under tension and revealed that the microstructure experiences highly concentrated tensile stress but also significant compressive stresses in response to macroscopic tension, and that failure of bonds occurs for very small strain ($< 10^{-4}$) and creates a pseudo-plastic yield curve. The modeling approach is however limited to the tested snow type, to tension loading and to relatively small volumes. Indeed, the used bond detection algorithm (distance-based watershed) works only for rounded grains, the model does not take into account the creation of new contacts in the ice matrix and the description of the microstructure with elements of homogeneous size requires a large amount of computing power.

This work was published as *Hagenmuller, P., T. Theile, and M. Schneebeli (2014a), Numerical simulation of microstructural damage and tensile strength of snow, Geophys. Res. Lett., 41(1), 86-89, doi:10.1002/2013GL058078.* I conducted the corresponding microtomography measurements and cold-room experiments during my master thesis in Davos, Switzerland (March-July 2011). Numerical simula-

tions and final writing of the article was done during the first six months of my PhD.

Chapter 5 A novel method to model snow as a granular material is proposed. The finite element simulations, developed in Chapter 4, revealed that high stresses are concentrated at constrictions between grains and that, under brittle regime, the overall mechanical behavior of snow is controlled by the failure of bonds. Simplifying the description of the snow microstructure into a set of rigid grains interacting through their contacts is therefore relevant in this regime. We proposed a new method to directly identify individual snow grains defined as zones separated by regions of potential mechanical weakness, in the microtomographic images. Our new method, based on local geometrical criteria, is shown to successfully detect contacts directly inferred from an explicit numerical mechanical experiment. The new grain segmentation algorithm enables to apply the previously developed tensile strength FEM model (Chapter 4) to different snow types, and not only to rounded grains, and opens perspectives to model the deformation regimes governed by contact interactions and particle re-arrangement (Chapter 6).

This work was published as *Hagenmuller, P., G. Chambon, F. Flin, S. Morin, and M. Naaim (2014), Snow as a granular material: assessment of a new grain segmentation algorithm, Granul. Matter, 16(4), 421-432, doi:10.1007/s10035-014-0503-7.*

Chapter 6 In this chapter, the outputs of the grain segmentation algorithm are used to develop a discrete element model based on the full three-dimensional microstructure captured by microtomography. The model assumes that snow is composed of rigid grains interacting through localized contacts accounting for cohesion and friction. Single grains are represented as rigid clumps of spheres. The model is applied to different snow samples subjected to confined compression. The sensitivity analysis of the model to its parameters shows that artefacts introduced by the modeling approach are limited compared to variations due to the geometry of the microstructure. The model evidences that the compression behavior of snow is mainly controlled by the density of the sample, but that deviations from a pure density parameterization are non negligible during the first phase of compression (density < 300 kg m^{-3}). In particular, the model predicts that, for a given density, faceted crystals are less resistant to compression than rounded grains or decomposed snow. For higher compaction regime (density > 300 kg m^{-3}), no clear difference between snow types has been observed in the model prediction.

This work is under preparation for publication in The Cryosphere.

Chapter 7 An appealing approach to characterize the bonding system of the snow microstructure is to derive parameters directly from the grain segmentation results (Chapter 5), such as the specific grain contact area. However, the definition of grains is always relative to a certain threshold. Interpreting the geometrical

characteristics of the grains assembly is therefore challenging since they depend on both microstructure and grain segmentation algorithm. In order to characterize the bonding system independently of a grain segmentation procedure, we introduced a new microstructural indicator, *the minimum cut density*. This variable quantifies, on three-dimensional (3D) microtomographic images of snow, the minimal areal density of a surface that disconnects two opposite faces of the sample. We correlate the minimum cut density to thermal conductivity and elasticity properties derived from numerical simulations based on the same microtomographic images. The significant correlation between these variables indicates that the minimum cut density is a promising geometrical variable for the parameterization of mechanical properties. Moreover, the structural anisotropy of faceted crystals and depth hoar is well estimated by the minimum cut density.

This work is under minor revision for publication as *Hagenmuller, P., N. Calonne, G. Chambon, F. Flin, C. Geindreau, and M. Naaim (n.d.), Characterization of the snow microstructural bonding system using the minimum cut density, Cold Reg. Sci. Technol.*

Chapter 8 The last chapter summarizes the main results obtained during the thesis and opens perspectives for future research.

1.A Appendix

1.A.1 Description of the calculation of the shear strength τ_{max} in MEPRA

In this section, the numerical relations between the shear strength of MEPRA and the output variables of CROCUS are detailed. The relation between the shear strength and the properties of the snow layer is of the general form:

$$\tau_{max} = C \cdot (10^{-4} \cdot \rho^2 - 0.6) + 0.12$$

where C is a factor which depends on the snow type and the volumetric liquid water content d_l:

$$C = C_{sph}(s,h) \cdot C_{den}(d) \cdot C_{mts}(g_s,d,s) \cdot C_{fe}(d_l,\rho) \cdot C_{fre}(d_l,\rho,h,s,C_{mts}).$$

The coefficients C_{sph}, C_{den}, C_{mts}, C_{fe}, C_{fre} respectively take into account the effects of dendricity, sphericity, grain size, liquid water content, freeze-melt cycle on the shear strength as following:

Sphericity coefficient $C_{sph}(s,h)$:

$s_h = \min(s, 0.8)$ if $h \in \{3,5\}$
$s_h = s$ elsewhere
$C_{sph} = 0.450 + 0.7 \cdot (s_h - 0.00)$ if $s_h \leq 0.25$
$C_{sph} = 0.625 + 1.0 \cdot (s_h - 0.25)$ if $0.25 < s_h \leq 0.50$
$C_{sph} = 0.875 + 0.6 \cdot (s_h - 0.50)$ if $0.50 < s_h \leq 0.75$
$C_{sph} = 1.025 + 0.5 \cdot (s_h - 0.75)$ if $0.75 < s_h$

Dendricity coefficient $C_{den}(d)$:

$C_{den} = 1.0 - 0.4 \cdot (d - 0.00)$ if $d \leq 0.25$
$C_{den} = 0.9 - 0.4 \cdot (d - 0.25)$ if $0.25 < d \leq 0.50$
$C_{den} = 0.8 - 0.8 \cdot (d - 0.50)$ if $0.50 < d \leq 0.75$
$C_{den} = 0.6 - 0.6 \cdot (d - 0.75)$ if $0.75 < d$

Grain size coefficient $C_{mts}(g_s,d,s)$:

Mean grain size $\bar{g_s} = 0.4 - s$
$C_{mts} = 1$ if $d > 0$
$C_{mts} = 1 - (0.8 - 0.2 * s) \cdot 0.53 \cdot (g_s - \bar{g_s})$ elsewhere

Liquid water content coefficient $C_{fe}(\rho, d_l)$:

Ratio to reference liquid water content $e_c = d_l/[0.05 \cdot (1 - \rho/\rho_{ice})]$
$C_{fe} = 1.000$ if $e_c \leq 0$
$C_{fe} = 1.000 + 1.00 \cdot e_c$ if $0.0 < e_c \leq 0.1$
$C_{fe} = 1.335 - 2.35 \cdot e_c$ if $0.1 < e_c \leq 0.3$
$C_{fe} = 0.750 - 0.40 \cdot e_c$ if $0.3 < e_c \leq 0.9$
$C_{fe} = \max(\min(\rho/1000 - d_l, 0.35), 0.15)$ if $0.9 < e_c$

Melt-freeze cycle coefficient $C_{fre}(h, d_l, \rho, s, C_{mts})$*:*
Dry snow coefficient $C_{fre,dry} = 1.5 \cdot ((1.15 + 0.2 \cdot (1 - s))/1.15) \cdot (1 + 0.2/C_{mts})$
$C_{fre} = 1.0 \quad \text{if } h \leq 1$
$C_{fre} = C_{fre,dry} \quad \text{if } 1 < h \leq 3 \text{ and } e_c = 0$
$C_{fre} = 1.0 \quad \text{if } 1 < h \leq 3 \text{ and } e_c > 0$
$C_{fre} = C_{fre,dry} \quad \text{if } 3 < h \text{ and } e_c = 0$
$C_{fre} = -2.00 \cdot ec + 1.500 \quad \text{if } 3 < h \text{ and } 0.0 < e_c \leq 0.1$
$C_{fre} = -0.75 \cdot e_c + 1.375 \quad \text{if } 3 < h \text{ and } 0.1 < e_c \leq 0.5$
$C_{fre} = 1.0 \quad \text{if } 3 < h \text{ and } 0.5 < e_c$

Chapter 2

Energy-based binary segmentation of snow microtomographic images

Abstract X-ray microtomography has become an essential tool to investigate the mechanical and physical properties of snow, which are tied to its microstructure. To allow a quantitative characterization of the microstructure, the grayscale X-ray attenuation coefficient image has to be segmented into a binary ice/pore image. This step, called binary segmentation, is crucial and affects all subsequent analysis and modeling. Common segmentation methods are based on thresholding. In practice, these methods present some drawbacks and often require time-consuming manual post-processing. Here, we present a binary segmentation algorithm based on the minimization of a segmentation energy. This energy is composed of a data fidelity term and a regularization term penalizing large interface area, which is of particular interest for snow where sintering naturally tends to reduce the surface energy. The accuracy of the method is demonstrated on a synthetic image. Then, the method is successfully applied on microtomographic images of snow and compared to the threshold-based segmentation. The main advantage of the presented approach is that it benefits from local spatial information. Moreover, the effective resolution of the segmented image is clearly defined and can be chosen a priori.

Contents

2.1 Introduction

The microstructure of snow, i.e. the three-dimensional (3D) configuration of the ice matrix determines crucial snow properties as, for instance, albedo which is relevant for the computation of the surface energy balance, or mechanical strength for avalanche hazard forecasting and evaluation. The microstructure characterization based only on bulk parameters such as density is often insufficient to model precisely the mechanical and physical behavior of snow [Mellor, 1975, Shapiro et al., 1997]. A better understanding of the physical and mechanical snow properties requires a 3D representation of the microstructure at a scale of a few microns [Schneebeli, 2002]. Thanks to an easier access to 3D imaging facilities such as X-ray computed microtomography, and increasing computational capabilities, 3D images of the snow microstructure have now become available. Numerical simulations directly based on the real 3D microstructure of snow have been successfully applied to model thermal conductivity [Calonne et al., 2011, Kaempfer et al., 2005], snow metamorphism [Brzoska et al., 2008, Flin and Brzoska, 2008, Flin et al., 2003] and mechanical properties [Pieritz et al., 2004, Schneebeli, 2004, Srivastava et al., 2010, Theile et al., 2011]. Acquiring 3D images of snow is, therefore, a key issue in snow research.

Different techniques can be used to capture the 3D microstructure of snow, among which the most common are serial sectioning [Good, 1987, Perla et al., 1986, Schneebeli, 2000] and X-ray micro-computed tomography (μCT) [Brzoska et al., 1999, Chen and Baker, 2010, Coléou et al., 2001, Freitag et al., 2004, Schneebeli and Sokratov, 2004]. These methods differ in the way used to reconstruct a 3D volume from two-dimensional data. Serial sectioning consists in an iterative slicing of the sample and 2D imaging with an optical camera. μCT uses back projection algorithms to obtain a spatial image from several radiographs recorded at different projection angles. μCT measures the 3D distribution of the X-ray attenuation coefficient, which differs between materials with different chemical composition and density. Regardless of the imaging technique, the measurement output consists in a 3D grayscale image, whose gray levels are supposed to be distinct between the different materials.

The material of interest then needs to be extracted from the grayscale image. This image processing step is called binary segmentation. It consists in reducing the grayscale image to a binary image object / background, that then enables the quantitative characterization of the microstructure. In the present case, the object of interest is ice and the background is generally constituted of air and possibly an impregnation product used to strengthen fragile snow samples. Unfortunately, the grayscale image is noisy and the transition between materials is generally fuzzy. Thus, the binary segmentation is not straightforward and might bias the microstructure characterization and the result of subsequent numerical models.

Usually, the segmentation technique used for snow is based on thresholding (e.g. [Coléou et al., 2001, Flin et al., 2003, Heggli et al., 2009, Kerbrat et al., 2008, Schneebeli and Sokratov, 2004]): single gray values are used to separate different materials. These methods based on thresholding are commonly used in the snow community

because they are fast and their implementation is straightforward. However, they are not robust in practice [Boykov and Funka-Lea, 2006], and operator-biased because of the subjectiveness involved in the choice of the threshold values [Iassonov et al., 2009].

Nowadays, numerous advanced segmentation techniques have been developed in computer sciences, benefiting from increasing computational capabilities of personal computers. Iassonov et al. [2009] compared different segmentation techniques on μCT images and concluded that "the use of local spatial information is crucial for obtaining good segmentation quality". Therefore, global thresholding methods might not be suited to derive the maximum information out of the grayscale image. One class of segmentation relying on the optimization of some energy functions are particularly powerful [Boykov and Funka-Lea, 2006]. These methods are called hereafter energy-based segmentation in comparison to threshold-based segmentation. In the comparison conducted by Iassonov et al. [2009], the energy-based segmentation has been shown to overcome the other tested segmentation techniques. The energy definition makes these methods flexible and explicitly specifies the segmentation criteria. In addition, global optimization via the graph cut approach [Boykov and Funka-Lea, 2006, Boykov et al., 2001] makes these methods repeatable and robust. Here, we propose to take advantage of the formalism of energy-based techniques and to adapt it to the binary segmentation of snow microtomographic images.

Energy-based segmentation techniques can benefit from the a priori knowledge that the segmented object is snow. Density and specific surface area (SSA) are classical indicators to characterize the microstructure and can be measured from snow samples using dedicated instruments independent from the μCT based techniques [Arnaud et al., 2011, Gallet et al., 2009, Kerbrat et al., 2008, Matzl, 2006]. Threshold-based segmentation techniques can already take into account the density prior information by choosing the right threshold value. However, it is the only information that can be added in the segmentation process. The energy-based segmentation is more flexible and can also consider local spatial image information as curvature [El-Zehiry and Grady, 2010], local smoothness [Boykov and Kolmogorov, 2003], shape [Freedman, 2005], etc.

Once fallen on the ground, snow undergoes metamorphism [Fierz et al., 2009]. Under equilibrium conditions, snow tends to evolve to a structure that minimizes its surface and grain boundary energy [Flin et al., 2003, Vetter et al., 2010]. As a result, the ice surface of aged snow tends to be smooth below a certain spatial scale. Kerbrat et al. [2008] compared the specific surface area (SSA) measured by gas adsorption and X-ray tomography. Except for fresh snow, both measurements give identical results, with an uncertainty of 3%. They concluded that the ice surface in an alpine snow pack is essentially smooth up to a scale of about 30 μm which corresponds to the effective resolution of their X-ray images. Flin et al. [2011] estimated the SSA of snow using microtomographic images of various snow types. They compared the computed SSA for different image resolutions. For coarse rounded or melt-refrozen grains with a low SSA ($<$20 m^2 kg^{-1}), the computed SSA is almost independent of the image resolution in the range [5,80] μm. As a consequence, snow structures

Name	Type	Voxel size (μm)	Density (kg m^{-3})	SSA (m^2 kg^{-1})
A	MFcr	9.6	280	8
B	FCso	9.6	215	19
B7m		7.2		19
D	DH/FC	9.6	125	25
D7m		7.2		28

Table 2.1: Description of the snow samples used in this study. Density was measured in the field by weighting snow samples with a volume of 50 cm^3. The indicative SSA values correspond to estimates obtained on the binary image resulting from the energy-based segmentation (for $r = 1.0$ voxel, see below).

smaller than 80 μm do not contribute significantly to the overall SSA for these types of snow. Thus, we can expect aged snow or melt-refrozen snow with a low SSA to be globally smooth even at a scale of 80 μm. In this paper, we attempted to include this prior information about local smoothness, which is linked to the overall SSA, in the segmentation process.

First, the sampling and X-ray μCT measurement procedures used to obtain grayscale μCT images are described. The gray level distribution is analyzed and used to explain why the measurement artefacts significantly complicate the segmentation process. Second, the threshold-based segmentation, commonly used in snow research, and the new proposed energy-based segmentation are presented. Finally, the segmentation techniques are applied on a 2D reference image and on the μCT images of snow, and the obtained results are compared.

2.2 X-ray μCT images

2.2.1 Sampling and μCT measurement procedure

The natural snow samples used in this work were collected at Col de Porte, Chartreuse, French Alps, during winter 2011-2012. Three different types of snow were sampled. Sample A is a melt-freeze crust (MFcr according to the International Classification for Seasonal Snow on the Ground, ICSSG, [Fierz et al., 2009]). Sample B is composed of solid faceted crystals (FCso) and presents a very fine crust of frozen drizzle. Sample D is composed of depth hoar (DH) and faceted crystals (FC). Density and SSA of these samples are summarized in Table 2.1.

The snow samples were prepared according to the procedure detailed in Flin et al. [2003] and Flin [2004]. We only recall here the main steps. Once sampled in the field, each snow core was impregnated by liquid 1-chloronaphthalene (melting point -15/-20°C) at a temperature about -8°C. Then, the mixture ice / chloronaphthalene was allowed to freeze and stored in a refrigerator at -20°C. After complete freezing and strengthening, each sample was machined into the shape of a cylinder with

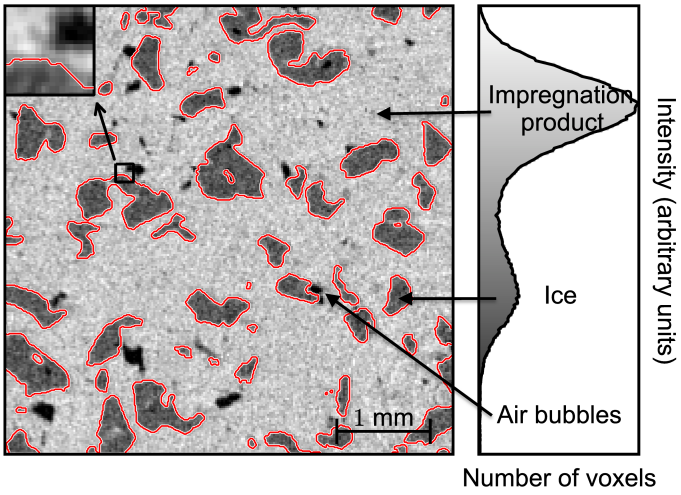

Figure 2.1: Grayscale image (500^2 pixels) extracted from sample B and its corresponding grayscale histogram. The image is composed of three materials: the impregnation product (1-chloronaphthalene, light gray), ice (intermediate gray) and residual air bubbles (dark gray). The contour of ice resulting from segmentation is plotted in red. The zoom box (top right) was enlarged 5 times to show the fuzzy transition between the different materials.

16 mm diameter and 21 mm height. This impregnation procedure enables handling of very fragile snow samples and blocks the metamorphism of the snow structure.

The X-ray attenuation coefficient 3D images were acquired with a cone beam tomograph (RX Solutions, generator voltage of 100 kV, generator current of 100 μA) using a specifically designed refrigerated cell. The image borders are slightly distorted due to the conic form of the X-ray beam. Thus, cubes of 1000^3 voxels were extracted from the inside of the whole 3D grayscale images ($\sim 1500^3$ voxels). The voxel side-length of sample A is 9.6 μm. Samples B and D were scanned twice with a voxel size of 7.2 μm (images B7m, D7m) and 9.6 μm (images B, D).

With this sampling procedure, the scanned samples present two main materials: ice and chloronaphthalene (chl), and a secondary material composed of residual air bubbles due to incomplete impregnation of the sample (Figure 2.1). These three materials can be distinguished by their X-ray attenuation coefficient, i.e. their grayscale value I. The attenuation coefficients, initially encoded on 4-bytes floats, were rescaled and encoded with unsigned shorts (0 to 65535). In the figures, they are plotted with a gray level (0: black; 65535: white). Dark, intermediate and light gray values correspond to air, ice and chl, respectively.

The segmentation method described in this paper is thus applied to X-ray images composed of three materials, resulting from snow samples impregnated with 1-chloronaphthalene. However, this approach is, in fact, rather general and can be applied to any multiple-material grayscale image out of which one material needs to be extracted. Other sampling procedures exist in the literature to prepare snow

samples for μCT imaging. When a μCT is directly available in a cold room, the snow samples generally do not require any specific preparation to be scanned (e.g. [Kerbrat et al., 2008]). In this case, the μCT image is composed of only two phases: air and ice. Besides the technique described in this paper, fragile snow samples can also be prepared for a μCT scan using the snow replica method [Heggli et al., 2009]. This method consists in casting snow samples with diethyl phtalate and then sublimating ice in high vacuum. In this case, the scanned sample is composed of two materials: the impregnation product and air. In all cases, however, regardless of the reconstruction technique or the sampling procedures, the measurement output consists in a 3D grayscale image whose values are supposed to be distinct between the different materials, and to which the developed segmentation technique can be applied.

2.2.2 Images artefacts: noise and fuzzy transition between materials

The μCT output images are only approximate representations of the true X-ray attenuation coefficient. The grayscale images are affected by optical transfer function, scatter and noise [Kaestner et al., 2008]. As a consequence, the grayscale images are altered by two main artefacts: (1) the gray value of voxels belonging to the same material are slightly spread around the noiseless attenuation coefficient of the material, and (2) the transition between different materials is fuzzy (Figure 2.1).These artefacts yield "mixed voxels" whose gray value does not directly determine whether they belong to ice or to the background, and the segmentation of these mixed voxels can significantly affect the final segmented image. This explains why binary segmentation of μCT images is not straightforward.

The grayscale histogram representing the distribution of voxels with a given gray level (Figure 2.2) can be used to estimate the material proportions and their intensity peaks. Its analysis can also be used to quantify the noise amplitude and the size of the transition zone between materials. Noise is inherent to the X-ray sensor and the measurement environment. Due to the acquisition method, noise is often spatially correlated along annuli centered on the rotation axis of the μCT scan. As shown in Figure 2.2, the noisy gray level distribution for each material can be fitted by a Gaussian distribution $\mathcal{N}(\mu, \sigma)$, defined as

$$\mathcal{N}(\mu, \sigma)(I) = \frac{1}{\sigma\sqrt{2\pi}} \exp\left(-\frac{(I-\mu)^2}{2\sigma^2}\right). \tag{2.1}$$

The standard deviation σ and the mean μ of these distributions can be automatically determined using data adjustment algorithms (minimization of the square error), for ice and chl. Automatic fit for air is generally not possible because the amplitude of the air peak is too small to clearly emerge in the histogram. As expected, it is found that the standard deviation of noise is the same for chl and ice, since noise does not depend on the material but is inherent to the imaging procedure. The fitting domain was thus reduced by using the same σ-value for ice and chl. In the

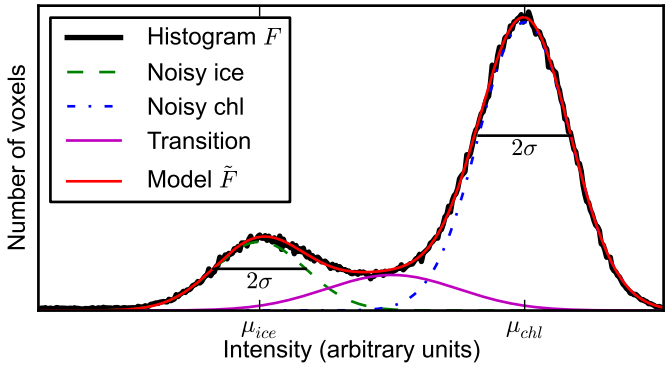

Figure 2.2: Analysis of the grayscale histogram of the image shown in Figure 2.1. The normalized grayscale distribution F is well reproduced by the intensity model $\tilde{F}$ described in Equation (2.2) ($\int |F - \tilde{F}| dI = 0.02$).

example images (Figures 2.1, 2.3, 2.10), the value of this standard deviation of noise σ is about 20% of the contrast between ice μ_{ice} and chl μ_{chl}.

The fuzzy transition between different materials is partly due to partial volume effect (Figure 2.1). The real limit between materials does not exactly follow the voxel grid. Therefore, the gray value of a frontier voxel is a barycenter between gray values of pure materials. In principle, the transition width should thus be on the order of the voxel side-length. In fact, this zone is slightly larger (about 2-3 voxels). This is due to the tomography back-projection reconstruction algorithm that is affected by a noisy input. On the histogram, this effect leads to a transition zone between ice and chl (Figure 2.2). Empirically, a Gaussian distribution centered on the mean gray level $\bar{\mu} = (\mu_{chl} + \mu_{ice})/2$ and with a standard deviation of $\tilde{\mu} = (\mu_{chl} - \mu_{ice})/4$ was found to provide a good fit to this transition zone (Figure 2.2).

Hence, the normalized grayscale histogram F can be well reproduced by the following model $\tilde{F}$:

$$\begin{aligned} \tilde{F} &= \lambda_{ice} \cdot \mathcal{N}(\mu_{ice}, \sigma) + \lambda_{chl} \cdot \mathcal{N}(\mu_{chl}, \sigma) \\ &\quad + (1 - \lambda_{ice} - \lambda_{chl}) \cdot \mathcal{N}(\bar{\mu}, \tilde{\mu}). \end{aligned} \tag{2.2}$$

where $(\lambda_{ice}, \lambda_{chl})$ represent the proportions of ice and chl, respectively. As a consequence, the undetermined voxels whose gray value is in between ice and chl are either very noisy pure material or transition voxels between the two materials. As it will be described below, this automatic histogram analysis is used to set the parameters of the energy-based segmentation algorithm.

2.3 Method

Various binary segmentation methods have been proposed in the literature [Boykov and Funka-Lea, 2006, Iassonov et al., 2009]. In the snow community, global thresholding combined with pre- and post-processing smoothing filters is commonly used

(e.g. [Coléou et al., 2001, Flin et al., 2003, Heggli et al., 2009, Kerbrat et al., 2008, Schneebeli and Sokratov, 2004]). This threshold-based segmentation method and its drawbacks, which have motivated the development of a more advanced segmentation method, are first described. Then, the proposed energy-based segmentation is presented.

2.3.1 Threshold-based segmentation

Threshold-based segmentation is the most commonly used segmentation technique because it is simple and fast. The method is based on two main steps: smoothing and thresholding. These steps differ depending on whether the image is composed of two or more phases.

2.3.1.1 Two materials

During the thresholding process, individual voxels in the image are marked as object or background voxels according to whether their value is greater or smaller than a global threshold value. This threshold can be estimated from the grayscale histogram of the image. For instance, its value can be determined as the local minimum between the two intensity peaks in the grayscale histogram (Figure 2.1, e.g. in [Heggli et al., 2009]). However, for snow samples with a very high SSA, these two peaks are not distinct (uni-modal histogram) because of the large number of mixed voxels whose grayscale value lies between those of the two materials. In this case, the threshold can be determined by fitting a particular intensity model. For instance, Kerbrat et al. [2008] determined the optimum threshold by fitting a sum of two Gaussian curves on the histogram and calculating their intersection. Nevertheless, using a strict gray threshold generally truncates the tail distribution of the intensity distribution of pure material voxels and results in a number of incorrectly classified voxels (see [Kaestner et al., 2008] and Figure 2.3). The amount of wrongly segmented voxels is particularly large when the histogram is uni-modal. The resulting segmented object is thus disturbed and structural parameters such as SSA are significantly affected.

In order to smooth the ice/background interface and to accentuate the intensity peaks in the histogram, a smoothing filter that reduces noise is first applied on the initial image. Common smoothing filters are convolution filters such as mean and Gaussian filters. The spatial size σ_s of the smoothing filter (box size of the mean filter or standard deviation of the Gaussian filter) are usually set to the size of a few voxels. These filters efficiently smooth intensity variations inside homogeneous regions but also affect sharp features in the image. Consequently, the effective resolution of the binary image is negatively affected. Moreover, setting the size of the smoothing filter σ_s to a certain value does not guarantee that the segmented object is free of artificial details smaller than σ_s (Figure 2.3b) because the thresholding applied afterward is a discontinuous operation.

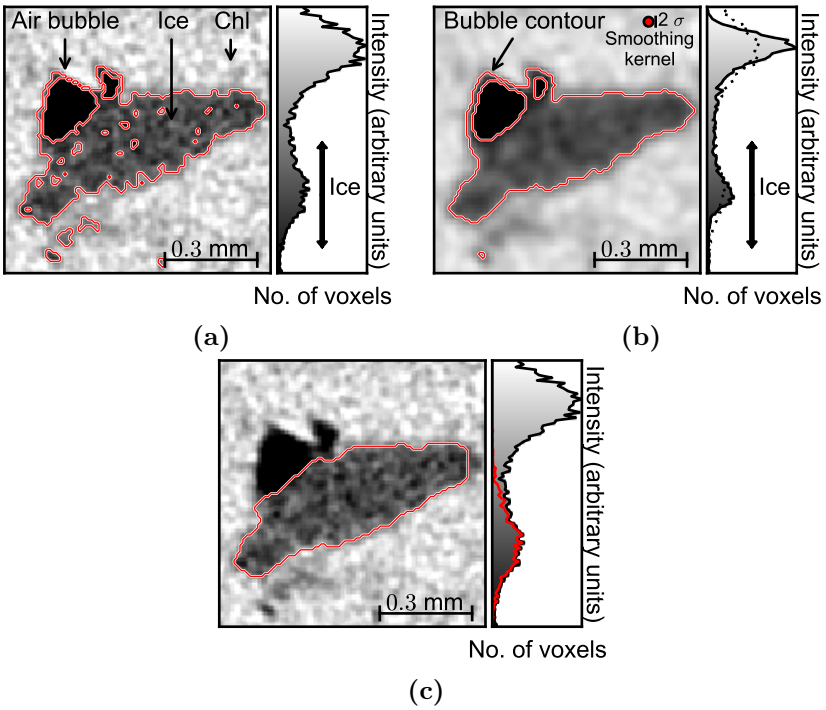

Figure 2.3: (a) Threshold-based segmentation without smoothing. The used thresholds are indicated by the black arrow on the histogram. (b) Threshold-based segmentation with smoothing of the grayscale image through a Gaussian filter ($\sigma_s = 1.6$ pixels). To visualize the size of the smoothing kernel, a disk of radius σ_s voxels is plotted in red. The histogram of the non filtered image is plotted with dots. (c) Expected segmentation (best segmentation obtained with the energy-based technique). The grayscale distribution of the segmented ice pixels is plotted in red on the histogram. Despite the clear visual differences, the threshold-based segmentation without smoothing (a) differs from this expected segmentation (c) by only a small number of voxels (∼5%).

2.3.1.2 Three or more materials

When the initial image is composed of three or more materials, the smoothing step is not applicable directly. For instance, a smoothing filter directly applied on our X-ray images smooths the transition between air bubbles and 1-chloronaphthalene. The contour of air bubbles in chl then appears as an ice contour (see Figure 2.3b). The image has thus to be reduced to a two-materials image before applying the smoothing / thresholding steps.

A semi-automatic threshold-based segmentation procedure was developed to process X-ray images of impregnated snow obtained from synchrotron tomography (Flin 2004, Flin et al. 2003). This approach was recently improved and now consists in the following steps:

- *Air bubble detection.* First, a threshold is used to locate dark voxels corresponding to air. These voxels are then dilated (2 iterations) where the grayscale gradient is high. This procedure enables labeling the contour of air bubbles that have the same gray value as ice. Dilating only in high gradient zones prevents labeling real ice next to a bubble that is touching ice. Finally, the labeled voxels are replaced by the mean gray value of 1-chloronaphthalene. With this step, the initial image is reduced to two materials.

- *Smoothing and thresholding.* The modified image is smoothed with a mean filter of size $3 \times 3 \times 3$ and binarized with a threshold obtained from a visual analysis of the grayscale histogram.

- *Final processing.* To remove residual noise, the segmented image is post-processed via binary morphological operations (closing, erosion/reconstruction, opening, etc. with structural elements of size $3 \times 3 \times 3$) and via a last smoothing / thresholding step (mean filter of size $5 \times 5 \times 5$). Finally, ice zones not connected to the main structure or to the borders of the image are identified by using a connected component labeling algorithm and deleted. This step prevents having small artificial ice zones floating in the snow structure.

This procedure is straightforward and fast (about 1 to 2 hours on a personal computer -2 GHz, 16 Gb RAM- for a 1000^3 voxels image). Nevertheless, its outcome critically depends on the skills of the operator who has to manually fix the different segmentation parameters (thresholds, smoothing filters size, etc.) as a function of the snow type and the tomograph settings. Moreover due to the sequential nature of the segmentation procedure, information might be lost between each step of smoothing and thresholding. For instance, the initial smoothing step affects the whole image and does not preserve sharp edges. On the contrary, it tends to increase the partial volume effect. Lastly, the parameters used cannot be directly related to the effective resolution of the resulting binary image (i.e, the size of the smallest details that can be imaged).

2.3.2 Energy-based segmentation

Energy-based segmentation methods consist in finding the optimal segmentation according to an energy function. These methods are more robust because the segmentation criteria are objectively defined in the energy functional and the optimization process is automatic. Energy-based segmentation methods can be distinguished by the type of function used and by the minimization algorithm. They can be divided in two main groups [Boykov and Funka-Lea, 2006]:

1. Optimization of a functional defined on a continuous contour or surface (e.g. snakes, geodesic active contours, methods based on level-sets). The optimization generally uses a variational approach that finds a local optimum, but cannot guarantee to find a global optimum.

2. Optimization of a cost function directly defined on a discrete set of variables (e.g. intelligent scissors, live-wire, graph-cut). The graph cut approach introduced by Boykov et al. [2001] belongs to this group and enables the global optimization of the energy function in any dimension. In this paper, the graph-cut approach was adapted to the binary segmentation of snow X-ray microtomographic images.

Let us consider that the grayscale image I is constituted of n voxels of side length δ. The spatial position and the intensity of voxel i are denoted x_i and I_i, respectively. The segmented image is $L \in \{0,1\}^n$, where 0 stands for the background and 1 for ice. L_i is the segmentation label (0 or 1) of voxel i. A segmentation L costs the energy $E(L)$. The best segmented image L_{min} is the one that minimizes the energy E. In general, the energy E is composed of two terms: a local data fidelity term (E_v) and a non-local spatial regularization term (E_s), whose expressions in our case are described in the following subsections.

2.3.2.1 Local intensity model

The local gray value is the most obvious criterion that needs to be accounted for in the segmentation process. For instance, a voxel whose intensity is very close to the intensity of air is inclined to be air, i.e. to belong to the background. This idea can be formalized with proximity functions P that quantify the penalty of assigning a voxel to ice or to the background. The proximity function ranges from 0 (furthest) to 1 (closest). Using proximity functions, the data fidelity term E_v of the segmentation energy can be defined as:

$$E_v(L) = v \cdot \sum_i \left((1 - L_i) \cdot P_0(I_i) + L_i \cdot P_1(I_i)\right) \tag{2.3}$$

where P_0 is the proximity to the background (0), and P_1 the proximity to ice (1). This energy is scaled by the volume of one voxel $v = \delta^3$. To set these proximity functions, we rely on the analysis of the grayscale distribution (see above and Figure 2.2). Using the decomposition of the grayscale histogram described in Equation (2.2), the ratio $\lambda_{ice} \cdot \mathcal{N}(\mu_{ice}, \sigma)/\tilde{F}$ quantifies "how close to ice a voxel of a given gray value level is" and could be used as the proximity function to ice P_1. Here, a simpler model that approximates this ratio based on truncated Gaussian functions, is used (Figure 2.4):

$$\begin{aligned} P_0(I) &= \begin{cases} 1 \text{ if } I < \mu_{air} \text{ or } \mu_{chl} < I \\ \min\left(1, e\mathcal{N}(\mu_{air}, \sigma)(I) + e\mathcal{N}(\mu_{chl}, \sigma)(I)\right) \text{ elsewhere} \end{cases} \\ P_1(I) &= \min\left(1, e\mathcal{N}(\mu_{ice}, \sigma)\right)(I) \end{aligned} \tag{2.4}$$

with $e = \exp(1)$. The absorption value of air μ_{air} cannot be directly derived from the histogram. This parameter is estimated from the values of μ_{ice} and μ_{chl} by assuming a constant relative contrast between materials. Using these proximity functions actually amounts to transforming the initial grayscale image into a new

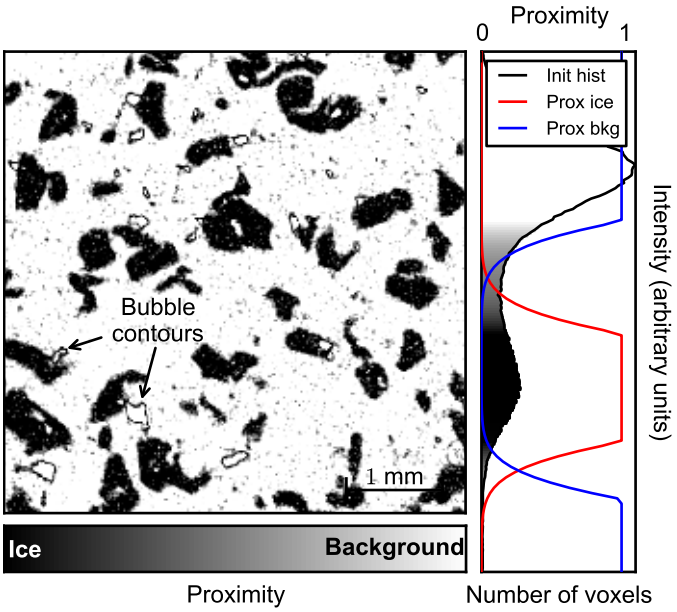

Figure 2.4: Proximity image. The gray value is here proportional to $P_0 - P_1$, so that a voxel close to the background is white and a voxel close to ice is dark. The voxels with an intermediate gray value are the undetermined voxels. The contours of air bubbles are visible. The same plot can be done with a pre-processed image where the bubbles contours are replaced by chl, but then a peak appears in the histogram for the chosen "replacement" intensity.

grayscale image (Figure 2.4), which is sharper because the noise has been reduced. The main idea behind this definition of the proximity functions is to distinguish the fuzzy transition from noise and add this information to the segmentation process.

Even if no smoothing filter is applied to the grayscale image, the contour of air bubbles generally shows gray values close to those of ice, due to the partial volume effect (Figure 2.3 and 2.4). To eliminate this artefact, "ice-like" ($\mu_{ice} - 2\sigma < I < \mu_{ice} + 2\sigma$) voxels simultaneously close (distance < 4 voxels) to "chl-like" ($I > \mu_{ice} - \sigma$) and "air-like" ($I < \mu_{air} + \sigma$) voxels are replaced by "chl-like" voxels ($I = \mu_{chl} - \sigma$). All μCT images used to test the energy-based segmentation method were pre-processed this way.

The minimization of E_v alone gives the same result as a threshold-based segmentation, with the advantage of also providing the uncertainty of the segmentation $E_v(L_{min})$. However, the energy-based segmentation is really interesting when E_v is combined with additional non-local energy terms.

2.3.2.2 Surface area

The complete energy function used in this paper is composed of two components:

$$E(L) = E_v(L) + r \cdot S(L), \tag{2.5}$$

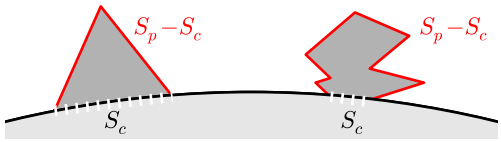

Figure 2.5: Protuberances on a surface of a smooth object. For the equilateral triangular protuberance, $\alpha = 1/3$. For the "sharper" protuberance, $\alpha = 0.8$.

where the spatial regularization term is $E_s(L) = r \cdot S(L)$ with $S(L)$ the surface area of the segmented object and r ($r \geq 0$) which has the dimension of a length. Accounting this term in the energy leads to penalizing large interface areas: a voxel with a mixed gray value will be segmented so that the interface ice/background area is minimized. The parameter r assigns a relative weight to the surface area term so that the smoothness of the segmented ice can be controlled. In principle, other non-local terms such as gradient, curvature or shape penalties could also be considered in the segmentation. The flexible definition of the energy functional is one of the powerful assets of energy-based segmentation.

The regularization term minimizing the ice/air interface is of particular interest for materials such as snow where sintering naturally tends to reduce the surface and grain boundary energy. This process is particularly effective on snow types resulting from isothermal metamorphism. For other snow types, such as precipitation particles (PP), faceted crystals (FC) or depth hoar (DH), the surface regularization term is expected to perform well in recovering the facet shapes but might induce some rounding at facet edges.

The parameter r is a geometrical parameter related to the smallest detail size preserved by the segmentation. Let us consider a protuberance P on a globally smooth interface, with a volume V_p, a total surface S_p and a contact area with the smooth object S_c (Figure 2.5). If P is considered as ice, the segmentation energy is $E = C + r \cdot (S_p - S_c)$ where C is a constant. If P is considered as background, then $E = C + V_p + rS_c$. Hence, the protuberance P is segmented as ice if:

$$V_p \geq r(S_p - 2S_c). \tag{2.6}$$

In addition, the contact area S_c can be generically expressed as a function of the total surface area S_p: $2S_c = (1 - \alpha)S_p$ where α is a numerical factor that depends on the protuberance shape. This factor α ranges from 0 to 1 for flat to distinct protuberances, respectively. For instance for an equilateral triangle protuberance, $\alpha = 1/3$. Let r_p be an apparent radius, defined by V_p/S_p. Finally, P is segmented as ice if:

$$\frac{r_p}{\alpha} \geq r. \tag{2.7}$$

Accordingly, the segmentation parameter r thus enforces the minimum radius of protuberances preserved on the segmented object.

2.3.2.3 Minimization of the energy: graph-cut approach

The energy functional defined in Equation (2.5) has to be minimized to find the optimal segmentation. For this purpose, the optimization of binary energy via graph cut is well suited [Boykov et al., 2001]. This method consists in transforming the binary energy optimization problem into the problem of finding an optimal cut in a graph, which is solvable in polynomial time [Ford and Fulkerson, 1956]. The cut metric induced in this graph can be chosen as close as desired to the continuous euclidean metric [Boykov and Kolmogorov, 2003] and can also be used to compute surface area very efficiently [Lehmann et al., 2012]. Details of the graph-cut approach can be found in the Appendix. The graph-cut algorithm developed by Delong and Boykov [2008] that enables the segmentation of massive grids up to 400^3 voxels on a personal computer was used. Since segmentation is a local process at the scale of a snow grain, it was possible to apply a "divide and conquer" (D&C) algorithm (segmentation on smaller overlapping sub-volumes) in order to segment large images ($\sim 1000^3$ voxels) in about 10 hours on a personal computer (4 processors 2.7 GHz, 6 Gb RAM memory).

2.4 Results

The absence of ground truth, i.e., the absence of prior knowledge of the optimal binarization result, makes the comparison of different segmentation techniques difficult. Thus, the accuracy and the behavior of the energy-based segmentation is first tested on a reference artificial image: the 2D Koch flake. Then, the technique is applied on μCT snow images and 3D results are shown. Results of the energy-based and threshold-based segmentations are compared, and the accuracy of the energy-based segmentation is indirectly checked on global structural parameters (density and SSA).

2.4.1 Segmentation of a reference 2D image

The Koch flake (Figure 2.6) is chosen as a reference for its multiscale properties [Mandelbrot, 1982] that can grossly mimic the structure of certain types of snow. By varying the number of iterations in the fractal construction, the scale of the smallest detail on the flake can be freely set, and the exact perimeter length and surface area can be theoretically computed. First, the discretization of the Koch flake into a pixel binary image is discussed. Then, this binary image is artificially degraded to reproduce the imperfect μCT output image. Finally, the energy-based segmentation method is applied on the degraded image and its accuracy is examined.

2.4.1.1 Discretization artefact

The flake is discretized into a binary image of size 500^2 pixels: the value of each pixel was set to 1 or 0 according to whether the pixel center is inside or outside the closed Koch curve, respectively. Figure 2.7 shows measurements of the area

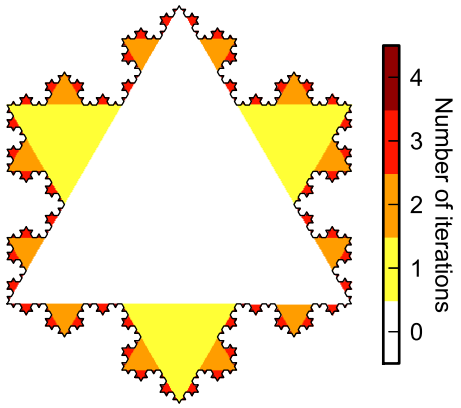

Figure 2.6: Koch flake with 4 iterations (500^2 pixels). At each iteration, a smaller triangle is added in the middle of all perimeter segments.

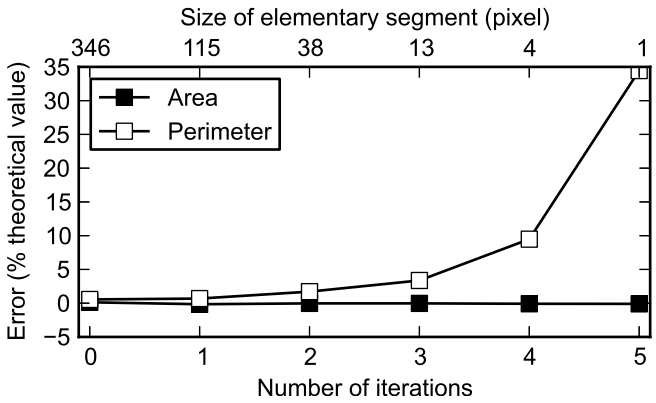

Figure 2.7: Measurement of area and perimeter of the discretized Koch flake as a function of the number of iterations in the fractal construction (see Figure 2.6).

and the perimeter (computed with the graph-cut approach: see Appendix) of the discretized Koch flake as a function of the iteration number in the construction of the fractal object. The measured area corresponds well to the theoretical value. The measured perimeter, however, differs more and more from the theoretical value when the number of iterations increases, i.e., when the length of the elementary segment of the Koch curve becomes small compared to the pixel size. Typically, the perimeter measurement remains consistent with the theoretical value, with an uncertainty of 10%, for objects whose details are larger than about 4 pixels. For smaller details, discretization artefacts become significant; in this case, the pixel discretization and the graph cut length calculation are not precise enough to correctly reproduce the flake contour length. In the following, the Koch flake with 4 iterations, which presents smallest details of side-length equal to 4 pixels and whose contour length can be regarded as correctly reproduced, is considered as the reference object.

2.4.1.2 Input images for the segmentation algorithm

The discretized Koch flake with 4 iterations was then blurred with a Gaussian filter of standard deviation equal to 1.5 pixels in order to reproduce the fuzzy transition between two materials (blurred image). Then, two synthetic images were created by adding different types of noise to the blurred image. On the first one (CT noise image), noise derived from a CT-scan of an empty sample was added to the blurred image, in order to mimic μCT noise as close as possible (Figure 2.8). On the other one (Gaussian noise image), uncorrelated Gaussian noise was added. Both additive noises were scaled so that their standard deviations are equal to 20% of the contrast between the two materials, as in our snow μCT images. Note that the specific surface area of the Koch flake expressed in pixels is relatively small compared to that of the scanned snow grains since the center of the Koch flake is massive. Thus, only a small number of transition pixels are present, as revealed by the grayscale histogram (Figure 2.8).

2.4.1.3 Segmentation artefact

The energy-based segmentation algorithm was applied to the initial image and the degraded images (blurred, CT noise and Gaussian images) for various values of the parameter r. Note that the blurring of the initial image irreversibly affects details of the Koch flake which therefore cannot be recovered by any segmentation technique. Hence, the segmentation of the CT and Gaussian noisy images is expected to be, at best, as good as the segmentation of the blurred image.

Figure 2.9 shows the number of pixels that are wrongly segmented compared to the reference Koch flake image, as a function of the segmentation parameter r. For both noisy images, the lowest number of wrongly labeled pixels (equal to 0.84% of the total number of pixels with the CT noise and 0.66% with Gaussian noise) is obtained with $r = 0.4$ pixel. As explained above (see Equation 2.7), r controls the apparent radius of surface protuberances deleted by the segmentation. The optimal

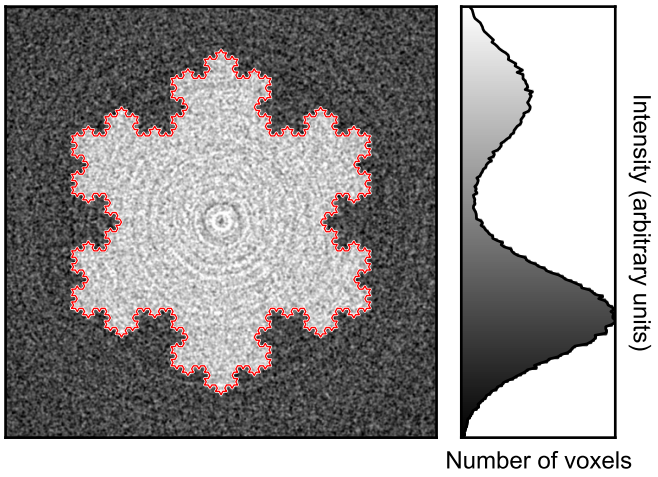

Figure 2.8: Koch flake blurred with a smoothing filter ($\sigma_s = 1.5$ pixels) and degraded with noise extracted from an empty CT-scan. The CT-scan noise presents circular spatial correlations due to the data acquisition procedure.

value of r is obtained when protuberances induced by noise are deleted, but as few object details as possible are smoothed. Therefore, the optimal value of r can be regarded as corresponding to the typical length of noise-induced protuberances. Globally, the segmentation result is more accurate on the image with Gaussian noise, which can be attributed to the effect of spatial correlations of the μCT noise that tends to hinder the efficiency of the non-local segmentation energy term (E_s).

Figure 2.9 also shows how the perimeter length of the segmented object varies with r. As expected, when r increases, the perimeter becomes smoother and its length decreases. Two regimes can be distinguished: (1) For small values of r, the perimeter length strongly decreases with r. Due to noise, the length computed with $r = 0$ is highly overestimated. In this regime, smoothing induced by E_s affects small details that are due to noise, but not real details of the image. (2) For larger values of r, the computed perimeter length decreases more slowly with r, and with a quasi constant slope. In this regime, the smoothing induced by E_s affects real details of the object. This is indicated by the fact that the computed perimeter length on the images without noise (initial and blurred images) also clearly decreases in this regime. Interestingly, the perimeter decrease rates with r for the noisy images and the blurred image are almost equal, and presumably linked to the multiscale property of the segmented object. Note that for very large values of r, the smoothing is so strong that there are almost no more differences between the result obtained from the four images (Figure 2.9).

Interestingly, we observe that the segmentation with the smallest number of wrong segmented pixels is obtained at the transition between the two previously described regimes, i.e., when most artificial details induced noise are smoothed out. We also note that the best segmentation is not able to recover the exact Koch flake:

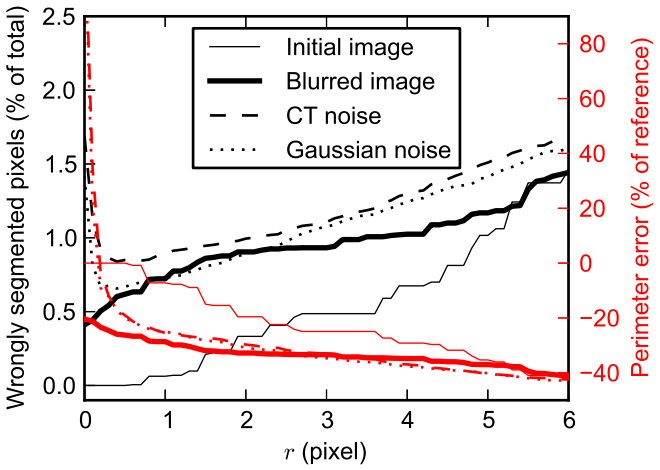

Figure 2.9: Accuracy of the segmentation on the Koch flake image as a function of the parameter r. The reference perimeter is the perimeter measured on the discretized flake with 4 iterations (Figure 2.7).

about 1% of the total number of pixels are wrongly segmented and the perimeter length is underestimated by 20% compared to the perimeter length computed directly on the initial image. As already explained, this discrepancy is mainly due to the application of blur, which leads to an irrecoverable loss of the smallest details in the image. It is thus satisfactory to observe that the perimeter length recovered by the best segmentation on the noisy images is almost equal to that obtained with the best segmentation ($r = 0$) on the blurred image.

2.4.2 Segmentation of snow 3D images

The energy-based segmentation algorithm is now applied on the snow samples described previously (Table 2.1) for various values of segmentation parameter r. Examples of segmented slices (Figure 2.10) and segmented volumes (Figure 2.11), qualitatively illustrate the effect of the parameter r on the segmented object. It is clearly observed that when r increases, the segmented snow becomes smoother and smoother. The effect of r is all the more evident for snow presenting a high SSA value (sample D).

In the following, we first investigate how the segmentation parameter affects structural variables such as density and specific surface area (Figure 2.12). Then, the results obtained for similar snow samples scanned with different resolutions are compared. Finally, the energy-based segmentation results are compared to the threshold-based segmentation results.

2.4.2.1 Evolution with parameter r

As shown in Figure 2.12a, the density of the segmented object is almost constant with r. The slight decrease observed is due to the fact that the snow structure is

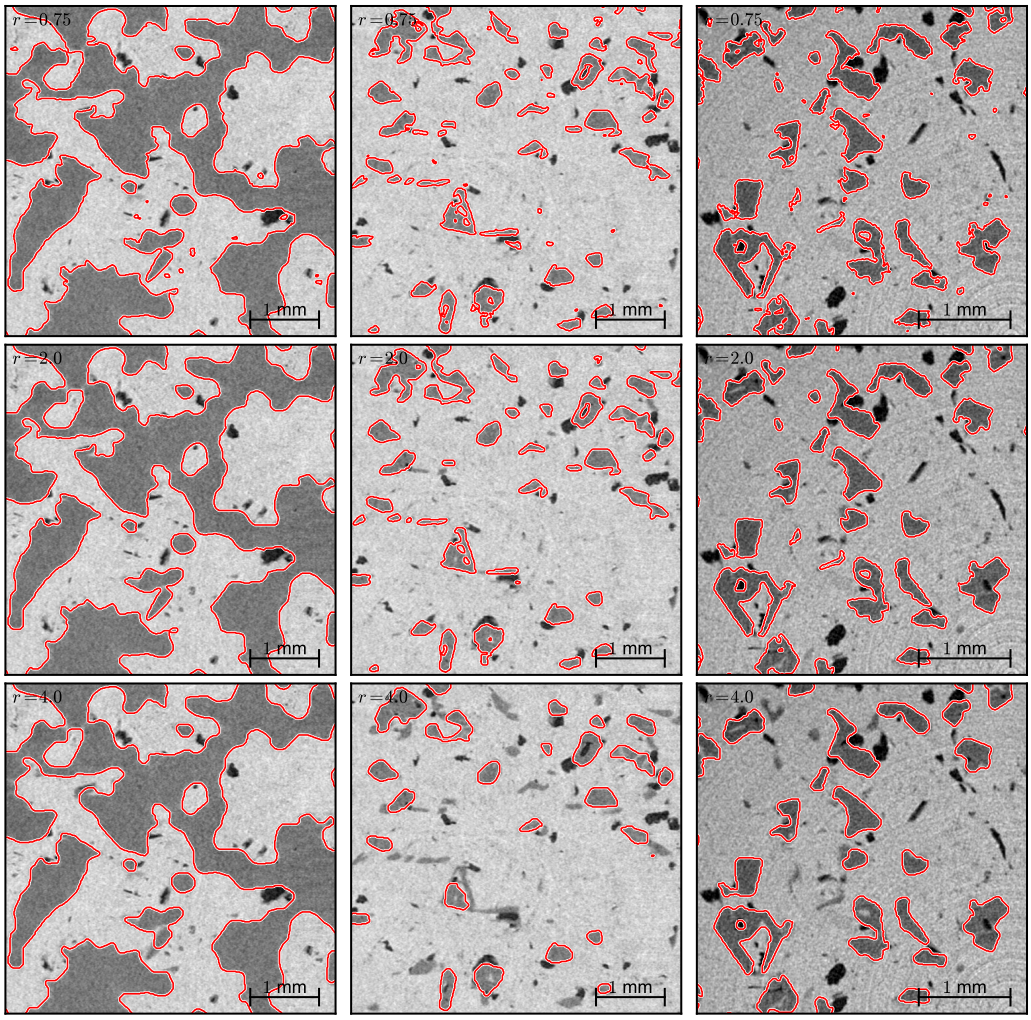

Figure 2.10: Segmentation for different snow samples (A, D and D7m from left to right) and parameter r (0.75, 2.0 and 4.0 voxel from top to bottom). The segmentation is computed on a 3D volume. As a consequence, the segmentation presented on these 2D sub-slices (500^2 pixels) may be affected by neighboring slices.

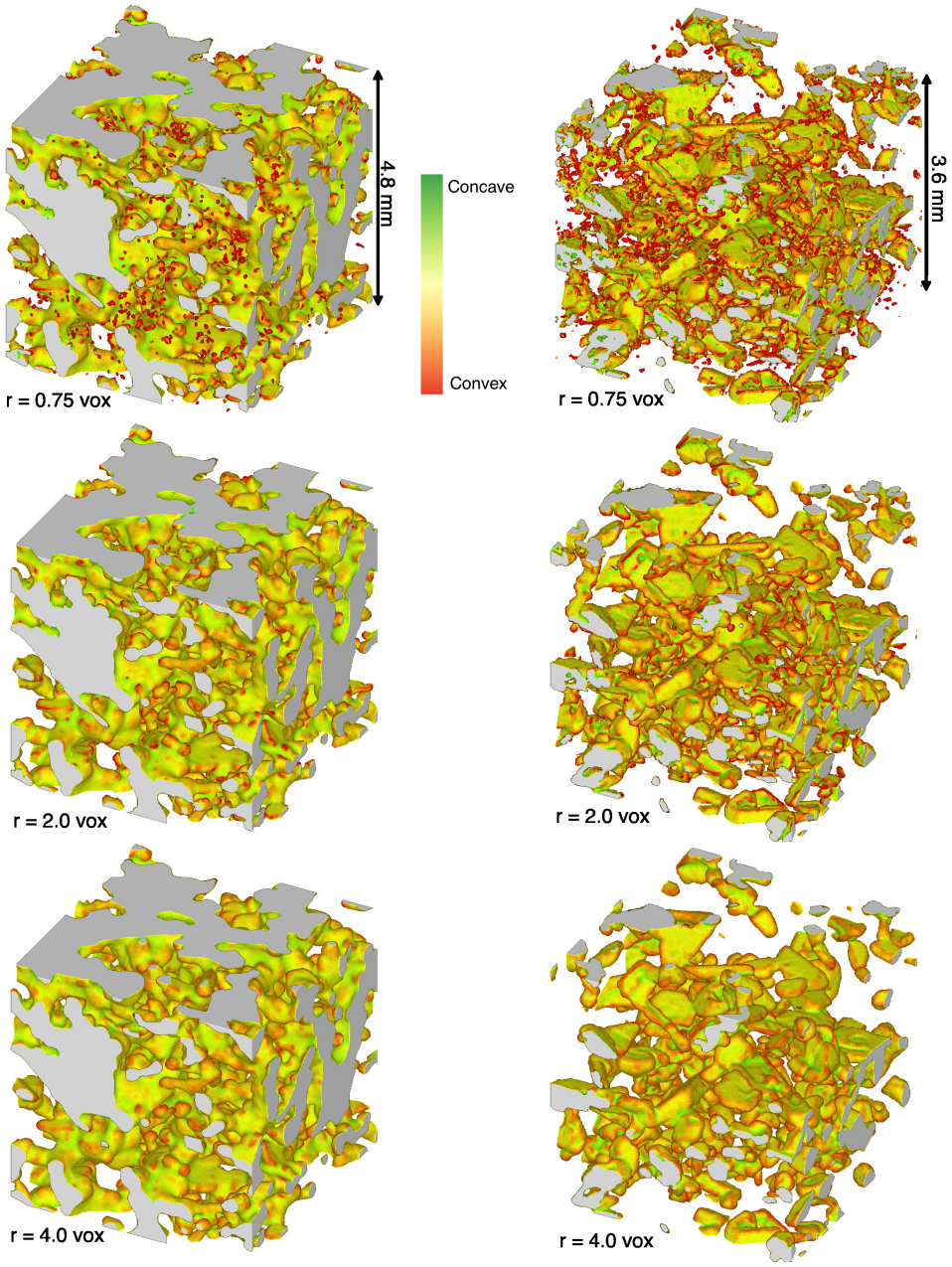

Figure 2.11: Segmentation for different snow samples (A on the left and D7m on the right) and parameter r (from top to bottom 0.75, 2.0 and 4.0 voxel). The segmentation are presented on subvolumes (500^3 voxels) of the whole images (1000^3 voxels) and may be affected by neighboring slices. The surface was colored according to its curvature to emphasize the smallest structure details.

generally convex and accounting for E_s in the segmentation energy tends to erode convex zones. The density variations are also slightly larger for small snow grains (samples D, D7m) since their details are more affected by smoothing induced by E_s (Figure 2.10).

SSA, on the contrary, is more sensitive to the segmentation parameter r (Figure 2.12b). As for the Koch flake, two regimes can be distinguished. For very low values of r [0-10 μm], the SSA decreases rapidly when r increases. Similarly as for the synthetic images, this regime probably corresponds to the progressive smoothing of the noise on the interface. For larger values of r [10-40 μm], the SSA decreases much slower with r. For sample A composed of a melt-refrozen crust, there is actually almost no variation of the SSA with r in this regime, which can be related to the fact that the interface is already naturally smooth at these scales. For samples B and D, the SSA continuously decreases with r with an almost constant slope, because the real details of the snow structure contributing to the overall SSA are progressively smoothed out. This behavior is a clear indication of the multiscale characteristics of these types of snow: the wide size distribution of the details impacts the SSA when computed at different scales.

Hence, when the scale of noise is clearly separated from the detail scale as on sample A, the segmentation parameter can be almost indifferently taken in the range [10-40 μm]. When these two scales are not clearly separated, the optimal choice for r is more difficult. The best segmentation is obtained when most of the noise is smoothed out, but the snow details are optimally preserved. According to the analysis of the Koch flake, we can assume that the best segmentation parameter is obtained at the transition between the two described regimes, i.e. when the SSA starts to vary slowly with r. In the presented images, this optimal value corresponds to $r \simeq 10-15\,\mu$m, i.e. $r \simeq 1-1.5$ voxel. As expected, choosing a value of r less than this optimal value amounts to trying to extract artificial information from the image and to amplifying the influence of the noise. In our case, finding an optimal value on the order of the voxel size indicates that the tomograph settings are optimal.

2.4.2.2 Influence of image resolution

Segmentation results can be compared for the pairs of images B and B7m, and D and D7m, which were obtained using different resolutions (9.2 μm and 7.6 μm, respectively). For both density and SSA, the segmentation results are globally consistent with each other for all values of r larger than the highest resolution (Figure 2.12). We recall that, even if they are extracted from the same sample, the volumes scanned at different resolutions are not exactly the same. This might explain the small density and SSA differences observed. The agreement observed for both pairs of images constitutes a clear validation of the robustness of the presented method. The parameter r can be regarded as the effective resolution of the segmented image. For images B and B7m, both SSA and density remain independent of r even for values less than 9.2 μm. This indicates that, in this case, both resolution values are sufficient to capture the details of the tested snow type. On the contrary, for

images D and D7m, the SSA values tend to show a difference that increases when r decreases below 9.2 μm. This can be attributed to the influence of snow details smaller than the image resolution whose existence is expected for this type of snow with a high SSA value. The observed difference can also be enhanced by the slightly poorer quality of the D7m scan where the noise-to-signal ratio is larger.

2.4.2.3 Comparison with threshold-based segmentation

Globally, as shown in Figure 2.12c, the number of voxels differing between both segmentation techniques always remains relatively small (1-5%). In detail, this number slightly depends on the considered image.

Concerning the density, it can be argued that good agreement between both segmentation techniques is found for all tested images (Figure 2.12a). The differences observed on Figure 2.12a can actually be attributed to the uncertainty inherent to the segmentation technique. For instance, a detailed investigation conducted on image A revealed that the differences between both techniques is essentially due to systematic variations of about one voxel in the position of the ice/background interface (Figure 2.13). Given the typical size of the fuzzy transition between materials in our image, such variations of one voxel can be due to slight differences in the chosen thresholds and can be regarded as measurement uncertainties. Due to the connectivity test, some snow grains also tend to be deleted in the threshold-based segmentation (Figure 2.13), but their effect on the overall density remains negligible. Finally, it can also be noted that the density values measured in the field (Table 2.1) are in reasonable agreement with the values derived from the binary images, considering once again the measurement uncertainties, and the representativity issues linked to the small size of the scanned samples.

Concerning SSA, we also observe a good agreement between the values derived from the threshold-based segmentation and those obtained from the energy-based segmentation, in particular when the parameter r is on the order of the image resolution (Figure 2.12b). This comparison reveals that the effective resolution associated with the threshold-based segmentation is actually close to the image resolution. Note that the apparently large difference in SSA values yielded by the threshold-based segmentation for images D and D7m, is actually essentially due to the difference in the obtained densities and not in the obtained surface areas (Figure 2.12a).

In conclusion both energy-based and threshold-based segmentation have been shown to produce essentially identical results, which can be considered as a cross validation of the two techniques. Nevertheless, the threshold-based technique appears less robust since, in particular, different density values are obtained for the same samples scanned at different resolutions. The greater robustness of the energy-based technique is promoted by the fact that the segmentation parameters are automatically derived from the histogram analysis, and not subjectively chosen as in the threshold-based segmentation. This robustness is also enhanced by the greater flexibility offered by the use of smooth proximity functions instead of fixed threshold

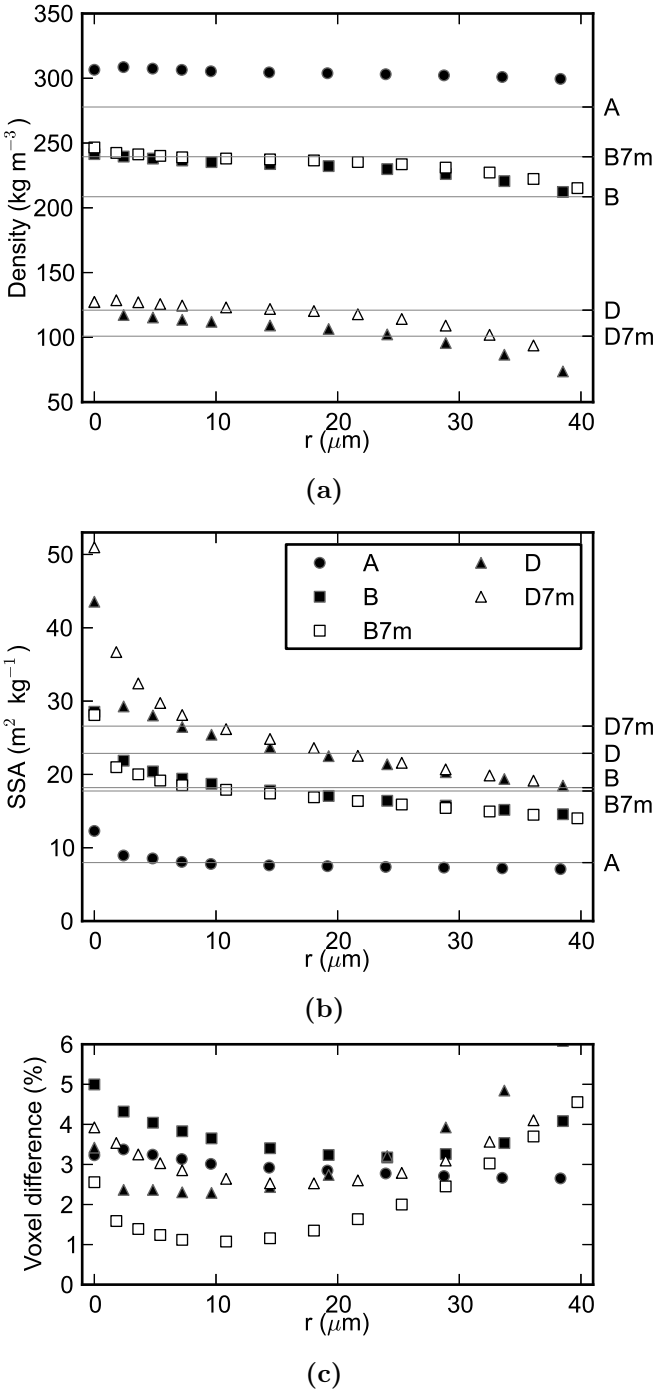

Figure 2.12: Evolution of segmentation results as a function of the segmentation parameter r. Figures (a) and (b) show the evolution of density and specific surface area as a function of r, respectively. Density and SSA values obtained from the threshold-based segmentation are indicated on the right axis. Figure (c) shows the proportion of voxels that differ between the energy-based and the threshold-based segmentations.

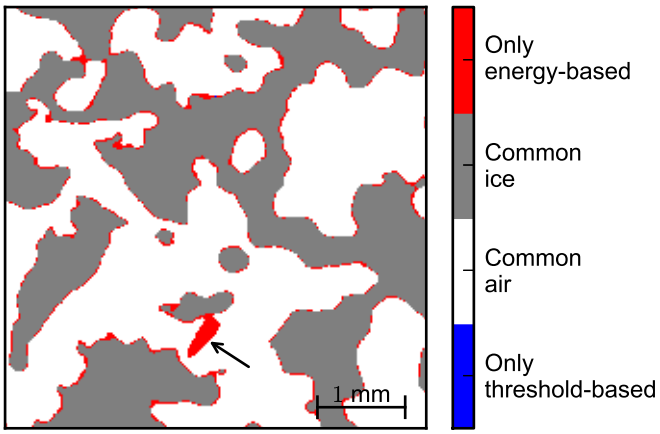

Figure 2.13: Differences between the threshold-based segmentation and the energy-based segmentation computed for $r = 2.0$ voxels on a slice of sample A (500^2 pixels). The grain indicated with the arrow was disconnected from the overall snow structure by the threshold-based technique and deleted by the connectivity test. Almost no blue pixel, which is segmented as ice only with the threshold-based method, is visible on the figure. On the threshold-based segmented image of sample A, a one voxel dilation increases the computed density from 278 kg m^{-3} to 294 kg m^{-3}, a value close to that obtained with the energy-based segmentation (Figure 2.12a).

values that separates voxels regardless of the grayscale difference between them.

2.5 Conclusion and discussion

We successfully applied an energy-based segmentation with a graph-cut minimization technique, to snow microtomographic images. The segmentation criteria are chosen according to our prior knowledge of the snow microstructure. In particular, a spatial regularization term, that penalizes large interface area, has been introduced to account for the sintering effect that naturally tends to reduce snow surface energy.

Our approach has first been shown to produce accurate results on a synthetic image, the Koch flake. Then, the energy-based segmentation was successfully applied on microtomographic images of snow and compared to the threshold-based segmentation. In the absence of ground truth on snow images, it is difficult to conclude about the absolute quality of the obtained segmentations. However, both methods produced similar results. The main advantages of our approach compared to the threshold-based segmentation can be summarized as follows:

1. All segmentation parameters (intensity peaks, noise amplitude, ...), except the relative weight of the surface area term r, are automatically determined from

the histogram analysis in which both noise and fuzzy transition are considered. Thus, the approach is reproducible and does not involve subjective choices.

2. The method benefits from local spatial information: voxels are segmented according to their local gray value but also such as to minimize the ice/background interface, which is physically meaningful. The segmentation parameter r is formally linked to the local smoothness of the segmented object. It clearly defines the effective resolution of the final binary image.

3. With the energy formalism and the global optimization via graph-cut, all criteria and available information are treated simultaneously in the segmentation process, which leads to enhanced robustness. In the threshold-based segmentation, the image processing is sequential. At each step, the "working" image is modified and some information might be lost.

The density of the segmented image has be shown to be almost independent of the parameter r. Thus, density values are essentially governed by the volumetric term in the segmentation energy. As a consequence, an a priori knowledge of the density might be added in the segmentation process. This can be done by adding this constraint to the histogram analysis phase, and adjusting the values of μ_{air}, μ_{ice} and μ_{chl}. In our case, such an addition of prior information was not considered since the density field measurements cannot be regarded as representative for the small scanned snow samples.

The choice of the segmentation parameter value r is not automatic and should be made according to the image quality. As shown previously, the best segmentation, i.e. the segmentation that preserves the smallest snow details while deleting most of noise-induced protuberances, is obtained when the computed SSA starts to vary slowly with r ($r \simeq 1 - 1.5$ voxel, here). The dependence of the computed SSA value on the effective resolution r also points out two important considerations: (1) if they are not carefully smoothed out, noise induced protuberances can significantly contribute to the overall SSA, which will then be overestimated; (2) for snow with structure details on the order of the voxel size, as fresh snow, the SSA value cannot be measured independently of the used resolution.

In addition, the choice of r should also depend on the subsequent use of the binary image. For analyzes that are not affected by small structural details, the effective resolution r of the binary image can be chosen larger than the optimal value defined above. For instance, for mechanical analysis with finite or discrete elements, the segmentation should correctly reproduce the grain connectivity while modeling the grain shapes with the fewest elements as possible. Usually, the downscaling of the 3D image of snow is performed by merging voxels in the binary image. This downscaling leads to a threshold uncertainty when exactly half of the subvoxels belong to ice or to the background. The downscaled image is therefore grid dependent. The energy-based segmentation presented here has the advantage of enabling the effective downscaling of the 3D representation of snow to a chosen resolution represented by the segmentation parameter r, without any grid artefact.

Acknowledgments Funding by the VOR research network (Tomo_FL project) is acknowledged. We thank the scientists of 3SR laboratory (J. Desrues, P. Charrier, S. Rolland du Roscoat), where the 3D images have been obtained. We also acknowledge the CEN staff (P. Pugliese and J. Roulle) for technical support during the experiments. Special thanks are due to N. Calonne for her significant contribution to the data acquisition.

2.A Appendix

In this appendix, the implementation of the segmentation energy and its optimization via graph cut is detailed.

2.A.1 Link between graphs and binary energy

Graph cut can be used to minimize binary energies. A binary energy is a function of a finite set of binary variables. For instance, the segmentation energy defined in Equation (2.5) is a binary energy whose binary variables are the label ice/background of each voxel. Let $\mathcal{G} =< \mathcal{V}, \mathcal{E} >$ be a graph defined with a set of nodes $\mathcal{V}$ and a set of undirected edges $\mathcal{E}$ that connect the nodes. The set of nodes contains two special nodes: the source s and the sink t. They are called terminal nodes (t-nodes). The rest of the nodes $\mathcal{P}$ are non-terminal nodes (n-nodes), so that $\mathcal{V} = \{s, t\} \cup \mathcal{P}$. Each edge (p, q) between node p and q has a non negative weight ω_{pq}. A cut C between the source and the sink is a partitioning of the nodes into two disjoint subsets $\mathcal{S}$ and $\mathcal{T}$ such that s is in $\mathcal{S}$ and t is in $\mathcal{T}$ (see Figure 2.14). The cost of a cut C, denoted $\mathcal{L}_{\mathcal{G}}(C)$, is the sum of the weights of edges (p, q) such that $p \in \mathcal{S}$ and $q \in \mathcal{T}$:

$$\mathcal{L}_{\mathcal{G}}(C) = \sum_{p \in \mathcal{S}} \omega_{pt} + \sum_{q \in \mathcal{T}} \omega_{sq} + \sum_{(p,q) \in \mathcal{S} \times \mathcal{T}} \omega_{pq}. \tag{2.8}$$

Let us define the binary variable $L_p(C)$ associated to each non-terminal node p as $L_p(C) = 1$ if $p \in \mathcal{S}$, 0 else. Denoting $\omega_{sp} = P_1(p)$, $\omega_{pt} = P_0(p)$ and $\omega_{pq} = V_{pq}$, we have

$$\mathcal{L}_{\mathcal{G}}(C) = \sum_{p} ((1 - L_p) \cdot P_0(p) + L_p \cdot P_1(p)) + \sum_{(p,q)} \mathbb{I}_{L_p \neq L_q} V_{pq} \tag{2.9}$$

where $\mathbb{I}$ is the indicator function. Thus, a cut in a graph can be directly associated to a binary energy function composed of a local term (P_0, P_1) and a pair interaction potential V. Finding the minimum cut, i.e. the cut with the minimum cost among all cuts, is therefore equivalent to finding the associated energy minimum.

2.A.2 Measurement of binary object surface area with graphs

According to Equation (2.9), the segmentation energy associated to the local intensity model can be directly translated into the graph by correctly setting the edge weights with the terminal nodes. Translating the surface area in terms of edges weight is more complex and requires being capable to relate lengths to the pair interaction potential V_{pq}. Boykov and Kolmogorov [2003] first formalized the link between graph cut and length calculation using the Cauchy-Crofton formula. In two dimensions, the Cauchy-Crofton formula relates the euclidean length of a curve $|C|_{\mathcal{E}}$ to the number n_c of intersects with all straight lines in $\mathbb{R}^2$:

$$2|C|_{\mathcal{E}} = \int n_c d\mathcal{L} \tag{2.10}$$

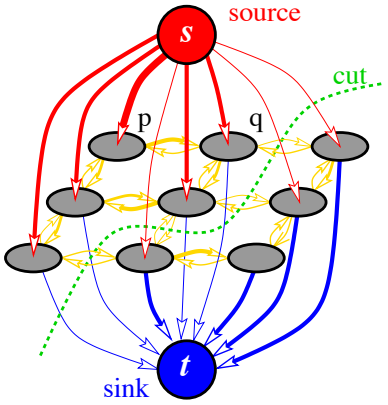

Figure 2.14: A cut in graph. The non terminal nodes corresponding to each pixel are represented by gray circles. Taken from [Boykov and Kolmogorov, 2004].

with $d\mathcal{L}$ a proper "measure" of the lines subset. This formula can be discretized to provide an approximate length measurements. For example, in Figure 2.15, only four types of lines directed by a certain neighborhood system are considered: vertical, horizontal and $\pm 45°$ diagonal lines. The contour of the segmented object intersects one of these lines when it disconnects two nodes linked by these lines. The edge weight associated to each of these lines can thus be set according to the discretized version of Cauchy-Crofton formula that uses the Voronoi segmentation of the unit sphere [Danek and Matula, 2011a,b]. In Figure 2.15, the edge weights associated to a 2D example neighborhood system are shown. The neighborhood system used in this work on 3D images is composed of the 26 first neighbors. Note that computing lengths via the graph-cut approach is consistent with the voxel projection approach [Flin et al., 2011] and that it provides a very fast (about two minutes for a 1000^3 voxels image on a personal computer; 4×2.7 GHz and 6 Gb RAM) and accurate way to compute the surface area of a binary object [Lehmann et al., 2012, Liu et al., 2010].

2.A.3 Minimization algorithm

Finding the minimal cut can be solved by finding a maximum flow from the source to the sink, which is a problem solvable in polynomial time [Ford and Fulkerson, 1956]. This proposition is called the "Min-cut / Max-flow" theorem [Ford and Fulkerson, 1956]. The maximum flow between s and t can be imagined as the maximum flood of water that goes through the graph using the edges as pipes with a limited capacity (the weights). Finding the maximum flow of water is equivalent to finding the "limiting pipes". There exist several polynomial algorithms to solve the min-cut/max-flow problem. The main limitation of these algorithms is the memory usage. Currently, the initial image resulting from a microtomographic scan is very large ($>1000^3$ voxels). The corresponding graph is composed of $n = 1000^3 + 2$ nodes

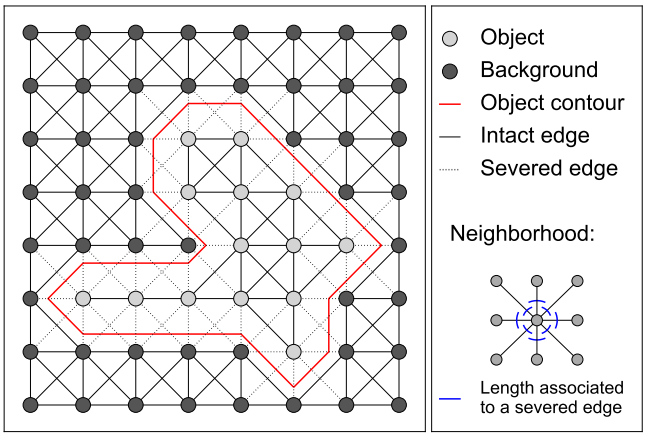

Figure 2.15: Graph cut method to compute a length (2D case).

and about $13n$ edges, and requires more than 200 Gb of memory with usual min-cut/max-flow algorithms (BK2.2 , [Boykov and Kolmogorov, 2004]). This amount of RAM is not available on a personal computer. The exact optimal segmentation on such huge image is therefore not computable easily. The scalable graph-cut algorithm developed by Delong and Boykov [2008] uses the grid structure of the graph to optimize the memory usage. We use an adapted version of their algorithm (freely available for research purposes on http://vision.csd.uwo.ca/code/) that enables the segmentation of massive grids up to 400^3 voxels on a personal computer (6 Gb RAM). It is still not large enough to compute a global optimum on the whole image. However, segmentation is a regional process with relatively small boundary effects. The initial image was thus divided in small overlapping sub-volumes on which the segmentation algorithm is applied.

Chapter 3

Evaluation of the accuracy of the specific surface area measurements obtained from microtomographic data

Abstract Microtomography measures the X-ray attenuation coefficient in a 3D volume of snow with a high spatial resolution of a few microns. In order to provide quantitative characteristics of the microstructure such as the specific surface area, the grayscale image first needs to be segmented into a binary image ice/background, which inevitably biases the subsequent microstructure characterization. The surface area of the binary image is then approximated via numerical algorithms, which influence the computed specific surface area value. In this study, the effect of numerical processing of microtomographic images on density and specific surface area is evaluated based on a set of 38 X-ray attenuation images of snow without impregnation and commonly used image processing techniques. It is shown that the variability of microstructure characteristics due to numerical processing can be limited to the same order of the one due to the spatial variability observed within one snow layer. However, some techniques used to determine the segmentation threshold (local minimum) or the surface area on the binary image (marching cubes) introduce a systematic bias in the computation of density and specific surface area and are not recommended. Moreover, it is recalled that the computed surface area value is dependent on the effective resolution of the image and may thus not account for essential small structural details.

Contents

3.1 Introduction

The specific surface area (SSA) of snow is defined as the area S of the ice-air interface per unit mass M, i.e. $SSA = S/M$ expressed in $m^2\ kg^{-1}$. It is an essential variable for the modeling of the physical and chemical properties of snow because it is an indicator of potential exchanges with the surrounding environment. For instance, SSA can be used to predict snow electromagnetic characteristics such as light scattering and absorption (albedo in the near infrared) [e.g. Flanner and Zender, 2006, Warren, 1982] or microwave behavior [e.g. Brucker et al., 2011]. SSA variations are driven buy snow metamorphism [e.g. Domine et al., 2007, Flin et al., 2004]. Precise knowledge of this quantity is required for many applications such as cold regions hydrology, predicting the role of snow in the regional/global climate system, optical and microwave remote sensing, snow chemistry, etc.

SSA can also be used to define the equivalent spherical radius as $r_{eq} = 3/(\rho_{ice} \times SSA)$ with ρ_{ice} the density of ice. The equivalent spherical radius somehow defines a "grain size". However, in practice, the generic term "grain size" can refer to other definitions such as the optical radius, i.e. the radius of a collection of spheres with the same infrared albedo as the one of the snow microstructure [Warren, 1982], the diameter of individual particles detached from the snowpack [Fierz et al., 2009] or the size of single snow crystals [Riche et al., 2012] etc. In the last decade, many field and laboratory instruments were developed by different research groups to measure grain size. Because of the co-existence of different methods (optical, gas adsorption, tomography, stereology) and inconsistent definitions of grain size, an intercomparison of different grain size measurement methods was organized by the International Association of Cryospheric Sciences (IACS) working group "From quantitative stratigraphy to microstructure-based modeling of snow". One of the main objectives of the intercomparison is to discuss about the accuracy, comparability and quality of existing measurement methods.

In the context of this workshop, the focus of the present study is on the measurement of SSA, which can refer to a certain "grain size" as shown above, derived from microtomographic data. Microtomography measures the X-ray attenuation coefficient in a three-dimensional (3D) volume with a high spatial resolution of a few microns. The resulting 3D grayscale image is an approximate representation of the microstructure because of scatter and noise inherent to the measurement procedure, and does not provide directly quantitative characteristics of the microstructure such as the SSA. In practice, the grayscale image needs to be segmented into a binary image ice/background. This step called binary segmentation inevitably biases the subsequent microstructure characterization, especially when the tomograph resolution is close to the typical size of microstructural details. The way the surface area of the ice-air interface is computed on the binary image also affects the SSA estimation. Here we investigate the impact of binary segmentation and surface area calculation

on the computed SSA, in order to provide guidelines for using SSA values derived from microtomographic data.

Comparative studies of image processing of images obtained via X-ray microtomography have already listed the performance of several segmentation methods with respect to a certain quality measure [e.g. Iassonov et al., 2009, Kaestner et al., 2008, Schlüter and Sheppard, 2014]. These studies emphasize the importance of using local image information such as spatial correlation to perform suitable segmentations and highlight the high performance of Bayesian Markov random field segmentation [Berthod et al., 1996], which find the segmentation with minimum boundary surface that at the same time respects the gray value data in the best possible way. However, none of the mentioned studies were interested in snow which exhibits specific features such as its natural tendency to minimize its surface energy along with snow metamorphism [e.g. Flin et al., 2003, Vetter et al., 2010]. Moreover, the focus was on relative volumetric material content and less attention was paid to the surface area of the segmented object. Hagenmuller et al. [2013b] applied an energy-based segmentation method (same principle as the Bayesian Markov random field segmentation but with a different optimization technique) on images of impregnated snow samples, which are three-phase material (impregnation product, ice and residual air bubbles) and compared it to a segmentation method based on global thresholding. The energy-based method takes advantage of the knowledge that the surface energy of snow reduces because of metamorphism, is shown to be accurate on a synthetic grayscale mage. However the set of snow microtomographic images used by Hagenmuller et al. [2013b] was limited to impregnated samples and to a few different snow types only. Moreover, no independent SSA measurements were available to provide a reference or at least a comparison. Here, the flexible energy-based segmentation method was adapted to two-phase images (air-ice) and applied to 38 images on which SSA measurements were conducted with independent instruments.

First, the sampling and X-ray measurement procedures to obtain grayscale images are described. Attention is paid to the fact that the parameters used for binary segmentation also depend on the scanned sample and not only on the setup of X-ray source. Second, two different approaches of binary segmentation are presented. The first one is commonly used in the snow community and consists of a sequence of filters: Gaussian smoothing, global thresholding and morphological filtering. The second one is based on the minimization of a segmentation energy. Third, different methods to compute surface area from binary image are presented. Finally, the different methods of binary segmentation and area computation are applied to the microtomographic images and the results are compared to provide an estimation of the scatter of SSA measurements due to numerical processing of the grayscale image.

3.2 Material and methods

3.2.1 Data set

Snow sampling, preparation and scanning were conducted by M. Matzl in the WSL-institute for snow and avalanche research (SLF), Davos, Switzerland, during the Snow Grain Size Workshop in March 2014.

Sampling Thirteen snow blocks of apparently homogeneous snow were collected in the field or prepared in a cold laboratory. These blocks span different snow types (decomposing and fragmented snow, rounded grains, faceted crystals and depth hoar, Figure 3.1). Smaller specimens were taken out of these blocks to conduct grain size measurements with different instruments. Two snow cylinders of radius 35 mm and height of 60 mm and one snow cylinder of radius 20 mm and 60 mm height were extruded from each block to perform microtomographic measurements.

X-ray scanning The grayscale images were obtained with a commercial micro-computer tomograph (Scanco Medical μCT40) with a X-ray source set to an energy of 55 keV. The two samples with a radius of 37 mm were scanned with a resolution of 18 μm and the smaller sample with a resolution of 10 μm. To avoid edge effects a sub image of size about 1000^3 voxels was extracted from each image. In the following, the images corresponding to a resolution 18 μm are identified by the suffixes "s1" and "s2", the 10 μm by "10micron". The prefix (e.g. A5, M2-2, see Figure 3.1) denotes the snow block out of which the scanned samples were extruded. The output of the tomograph is a 3D grayscale image with values encoded as unsigned short integer in the range $[0, 65535]$ (Figure 3.2). The grayscale value quantifies the X-ray attenuation coefficient.

Images artefacts As shown in Figure 3.2, air and ice can be distinguished by their respective attenuation coefficient, i.e. by their grayscale value or intensity. However, the grayscale distributions in ice and air are not completely disjoint, which leads to indeterminate voxels whose gray value does not directly indicate whether they correspond to air or ice. This indetermination can be attributed to noise and to the fuzzy transition between air and ice, and makes the binary segmentation not straightforward.

Figure 3.3 shows the grayscale distributions for all images. The exact position of the attenuation peaks and the scatter around the peaks depend on the resolution and on the sample. Slight differences are also observed between the grayscale distribution of the two images of the same snow block scanned with the same resolution. Hence, it is unclear whether binary segmentation parameters "optimized" for one image can be systematically used to segment other images even of the same sample with the same resolution. For instance, the temperature of the X-ray source operating in a cold room at $-15°C$, may increase during successive scans and slightly change the

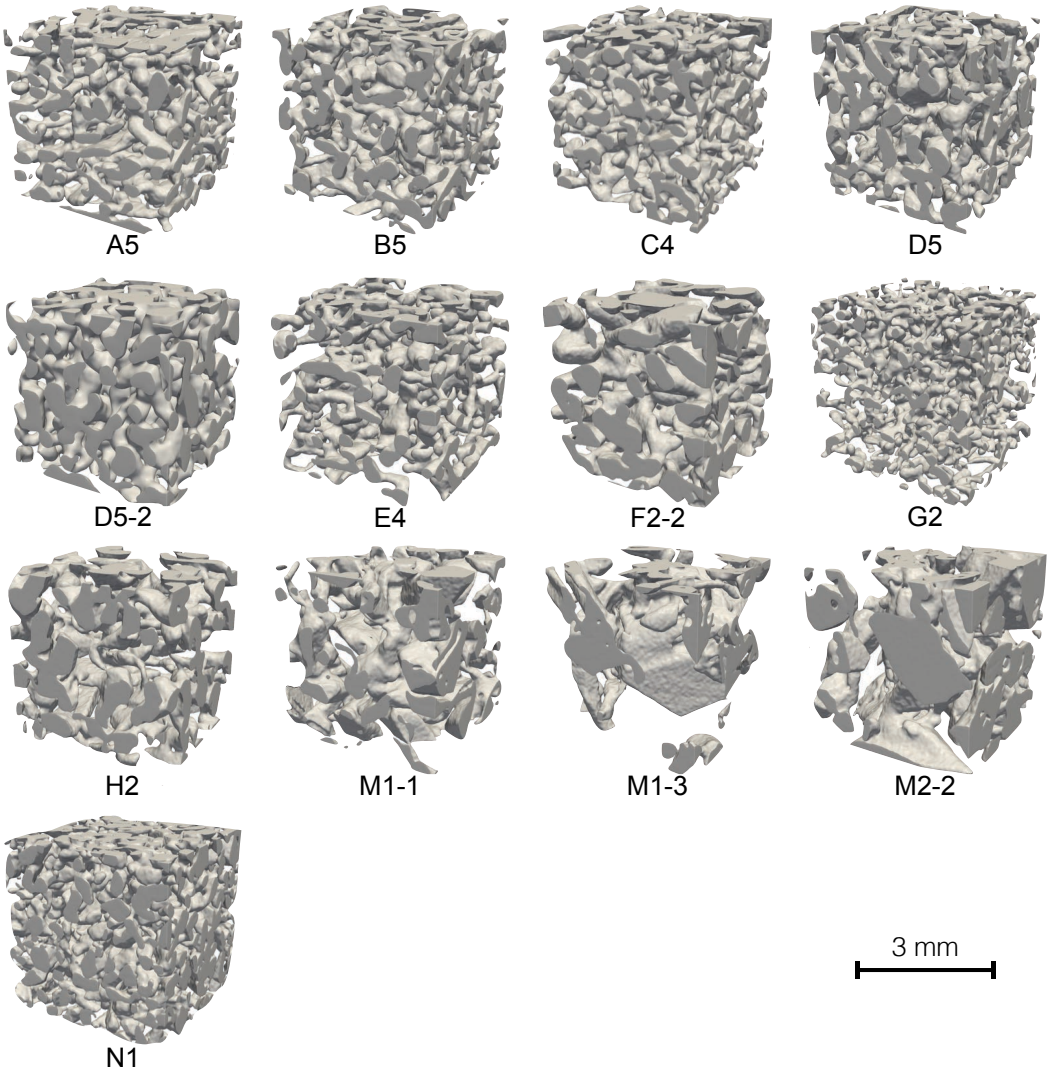

Figure 3.1: The different snow types and microstructural patterns used in this study. The 3D images shown have a side-length of 3 mm and correspond to a subset of the images analysed in the present study.

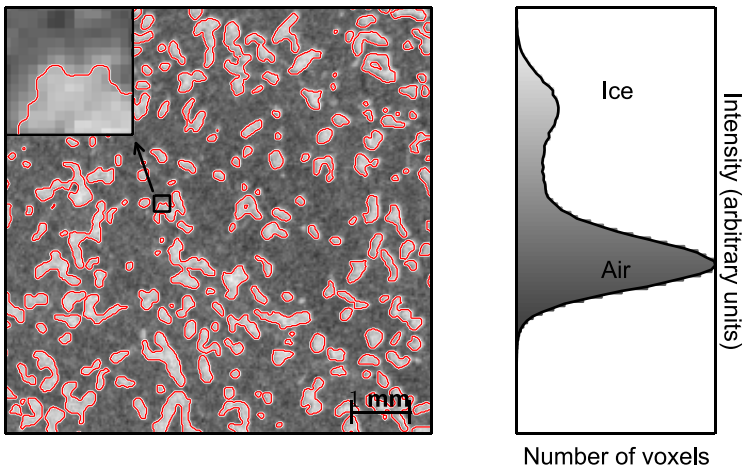

Figure 3.2: Grayscale image (400^2 pixels) representing the X-ray attenuation coefficient and its corresponding grayscale histogram. The 2D slice is extracted from image G2-s1. The image exhibits two materials: air (dark gray) and ice (light gray). The contour of ice resulting from binary segmentation is plotted in red. The zoom box (top right) was enlarged eight times to emphasize the fuzzy transition between air and ice.

measured attenuation of ice and air. Therefore, it may be necessary to determine the segmentation parameters on each image independently.

3.2.2 Segmentation methods

In this section, two binary segmentation methods are presented. First, the common method based on global thresholding combined with denoising and morphological filter is described. This method is hereafter referred to as sequential filtering. Then a method based on the minimization of a segmentation energy, referred to as energy-based segmentation, is presented.

3.2.2.1 Sequential filtering

Sequential filtering is commonly used in the snow community to segment grayscale microtomographic images because it is simple and fast and is implemented in packages of many different programming languages. It consists of a sequence of denoising, global thresholding and post-processing. We refer to this method as sequential filtering because the input of each step is the output of the previous step.

Denoising with Gaussian filter There exist numerous filters to remove noise from images, the most common being Gaussian filter, median filter, anisotropic diffusion filter and total variation filter [Schlüter and Sheppard, 2014]. The objective

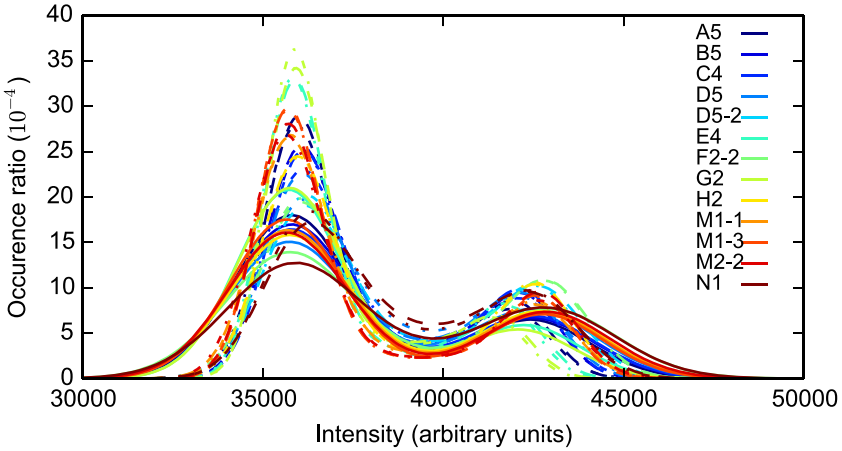

Figure 3.3: Grayscale distributions for all images. The solid lines and dashed lines respectively represent the distributions for the images scanned with the resolution 10 μm and 18 μm. The grayscale distribution is computed on 1000 bins of homogeneous size in the intensity range $[30000, 50000]$ (arbitrary units).

of denoising is to smooth intensity variations in homogeneous zones (i.e. characterized by low-intensity gradient) while preserving sharp variations of intensity in the transitions between materials (i.e. characterized by high-intensity gradient). In the snow community, the most popular denoising filter is the Gaussian filter [e.g. Kerbrat et al., 2008, Lomonaco et al., 2011, Schleef and Löwe, 2013, Theile et al., 2009]. Gaussian filtering consists in convoluting an image with a Gaussian kernel $\mathcal{N}(\mu, \sigma)$ defined as:

$$\mathcal{N}(\mu, \sigma)(I) = \frac{1}{\sigma\sqrt{2\pi}} \exp\left(-\frac{(I-\mu)^2}{2\sigma^2}\right) \tag{3.1}$$

with a mean $\mu = 0$ and a positive standard deviation σ. The support of the Gaussian kernel can be truncated (here to $\lfloor 4\sigma \rfloor$) to speed up the calculations. This filter is very efficient to smooth homogeneous zones. However it fails to preserve sharp features in the image by indifferently smoothing low-intensity and high-intensity gradient zones, which therefore reduces the effective resolution of the image. The effect of the standard deviation of the Gaussian filter on the final segmented image is evaluated in section 3.3.2.2.

Global thresholding After the denoising step, a global threshold T is chosen for the entire image and the voxels are classified as air or ice whether their grayscale value is smaller or greater than the threshold value. The choice of the threshold is based on the grayscale histogram without considering how the grayscale values are spatially distributed. Different methods exist and an exhaustive review can be

found in Sezgin and Sankur [2004]. Here the focus in on common methods used in the snow community: local minimum (1), Otsu's method (2) and mixture modeling (3).

1. *Local minimum:* One extremely simple way to obtain a suitable threshold is to determine the attenuation peaks of ice and air and then find the local minimum in the valley between them (Figure 3.3) [e.g. Flin, 2004, Heggli et al., 2009, Pinzer et al., 2012]. However, the histogram may be noisy, resulting in several local maxima and minima, which makes this simple method inapplicable. It can also appear that, in some cases, the attenuation peaks of ice and air are too close, which creates a unimodal histogram without any valley [e.g. Kerbrat et al., 2008]. Moreover, the local minimum is generally affected by the height of the attenuation peaks: the less ice is in the image, the closer to the ice attenuation peak the local minimum is. The threshold obtained with this method is denoted T_{valley} in the following.

2. *Otsu's method:* Another popular method, first introduced by Otsu [1975], is to find the threshold that minimizes the within-class variance σ_w defined as $\sigma_w^2 = n_{air}\sigma_{air}^2 + n_{ice}\sigma_{ice}^2$ with n_{air}, n_{ice} the numbers of voxels classified as air and ice respectively, and $\sigma_{air}, \sigma_{ice}$ the standard deviations of the grayscale value in each segmented class, respectively. This method is generic and does not require any assumption on the grayscale distribution. However, this is also a drawback of the method: in practice the knowledge of the origin of the image artefacts can explain the grayscale distribution and this information can help to find the optimal threshold. The threshold obtained with this method is denoted T_{otsu} in the following.

3. *Mixture modeling:* The classification error induced by the thresholding can be also minimized by assuming that each class is Gaussian-distributed. Different methods can be considered to decompose the grayscale histogram in a sum of grayscale distributions:

   - The grayscale histogram of the image masked on high-intensity gradient can be perfectly decomposed with the sum of two Gaussian distributions $\mathcal{N}$ centered in μ_{air} and μ_{ice} and with the same standard deviation σ (Figure 3.4a). The mask on high-intensity gradient enables to mask the fuzzy transition between ice and air. Therefore on the masked histogram, the scatter around the peak attenuation can be attributed only to noise which appears to be Gaussian distributed. Assuming that the attenuation coefficient in the transition between air and ice is the weighted sum of the attenuation of air and ice linearly weighted by the material proportion, the optimal threshold value derived from this method is $T_{mask} = (\mu_{ice} + \mu_{air})/2$. Note that the ratio $Q_{noise} = \sigma/(\mu_{ice} - \mu_{air})$ quantitatively estimates the quality of the grayscale image regarding the noise artefacts. Masking the grayscale image on high-intensity gradient

zones is time consuming and not straightforward in existing segmentation softwares. Moreover, in case of a very thin ice matrix, homogeneous ice zones are almost inexistent.

- Kerbrat et al. [2008] directly fitted the sum of two Gaussian distributions on the complete grayscale histogram (Figure 3.4b). Note that the partial volume effect at the transition between materials changes the position of the fitted distribution and the agreement between the fit and the histogram is lower. The threshold defined as the mean of the center of the Gaussian distribution obtained with this fit is denoted $T_{kerbrat}$.
- Hagenmuller et al. [2013b] fitted the sum of three Gaussian distributions to take into account the fuzzy transition between materials. They adjusted the parameters $(\lambda_{air}, \lambda_{ice}, \mu_{air}, \mu_{ice}, \sigma)$ so that the function

$$\tilde{F} = \lambda_{air} \cdot \mathcal{N}(\mu_{air}, \sigma) + \lambda_{ice} \cdot \mathcal{N}(\mu_{ice}, \sigma) + (1 - \lambda_{air} - \lambda_{ice}) \cdot \mathcal{N}(\bar{\mu}, \tilde{\mu}) \quad (3.2)$$

with $\bar{\mu} = (\mu_{air} + \mu_{ice})/2$ and $\tilde{\mu} = (\mu_{ice} - \mu_{air})/4$, fits the grayscale distribution. The distribution $\lambda_{air} \cdot \mathcal{N}(\mu_{air}, \sigma) + \lambda_{ice} \cdot \mathcal{N}(\mu_{ice}, \sigma)$ models the grayscale distribution in low-intensity gradient zones and the distribution $(1 - \lambda_{air} - \lambda_{ice}) \cdot \mathcal{N}(\bar{\mu}, \tilde{\mu})$ models the grayscale distribution in high-intensity gradient zones. The choice $\tilde{\mu} = (\mu_{ice} - \mu_{air})/4$ is arbitrary but was found to provide a good fit to this transition zone. The agreement of this model with the grayscale histogram is generally very good, although no additional free parameters was added in comparison to the two-Gaussian distributions model (Figure 3.4c). The optimal threshold value derived from this method is $T_{hagen} = (\mu_{ice} + \mu_{air})/2$. Note that the value $Q_{blur} = 1 - \lambda_{air} - \lambda_{ice}$ quantitatively estimates the quality of the grayscale image regarding the fuzzy transition artefact.

Post-processing The binary segmented image can be further corrected to erase remaining artefacts. This can be done manually for each plane but it is time consuming [Flin et al., 2003]. The continuity of the ice matrix can also be used to correct the binary image: in this case, ice zones not connected to the main structure or to the edges of the image are identified by using a connected component labelling algorithm and deleted [Calonne et al., 2014, Hagenmuller et al., 2013b, Schleef et al., 2014]. Among generic and automatic post-processing methods, the morphological operators erosion and dilation are the most popular. The combination of these operators enables to delete small holes in the ice matrix or small protuberances on the ice surface. In the present work, the sensitivity to the support size d of the morphological filters is analysed in section 3.3.2.3 by applying closing (erosion then dilation) and opening (dilation then erosion) filters of different sizes.

3.2.2.2 Energy-based segmentation

Energy-based segmentation methods consist in finding the optimal segmentation according to an energy function. These methods are robust and flexible because the

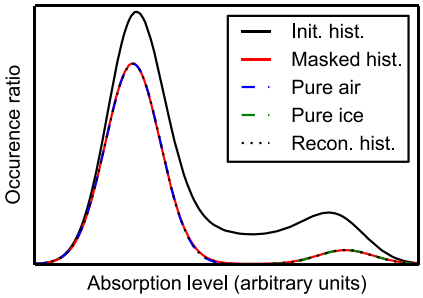

(a) Mixture model composed of two Gaussian distributions to reproduce the grayscale distribution on the low-intensity gradient zones. L_1 error is 0.006.

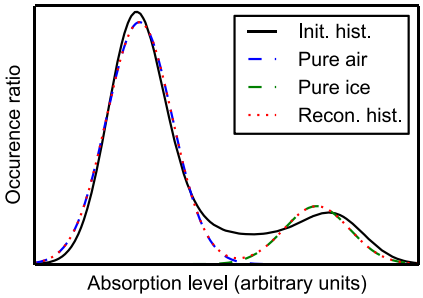

(b) Mixture model composed of two Gaussian distributions to reproduce the whole grayscale distribution. L_1 error is 0.14.

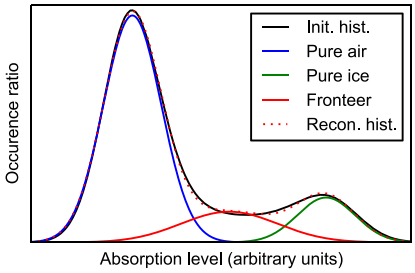

(c) Mixture model composed of three Gaussian distributions to reproduce the whole grayscale distribution. L_1 error is 0.03.

Figure 3.4: Different intensity models based on the grayscale distribution. The L_1 error is the integral of the absolute difference between the measured and the modeled grayscale distributions. Note that the area under the grayscale distribution on the entire image is 1.

best segmentation is automatically found by the optimization process, according to an energy function which can incorporate various segmentation criteria. In general, the optimization of functions composed of billion of variables can be complex and time consuming. However, knowing that the variables are binary and with some restrictions on the form of the energy function, very efficient global optimization methods can be applied. For instance, functions that involve only pair interactions can be globally optimized in a very efficient way with the graph cut method [Kolmogorov and Zabih, 2004].

The energy function E used in the present work is composed of two components: a data fidelity term E_v and a spatial regularization term E_s. The definition of E is similar to the one proposed by Hagenmuller et al. [2013b] for the binary segmentation of impregnated snow samples, except that the data fidelity term is, here, adapted for the processing of air/ice images. The data fidelity term assigns penalties for classifying a voxel to ice or air, according to its local grayscale value. Qualitatively, it "costs" more to assign a voxel with a grayscale value close to the attenuation peak of ice, to air instead of ice. Quantitatively, we define E_v as follows:

$$E_v(L) = v \cdot \sum_i \Big((1 - L_i) \cdot P_0(I_i) + L_i \cdot P_1(I_i) \Big) \tag{3.3}$$

where L is the segmentation label (0 for air, 1 for ice), P_0 is the proximity to air, and P_1 the proximity to ice. This energy is scaled by the volume of one voxel v. The proximity functions quantify how close a grayscale value is to a certain material. They are defined with the variables adjusted by the three-Gaussian fit (equation 3.2) of the histogram as following:

$$P_0(I) = \begin{cases} 1 \text{ if } I < \mu_{air} \\ \min\left(1, e\mathcal{N}(\mu_{air}, \sigma)(I)\right) \text{ elsewhere} \end{cases} \tag{3.4}$$

$$P_1(I) = \begin{cases} 1 \text{ if } I > \mu_{ice} \\ \min\left(1, e\mathcal{N}(\mu_{ice}, \sigma)(I)\right) \text{ elsewhere} \end{cases} \tag{3.5}$$

with $e = \exp(1)$

The spatial regularization term $E_s(L)$ is defined as $r \cdot S(L)$ with $S(L)$ the surface area of the segmented object L and r ($r \geq 0$), a parameter, which has the dimension of a length. Accounting for this term in the energy leads to penalizing large interface areas: a voxel with an intermediate gray value is segmented so that the interface air/ice area is minimized. The parameter r assigns a relative weight to the surface area term in the total energy function E. The segmentation parameter r enforces the minimum radius of protuberances preserved on the segmented object [Hagenmuller et al., 2013b]. The regularization term minimizing the ice/air interface is of particular interest for materials such as snow where metamorphism naturally tends to reduce the surface and grain boundary energy. This process is particularly effective on snow types resulting from isothermal metamorphism. For other snow types, such as precipitation particles (PP), faceted crystals (FC) or depth

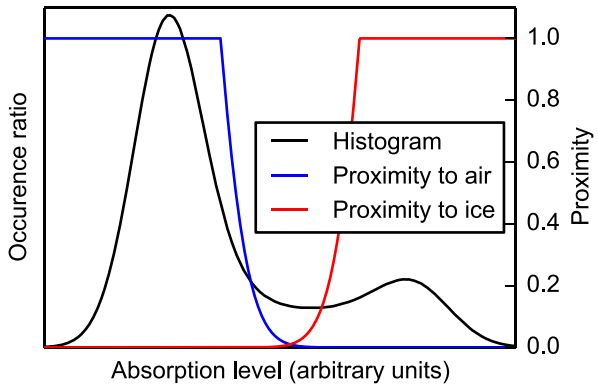

Figure 3.5: Proximity functions obtained with equation 3.5 and the histogram fit (equation 3.2) obtained on image G2-s1.

hoar (DH), the surface regularization term is expected to perform well in recovering the facet shapes but may induce some rounding at facet edges, which, however, does not significantly impact the overall specific surface area.

The sensitivity of the segmentation results to the parameter r is investigated in Section 3.3.3.

3.2.3 Surface area computation

Flin et al. [2011] evaluated three different approaches to compute the area of the ice-pore interface from 3D binary images: the stereological approach [e.g. Torquato, 2002], the marching cubes approach [e.g. Hildebrand et al., 1999] and the voxel projection approach [Flin et al., 2005]. Flin et al. [2011] showed that these approaches provide globally similar results but each method has its own inherent drawbacks: the stereological approach does not handle anisotropic structures properly, the marching cubes tends to overestimate the surface, and the voxel projection method is highly sensitive to image resolution. In the present work, in order to estimate if the variations of SSA due to different surface area computation approaches are significant compared to the effect of binary segmentation, we tested three different methods to quantify the surface area: the stereological approach, the marching cubes approach and the Crofton approach. We did not evaluate the voxel projection method because its implementation is sophisticated and the method is not widely spread in the snow and material community.

Stereological approach The stereological approach consists in counting the number of interface points on linear paths along the x, y or z directions. The surface area is twice the number of intersections times the area of a voxel face. A surface area value is given for each direction.

Marching cubes approach The marching cubes approach consists in extracting a polygonal mesh of an isosurface from a three-dimensional scalar field. Summing the area contributions of all polygons constituting the mesh provides the surface area of the whole image. We used a homemade version of the algorithm developed by Lorensen and Cline [1987]. It computes the surface area of the 0.5-isosurface of the binary image. Our version of the algorithm is adapted to compute only the surface area without saving all the mesh elements that are required for 3D visualization.

Crofton approach The Crofton approach is a generalization of the stereological method with the mathematical formalism provided by the Cauchy-Crofton formula. The Cauchy-Crofton formula relates the area of a surface to the number of intersections with straight lines [Boykov and Kolmogorov, 2003]. This formula can be discretized by using only a finite number of straight lines oriented along certain directions. In the stereological approach only 3 directions are considered. We presently used 13 and 49 directions, and the improved approximations based on Voronoi diagrams proposed by Danek and Matula [2011b].

3.3 Results

In this section, the methods to compute the area of the ice-air interface are first evaluated. This evaluation is presented first because the sensitivity of the surface area to computation methods can be investigated on reference objects, whose area is theoretically known, without accounting for the interplay with the binary segmentation method. The Crofton approach, which is shown to perform at best, is selected to compute the SSA in the rest of this study. Second, the sensitivity of SSA to the segmentation parameters of the sequential filtering approach and the energy-based method is evaluated on the entire set of snow images. Finally the variability of SSA due to numerical processing is compared to the variability of SSA due to snow spatial variability and scanning resolution.

3.3.1 Surface area estimation

First, the different surface area computation methods are compared on a binary image describing a simple shape whose surface area is known theoretically. An oblate spheroid (or ellipsoid of revolution) was chosen as reference shape and discretized into a binary image. This shape was chosen because it is simple, anisotropic and its surface area is directly a function of the length of its semi-axes. Spheroids of different sizes but same shape were used to evaluate the impact of the discretization on the surface area computation. Figure 3.6 shows that the surface area calculated with the Crofton approach is in excellent agreement with the theoretical area: for sufficiently large spheroids, i.e. surface area larger than 200 voxels^2 or largest semi-axis larger than 5 voxels, the relative error is less than 1% for the Crofton approach with 49 different directions and 2% for the Crofton approach with 13 different directions. Adding more directions does not significantly improve the accuracy of the

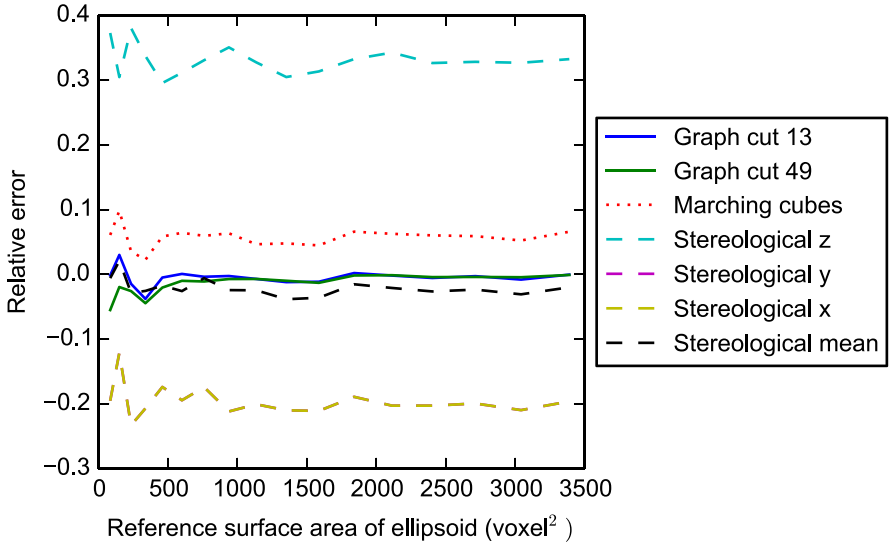

Figure 3.6: Surface area of a oblate spheroid, obtained with different calculation methods. The spheroid has a horizontal (x, y) semi-axis a varying in $[3, 19]$ voxel and a vertical (z) semi-axis $c = 0.6 \cdot a$. The reference surface area of the spheroid is computed analytically. The Crofton approach is computed with 13 or 49 different directions.

Crofton approach while it increases the computation time. In the following, only 13 directions are used in the Crofton approach. The marching cubes systematically overestimates the surface area by about 5%. Indeed, the triangulation of the isosurface is affected by series of artificial steps. As expected, the stereological method shows scatter in the results obtained between the vertical (z) and horizontal components (x, y) since the spheroid is anisotropic. The mean value of the different components provides a fair estimation of the surface area. Indeed this mean value underestimates the area by only about 2%. These observations on the stereological and marching cubes approaches corroborate previous results obtained by Flin et al. [2011] on snow images.

Second, the different surface area computation methods are evaluated on the entire set of snow images segmented with the energy-based method ($r = 1$). According to the results obtained on the spheroid, the Crofton approach was chosen as a reference. As shown in Figure 3.7, the SSA obtained with the direction-averaged stereological method is in excellent agreement with the one obtained with the Crofton method. The results of the marching cubes method are in fair agreement but show a systematic over-estimation of the SSA (+6% average relative deviation).

In summary, all presented area computation method showed consistent results. The Crofton approach showed the best accuracy on an artificial anisotropic structure whose surface area is theoretically known. The stereological approach is negatively affected by strong anisotropy of the imaged structure. However on the tested snow

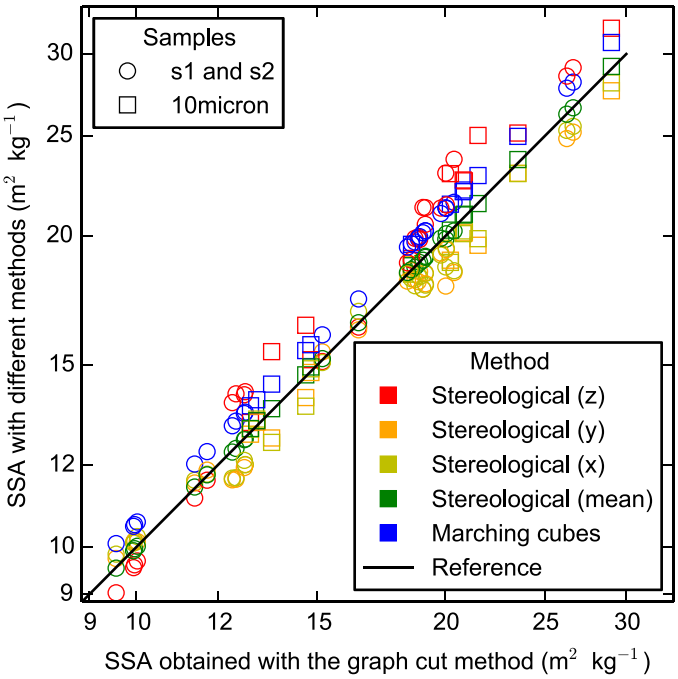

Figure 3.7: Comparison of the specific surface area obtained with different surface area calculation methods on all images binarized with the energy-based segmentation ($r = 1$ voxel). The root mean square error of the SSA computed as the direction-average of the stereological method is 0.008 $m^2\ kg^{-1}$ according to the SSA computed with the Crofton approach. This error is 1.13 $m^2\ kg^{-1}$ for the marching cube approach. The black line represents the 1:1 line.

images, the surface anisotropy is low and this method is in excellent agreement with the Crofton approach. The marching cubes approach always overestimates the specific surface on the order of 5%. For the following analysis of the sensitivity to binary segmentation, the SSA is computed via the Crofton approach with 13 directions.

3.3.2 Sequential filtering

The binary image image resulting from the sequential filtering approach depends on:

- the standard deviation σ of the Gaussian filter,
- the threshold value T,
- the size d of the morphological filters (opening/closing).

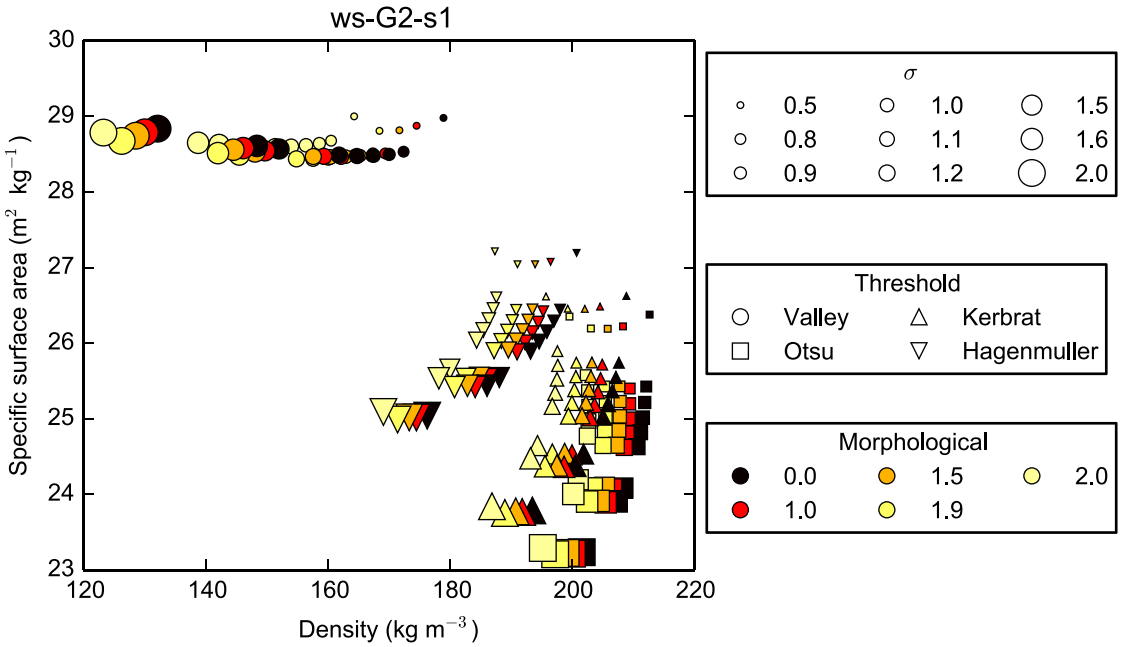

Figure 3.8: SSA and density of image G2-s1 obtained with sequential filtering for different segmentation parameters.

As shown in Figure 3.8, SSA and density are sensitive to these segmentation parameters. The relation between SSA and density, on the one hand, and σ and d, on the other hand, depends significantly on the chosen threshold. In the following, the dependence of SSA and density on the threshold is first investigated. Then the effects of σ and d on the binary segmentation are analysed with a threshold obtained with the mixture model of Hagenmuller et al. [2013b].

3.3.2.1 Choice of threshold

The threshold obtained with the two-Gaussian fit on the grayscale histogram computed on the low-intensity gradient zones is chosen as a reference since this value is not affected by the fuzzy transition artefact. Moreover, in practice, all threshold-determination methods yield the same threshold on this histogram. The reference threshold value ranges between 38800 and 39500 (Figure 3.9). The mean values of the attenuation peaks of air and ice are $\mu_{air} = 36000$ and $\mu_{ice} = 43000$, respectively. The variations of the reference threshold value are small compared to the contrast between the two attenuation peaks ($\mu_{ice} - \mu_{air} = 7000$). However, these variations indicate, once again, that the same threshold value cannot be used for all images. The origin of these variations is not clear but could be explained by slight variations in the X-ray source energy level or deviations from the Beer-Lambert attenuation law depending on the total ice content of the sample.

The computed threshold depends significantly on the determination method (Figure 3.9). This scatter affects the density of the binary image segmented with these thresholds (Figure 3.10a). The scatter on density due to the choice of the threshold remains the same even if a Gaussian filter is applied on the grayscale image before thresholding (Figure 3.10a). The SSA values are also affected by the choice of the threshold but in a smaller proportion since this choice tends to affect density and total surface area in the same proportions (Figure 3.10b). The variations of SSA due to smoothing are much more important than those due to the choice of the threshold (Figure 3.10b).

The valley method, which consists in finding the local minimum between the two attenuation peaks, systematically overestimates the threshold value, leading to a systematic underestimation of the snow density by about 10 kg m^{-3} on average. Otsu's method, which consists in finding the threshold minimizing the intra-class variance, tends to underestimate the threshold value, leading to an overestimation of the snow density by about 6 kg m^{-3} on average. Kerbrat's method, which consists in finding the threshold by fitting the sum of two Gaussian distributions on the grayscale distribution, tends to underestimate the threshold value, leading to an overestimation of the snow density by about 4 kg m^{-3} in average. Note that the density overestimation by Kerbrat's method is more pronounced on low-density snow samples scanned with a 18 μm resolution. Eventually, the method introduced by Hagenmuller et al. [2013b], which consists in finding the threshold by fitting the sum of three Gaussian distributions on the grayscale distribution, slightly underestimates the threshold value and therefore overestimates the snow density with a mean absolute difference to the reference of 2 kg m^{-3}.

In summary, the threshold value obtained with the valley method, a method widely used in the snow community, clearly leads to an underestimation of the snow density. The mixture models of Kerbrat et al. [2008] or Hagenmuller et al. [2013b], which assume that noise is Gaussian distributed provides a threshold value in good agreement with the reference method. The model of Hagenmuller et al. [2013b] also accounting for the fuzzy transition between materials yields the threshold which is the closest to the reference value obtained on the masked image.

3.3.2.2 Gaussian filtering

The sensitivity of density and surface area to the standard deviation σ of the Gaussian smoothing kernel is shown on Figure 3.11. The segmentation was performed with the threshold derived with the method of Hagenmuller et al. [2013b].

For σ in the range [0, 20] μm, density varies in the range [-8, +2]% with respect to the value obtained without smoothing ($\sigma = 0$) (Figure 3.11a). No density variations are observed for values of σ much lower than the resolution voxel size. For larger values of σ, the average decrease with σ is due to the fact that the snow structure is generally convex and smoothing tends to erode convex zones. Systematic differences are observed between the images with a resolution of 10 μm and 18 μm. For all images at a resolution of 10 μm, the decrease of density is significantly faster in the

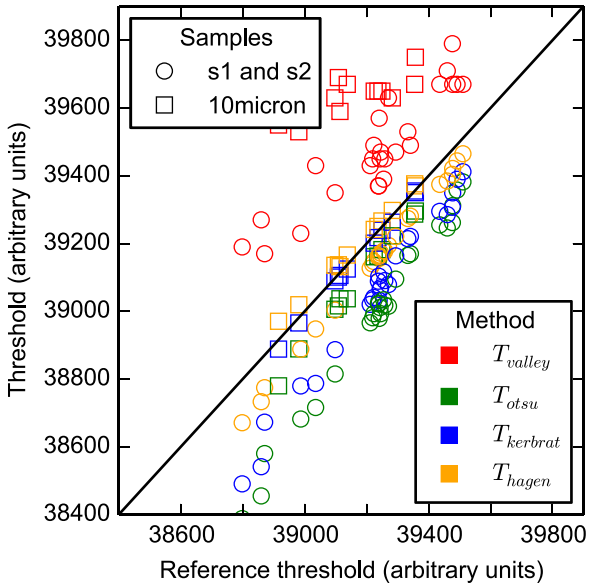

Figure 3.9: Threshold values obtained on the entire set of images with the different intensity models. The black line represents the 1:1 line.

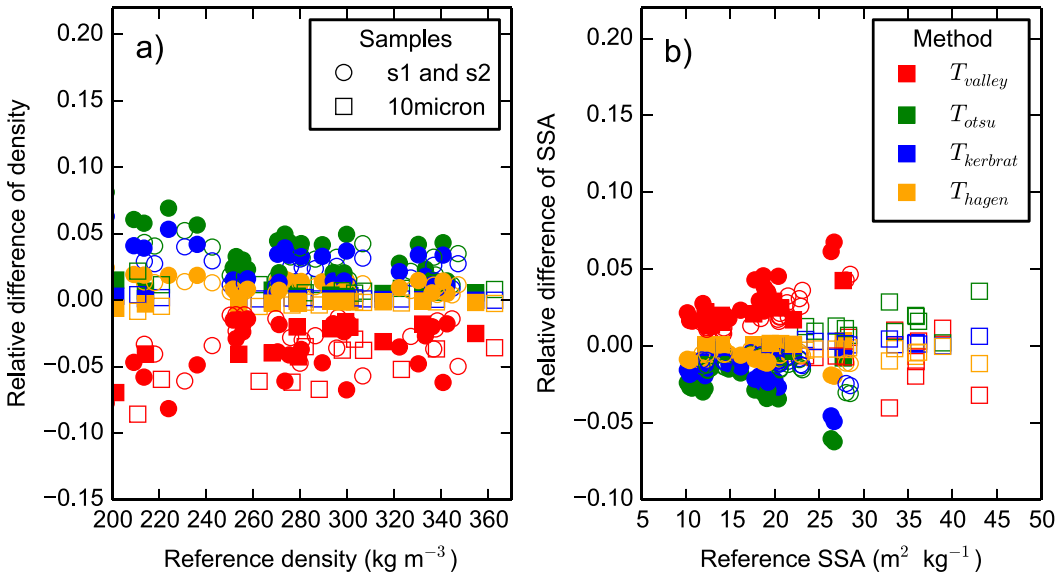

Figure 3.10: Relative variation of density (a) and SSA (b) computed with different threshold-determination method, with respect to the reference values computed with T_{mask}. The markers with a white face (respectively faces in color) correspond to values obtained without any smoothing (respectively with a Gaussian filter of standard deviation $\sigma = 1$ voxel).

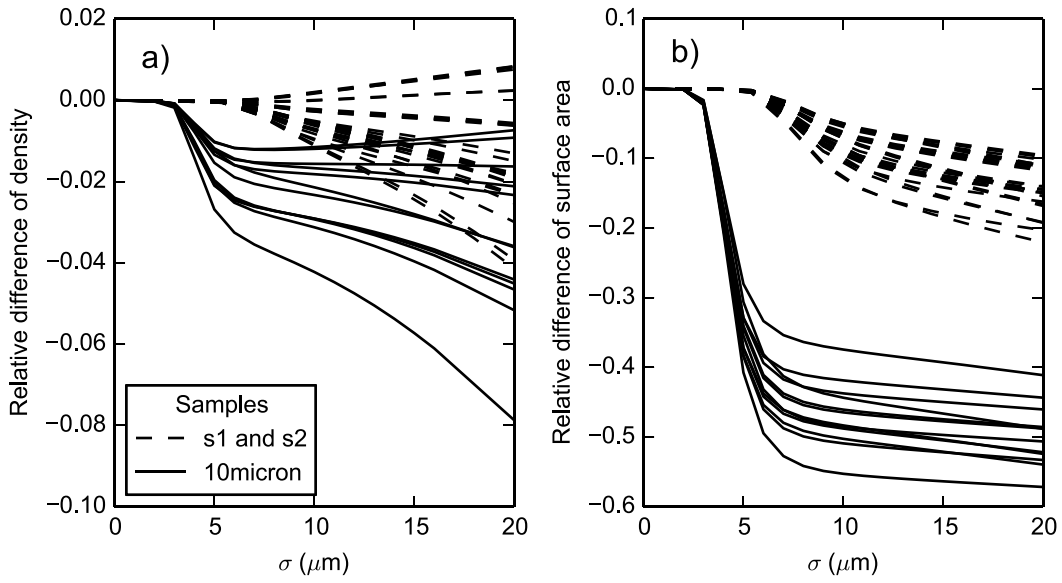

Figure 3.11: Relative variations of density (a) and surface area (b) with σ. The variations were calculated according to density and surface area obtained without smoothing filters. Note that since the variations of density with σ are small compared to the variations of the surface area with σ, the variations of SSA with σ are very similar to the one observed for the surface area.

range [3, 6] μm. For larger values of σ, the effect of σ on density is similar to the one observed on the 18 microns images, and depends on the snow type. This difference is due to a stronger noise in the 10 μm images, which creates many grayscale local variations that are generally smoothed out when $\sigma > 6$ μm.

The computed surface area significantly decreases when σ increases (Figure 3.11b). Relative variations up to 50% are observed. On the 10 μm images and with σ in [3, 6] μm, the surface area decreases rapidly when σ increases. These variations probably correspond to the progressive smoothing of the noise on the interface. For larger values of σ, the surface area decreases much more slowly with σ, which corresponds to the progressive smoothing of real microstructural details. On the 18 μm images, these two regimes cannot be distinguished because there are less noise artefacts that could affect the overall surface area and there exist real structural details of the size on the order of a few voxels. The same variations with σ can be observed on SSA since the variations of density with σ are small compared to the one observed on the surface area. Note that the absolute values of density and SSA for the different snow images are shown on Figure 3.15.

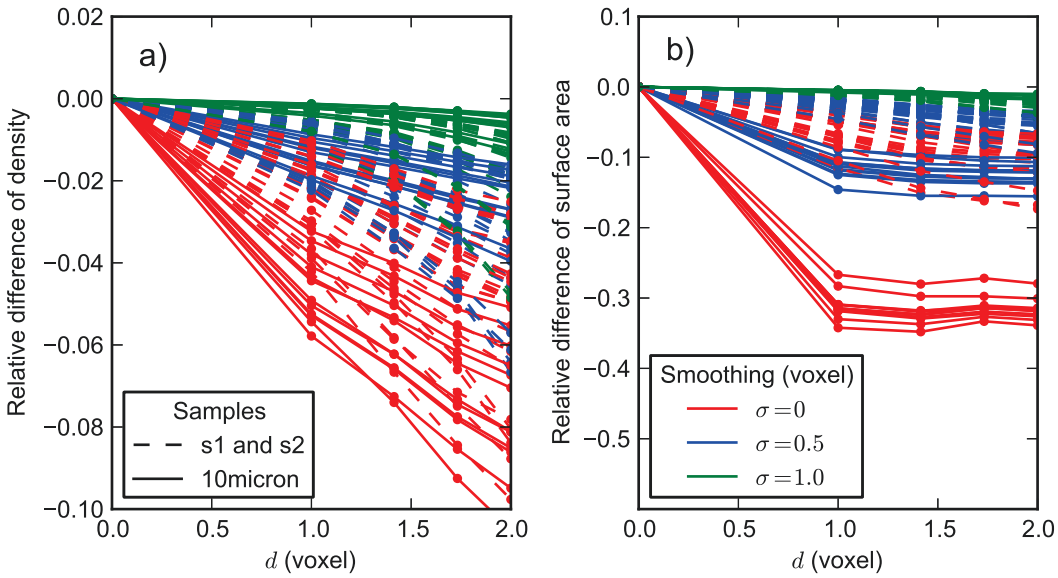

Figure 3.12: Relative variations of density (a) and surface area (b) as a function of d for different values of σ. The legends in the subplots apply on both subplots.

3.3.2.3 Morphological opening/closing

Figure 3.12 shows the relative variation of density and surface area with morphological filters of different sizes. Note that the size d of these filters is constrained by the voxel grid and is thus discrete (1, $\sqrt{2}$, $\sqrt{3}$, 2 voxel, etc.). The opening and closing filters delete holes in the ice matrix or ice elements in the air, of a typical size d. Therefore, the surface area decreases when d increases. Density is not very sensitive to d, as it was observed with σ. When no Gaussian filter is applied on the grayscale image, thresholding yields a lot of small details in the binary image, which enhances the effect of morphological filters (Figure 3.12b). When the image is already smoothed by Gaussian filtering, the morphological filters affect less the overall density and specific surface area. However, note that using a Gaussian filter of standard deviation σ does not guarantee the complete absence of details "smaller" than σ. Certain algorithms based on the binary images, such as grain segmentation [e.g. Brzoska et al., 2007, Theile and Schneebeli, 2011] are highly sensitive to the presence of residual artefacts in the ice matrix and require these additional morphological filters.

3.3.3 Energy-based approach

The binary image image resulting from the energy-based approach depends on the parameter r which controls the smoothness of the segmented object. The other parameters involved in the volumetric term E_v of the segmentation energy are directly

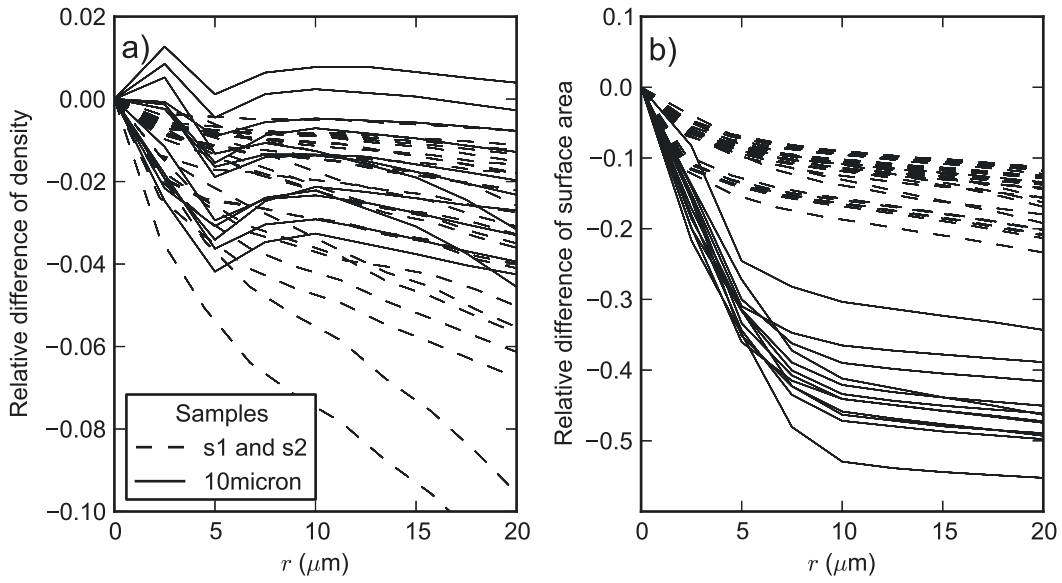

Figure 3.13: Relative variations of density (a) and surface area (b) as a function of r.

derived from the three Gaussian mixture model.

As shown in Figure 3.13a, the density of the segmented object slightly varies with r. On the 10 μm images, the evolution of density with r is not monotonic and relative variations are limited in the range [-4, +1]%. On the 10 μm images, density clearly decreases when σ increases. The higher sensitivity of density to r on the 18 μm images can be explained by the fact that the fuzzy transition visually appears to be larger than on 10 μm images, which yields a higher indetermination of the exact position of the interface between ice and air in this moderate intensity gradient zone (Figure 3.14). In the fuzzy transition, the data fidelity term E_v in the segmentation energy is thus not determinant since the grayscale values are in between the attenuation peaks of air and ice. Therefore, accounting of the surface area energy term E_s is dominant in the segmentation process of the transition zone, which tends to erode the convex snow microstructure.

As shown in Figure 3.13b, surface area is, unlike density, more sensitive to r and decreases significantly when r increases. Two regimes can be distinguished. For very low values of r ([0, 10] μm), the surface area decreases rapidly when r increases. For larger values of r ([10, 20] μm), the surface area decreases much slower with r. As already shown by Hagenmuller et al. [2013b], for large values of r, the surface area decreases with r with an almost constant slope, because the real details of the snow structure contributing to the overall surface area are progressively smoothed out. This behavior indicates a continuum of the size of structural details in the snow microstructure. The distinction between the two regimes is more pronounced on the 10 μm images which are more affected by noise (Figure 3.14).

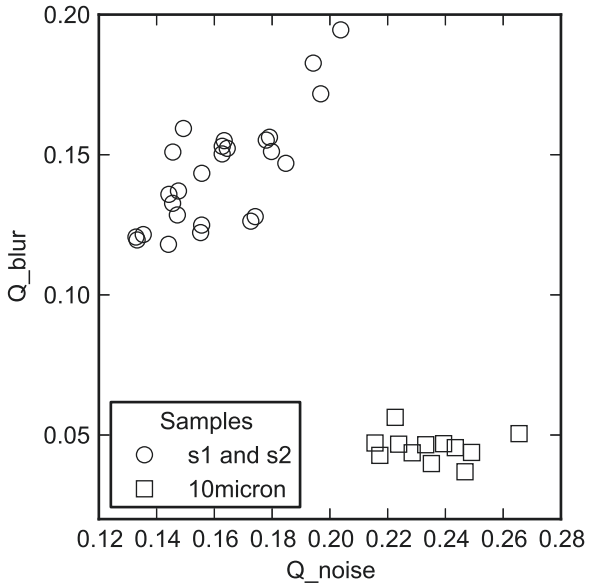

Figure 3.14: Estimation of the importance of the artefacts due to noise (Q_{noise}) and to the fuzzy transition (Q_{blur}). Q_{noise} corresponds to the ratio between the standard deviation of the Gaussian distributions fitted on the attenuation peaks and the difference between the peak attenuation intensity of ice and air (see Section 3.2.2.1). Q_{blur} corresponds to the area of the Gaussian representing the fuzzy transition in Hagenmuller's mixture model (see Section 3.2.2.1).

3.3.4 Comparison between images and methods

The sensitivity of the surface area to σ and r is similar but the energy-based and sequential filtering approaches are conceptually different (Figures 3.11 and 3.13). The Gaussian filter smoothes high-frequency intensity variations with a small amplitude, without considering the subsequent binary thresholding. Small details due to noise artefacts and remaining in the binary image are then deleted by applying morphological filters. The energy-based approach smoothes the segmented object so that the ice-air interface area is minimized while respecting at best the grayscale intensity model. The grayscale smoothing and morphological are somehow done simultaneously in the energy-based approach. The Gaussian filter is "grid-dependent": as shown in Figure 3.11b, this filter does not affect the segmented object if σ is to small compared to the voxel size. The noise artefacts remaining after thresholding are deleted from the binary image independently of the initial grayscale value. In contrast, for the energy-based approach, smoothing of the ice-air interface occurs for very low values of r (Figure 3.13b) because voxels with a grayscale value very close to the threshold value between ice and air can be segmented as air and ice without much changing the data fidelity term E_v but with a clear change of surface term E_s. The parameter r defines the largest equivalent spherical radius of details in the segmented image, whereas σ does not directly correspond to the size of the smallest detail.

Figure 3.15 shows density and specific surface area computed on the set of snow images segmented with the sequential filtering approach ($\sigma = 1.0$ voxel, $T = T_{hagen}$, $d = 1.0$ voxel) and the energy-based approach ($r = 1.0$ voxel). The "smoothing" parameters (σ and r) were chosen equal to 1.0 voxel because the segmentation that preserves the smallest snow details while deleting most of noise-induced protuberances, is obtained when the computed surface area starts to vary slowly with σ and r (Figures 3.11b, 3.13b). For all 10 microns images, this transition is clear. For the sequential filtering method, it occurs for $\sigma = 1.0$ voxel ($\sigma = 10$ μm) (Figure 3.11b). For the energy-based method, it occurs for the value $r = 1.0$ voxel ($r = 10$ μm) (Figure 3.13b). For the 18 microns images, this transition is less evident. To be consistent with the chosen values of σ and r for the 10 microns images and in order to ensure that all noise artefacts are smoothed out, we chose also a value of $\sigma = 1.0$ voxel ($\sigma = 18$ μm) and $r = 1.0$ voxel ($r = 18$ μm).

The two approaches produce similar results in terms of density (root mean square deviation between the two segmentation methods is 6 kg m^{-3}) and specific surface area (root mean square deviation of 0.7 m^2 kg^{-1}). The largest differences are observed on the snow types presenting the highest SSA. In general, the density provided by the sequential filtering is slightly larger than the one computed with the energy-based approach. The opposite difference is observed on SSA.

Three samples of the same snow block were scanned. It is expected that the density and SSA derived from images of the same snow block are similar. However, scatter is observed between the characteristics derived from the images of same snow block because of spatial variability inside one snow block. Indeed, the averages

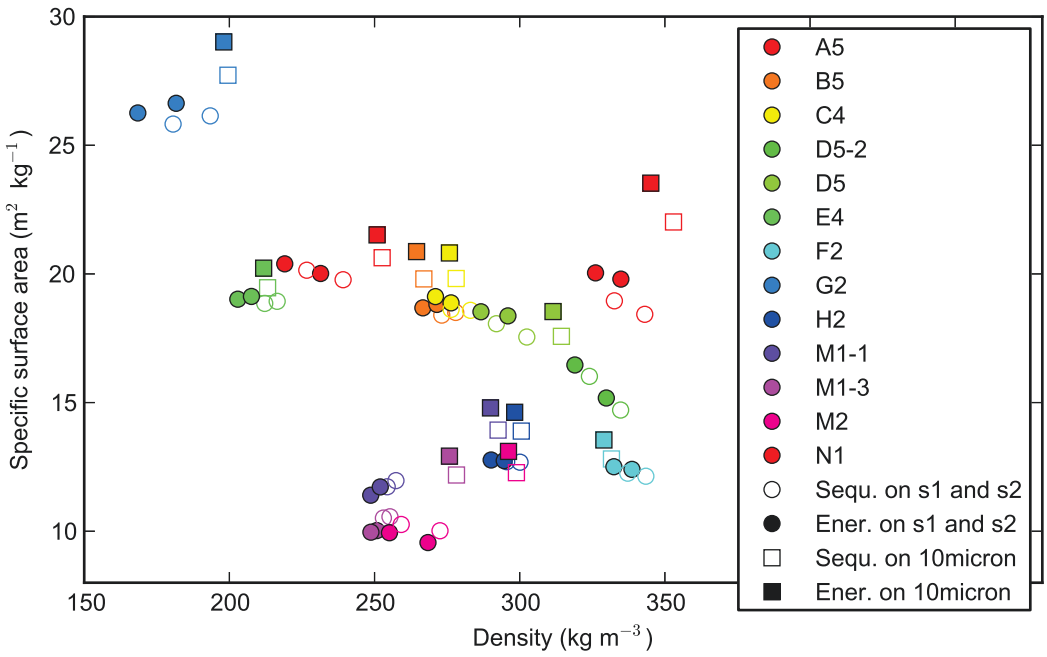

Figure 3.15: Specific surface area as a function of density for the entire set of images and the two different binary segmentation method. The sequential filtering ("Sequ." in the legend) was applied with $\sigma = 1.0$ voxel, $T = T_{hagen}$ and $d = 1.0$ voxel. The energy-based approach was applied with $r = 1.0$ voxel. The surface area was commuted with the Crofton approach.

of the standard deviations calculated for each snow block, for density and SSA are respectively, 9.0 kg m^{-3} and 1.0 m^2 kg^{-1} (density and SSA calculated from images segmented with the energy-based approach). Nevertheless, the intra-block variability appears to be limited compared to the inter-block variability (Figure 3.15). Moreover, note that the intra-block variability is of the same order as the variability due to the image processing technique (see above).

A systematic larger density and SSA values are found on the images scanned with a 10 μm voxel size. It could be argued that this difference is due to a better imaging of small details with a lower voxel size. However, as already noticed, the 10 μm images present stronger noise artefacts (Figure 3.14) and it is difficult to asses whether the effective resolution of these images is, in practice, finer than the one of the 18 μm images.

3.4 Conclusion

We investigated the effect of numerical processing of microtomographic images on density and specific surface area derived from these data. To this end, a set of

38 X-ray attenuation images of non-impregnated snow were analysed with different numerical methods to segment the grayscale images and to compute the surface area on the binary images.

To allow quantitative characterization, the grayscale images need to be segmented into binary images. This step is not straightforward because the grayscale images present noise and blur. It is shown that noise artefacts can significantly affect the overall SSA and that the fuzzy transition between ice and air makes the choice of the threshold critical and determinant for the computed density.

The sequential filtering depends on the threshold used to separate ice and air. The grayscale histogram on low-intensity gradient zones presents two disjoint attenuation peaks, whose characteristics are not affected by blur. The threshold derived from this method was used as a reference to evaluate other methods based on the analysis of the grayscale histogram of the entire image. The mixture models which consist in decomposing the histogram into a sum of Gaussian distributions are shown to be accurate. On the contrary, the local minimum method is shown to be not suitable as a threshold, in general.

Smoothing induced by the Gaussian and morphological filters in the sequential approach or accounting for the surface area term in the energy-based method efficiently remove noise artefacts from the segmented binary image. The advantage of the energy-based method is that r defines a continuous effective resolution of the binary image. Morphological filters applied on the binary image miss the initial gray value information. However, it seems that their effect are negligible if the applied Gaussian filter is strong enough. The smoothing also induces the disappearance of real structural details contributing to the overall SSA. The transition between smoothing of noise and smoothing of real details can be well estimated on the curve showing the evolution of SSA as a function of σ or r. However, it is unclear whether structural details of the size smaller than the voxel size can significantly contribute to the overall SSA. The comparison with independent SSA measurements at a submicrometric resolution such as methane absorption could help investigating this issue.

The presented area computation methods showed consistent results on a synthetic image and the set of snow images. On the synthetic image (oblate spheroid), the Crofton approach computes the surface area with highest accuracy (less than 2% for sufficiently large spheroids) whereas the stereological approach is negatively affected by strong anisotropy of the imaged structure and the marching cubes approach overestimates the specific surface on the order of 5%. However on the tested snow images, the surface anisotropy is lower and the stereological method is in excellent agreement with the Crofton approach. On the snow images, the marching cubes approach still overestimates the specific surface on the order of 5%.

The comparison of the sequential filtering and energy-based methods shows that density and SSA can be estimated from X-ray tomography images with an "numerical" variability of the same order as the spatial variability of the microstructure within one snow layer.

Chapter 4

Numerical simulation of microstructural damage and tensile strength of snow

Abstract This contribution uses finite-element analysis to simulate microstructural failure processes and the tensile strength of snow. The 3D-structure of snow was imaged by microtomography. Modeling procedures used the elastic properties of ice with bond fracture assumptions as inputs. The microstructure experiences combined tensile and compressive stresses in response to macroscopic tensile stress. The simulated non-localized failure of ice lattice bonds before or after reaching peak stress creates a pseudo-plastic yield curve. This explains the occurrence of acoustic events observed in advance of global failure. The measured and simulated average tensile strengths differed by 35%, a typical range for strength measurements in snow given its low Weibull modulus. The simulation successfully explains damage, fracture nucleation and strength according to the geometry of the microstructure of snow and the mechanical properties of ice. This novel method can be applied to more complex snow structures including the weak layers that cause avalanches.

Contents

4.1 Introduction

The fracture of snow causes avalanches [Schweizer et al., 2003], which constitute a major natural hazard in alpine environments. Persistent uncertainties in how initial cracks form in snow require investigation into tensile strength and damage formation in snow at the microstructural level. Current models assume a weak zone when applying fracture mechanics to failure predictions for real-world conditions [McClung, 2011]. How this weak zone initially forms is unknown. This lack of understanding is partly due to difficulties in measuring the mechanical properties of snow, given its brittle and friable nature.

Snow consists of air and sintered ice crystals or grains. These grains fuse to form bonds, or junctures, that range in size from 10 - 1000 μm and which concentrate stress. The bonds are more likely to fail than other structural elements but their failure processes have not been systematically studied. The primary failure of slab avalanches occurs in layers having a thickness of less than a few centimeters. Field and laboratory tests have provided only a very limited number of direct mechanical tests of this surface [Reiweger et al., 2010]. Snow under tensile stress fails at very low levels of strain (less than 0.1%) and high strain rates [Narita, 1980]. Three-dimensional modeling of mechanical processes could therefore significantly improve understanding of fracture initiation at the microstructural level.

The 3-D reconstruction of snow has become a standard technique over the past decade [Heggli et al., 2011, and references therein]. The use of the 3-D microstructural simulations has informed understanding of both thermal properties [Riche and Schneebeli, 2013] and metamorphism [e.g. Chen and Baker, 2010, Pinzer et al., 2012]. Schneebeli [2004] also used microstructural modeling to simulate the elastic modulus of snow.

This paper describes results from numerical simulations of microscopic and macroscopic damage processes in snow that can ultimately lead to its failure. Empirical observations of mechanical properties of ice in the brittle regime [Schulson and Duval, 2009] and the 3-D microstructure provided inputs to the simulations. This research specifically focused on fast, brittle deformation under tensile load as a damage process. The tensile strength of snow ranges from 0.1 kPa to 1000 kPa for a density of 100 to 600 kg m^{-3}. This non-linear, approximately logarithmic relationship between strength and density, arises from microstructural variation in snow. Experimental results by Narita [1980] for example have shown that identical snow samples having a density of 300 kg m^{-3} range in strength from 20 kPa to 70 kPa.

4.2 Data and methods

4.2.1 Snow and sample preparation

A 30 x 30 x 30 cm^3 snow block was collected during the 2010 –2011 winter from a field locality near Davos, Switzerland, and stored at -20° C. The block was homogeneous

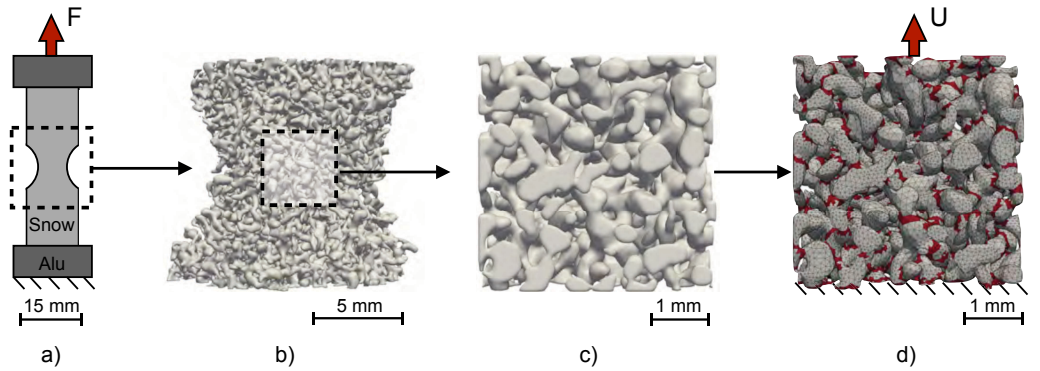

Figure 4.1: Description of methods: a) Configuration of the mechanical test and measurement of the maximum tension force, F. b) μCT scan. c) Subvolume on which the simulation was performed. d) Finite-element mesh and potential intergranular cracks (red).

and consisted of small rounded grains (RGsr). Eleven cylindrical samples (13 mm radius by 40 mm height) were cored from the block. Small aluminum plates were thermally welded to the top and bottom of the sample columns in order to evenly distribute the applied tensile force. A volume near the center of the column was pared down to a diameter of 7 - 10 mm (Figure 4.1a), so that the columns resembled a standard notched tensile test specimen.

4.2.2 Experimental methods

The sample columns were imaged using micro computed tomography (micro-CT). A micro-CT 40 (Scanco Medical) operated at a resolution of 16 μm (Figure 4.1b) provided Gaussian filtered 3-D grayscale images (standard deviation 2 voxels). The ice phase was segmented according to the minimum of the bimodal attenuation histogram. A segmented volume of 125 x 125 x 125 voxels (4 x 4 x 4 mm^3) at 32 μm resolution was extracted within the pared zone (Figure 4.1c). Sensitivity analysis showed constant elastic moduli and tensile strengths for volumes greater than about 22 mm^3 (2.8 mm x 2.8 mm x 2.8 mm; Figure 4.8 in the appendix). These dimensions may vary for different types of snow.

Following collection of each μCT image, the snow columns underwent a tensile test performed at -20° C. The tests consisted of a manually guided vertical (z-axis) force imposed to the point of sample failure (Figure 4.1a). A dynamometer (0.1 N resolution) recorded maximum force with an uncertainty of about 10%. Manual loading did not allow precise control of the strain rate. The strain rate was around 10^{-4} s^{-1}, given a 1 s mechanical test and a simulated strain at failure of around 10^{-4}. The measured tensile strength, Σ_{max}, was derived from the maximum force, F, and the cross section minima of the snow column within the pared zone, S, as determined from the μCT-image, with $\Sigma_{max} = F/S$.

4.2.3 Numerical simulation

The extracted 3D volume was modeled into tetrahedral finite elements using ANSYS ICEM mesh generation software (www.ansys.com) (Figure 4.1d). The mesh was generated from the triangulated surface of the ice volume using a marching cube algorithm. A curvature-based refinement algorithm was used to coarsen the mesh along flat surfaces. This step reduced the number of elements but retained smaller elements at junctures between snow grains, which experience the highest stress gradients.

The micro-mechanical model used the following material properties of ice as inputs. The model assumes brittle properties (i.e., elastic until failure), consistent with the range of strain rates observed [Schulson and Duval, 2009]. Because absorption tomography cannot determine ice grain orientation, and given ice's anisotropic mechanical properties, we used orientation-averaged values. Tensile strength may vary from 2 to 6 MPa and unconfined compressive strength may vary from 12 to 32 MPa, depending on crystal orientation [Schulson and Duval, 2009]. For averages, we assumed a Young's modulus $E_{ice} = 9.5$ GPa, a Poisson's ratio, $\nu_{ice} = 0.3$, a tensile strength $\sigma_{ice,t} = 4$ MPa and a compressive strength $\sigma_{ice,c} = 20$ MPa [Schulson and Duval, 2009]. The maximum stress criterion (Rankine criterion) was used as a fracture criterion. This criterion states that failure occurs in a mesh element if one of the principal stresses reaches either $\sigma_{ice,t}$ or $\sigma_{ice,c}$.

To expedite simulation, failure was assumed intergranular. If a given junction between two grains reached fracture criterion, a crack instantly disconnected the two grains. A watershed segmentation algorithm mapped possible crack paths (see Figure 4.1d) and outlined rounded grains [Theile and Schneebeli, 2011]. The model used iterative elastic simulations on an evolving ice microstructure with progressive micro-crack formation to image the overall failure of the sample. In simulations, the meshed microstructure was subjected to a vertical tensile load. In keeping with mechanical experiments, a vertical displacement, U, (strain prescribed) was imposed on the top face (Figure 4.1d), with the bottom face fixed.

4.3 Results

In terms of structural properties, samples exhibited a mean density of 354±17 kg m^{-3}(1σ) and a mean specific surface area of 12.6±0.3 m^2 kg^{-1} (Table 4.1 in appendix). For the sake of brevity, we plot simulation results for one sample (Figures 4.2, 4.3 and 4.4). These results resembled those measured for the entire set of samples (Figures 4.5, 4.6 and 4.7).

4.3.1 Microscopic aspects of snow failure

Analysis of the stress distribution within the undamaged microstructure revealed a high degree of localization in the spatial distribution of the vertical stress, σ_{zz} (Figure 4.2a). Junctures between grains seemed to concentrate stress. Bending ef-

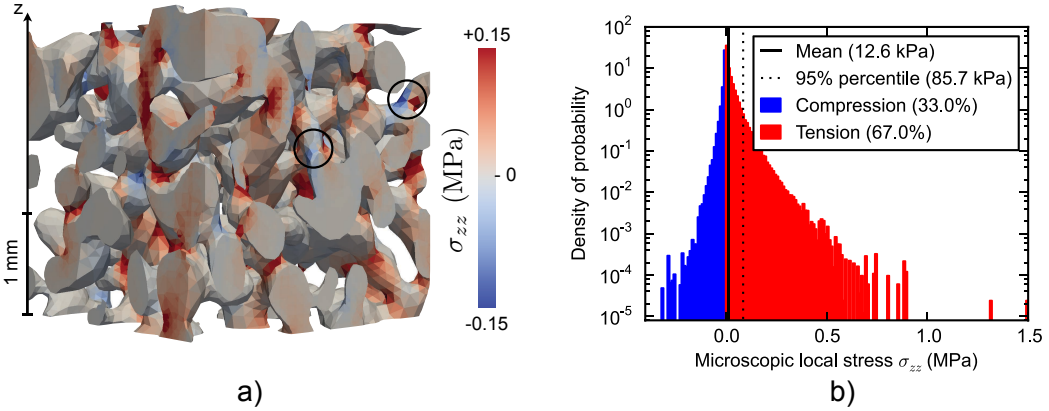

Figure 4.2: Distribution of the microscopic stress σ_{zz} subjected to a macroscopic vertical strain of 2×10^{-5}. a) 3-D representation for a $3 \times 3 \times 3$ mm^3 subvolume. Circled areas show two bonds undergoing bending deformation. b) Histogram of the stress distribution. By definition, 95% of the local stress values fall below the 95th percentile.

fects also enhance this localization by creating local compression ($\sigma_{zz} < 0$) on the opposite side of a bond experiencing local tension ($\sigma_{zz} > 0$) (Figure 4.2a). In quantitative terms, the stress distribution histogram (Figure 4.2b) shows that the 95th percentile of σ_{zz} values exceeds mean values by a factor of six. The maximal stress exceeds the mean value by a factor of 100. Thirty-three percent of the ice matrix experiences compression under macroscopic tensile deformation (Figure 4.2b).

The iterative numerical simulation also offers insight into progressive damage from increasing strain (Figure 4.2b). Damage occurred first in a spatially distributed manner (macroscopic strain in z direction $\mathcal{E}_{zz} < 2.5 \times 10^{-4}$) (Figure 4.4). A few bonds (less than 5%) experience damaged at relatively low strain. Towards the end of the simulation, the broken bonds form a failure surface that propagates into a complete fracture. About 75% of the broken bonds contribute to the final failure surface.

4.3.2 Macroscopic aspects

Young's modulus, E, was calculated from the ratio between the simulated macroscopic strain ($\mathcal{E}_{zz}$) and stress Σ_{zz}. Damage, D, is defined as $D = 1 - E/E_0$. E_0 and E are Young's moduli of the intact and damaged microstructure, respectively. Strain $\mathcal{E}_{zz}$ and stress Σ_{zz} share a linear relationship up to a macroscopic strain of $\mathcal{E}_{zz} < 0.4 \times 10^{-4}$ (Figure 4.2b). The value for E_0 was 226 MPa. Values for E decreased very slowly until about 5% damage. The stress eventually reached its maximal value of $\Sigma_{max} = 23.7$ kPa at a strain of $\mathcal{E}_{zz} = 1.4 \times 10^{-4}$. Σ_{max} is often reached after substantial damage, but here it was reached at about 20% damage. The simulations are strain-controlled, such that post-peak softening can be monitored until the sample has completely severed into two parts (Figure 4.4).

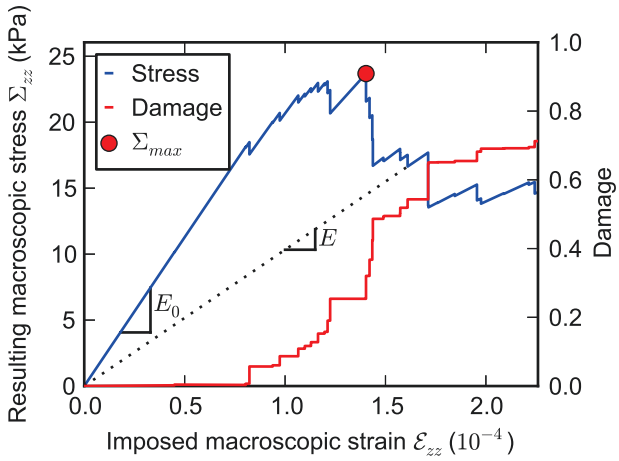

Figure 4.3: Macroscopic stress and percentage of damage as a function of macroscopic strain. The red dot indicates maximal stress reached.

The stress remained almost constant after damage reached about 20%, apparent as pseudo-plastic behavior in the strain-stress curve.

The measured tensile strength of all samples (17±8.5 kPa) was 35% less than the simulated strength (23 ± 10 kPa). The measured and simulated strengths are not strongly correlated ($R^2 = 0.09$, $p = 0.36$, residual standard error = 10 kPa). The density and simulated tensile strength however are strongly correlated ($R^2 = 0.85$, $p < 0.001$), as are density and simulated Young's modulus ($R^2 = 0.94$, $p < 0.001$). Simulated Young's modulus is also strongly correlated with simulated tensile strength ($R^2 = 0.93$, $p < 0.001$).

4.4 Discussion

4.4.1 Microscopic features

We observed a tensile macroscopic strain causing microscopically compressive (30%) and tensional stress (70%) in snow samples. An imposed macroscopic compressive strain will have the opposite effect, but failure will be induced still due to the significantly lower tensile strength of ice. Rock fracture experiments and observations have documented the effects of tensile stress concentration under compressive macroscopic stress [Bessinger et al., 1997]. Under conditions of micro-compressive damage, the resultant bending of the bonds (Figure 4.2a), creates gaps that will not easily re-sinter. These findings can help inform fiber-bundle models, in which re-sintering plays an important role [Reiweger, 2009].

The simulations show that damage of several bonds does not immediately result in macroscopic crack formation. The random initiation of micro-cracks prior to peak stress explains both the spatial distribution of cracks [Narita, 1980], as well as observations of acoustic emissions in advance of actual fracture [St. Lawrence

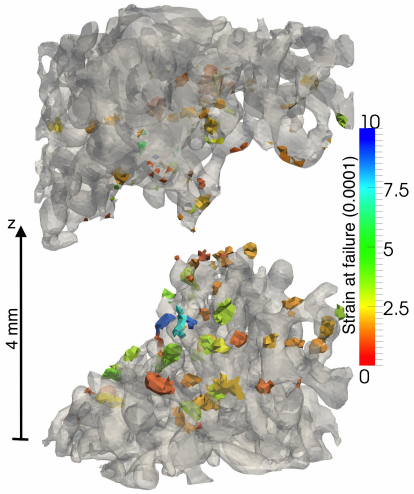

Figure 4.4: Spatial distribution of the damaged bonds. Color indicates the macroscopic strain level where damage occurred. Undamaged ice appears semi-transparent.

et al., 1973]. Random fuse models have helped explain damage percolation and crack nucleation [e.g. Shekhawat et al., 2013]. These models could also apply the parameters reported here for snow.

The simulated failure surface (Figure 4.4) indicates that damage first occurs randomly, at low strains within the sample volume. Upon reaching peak stress, fracture nucleation began in the center of the simulated volume. The artificial boundary created by removing the simulated volume had no effect on crack nucleation.

4.4.2 Macroscopic features

The simulated yield curves of all snow samples exhibited initial elastic deformation and subsequent pseudo-plastic behavior caused by damage (Figures 4.4, 4.6 and 4.7). Manifesting as pseudo-plastic macroscopic strain, this strain makes up to about 10 - 50% of the total strain before the peak stress. The observed behavior also illustrates the difficulty of measuring the elastic modulus of snow, as damage occurred at relatively low strain levels, below even those observed by Narita [1980]. This indicates that constraining elastic properties from macroscopic deformation fields requires relatively high spatial and temporal resolution. These measurement capabilities are not yet possible in field environments [van Herwijnen et al., 2010].

The mean measured tensile strength was 35% smaller than the simulated value. This range in values arises from variation in the mechanical properties of ice. The tensile strength of ice ranges from 2 to 6 MPa [Schulson and Duval, 2009]. Measured tensile strength ranges from 5 to 50 kPa for rounded grains with a density of around 350 kg m^{-3} [Mellor, 1975]. An input tensile strength of 3 MPa for ice would have yielded a mean value equal to the measured value (t-test, p-value =

0.996) in simulations. Failure occurred preferentially at grain junctures, where the stress concentrates. The effective local tensile strength is dictated by the crystal orientation.

The strength between two bonded ice crystals therefore depends on crystal orientation and mean ice strength values may thus overestimate effective tensile strength. This research thus recommends an effective tensile ice strength of 3 MPa as an input to numerical simulations of snow. The low Weibull-modulus causes a high degree of variation among samples [Kirchner et al., 2004], obscuring relationships among different samples. Our results also affirm findings by Kirchner that sample size and strength of snow do not covary [Kirchner et al., 2004].

4.5 Conclusion

The tensile strength of snow can be simulated with a precision comparable to direct empirical observation. Three-dimensional numerical models that assume mechanical properties for ice can simulate microstructural damage and its evolution in snow. The constitutive elastic-brittle model described here offers a simple approach requiring only inputs of known elastic and brittle properties. The method demonstrates new techniques for observing damage initiation and crack nucleation in snow. Numerical simulations and experiments using acoustic emissions on other snow types, especially those having different densities, could provide further specific constraints on snow failure. These methods can determine the 3-D structure of snow more easily than direct mechanical experiments. If applied to weak layers for example, the method can help further elucidate avalanche formation and other fracture phenomena in snow and firn.

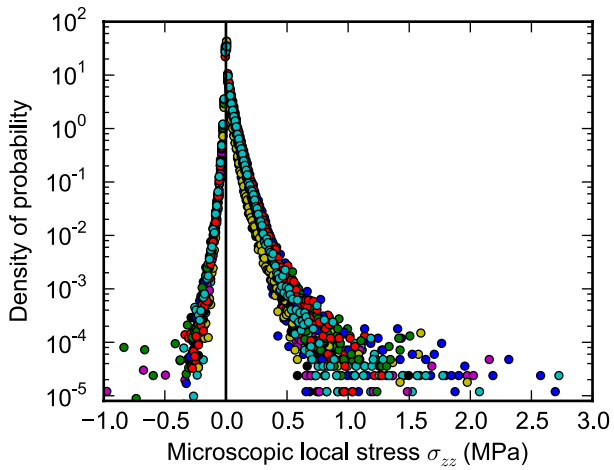

Figure 4.5: Histogram of the stress distribution σ_{zz} for all samples. Each color corresponds to one sample. The density of probability is computed on the percentage of the snow volume that is subjected to a given range of stress. All samples were undamaged and subjected to the same imposed macroscopic strain (2×10^{-5}).

4.A Appendix

In chapter 4, the numerical simulation of microstructural damage and tensile strength of snow is illustrated for one particular sample. However, comparable results were obtained for the entire set of samples. This appendix contains the stress distributions (Figure 4.5), the stress-strain curves (Figure 4.6) and the strain-damage curves (Figure 4.7) for all tested samples. The characteristics of all samples and the simulation results are listed in Table 4.1. This appendix also includes a study of the representative volume for tensile strength and Young's modulus (Figure 4.8), showing that the size of the snow volume on which the mechanical simulation was performed is expected to be representative for the entire sample. Last, a QuickTime movie, available at `https://www.researchgate.net/publication/259935664_movie_of_snow_fracture`, shows the evolution of the stress distribution in the 3D microstructure of snow and the progressive damage of the structure.

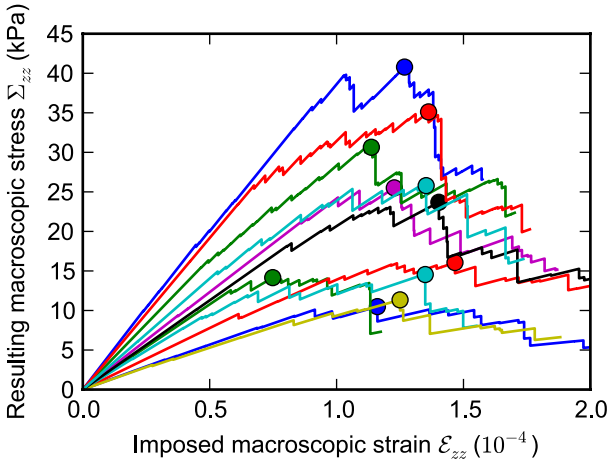

Figure 4.6: Macroscopic stress strain curves for all samples. A round point indicates the maximum macroscopic stress supported by the microstructure. Each color corresponds to one sample. The stress strain curves were computed until the damage reaches 70%.

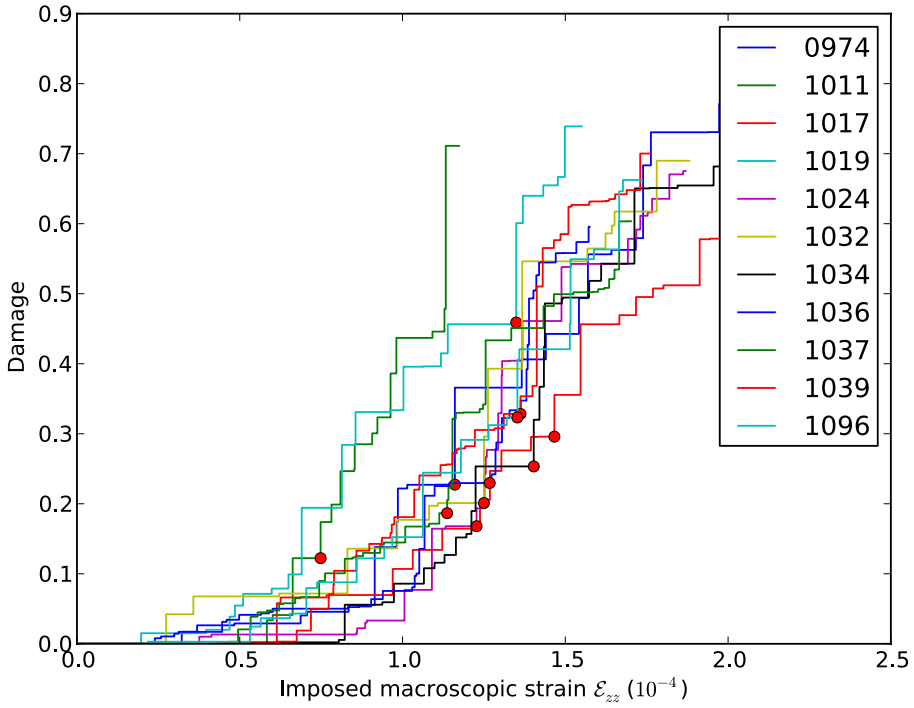

Figure 4.7: Macroscopic strain-damage curves for all samples. A round point indicates the maximum macroscopic stress supported by the microstructure. Each color corresponds to one sample.

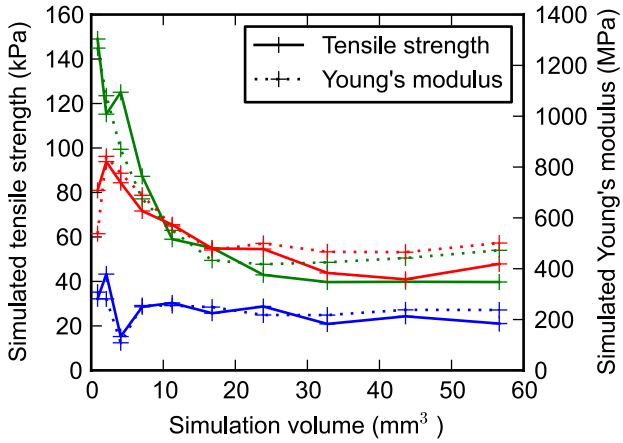

Figure 4.8: Simulated tensile strength and Young's modulus as functions of the size of the simulation volume. The simulation volumes are cubic and concentric. Three different samples (samples 1017, 1024 and 1039) were tested. The figure shows that the volume of 64 mm^3 used to simulated the tensile strength is representative of the whole sample.

Sample name	Density (kg m^{-3})	Specific surface area (m^2 kg^{-1})	Notch cross section (mm^2)	Measured maximum force (N)	Measured tensile strength (kPa)	Simulated tensile strength (kPa)	Simulated Young's modulus (MPa)
974	335.8	13.0	85	1.1	12.9	10.5	116
1011	350.1	12.6	58	0.5	8.6	14.2	215
1017	341.7	12.5	43	1.2	27.9	16.1	155
1019	344.7	12.2	51	0.9	17.6	14.5	199
1024	358.8	12.7	39	1.2	30.8	25.5	249
1032	330.4	12.6	43	0.3	7.0	11.3	113
1034	345.1	12.4	59	0.5	7.6	23.7	226
1036	377.5	12.8	79	1.9	24.1	40.8	417
1037	371.3	12.7	55	1.2	21.8	30.6	331
1039	378.4	12.8	50	0.5	9.0	35.1	383
1096	367.1	12.0	35	0.7	20.0	25.8	281

Table 4.1: Summary of the characteristics and simulation results of all samples. Sample 1034 is the one represented in Figures 4.2, 4.3 and 4.4 in chapter 4. The sample shown in Figure 4.5 and in the movie is a volume of size $120 \times 120 \times 120$ voxels (i.e. 3.84^3 mm^3) extracted from sample 1024.

Chapter 5

Snow as a granular material: assessment of a new grain segmentation algorithm

Abstract Rapid deformations in snow are mainly controlled by particle rearrangements and contact interactions. To study this deformation regime, the description of the snow microstructure in terms of grains, which could eventually be handled by discrete element models, is relevant. In practice, microtomography has become a standard method to image the three-dimensional distribution of ice and pores, as a set of binary voxels. Here, we propose a new method to directly identify individual snow grains defined as zones separated by regions of potential mechanical weakness, in the microtomographic images. In general, these grains are not well separated but rather sintered together. Our new method, based on local geometrical criteria, is shown to detect contacts directly inferred from an explicit numerical mechanical experiment. The developed algorithm is tested on snow but is generic and applicable to various geomaterials with a granular-like microstructure.

Contents

5.1 Introduction

Dry snow is made of air and sintered ice crystals. The three-dimensional (3D) arrangement of ice and pores, i.e. the microstructure of snow, determines crucial mechanical properties such as failure strength [Borstad, 2011] or friction coefficients [Casassa et al., 1989]. Precise knowledge of these properties is critical for diverse applications like avalanche hazard forecasting [Schweizer et al., 2003] or the design of tire patterns for snowy roads [Seta et al., 2003].

Snow exists on the ground at homologous temperatures above 0.9, i.e. its temperature is generally higher than 90% of its melting point using the Kelvin scale [Mellor, 1975, Schneebeli, 2002]. Its density ranges roughly between 20 kg m^{-3} (newly fallen snow) and 500 kg m^{-3} (settled old snow) [Fassnacht, 2011]. The high homologous temperature and the low density of snow promote intense water vapor exchanges between ice zones, which modify the shape and the bonding of the ice matrix [Blackford, 2007, Colbeck, 2001, Flin et al., 2003, Legagneux and Domine, 2005, Schneebeli, 2002, Vetter et al., 2010]. This process, called metamorphism, combines sublimation, vapor transport and deposition. It is very dependent on the environmental conditions and leads to a large variety of microstructure patterns classified in snow types [Fierz et al., 2009], and thus to a large variability in the mechanical properties [Mellor, 1975]. The mechanical characterization of this wide variety of microstructure patterns cannot be simplified only with bulk scalar variables such as density [Shapiro et al., 1997]. For instance, Keeler and Weeks [1968] exhibited samples with the same density but strength differing by as much as a factor of four. Therefore, as pointed out by Shapiro et al. [1997], it is necessary to better characterize the microstructure and to derive relevant indicators of the mechanical properties of snow.

Thanks to imaging facilities such as X-ray computed microtomography (μCT), the snow 3D microstructure can nowadays be captured at micrometer resolution [Coléou et al., 2001]. Using these 3D images as geometric input of numerical simulations enables to investigate the link between microstructure and the physical [Calonne et al., 2011, 2012, Kaempfer et al., 2005, Löwe et al., 2013] or mechanical [Hagenmuller et al., 2014c, Schneebeli, 2004, Srivastava et al., 2010, Theile et al., 2011] properties of snow. However, 3D imaging produces a large amount of information that direct mechanical simulations cannot always handle efficiently. On the one hand, the size of the scanned volume must be large enough to be representative, but on the other hand, the image resolution must be small enough to correctly include crucial structural details such as the ice matrix connectivity. For mechanical applications, especially for the computationally-expensive modelling of large deformations involving structural re-arrangements by bond breaking and sintering, this wealth of data needs to be simplified, keeping only the essential microstructural ingredients.

Under rapid deformation, the ice matrix in snow presents very localized deformation zones, as revealed by acoustic emissions [St. Lawrence, 1980] or by finite-element (FEM) simulations of the microstructure in elastic and brittle regimes

[Hagenmuller et al., 2014c, Schneebeli, 2004]. In these regimes, the 3D representation of the microstructure with voxels of a uniform size can thus be simplified. An appealing approach is to describe snow as a granular material i.e., as a set of rigid elements interacting by means of localized contacts. This assumption significantly reduces the complexity of the microstructure and allows to compute snow deformations using the discrete element method (DEM) [Cundall and Strack, 1979, Johnson and Hopkins, 2005, Radjai and Dubois, 2011]. The purpose of our study is to develop a procedure to translate the structural complexity of snow, as captured by μCT, into a simplified structural grain model which could be eventually handled by DEM simulations. Practically, our goal is to assign a grain label to each ice voxel of a μCT image. This procedure is called grain segmentation. One grain will be defined as the set of voxels with the same assigned grain label.

In the case of highly sintered materials as snow, the identification of individual particles is not straightforward because grains are not clearly demarcated [Colbeck, 1997]. Different definitions of a snow grain coexist in the snow literature: a grain can be either considered as a single snowflake [Kubo et al., 2009], a crystallographic single crystal [Riche et al., 2013] or a particle that can be easily detached from the snowpack [Fierz et al., 2009]. In some cases, these definitions coincide [Arnaud et al., 1998] but, in general, they correspond to different entities. Additionally, the term “optical grain size", i.e. the radius of a collection of disconnected ice spheres with the same infrared albedo as that of the snow microstructure, is often found in the literature [Warren, 1982] but is not linked explicitly to any grain segmentation. In this article, we consider grains as the elementary particles relevant to describe and model the mechanical behavior of snow.

For snow, three main approaches of grain segmentation are reported in the literature: distance-based watershed algorithms [Soille, 2003], skeleton-based algorithms [Liang et al., 2000] and curvature-based algorithms [Theile and Schneebeli, 2011, Wang et al., 2012]. When applied to snow types such as Rounded Grains (RG) or Melt Forms (MF), the segmentations obtained by curvature-based algorithms were reported to be in good agreement with crystal boundaries determined by serial sectioning [Theile and Schneebeli, 2011] or diffraction contrast tomography [Wang et al., 2012]. This agreement is explained by the fact that the mis-orientation at crystalline grain boundaries often yields a groove region on the ice surface [Colbeck, 1997], which is detectable by curvature-based algorithms. However, these algorithms might miss smooth narrow constrictions, which can significantly weaken the snow microstructure. Hence, additional geometrical constraints need to be introduced to improve the mechanical relevance of the segmentation.

In this article, we introduce a new approach to detect potential zones of mechanical weakness within a snow sample, with a local geometrical criterion combining curvature and constriction aspects. The objective of the developed method is to segment the microstructure of snow obtained by μCT into individual particles that are relevant to model the mechanical behavior of the material. To check the assumption that the chosen geometrical criteria are able to detect bonds characterized by high stress concentrations, we performed a FEM elastic simulation on the same mi-

crostructure. The obtained stress distribution was then used to evaluate the stress on the bonds detected by the geometrical segmentation.

5.2 Materials and methods

5.2.1 Dataset

The geometrical segmentation and the mechanical analysis have been applied on four snow images spanning different snow types (Rounded Grains RG, Faceted Crystals FC, Decomposing and Fragmented snow DF, and Melt Forms MF, [Fierz et al., 2009]). The characteristics of these samples are summarized in Table 1. The segmentation and the mechanical assessment will be introduced and discussed in detail on the example of the RG sample. This sample presents a density $\rho = 250$ kg m^{-3} and was obtained after three months of isothermal metamorphism in a cold room at -2°C. It has been scanned with μCT at a resolution of 4.91 μm. Details of the preparation, sampling and imaging procedures can be found in Flin et al. [Flin et al., 2004]. The grayscale image was binary segmented with the technique described by Hagenmuller et al. [Hagenmuller et al., 2013b] with an effective resolution of $r = 2$ voxels so that small structural details induced by noise artefacts are smoothed out. Eventually, the resolution was reduced to 9.82 μm and a sub-image of size 400^3 voxels ($\sim 4^3$ mm^3) was extracted from the entire image to allow reasonable processing times.

5.2.2 Geometrical segmentation algorithm

The objective of the grain segmentation algorithm is to identify grains by detecting preferential zones of mechanical weakness. The input of the algorithm is a 3D binary image which describes geometrically the snow microstructure. To interpret this microstructure in terms of mechanically relevant entities, we assume that rupture preferentially occurs in zones of stress concentration explained by two geometrical criteria: concavities with a significant curvature and constrictions. We developed a new segmentation algorithm which consists of the following steps:

1. *Local computation of the principal minimal curvature κ_{min} in the entire volume of ice* (Figure 1a). The curvature κ_{min} is estimated using a voxel-based approach similar to the one proposed by Ogawa et al. [Ogawa et al., 2006] and Brzoska et al. [Brzoska et al., 2007]. First, the Euclidean distance map ϕ is computed with Maurer's algorithm [Maurer Jr. et al., 2003]. The inside of the ice matrix is considered as having negative distances. The normal $\mathbf{n}$ of the isosurfaces of ϕ can thus be defined as $\vec{\nabla}\phi/\|\vec{\nabla}\phi\|$, where first derivatives are computed on the image via convolutions with first order gaussian kernels of standard deviation equal to 1.5 voxel [Van den Boomgaard and Van der Weij, 2001]. For each voxel of the image, let $\mathbf{e}$ be the Cartesian direction ($\mathbf{x}$, $\mathbf{y}$ or $\mathbf{z}$) so that $\max(|n_x|, |n_y|, |n_z|) = |n_e|$. We define the local base ($\mathbf{n}$,$\mathbf{p}$,$\mathbf{q}$) with $\mathbf{p} = \mathbf{n} \wedge \mathbf{e}/\|\mathbf{n} \wedge \mathbf{e}\|$ and $\mathbf{q} = \mathbf{n} \wedge \mathbf{p}/\|\mathbf{n} \wedge \mathbf{p}\|$. Finally, the principal minimal

Sample	RG	DF	FC	MF
Snow type	Rounded Grains	Decomposed Fragmented snow	Faceted Crystals	Melt Forms
Voxel size (μm)	9.82	8.59	8.37	37.84
Sample size (mm^3)	3.93^3	3.43^3	4.00^3	9.47^3
Density (kg m^{-3})	249	158	287	473
Equivalent spherical radius r_{eq} (voxel)	19.5	15.1	18.9	23.0
Number of geometrical grains	857	763	1542	378
Number of mechanical grains	395	353	492	208
% of mechanical bonds within a distance of 0.05 mm from the closest geometrical bond	72	72	57	25

Table 5.1: Characteristics of the snow images used in this study. The geometrical grains were obtained with the segmentation parameters $\kappa_t = 1/r_{eq}$ and $c_t = 0.25$ (see Section 2.2). The mechanical grains were obtained with the method described in Section 2.3.

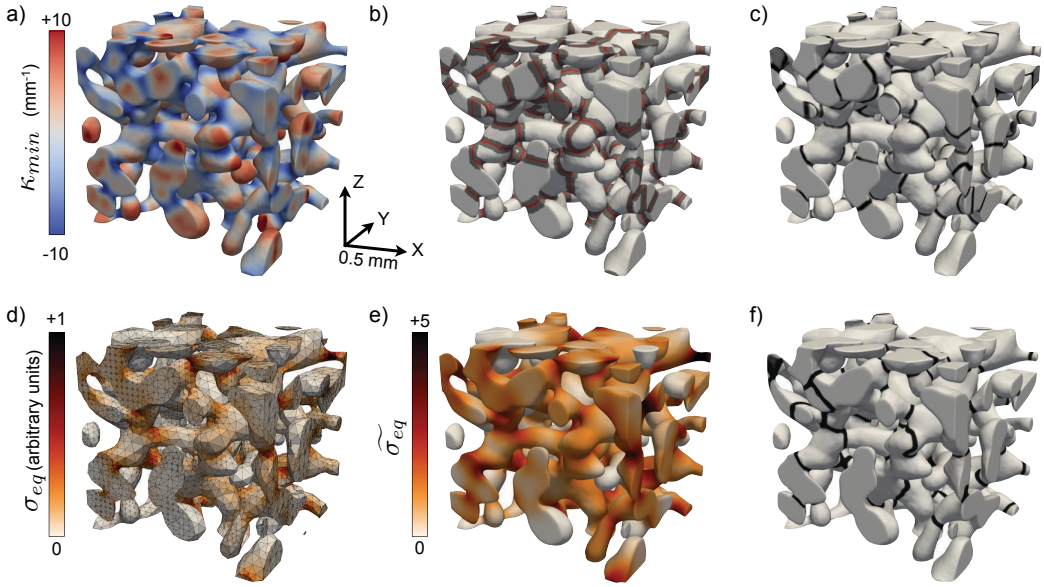

Figure 5.1: Description of the geometrical segmentation (a, b, c) and the mechanical evaluation (d, e, f). Illustrations correspond to a sub volume of size 2^3 mm^3 of the RG sample (full volume is 4^3 mm^3). a) Minimal principal curvature κ_{min}. b) Potential bond zones (gray) obtained through a watershed segmentation (red) on κ_{min} with $\kappa_t = 1/r_{eq}$. c) Final bonds (black) obtained after the refinement step with $c_t = 0.25$. d) Von Mises equivalent stress σ_{eq} on the finite element mesh. e) Normalized stress map $\widetilde{\sigma_{eq}}$. f) Final bonds (black) obtained via a watershed segmentation on $\widetilde{\sigma_{eq}}$.

curvature κ_{min} is the smallest eigenvalue of the Weingarten matrix H [Prinet et al., 1996] defined by:

$$H = \begin{pmatrix} \vec{n}.\left((\vec{p}.\vec{\nabla})\vec{p}\right) & \vec{n}.\left((\vec{p}.\vec{\nabla})\vec{q}\right) \\ \vec{n}.\left((\vec{q}.\vec{\nabla})\vec{p}\right) & \vec{n}.\left((\vec{q}.\vec{\nabla})\vec{q}\right) \end{pmatrix}.$$

The sign of κ_{min} distinguishes groove, neck and crater regions ($\kappa_{min} < 0$) from convex regions ($\kappa_{min} > 0$). Unlike the Gaussian curvature, κ_{min} properly detects triple junctions [Wang et al., 2012].

2. *Detection of bond candidates with a watershed algorithm on* κ_{min} (Figure 1b). The watershed algorithm [Soille, 2003] is applied on $-\kappa_{min}$, so that the grain centers are the seeds of the algorithm and the necks are the watershed edges. To avoid artificial over-segmentation, local minima of $-\kappa_{min}$ whose depth is lower than a certain threshold level κ_t are deleted (H-minima transform). This threshold is generally chosen to be on the order of $1/r_{eq} = S/(3V)$, where r_{eq} is the equivalent spherical radius, S is the ice-air interface area and V is the ice volume. We define $\kappa_t = \widetilde{\kappa}_t/r_{eq}$ with $\widetilde{\kappa}_t \in [0.7, 1.3]$. The sensitivity of the segmentation to the values of κ_t is evaluated in section 3.1.

3. *Refinement of bond candidates* (Figure 1c). Once detected by the watershed algorithm, the bond candidates are enlarged to a width of about 9 voxels by applying iteratively 4 binary dilations with a $3 \times 3 \times 3$ structuring element. Then the bonds of minimal area and lying within the dilated bond candidates, are computed via a graph cut approach with the GCoptimization C++ library [Boykov and Kolmogorov, 2004, Boykov et al., 2001, Kolmogorov and Zabih, 2004]. Details of the multi-label optimization via graph-cut can be found in Boykov et al. [Boykov et al., 2001]. Simultaneously to the bond area minimization, a merging criterion between grains is applied. One grain is merged to its neighbor if $S_{int} < c_t \times S_{tot}$, where S_{int} is the contact area between both grains, S_{tot} is the total grain surface area and $c_t \in [0, 1]$ is a local contiguity parameter. A value of c_t close to 1 will separate grains that share a large portion of their total surface, whereas a value of c_t close to 0 will only split well-separated grain clusters. Note that the width of the dilated bond candidates (9 voxels) has been chosen large enough to be able to find the bond of minimal area (see Figures 1b and 1c) and thin enough to allow reasonable computation time. The results of this segmentation procedure are called hereafter *geometrical grains*.

The described algorithm has been developed using external C++ and Python libraries. It was not optimized since it already runs in reasonable times on a standard personal computer. For instance, the processing time of the geometrical segmentation for the RG sample (400^3 voxels) is about 30 minutes on a PC with four CPU at 2.67 GHz and 6 Gb RAM. The main limitation of the algorithm is memory usage during the refinement of bond candidates: the graph corresponding to the voxels in

the largest bond candidate has to fit completely in the RAM memory. Thus, the memory usage does not only depend on the overall size of the image but also on the size of potential bond candidates, which is controlled by the snow microstructure and the segmentation parameters.

5.2.3 Mechanical model

In order to evaluate the relevance of the geometrical grain segmentation, we performed a numerical mechanical modelling on the same microstructure. The objective is to check if the detected bonds effectively agree with the zones of potential failure.

The ice matrix was meshed into quadratic tetrahedral finite elements using ANSYS ICEM mesh generation software (www.ansys.com) (Figure 1d). A homogeneous linear elastic material with a Young's modulus of 9.5 GPa and Poisson's ratio of 0.3 was used to model the mechanical behavior of ice [Schulson and Duval, 2009]. The meshed microstructure was numerically subjected to an isotropic tensile deformation using ANSYS finite-element software. This particular loading was chosen since it appeared as the best candidate to activate all potential force chains and to distribute the load in most of the microstructure (see also Section 4.2). As shown in Figure 1d, the resulting von Mises equivalent stress σ_{eq} is strongly heterogeneous in the ice matrix. High stresses are located at the narrow constrictions between grains (microscopic concentrations) and along force chains that transmit the load through the sample (mesoscopic concentrations). In order to better isolate microscopic stress concentration zones, which shall correspond to grain bonds, we compute the normalized stress $\widetilde{\sigma_{eq}} = \sigma_{eq}/\overline{\sigma_{eq}}$, where $\overline{\sigma_{eq}}$ is the mean value of σ_{eq} on a grain-scale neighborhood ($\overline{\sigma_{eq}}$ is obtained via a Gaussian filter with a standard deviation $d = \widetilde{d} \cdot r_{eq}$). We chose $\widetilde{d} = 1$ so that the averaging is performed on a neighborhood of the order of the structure size. Lastly, a watershed segmentation is used on the stress map $\widetilde{\sigma_{eq}}$ to identify grains called hereafter *mechanical grains* (Figure 1f). To avoid over-segmentation due to non-prominent local minima of $\widetilde{\sigma_{eq}}$, the H-minima transform was applied to $\widetilde{\sigma_{eq}}$ with a level $\widetilde{\sigma}_t = 0.5$, before applying the watershed segmentation.

The processing time of the mechanical segmentation for the RG sample (400^3 voxels) is about 10 hours on a PC with four CPU at 2.67 GHz and 6 Gb RAM. The mesh generation and FEM simulation are the most time consuming steps.

5.3 Results

5.3.1 Sensitivity of the geometrical grain segmentation to its parameters

The results of the geometrical segmentation depend significantly on the two algorithm parameters κ_t and c_t operating on curvature and contiguity aspects, as shown in Figure 2. For the same input image, the number of obtained grains ranges from 600 to 1200 depending on the chosen parameter values. Segmentations yielding a

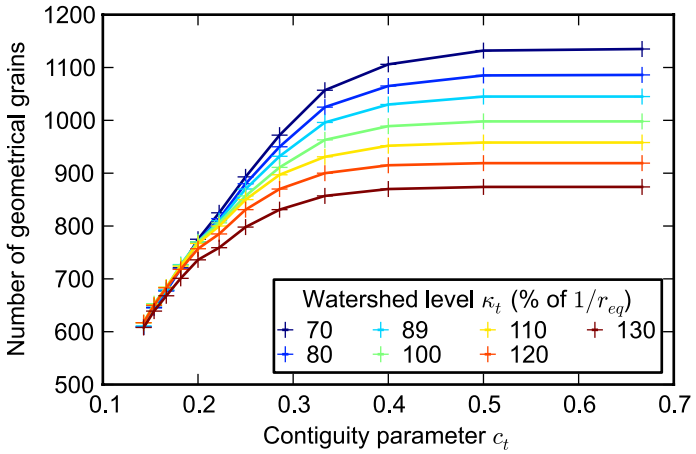

Figure 5.2: Number of geometrical grains as a function of c_t for different values of κ_t. Computations were performed on sample RG illustrated in Figure 1.

large number of grains are mainly controlled by the watershed pre-segmentation and thus by the parameter κ_t. For $c_t > 0.4$ typically, the bond candidates are not affected by the merging process since their local contiguity is always smaller than c_t. In contrast, segmentations with fewer grains depend mostly on the merging process, and thus on the parameter c_t. For $c_t < 0.2$ typically, the bond candidates that are preserved by the merging process were all present in the watershed pre-segmentation, regardless of the value of κ_t. For $0.2 < c_t < 0.4$ both criteria on curvature and constriction control the segmentation results.

5.3.2 Mechanical evaluation

5.3.2.1 Relevance of the curvature and contiguity criteria

In this section, we assess the assumption that microscopic stress concentrations are explained by the two retained geometrical criteria.

First, as can be seen in Figures 1a and 1e, the quantities κ_{min} and $\widetilde{\sigma_{eq}}$ are clearly spatially correlated. As shown in Figure 3a, high values of $\widetilde{\sigma_{eq}}$, i.e. local stress maxima, are located on concavities ($\kappa_{min} < 0$). Quantitatively, 91% of the values $\widetilde{\sigma_{eq}} > 2$ are located on concavities. Low stresses ($\widetilde{\sigma_{eq}} < 0.5$) are mainly located on convexities (78%) but can also appear on concavities (22%). Therefore, the negativity of κ_{min} appears as a relevant necessary condition for stress concentration, but is not a sufficient condition.

Second, we show that the minimality of the contact area and the contiguity criterion effectively refine the detection of stress concentration zones. To evaluate the stress distribution on the bonds, we define bond neighborhood zones as the sets of voxels in contact with two different grains and enlarged by 5 successive binary dilations with a $3 \times 3 \times 3$ structuring element. Then, we estimate the stress

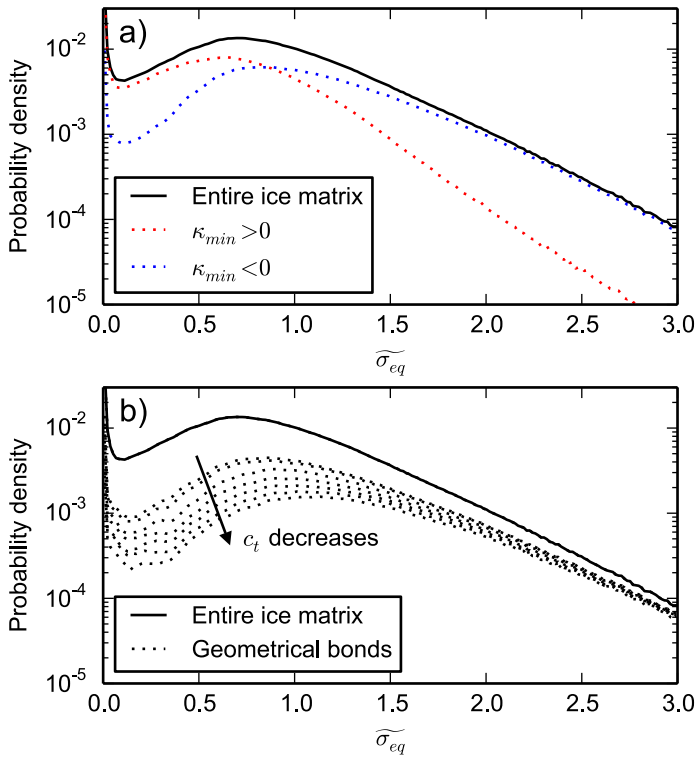

Figure 5.3: Mechanical evaluation of the geometrical segmentation criteria with the computed stress distribution. a) Distribution of $\widetilde{\sigma_{eq}}$ on concavities ($\kappa_{min} < 0$), convexities ($\kappa_{min} > 0$) and in the entire ice matrix. b) Distribution of $\widetilde{\sigma_{eq}}$ on the geometrical bonds obtained for different values of c_t in [0.125, 0.5] and $\kappa_t = 0.7/r_{eq}$. These distributions are expressed in number of voxels per total number of ice voxels and are computed on bins of homogeneous size equal to 0.015.

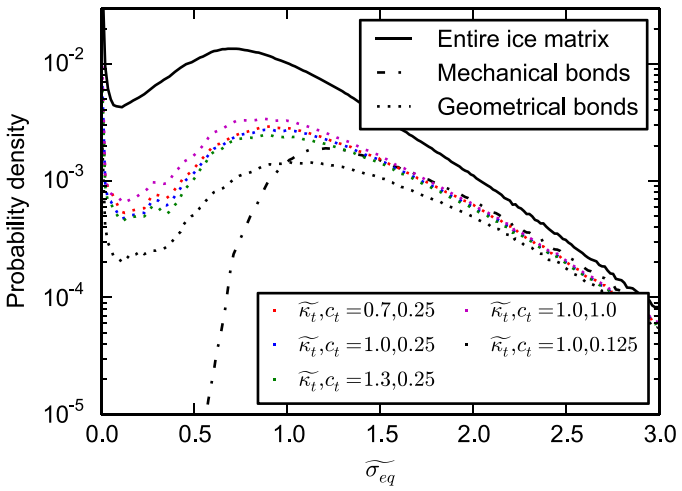

Figure 5.4: Distribution of the stress $\widetilde{\sigma_{eq}}$ in the entire ice matrix, on the mechanical bonds and the geometrical bonds obtained for different values of κ_t and c_t. These distributions are expressed in number of voxels per total number of ice voxels and are computed on bins of homogeneous size equal to 0.015.

distribution on these bond neighborhood zones. As shown in Figure 3b, the mean stress $\widetilde{\sigma_{eq}}$ on these zones globally increases when c_t decreases. More precisely, when c_t decreases, the bonds with the highest stresses are almost not modified while the bonds presenting the lowest stresses are no longer detected by the algorithm. This indicates that the merging criterion on local contiguity is able to select the bonds with the highest stress concentration among those detected by the segmentation on curvature. Note that the watershed segmentation on κ_{min} distinguishes grains separated by a concave zone. Therefore, asymmetrical bonds with a concave side and an opposite convex side are not identified by our algorithm, even if these bonds might concentrate the stress on their concave side. This explains why few voxels with high stresses are not located on any detected geometrical bonds (Figure 3b).

5.3.2.2 Mechanical evaluation of the geometrical segmentation

We recall that the quality of the grain segmentation is defined here as its capability to detect zones of high local stresses. According to this criterion, the mechanical bonds directly obtained by the watershed segmentation on $\widetilde{\sigma_{eq}}$ can be considered as a reference against which the geometrical segmentation has to be evaluated. Visual inspection of Figures 1c and 1f shows a good qualitative agreement between the geometrical grains and those detected from the stress distribution. In detail, however, a few bonds appear only in one of the two segmentations, and the exact location of bonds sometimes slightly differs. To evaluate more quantitatively the

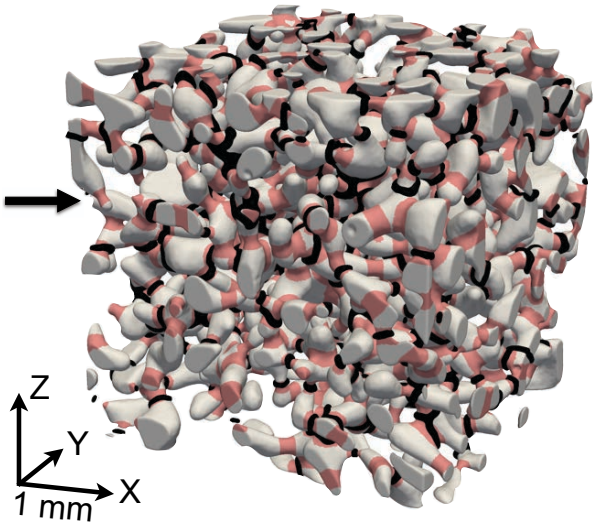

Figure 5.5: Inclusion of the mechanical bonds (black) in the geometrical bonds (red). The geometrical bonds were enlarged by 5 successive binary dilations with a $3 \times 3 \times 3$ structuring element. The black arrow highlights a geometrical bond that does not intersect any mechanical bond because the surrounding grains cannot transmit any force due to a microstructural dead-end. The geometrical segmentation was performed with $(\widetilde{\kappa_t}, c_t) = (1.0, 0.25)$.

mechanical relevance of the geometrical grain segmentation, we compared the stress distribution on both types of bonds (Figure 5.4) and computed the distances between each mechanical bond and the closest geometrical bond.

Figure 5.4 shows the stress distribution in the entire ice matrix, on the mechanical bonds and on the geometrical bonds obtained for different sets of segmentation parameters. It is observed that the stress distributions on the entire ice matrix and on the geometrical bonds are very close for high values of $\widetilde{\sigma_{eq}}$. This observation shows that high stresses are mainly located on the geometrical bonds. The stress distributions on mechanical and geometrical bonds are also almost identical for $\widetilde{\sigma_{eq}} > 1.5$. This indicates that, according to the evaluation of the capability of detecting high local stresses, the geometrical segmentation performs as well as the mechanical segmentation. The main difference between the mechanical and geometrical segmentations is observed on low stress zones. The stress $\widetilde{\sigma_{eq}}$ on the mechanical bonds is never lower than $\widetilde{\sigma_t} = 0.5$, which was the level imposed by the H-minima transform for the watershed segmentation, whereas numerous geometrical bonds appear to support no significant load. This leads to a significantly larger number of geometrical bonds than mechanical bonds. For instance, the geometrical segmentation with $(\widetilde{\kappa_t}, c_t) = (1.0, 0.25)$ is composed of 1072 bonds (857 grains) while the mechanical segmentation is composed of 578 bonds (395 grains) (Table 1). In

other words, a large part of the contacts detected by the geometrical criteria are not mechanically active, at least under the considered deformation regime (elastic).

Moreover, Figure 5.4 shows that the geometrical segmentation is able to identify zones of stress concentrations regardless of the values of the parameters κ_t and c_t in the ranges $[0.7, 1.3]$ and $[0.125, 1.0]$. As explained previously, the choice of c_t only affects bonds characterized by a low value of $\widetilde{\sigma_{eq}}$ (Figure 5.4). The choice of κ_t slightly affects bonds characterized by a low value of $\widetilde{\sigma_{eq}}$ but does not appear to be determinant for $c_t = 0.25$ (Figure 5.4). Hence, differences of segmentation results associated to the choice of segmentation parameters are mostly observed in zones of low $\widetilde{\sigma_{eq}}$ values.

Lastly, for $(\widetilde{\kappa_t}, c_t) = (1.0, 0.25)$, 72% of the mechanical bonds are located within a distance of $l = 0.05$ mm to the nearest geometrical bond (Figure 5.5, Table 1). As a comparison, the typical size of the microstructure measured by r_{eq} is 0.19 mm, and half of all ice voxels are at a distance larger than $l_{ref} = 0.11$ mm from the geometrical bonds. Hence, we found that $l = 25\% r_{eq}$, which is quite small compared to the typical grain size (see also Figure 5.5). Moreover, the fact that $l = 45\% l_{ref}$ indicates a clear correlation between the geometrical and the mechanical bonds. We can thus conclude that a large majority of the mechanical bonds is correctly detected by the geometrical segmentation. However, as already mentioned before, we observe again that a part of the geometrical bonds does not intersect any mechanical bonds (Figure 5.5).

5.4 Discussion and application to various snow types

5.4.1 Non-uniqueness of the segmentation

The results of the geometrical grain segmentation algorithm are very sensitive to the values of the parameters κ_t and c_t (Figure 2). However, this sensitivity and the numerous possible segmentation results are not specific to our algorithm, and similar observations can be found in the literature for other algorithms. For instance, Kry conducted the first identification of bonds on 2D slices of snow by assuming that a bond exists if its constriction is at least of 30% [Kry, 1975b]. Kry already noted that the value of 30% is partly subjective but did not conduct any sensitivity test to this value which can significantly affect the grain segmentation. More recently, the algorithms operating on 3D images proposed by Theile and Schneebeli [Theile and Schneebeli, 2011] or Wang et al. [Wang et al., 2014, 2012] also incorporate some threshold values that control the final number of grains. In fact, the definition of geometrical grains is always relative to a certain threshold. More generally, the definition of mechanically relevant grains can be seen as relative to the force applied to separate the grains from each other. In contrast to sand, for instance, snow is not characterized by a clear difference between inter and intra-granular strength. Defining a bond by its resistance force thus involves some arbitrariness since there is a continuum of cohesion force values. As a consequence, no absolute choice for κ_t and c_t can be proposed, not because our algorithm is wrongly designed, but because the

definition of mechanical grains is inherently scale dependent. For instance, during a compression test of snow, very fragile bonds between large grain clusters are first activated, then, after densification, the clusters themselves are broken into individual grains which might also break into sub parts and so on [Johnson, 2011]. The choice of κ_t and c_t thus depends on the subsequent use of the grain representation of the snow microstructure, especially on the degree of refinement needed. In the case of DEM modelling, for instance, the precise choice of the segmentation parameters results from a compromise between the accuracy of the model and the computing cost that can be afforded.

On the basis of the results shown above, reasonable choices for the segmentation parameters κ_t and c_t can nevertheless be proposed. Clearly, values leading to as many grains as voxels do not match our first objective of reducing the complexity of the snow microstructure. On the other extreme, parameters yielding only one grain for the entire sample are also not satisfactory. Between these two extreme segmentations, we suggest values for κ_t and c_t leading on average to grains of the same size as those identified visually in the snowpack [Fierz et al., 2009]: $\kappa_t \sim 1/r_{eq}$ and $c_t \sim 0.25$. The normalization of κ_t by r_{eq} enables to obtain identical segmentations for homothetic microstructures (same shape but different sizes). The proposed value for c_t implies that grains sharing more 25% of their total surface area are merged. We have shown that using stricter criteria (higher value of κ_t and lower value of c_t) will delete bonds supporting relatively low stresses. These bonds are expected to be not the most determinant to describe the mechanical behavior.

5.4.2 Representativeness of the mechanical evaluation

We evaluated the mechanical relevance of the geometrical grain segmentation using the stress distribution $\widetilde{\sigma_{eq}}$ obtained via a FEM elastic model of isotropic tensile deformation, and normalized on a grain-scale neighborhood. We discuss here the representativeness of these mechanical simulations.

First, the choice of linear elasticity as the constitutive law for ice in the mechanical model is discussed. The granular description of snow is intended, in our case, to be used as a geometrical input for computing fast deformations governed by contact interactions. It is not necessarily appropriate for slow deformations as creep, expected to be more controlled by intra-granular deformation [Theile et al., 2011]. According to this purpose, considering a purely elastic regime in the finite-element model thus seems to be sufficient to identify potential zones of brittle failure. The normalization of the stress distribution enables to reveal relative stress concentrations at the bonds, even on chains of grains that do not transmit much force at the sample scale. Note that although these chains do not transmit much force in the elastic regime, the force paths can evolve during the progressive damaging of the microstructure and might activate them [Hagenmuller et al., 2014c]. In order to have a unique granular description independent of the microstructure damage state, the mechanical evaluation via $\widetilde{\sigma_{eq}}$ thus appears to be relevant.

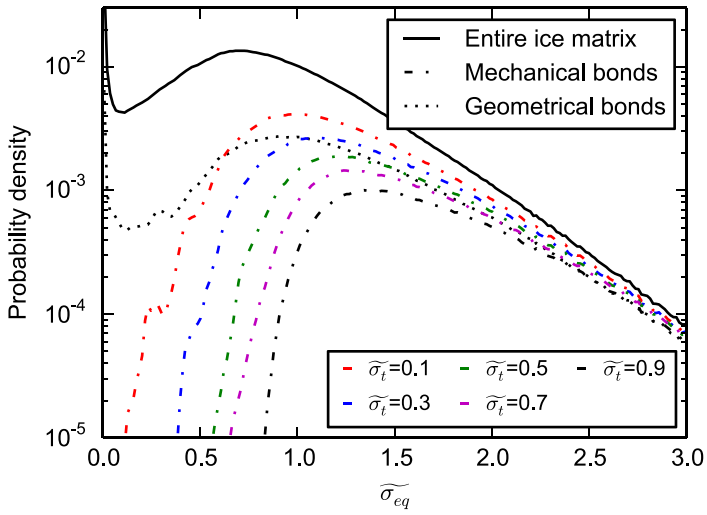

Figure 5.6: Distribution of the stress $\widetilde{\sigma_{eq}}$ in the entire ice matrix, on the geometrical bonds and on the mechanical bonds obtained for different values of $\widetilde{\sigma_t}$. The geometrical bonds were obtained with $(\widetilde{\kappa_t}, c_t) = (1.0, 0.25)$. These distributions are expressed in number of voxels per total number of ice voxels and are computed on bins of homogeneous size equal to 0.015.

Second, the relevance of the choice $\widetilde{\sigma_t} = 0.5$, which controls the watershed segmentation of the stress distribution $\widetilde{\sigma_{eq}}$, is discussed. As shown in Figure 5.6, the value of $\widetilde{\sigma_t}$ mostly affects the bonds characterized by low values of $\widetilde{\sigma_{eq}}$. When $\widetilde{\sigma_t}$ increases, the mechanical bonds undergoing the lowest stresses are not detected anymore. In regard to our main objective, i.e. the evaluation of the capability of the geometrical algorithm to recover bonds with the highest local stresses, the value of $\widetilde{\sigma_t}$ has thus little effect. However, the total number of detected mechanical grains significantly changes with $\widetilde{\sigma_t}$: it ranges between 675 and 197 for $\widetilde{\sigma_t} \in [0.1, 0.9]$. This sensitivity to $\widetilde{\sigma_t}$ is actually parallel to the one shown on the geometrical segmentation parameters (κ_t,c_t) and refers once again to the non-uniqueness of the grain segmentation (Section 4.1). To provide a reference for the evaluation of the geometrical segmentation, we chose to arbitrarily cut off the stress distribution on mechanical bonds by setting $\widetilde{\sigma_t} = 0.5$. This amounts to assuming that low stress concentrations $\widetilde{\sigma_{eq}} \leq 0.5$ can hardly lead to bond failure and should not be regarded as mechanical bonds.

Third, isotropic tensile deformation was chosen as loading condition for the mechanical evaluation. It is important to check that the results do not strongly depend on this choice. Other types of loading conditions (uniaxial tension and pure shear in each cartesian directions) were tested (Figures 6 and 7). Note that compression leads to the same stress distribution $\widetilde{\sigma_{eq}}$ as tension in the same direction, since the chosen constitutive law for ice is linear and the von Mises equivalent stress is an even function. As shown in Figure 7, the spatial distribution of $\widetilde{\sigma_{eq}}$ and the mechanical grains obtained for the different loading conditions show very similar features. In particular, the distribution of $\widetilde{\sigma_{eq}}$ on the entire ice matrix and on the geometrical bonds is identical for the different tested loading conditions (Figure 8). We have shown that 72% of the mechanical bonds obtained with isotropic tensile strain are located within a distance of $l = 0.05$ mm to the geometrical bonds. For the other tested loading conditions, this percentage is of the same order and ranges between 70% and 77%. Therefore, we argue that the geometrical segmentation is actually able to capture the mechanical behavior of snow under various loading conditions.

Lastly, let us comment on the observation that many geometrical bonds are not close to any mechanical bond (Figure 5). We observed that a large majority of the mechanically activated bonds are represented by a geometrical bond. Therefore, one could argue that many geometrical bonds are in excess to model the mechanical behavior of snow. However, the aim of this paper is not to derive geometrical variables describing the contact network but to provide appropriate means to simplify the snow microstructure for future mechanical simulations via DEM. Therefore, the microstructure should rather be over-segmented so that determinant mechanical bonds are well represented, i.e. included in the set of geometrical bonds, even if some considered bonds play only little role in the mechanical behavior. The DEM computations will then automatically reveal the bonds that are mechanically relevant.

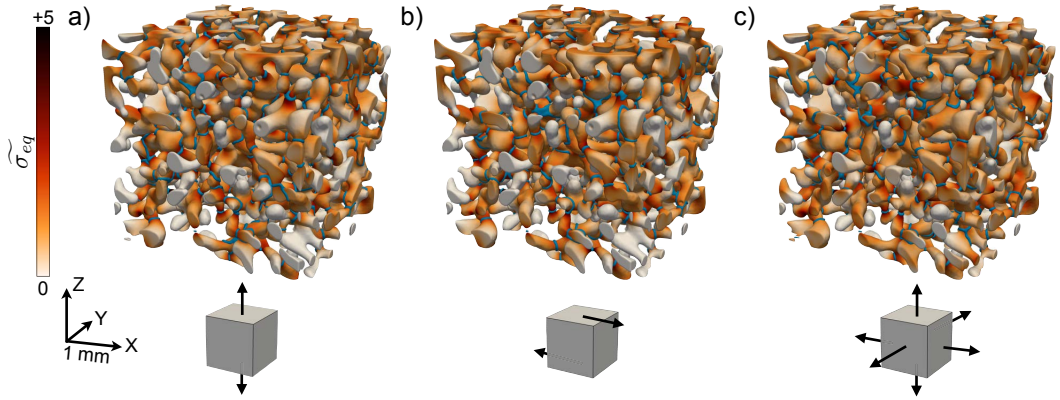

Figure 5.7: Distribution of the stress $\widetilde{\sigma_{eq}}$ and the corresponding mechanical bonds (blue) obtained for different loading conditions: uniaxial tension (a), pure shear (b) and isotropic tensile deformation (c).

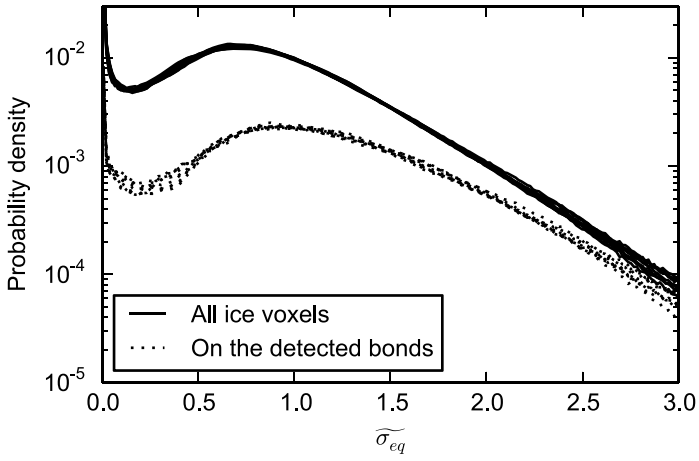

Figure 5.8: Distribution of the stress $\widetilde{\sigma_{eq}}$ in the entire ice matrix and on the geometrical bonds, for 9 different loading conditions. The different loading conditions correspond to imposed displacements along direction X,Y or Z on faces normal to X,Y or Z. The geometrical bonds were obtained with $(\widetilde{\kappa_t}, c_t) = (1.0, 0.25)$. These distributions are expressed in number of voxels per total number of ice voxels and are computed on bins of homogeneous size equal to 0.015.

5.4.3 Application to different types of snow microstructures

In addition to the image of Rounded Grains (RG), the geometrical and mechanical segmentations were applied on three other images representative of various snow types: Faceted Crystals (FC), Decomposing and Fragmented snow (DF) and Melt Forms (MF). The geometrical segmentation was directly applied to these images with parameters values $\kappa_t = 1/r_{eq}$ (r_{eq} depends on the snow sample) and $c_t = 0.25$ (Figure 9). The results of the segmentation are summarized in Table 1.

The DF sample, resulting from the evolution of fresh snow, is characterized by a very low density and connectivity (Figure 9a). Consequently, the stress distribution is very heterogenous. The load is supported by very few chains of grains and the von Mises stress is zero in a large part of the structure (Figure 9d). In this structure, we obtain twice as many geometrical bonds (879) as mechanical ones (440). Nevertheless, a large majority (72%) of the mechanical bonds are still close to the geometrical bonds (distance $l < 0.05$ mm), which validates here also the quality of the geometrical segmentation.

The FC sample, resulting from temperature gradient metamorphism, is characterized by flat ice surfaces (Figure 9b). Small protuberances on flat zones significantly affect the curvature map and segmentations based only on curvature lead, in this case, to some totally irrelevant grains. In this case, the regularization provided by the optimization step is of particular interest to locate bonds on real constrictions and to select mechanically relevant grains. The numerical mechanical model reveal that only few bonds support most of the load as for the sample DF (Figure 9e). Thus, once again, the mechanical bonds cannot directly match the geometrical bonds, but correspond approximately to a subset of the geometrical bonds. In detail, 57% of the mechanical bonds are at a distance smaller than 0.05 mm from the closest geometrical bond. This percentage increases to 70% with a less strict distance of 0.07 mm.

In contrast, on the MF sample, crystalline grains have formed marked concavities on the necks which are directly detected by the segmentation with curvature (Figure 9c). On this sample, crystalline grains are clearly detected by these grooves on the ice surface but they are strongly sintered with very large bonds (compared to the grain surface area) that do not concentrate stresses locally (Figure 9f). This illustrates the difference between crystalline and mechanical grains. The mechanical analysis shows a relatively homogeneous stress distribution. Actually, the bonding between those grains is so strong, that the granular nature of the material is questionable in this case. Consequently, for this type of snow, the geometrical grains are not really mechanically relevant.

5.5 Conclusion

We developed a new algorithm to segment the snow microstructure into grains. The algorithm is based on geometrical criteria that are defined to detect bonds supposed to be mechanically relevant. The originality of this work is to cross-check

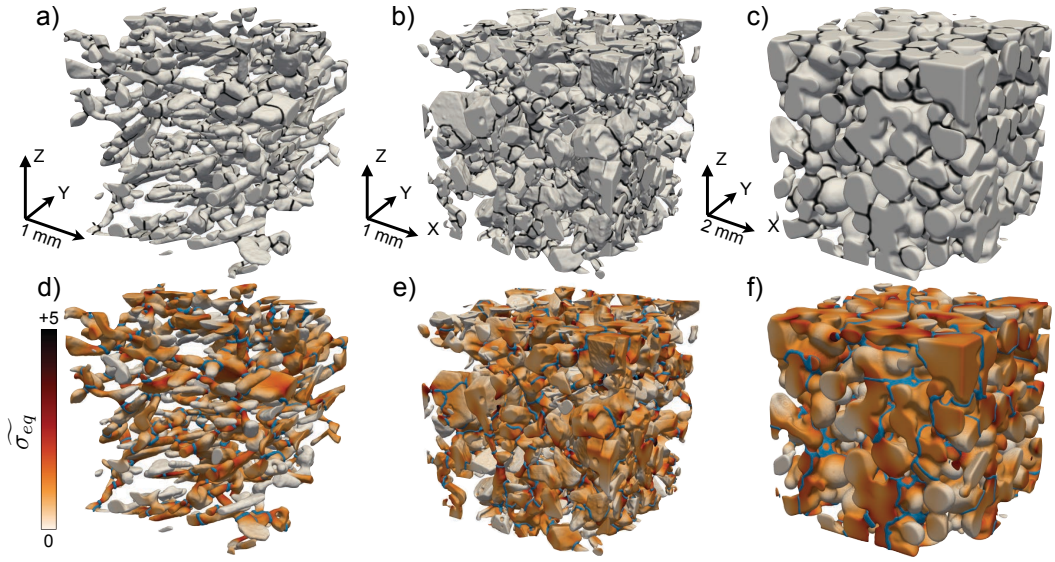

Figure 5.9: Geometrical segmentation (a,b,c) and mechanical evaluation (d,e,f) applied to different snow types: Decomposing and Fragmented snow (a,d), Faceted Crystals (b,e) and Melt Forms (c,f). The geometrical segmentation was performed with $(\widetilde{\kappa_t}, c_t) = (1.0, 0.25)$. The corresponding geometrical bonds are indicated in black. The stress distribution was performed with isotropic tensile deformation as loading conditions. The corresponding mechanical bonds are indicated in blue.

our approach with the stress distribution in the microstructure, computed by FEM. First, the mechanical results show large stress fluctuations with higher local stresses on the bonds, which confirms the picture of snow as a granular material. It was shown that the stress concentration at the grain level ($\widetilde{\sigma_{eq}}$) is not very sensitive to the applied loading conditions (pure shear, uniaxial tension, isotropic tensile strain). However, it has to be recalled that this granular description of snow is appropriate only for fast deformations governed by contact interactions, and not necessarily for slow deformations as creep or for highly sintered structures whose granular nature is questionable. Second, the stress distribution was used to evaluate the mechanical relevance of the bonds detected by the geometrical segmentation algorithm, assuming that these bonds should be preferentially located in zones of stress concentration. We showed that our geometrical segmentation is effectively able to detect bonds supporting locally the highest stresses and performs almost as well as segmentation directly inferred from the stress distribution. The refinement procedure composed of contact area minimization and merging of highly contiguous grains selects bonds that effectively concentrate stress, among those detected by the criterion on curvature. This is of particular interest for faceted snow types, where purely curvature-based algorithms are negatively affected by small protuberances on flat ice surfaces.

In all cases, significantly more geometrical grains than mechanical grains are required to reproduce the mechanical bonding system. Let us recall, however, that the mechanical grains defined in this study are relative to the modeled elastic stress distribution. Eventually, as strain increases, the progressive failure of bonds and the creation of new contacts might change the local distribution of stress. Hence, new geometrically-determined contacts might progressively be activated. In practice, the geometrical segmentation thus appears well suited to simplify the snow microstructure in grains regardless of the deformation regime (elastic/inelastic). Moreover, this segmentation is also much more computationally efficient (30 min for the RG image) compared to the complete mechanical simulation (10 h on the same image and PC).

Finally, the algorithm presented in this article appears as an efficient tool to represent the snow microstructure as a set of grains instead of as a collection of voxels. This representation can then be used, typically, for DEM simulations. However, a direct evaluation of such grain-based simulations against real experiments will certainly be necessary to help defining the optimal segmentation parameters which best capture the granular mechanical behavior of snow.

Acknowledgements This work was supported by VOR (Tomo_FL project) and the European Feder Fund (projects Interreg Alcotra MAP3, RiskNat). We thank B. Lesaffre and N. Calonne for data acquisition, and E. Podolskiy for comments. The authors thank the scientists of the ESRF ID19 beamline (J. Baruchel, E. Boller, W. Ludwig, X. Thibault) and of the 3SR laboratory (P. Charrier, J. Desrues, S. Rolland du Roscoat), where the 3D images have been obtained. Irstea and CNRM-

GAME/CEN are part of Labex OSUG@2020 (Investissements d'Avenir - Grant Agreement ANR-10-LABX-0056) and Irstea is member of Labex TEC21 (Investissements d'Avenir - Grant Agreement ANR-11-LABX-0030). The authors thank H. Löwe and an anonymous reviewer for their constructive feedback on the manuscript.

Chapter 6

Microstructure-based modeling of snow mechanics: a discrete element approach

Abstract Rapid and large deformations of snow are mainly controlled by grain rearrangements which are made possible by the failure of cohesive bonds and the creation of new bonds. We exploit this granular nature of snow to develop a discrete element model based on the full three-dimensional microstructure captured by microtomography. The model assumes that snow is composed of rigid grains interacting through localized contacts accounting for cohesion and friction. The geometry of the grains and of the intergranular bonding system are explicitly defined from microtomographic data. The bonds are detected in the microstructure with geometrical criteria based on curvature and contiguity. Single grains are represented as rigid clumps of spheres. The model is applied to different snow samples subjected to confined compression tests. A detailed sensitivity analysis shows that artefacts introduced by the modeling approach and the influence of numerical parameters, are limited compared to variations due to the geometry of the microstructure. The model evidences that the compression behavior of snow is mainly controlled by the density of the sample but that deviations from a pure density parameterization are non negligible during the first phase of compression (density < 300 kg m^{-3}). In particular, the model correctly predicts that, for a given density, faceted crystals are less resistant to compression than rounded grains or decomposed snow. For higher compaction, no clear difference between snow types has been observed.

Contents

6.1 Introduction

Knowledge of the mechanical properties of snow is required for many applications such as avalanche risk forecasting, optimizing over-snow vehicle traffic, quantifying loads on structures, etc. [Shapiro et al., 1997]. Snow is a material made of air, ice and sometimes liquid water and impurities. Snowflakes can take many different forms controlled by the atmospheric conditions [e.g. Bentley and Humphreys, 1931, Nakaya, 1954]. Once deposited on the ground, snow still evolves. Indeed, its high porosity and its temperature close to its melting point promote rapid changes of its microstructure through water vapor transport or melting/refreezing processes [e.g. Fierz et al., 2009, Flin, 2004, Schneebeli and Sokratov, 2004, Vetter et al., 2010]. As a consequence, the snow material is characterized by a wide range of densities and microstructural patterns classified in different snow types [Fierz et al., 2009]. In addition, the ice matrix of the snow microstructure exhibits different types of mechanical behavior such as elasticity, visco-plasticity and brittle failure, depending on the load, strain rate and temperature [Petrovic, 2003]. This variety of snow types and different deformation mechanisms of ice can be considered as the major scientific obstacles for the progress in the knowledge of the mechanical properties of snow [Brown, 1989].

Numerous studies have attempted to measure the macroscopic mechanical behavior of different snow types under various loading conditions (rate and direction) and temperatures. Mellor [1975], Salm [1982], Shapiro et al. [1997] reviewed the main results of these experimental studies. They show global trends of increasing strength and stiffness with increasing density. However, they pointed out that the majority of existing data characterize the microstructure only by density and a snow type, and do not include independent variables that reflect the influence of the microstructure. Hence, the large scatter in plots of mechanical properties versus density (e.g. Figure 1.7 in Chapter 1) reveals that density alone is insufficient to fully characterize snow material behavior [Keeler and Weeks, 1968, Shapiro et al., 1997, Voitkovsky et al., 1975]. Moreover, the current snow type classification [Fierz et al., 2009], which differentiates snow types according solely to the shape and size of individual grains, is poorly representative of the mechanical behavior. Therefore, it appears necessary to better account for the microstructure to derive relevant indicators of the mechanical properties of snow [Shapiro et al., 1997].

Stereological methods based on snow sections were developed to characterize the bonding between snow grains [e.g. Edens and Brown, 1995, Keeler, 1969, Kry, 1975a], which plays an important role in determining the mechanical properties. From these observations, models incorporating state variables describing microstructural features such as grain and bond size, or coordination number, were developed [Hansen and Brown, 1986, Mahajan and Brown, 1993, Nicot, 2004]. The macroscopic be-

havior of snow is statistically estimated from the system composed of a single grain surrounded by bonds characterized by a distribution of contact orientations. These models therefore assume the snow grain to be the fundamental unit of the mechanical behavior. However, this assumption is questioned by observations of Kry [1975b], who considered connected series of stress-bearing grains as the fundamental unit of snow structure. Moreover, in order to derive three-dimensional (3D) geometrical properties from two-dimensional (2D) observations, stereological methods require inherent assumptions about the shape and isotropy of the microstructure, which are not valid for all snow types [e.g. Alley, 1986].

In the last decade, the development of micro-computed tomography (μCT) on dry snow enabled a large progress toward deciphering snow's microstructure [Brzoska et al., 1999, Coléou et al., 2001, Schneebeli and Sokratov, 2004]. With μCT, it is possible to obtain a 3D image of the microstructure at resolutions down to a few microns. Besides observations of the evolution of the ice matrix and qualitative explanations of the observed deformation mechanisms [e.g. Schleef et al., 2014], μCT enables to develop mechanical models directly based on the real 3D microstructure. Schneebeli [2004] and Srivastava et al. [2010] computed the elastic modulus of snow, which is very difficult to measure in experiments, with a finite element (FE) simulation based on the 3D microstructure. Srivastava et al. [2010] used the results of the FE analysis on a snow sample evolving under temperature gradient to correlate the evolution of the mean intercept length of the structure and the evolution of the Young's modulus. Hagenmuller et al. [2014c] successfully reproduced tensile failure under high strain rate with a FE analysis. Chandel et al. [2014] modeled the softening behavior of snow under compression with a FE model and a material law incorporating elasto-plasiticty and damage. However, all these mentioned μCT-based models are extremely computationally expensive because the microstructure is meshed with finite elements of similar sizes and no degree of freedom is blocked. Therefore, such FE simulations are limited to relatively small snow volumes and relatively simple material models for ice.

On the other hand, rapid and large deformations of snow are mainly controlled by grain re-arrangements, which are made possible by bond failure and creation. This type of deformation is involved in the release of slab avalanches [Schweizer et al., 2003], in the characterization of a snow profile with an indenter [Bader and Niggli, 1939, Schneebeli and Johnson, 1998], or when a vehicle wheel comes in contact in snow covered terrain [Yong and Fukue, 1977]. To model these deformation regimes, we propose to take advantage of describing snow as a granular material: the microstructure is simplified into a set of rigid grains interacting through their contacts. The assumption of snow as a granular material is reasonable for high strain rates ($\dot{\varepsilon} > 10^{-4}$ s^{-1}) and natural seasonal snow with a relatively low porosity (> 0.6) [Hansen and Brown, 1988]. This assumption drastically reduces the number of degrees of freedom in the microstructure and enables to simulate snow deformation with the discrete element method (DEM). DEM is more suited then FE to model large discontinuous deformations governed by microscale processes such as bond breakage, and compaction of broken fragments. Johnson and Hopkins

[2005] modeled snow mechanics with DEM and a snow microstructure described by randomly oriented cylinders of random length and hemispherical ends. To reduce the inevitable bias introduced by such a simplification, we propose a new approach directly accounting the real 3D microstructure of snow captured by μCT.

In the present study, we propose to use the DEM approach with the 3D microstructure of snow captured by μCT to model dry snow deformation at high loading rates. First, the different microstructure images used to build the DEM are presented. Second, the DEM model is described. It requires a method to translate the microstructural information into discrete elements, and the definition of a contact law. The model capabilities are evaluated on one type of loading conditions: uniaxial confined compression, obtained through an imposed uniaxial strain and lateral periodic boundary conditions. This loading involves the creation of new contacts and particle re-arrangements which the model aims to capture. Third, a sensitivity analysis of the model is performed. Last the model is applied to different snow samples and the modeled compressive behavior is analysed.

6.2 Materials and methods

6.2.1 Dataset

The DEM model has been applied to five μCT snow images spanning different snow types (Decomposing and Fragmented precipitation particles (DF), Rounded Grains (RG), Faceted Crystals (FC), Depth Hoar (DH), [Fierz et al., 2009]) obtained from previous controlled cold-room experiments (samples I08, I15, I23 measured by Flin et al. [2004] during an isothermal metamorphism experiment, sample 2A measured by Calonne et al. [2011] during an temperature gradient experiment,) or field sampling (sample Ip04 measured by Flin et al. [2011] and samples 4, 9 measured by Hagenmuller et al. [2013b]). All samples were scanned with X-ray absorption tomography with casting procedures. The μCT images have a nominal resolution between 5 and 10 microns. The grayscale images were binary segmented with the technique described by Hagenmuller et al. [2013b] with an effective resolution of two voxels. The characteristics of the imaged samples are summarized in Table 6.1.

6.2.2 Snow microstructure representation

In practice, the microstructure captured by tomography is a binary image composed of air and a continuous ice matrix. No grains are distinguished in the ice matrix. So, first the grains need to be detected in the binary image, which is a difficult task since the grains are not well separated but rather sintered together. The algorithm developed by Hagenmuller et al. [2014b] was used in the present study and is briefly described in the following. Second, the detected grains which can have a complex shape different from standard simple geometrical units as spheres or cylinders, are described in terms of discrete elements by clumping spheres together.

Sample name	Type	Voxel size (μm)	Side length (mm)	Density (kg m^{-3})	Equivalent spherical radius (μm)
Ip04	DF	8.59	5.84	145	128
I08	DF/RG	9.82	4.91	145	111
4	FC/DF	9.65	5.79	163	191
2A	FC	8.37	5.00	319	183
9	FC/DH	9.65	5.79	183	179
I15	RG	9.82	4.91	182	146
I23	RG	9.82	4.91	242	191

Table 6.1: Description of the microtomographic images used in this study. All images are cubic. Density and equivalent spherical radius were computed from the binary images of the microstructure. The equivalent spherical radius is defined as $3V/S$ with V the volume of ice and S the snow surface area. It quantifies the typical size of the ice matrix.

Grain segmentation Hagenmuller et al. [2014b] developed an algorithm to segment the snow microstructure into grains that are mechanically relevant. The algorithm detects zones of reduced ice thickness, the bonds, based on geometrical criteria on curvature and contiguity. First, bond candidates are identified with the value of the minimal principle curvature κ_{min} in the ice matrix. The bonds candidates are located on concavities ($\kappa_{min}<0$) and separate the grains located on convexities ($\kappa_{min}>0$). A parameter $\widetilde{\kappa_t}$ sets the sensitivity of this pre-segmentation to curvature. A small value of $\widetilde{\kappa_t}$ yields numerous bond candidates, a larger value of $\widetilde{\kappa_t}$ yields less bond candidates located only on the most pronounced concavities. Second, the bond candidates are refined: their area is minimized and highly contiguous grains, i.e. grains which share a large proportion of their total surface, are merged. A contiguity parameter c_t defines the threshold for the merging: a grain is merged to its neighbor if $S_{int} < c_t \times S_{tot}$ where S_{int} is the contact area between the two grains and S_{tot} is the total grain surface area. Hagenmuller et al. [2014b] showed that this grain segmentation algorithm is able to detect the bonds supporting locally the highest stresses. With the assumption of homogeneous ice strength, the algorithm detects the potential failure paths in the microstructure and is thus relevant for the DEM approach.

On a given microstructure, the exact choice of $\widetilde{\kappa_t}$ and c_t determines the total number of segmented grains. These segmentation parameters must be set so that the granular description of the snow microstructure reasonably captures the mechanical behavior of snow under the given loading conditions. It might be necessary to decompose the microstructure in more or less grains depending on the subsequent use of the grains assembly.

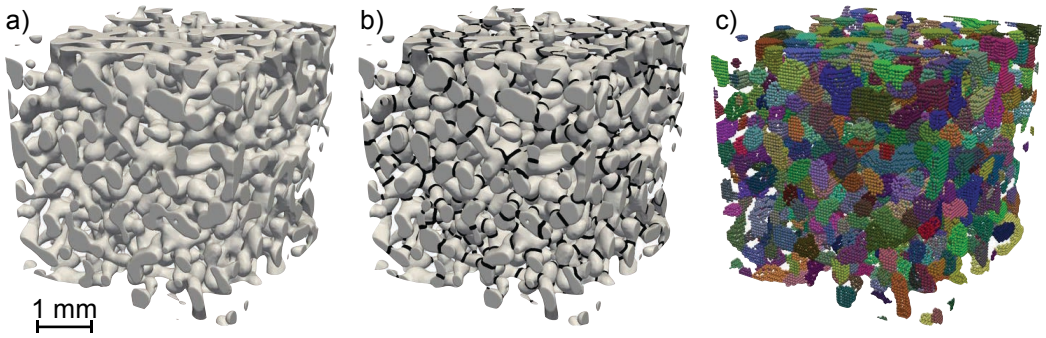

Figure 6.1: Granular description of the ice matrix. The binary image (a) is segmented into grains (b) separated by their bonds (black). The detected grains are represented as clumps of spheres (c).

Clump of spheres The segmented grains are represented by a set of voxels. The geometry described by these voxels must be translated into discrete elements which can be handled by the DEM model. Clumping of basic geometrical unit as spheres [e.g. Ferellec and McDowell, 2010] or meshing with polyhedra [e.g. Lee et al., 2009] can be used to capture the morphology of irregular 3D particles. The representation using clump of spheres is much simpler in terms of a numerical algorithm than the use of polyhedral particles, because the clumping approach is free of the singularity problem of contacts between faces, edges and points, which is difficult to handle and demanding in terms of calculation. The simplicity of the clumping approach ensures the stability of the computation [Matsushima et al., 2009].

In the present study, a very simple technique using non-overlapping spheres was used to describe (or mesh) the snow grains into discrete elements. First, the resolution of the 3D grain image was reduced by a certain factor. Then, all voxels at the interface between two grains or between air and ice, were replaced by a sphere with a diameter equal to the side-length of the voxel and with the same center position (Figure 6.1). The sphere diameter thus depends on the reduction of the initial resolution of the image. Each grain decomposed in numerous spheres behaves as a rigid body. The contact between grains is computed via the detection of contacts between the spheres which describe the grain shapes. Considering spheres only at the surface of the grains diminishes the total number of spheres required for DEM. The use of equally-sized spheres enables to take a relatively large time step for simulation.

6.2.3 Discrete element model

Each grain is represented by a single discrete particle called clump. It is composed of a rigid aggregate of spheres, called members. The motion equations are solved on the clump. The positions of its members are updated according to the clump overall motion and the relative position of the members in the clump. The forces and moments acting on the clump are the sum of the forces acting on its members. The

interactions between the members of two different clumps are frictional and cohesive, cohesion being active only for the contacts that exist in the initial undeformed microstructure. The discrete element modeling was performed with Yade DEM code (https://yade-dem.org/doc/). Main computation steps are described here with a focus on the contact law used (`Law2_ScGeom6D_CohFrictPhys_CohesionMoment`). Extensive documentation can be found in [Šmilauer et al., 2010].

Motion equations on a clump On a clump c, the motion is computed by the integration of Newton's equation for the translational and rotational degrees of freedom:

$$M_c\ddot{\mathbf{X}}_c = \mathbf{F}_c \text{ and } \mathbf{I}_c\dot{\boldsymbol{\Omega}}_c = \mathbf{T}_c \tag{6.1}$$

with M_c the mass of the clump, $\mathbf{I}_c$ its moment of inertia, $\mathbf{X}_c$ its centroid position, $\boldsymbol{\Omega}_c$ its angular velocity, $\mathbf{F}_c$ the total force and $\mathbf{T}_c$ the total torque applied on the clump. Newton's equations are integrated for each time step dt with a Verlet scheme [Šmilauer et al., 2010]. The mass M_c and inertia $\mathbf{I}_c$ were directly calculated with the grain-segmented image by summing the contributions of each voxels. The force $\mathbf{F}_c$ and torque $\mathbf{T}_c$ on the clump are defined as

$$\mathbf{F}_c = \sum_{i\in c}\mathbf{f}_i \text{ and } \mathbf{T}_c = \sum_{i\in c}\mathbf{l}_i \times \mathbf{f}_i + \sum_{i\in c}\mathbf{t}_i \tag{6.2}$$

where $\mathbf{l}_i$ is the relative position of the member i with regards to the clump centroid, $\mathbf{f}_i$ and $\mathbf{t}_i$ are the force and torque on the member i.

In the model, only contact forces are used and no volumetric forces such as gravity are considered. The used contact laws do not incorporate damping during collision. Therefore in order to dissipate kinetic energy, which is desirable in simulations of quasi-static phenomena, a numerical damping is used [Cundall and Strack, 1979]. A damping force $(\mathbf{F}_a)_c$ is added to each clump:

$$(\mathbf{F}_a)_c = -\lambda_a|\mathbf{F}_c|\text{sign}(\dot{\mathbf{X}}_c) \tag{6.3}$$

The integration of the motion equations thus depends on two model parameters: the time step dt and the the damping coefficient λ_a.

The force and torque on the spherical member i are computed by considering all sphere-sphere interactions acting on the member i. In the following paragraphs, the computation of the force/torque resulting from the interaction between two equally sized spheres composed of the same material is detailed.

Sphere-sphere contact geometry The geometry of the contact between two spheres has 6 degrees of freedom (DOF): both spheres are free to translate and rotate (6+6 DOF) but the cluster of the two interacting spheres can also translate and rotate (-6 DOF) (Figure 6.2). The computation of normal strain (1 DOF) and shear strain (2 DOF) is described in the following. Less attention is paid to bending (2 DOF) and twisting (1 DOF) between two spheres since their effects are not

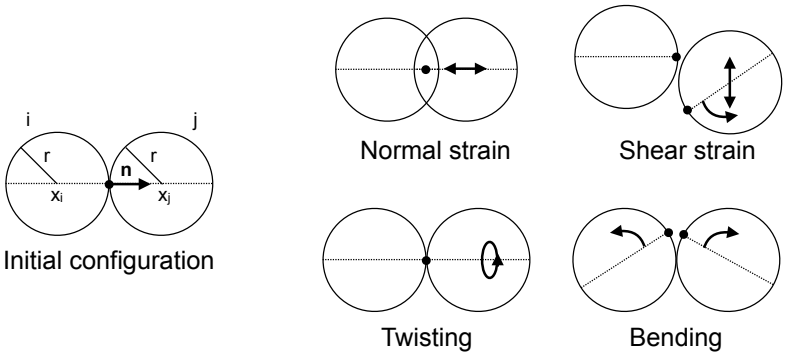

Figure 6.2: Degrees of freedom (DOF) of configuration of two spheres. Adapted from [Šmilauer et al., 2010].

determinant in the present modeling case where the intergranular cohesive contacts are composed of several sphere-sphere interactions.

Let us consider two spheres i and j with the same radius r (Figure 6.2). The position and velocity of the spheres is denoted $\mathbf{x}$ and $\mathbf{v}$. The angular velocity is denoted $\boldsymbol{\omega}$. The variable notation is underscored by i and j to indicate that the variable refers to sphere i or j (Figure 6.2). The interaction normal $\mathbf{n}$ is defined as $\mathbf{n} = (\mathbf{x}_j - \mathbf{x}_i)/|\mathbf{x}_j - \mathbf{x}_i|$. The normal strain ε_n is defined as the ratio between the spheres overlap δ and their radius r, with $\delta = 2r - (\mathbf{x}_j - \mathbf{x}_i) \cdot \mathbf{n}$. The overlap is positive if the spheres really overlap and negative if the spheres are disjoint. The equilibrium normal position is chosen to be the zero-overlap. The contact point is defined as the middle of the segment between the sphere centers. It is at a distance $d = (r - \delta/2)$ from the sphere centers.

The shear displacement $\mathbf{u}_t$, i.e. the relative sphere displacement in the plane normal to $\mathbf{n}$, is computed incrementally. The shear displacement increment $\Delta\mathbf{u}_t$ is due to the relative motion of spheres and the motion of the interaction in global space. The relative velocity of spheres at the contact point is $\mathbf{v}_{ij} = (\mathbf{v}_j + \boldsymbol{\omega}_j \times (-d\mathbf{n})) - (\mathbf{v}_i + \boldsymbol{\omega}_i \times (d\mathbf{n}))$. The increment $\Delta\mathbf{u}_t$ of shear displacement due to the relative sphere motion during one time increment dt is thus the projection of v_{ij} on the tangent plane times the time increment. Note that the displacement of the interaction needs to be also taken into account to ensure that the accumulated shear displacement $\mathbf{u}_t$ is still in the current tangent plane and is not affected by global displacement of the interaction (see [Šmilauer et al., 2010] for details).

Sphere-sphere contact law The contact law computes forces and torques acting on two interacting spheres, according to the material properties of the spheres and the contact geometry described before. In the presented model, the initial contacts are cohesive and frictional while the new contacts created during the simulations are only frictional. The material, ice, is thus described by Young's modulus E, Poisson's ratio ν, normal cohesion σ_n, shear cohesion σ_t and a friction angle φ.

The force $\mathbf{f}_n$ acting on sphere i in the normal direction depends on Young's

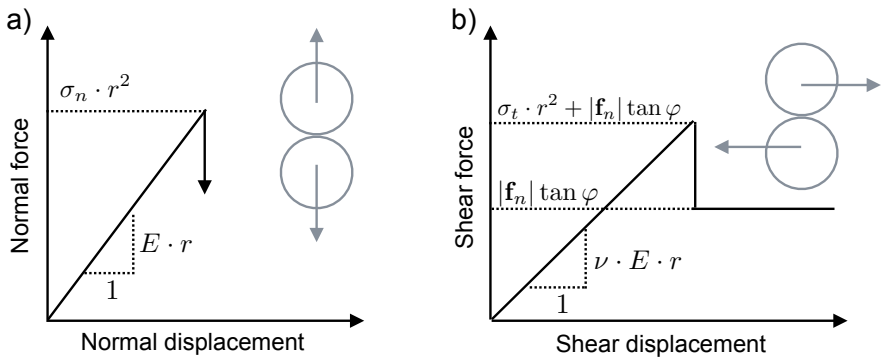

Figure 6.3: Behavior of the sphere-sphere contact in two simple cases: normal loading (a) and simple shearing (b).

modulus E and normal cohesion σ_n of the sphere material as following:

$$\begin{aligned} &\mathbf{f}_n = -(Er\delta)\mathbf{n} && \text{if } -Er\delta < f_{n,max} = \sigma_n r^2 \\ &\mathbf{f}_n = \mathbf{0} \text{ and cohesion is broken} && \text{if } -Er\delta \geq \sigma_n r^2 \end{aligned} \tag{6.4}$$

This describes simply a linear spring with a spring coefficient equal to $K_n = Er$ and a maximum force $f_{n,max} = \sigma_n r^2$ in tension before breakage (Figure 6.3). The new contacts do not have any cohesion. Note that if the cohesion is broken σ_n is set to zero but the shear cohesion σ_t is also set to zero for the contact.

The force $\mathbf{f}_t$ acting on sphere i in the tangent plane depends on Young's modulus E, Poisson's ratio ν, shear cohesion σ_t and friction angle φ. Let us define the elastic shear force $\mathbf{f}_t^e = -(\nu Er)\mathbf{u}_t$ and the frictional shear force $\mathbf{f}_t^s = (\mathbf{f}_t^e/|\mathbf{f}_t^e|)|\mathbf{f}_n|\tan(\varphi)$. The force $\mathbf{f}_t$ is:

$$\begin{aligned} &\mathbf{f}_t = \mathbf{f}_t^e && \text{if } |\mathbf{f}_t^e| < f_{t,max} + |\mathbf{f}_n|\tan(\varphi) \\ &\mathbf{f}_t = \mathbf{f}_t^s \text{ and cohesion is broken} && \text{if } |\mathbf{f}_t^e| \geq f_{t,max} + |\mathbf{f}_n|\tan(\varphi) \end{aligned} \tag{6.5}$$

with $f_{t,max} = \sigma_t r^2$. Note that if the cohesion is broken in shear, then σ_t and σ_n are set to zero on this contact. Main features of this contact law are summarized on Figure 6.3. The tangential force $\mathbf{f}_t$ adds a torque $\mathbf{t}_t = d(-\mathbf{n}) \times \mathbf{f}_t$ on the sphere.

In this study, cohesion strengths in tension (σ_n) and in shear (σ_t) are supposed to be equal and are simply denoted σ_{ice} ($\sigma_n = \sigma_t = \sigma_{ice}$).

Grain-grain contact law The intergranular contacts are composed of several sphere-sphere contacts, as described above. The force F between two grains in contact is the sum of the force resulting from the sphere-sphere interactions ss which compose the intergranular contact, i.e. $F = \sum_{ss} f_{ss}$, where f_{ss} is the force at the sphere-sphere contact ss (Figure 6.4).

In the case of pure tension with a relative displacement δ along the normal $\mathbf{n}$ of the contact surface, the resulting intergranular force is thus:

$$\begin{aligned} &\mathbf{F}_n = -N(Er\delta)\mathbf{n} && \text{if } -Er\delta < f_{n,max} \\ &\mathbf{F}_n = \mathbf{0} \text{ and cohesion is broken} && \text{if } -Er\delta \geq f_{n,max} \end{aligned} \tag{6.6}$$

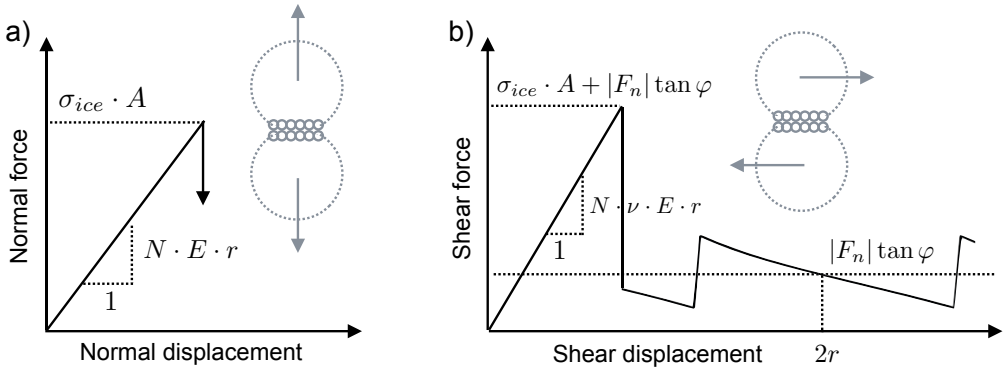

Figure 6.4: Behavior of the grain-grain contact in two simple cases: normal loading (a) and simple shearing (b). The grain-grain contact is here composed of seven sphere-sphere contacts. The small spheres have a radius r. The intergranular contact area is denoted A. The number of sphere-sphere interactions is denoted N.

with N the number of sphere-sphere interactions. For the initial cohesive contacts and if no discretization artefact is considered, N is equal to A/r^2, with A the surface area of the intergranular contact calculated on the initial grain-segmented image. The maximum tensile force supported by the equivalent intergranular contact is thus $A\sigma_{ice}$, which is consistent with the definition of microscopic strength. However, in practice, N slightly differs from the value A/r^2 due to discretization artefacts. Therefore, instead of the previously introduced definition of $f_{n,max} = \sigma_{ice} r^2$, the maximum tensile force at the sphere-sphere contact is adjusted to $f_{n,max} = \sigma_{ice} A/N$ to ensure that the maximum tensile force supported by the intergranular contact is effectively $A\sigma_{ice}$.

Similarly, the maximum shear force at sphere-sphere interactions is adjusted to $f_{t,max} = \sigma_{ice} A/N$. For friction, the bumpy surface at the contacts between grains yields a varying effective friction coefficient between grains (Figure 6.4). However, the mean effective intergranular friction coefficient is closed to the microscopic friction coefficient $\tan \varphi$.

6.2.4 Boundary conditions

The boundary conditions were chosen to reproduce strain-controlled vertical confined compression of snow. The grains were placed between two horizontal plates discretized by spheres of the same size of the spheres used to describe the grain shape (Figure 6.5). The bottom plate was fixed. A constant vertical velocity V_{plate} was applied to the top plate to reproduce compression. The contact law between the grains and the plates is the same as the intergranular one, i.e. cohesive frictional with the same material parameters. In the horizontal directions, periodic boundary conditions were applied. Periodic space was used by the repetition of a cell with the shape of the undeformed sample, in the horizontal directions. As shown on Figure

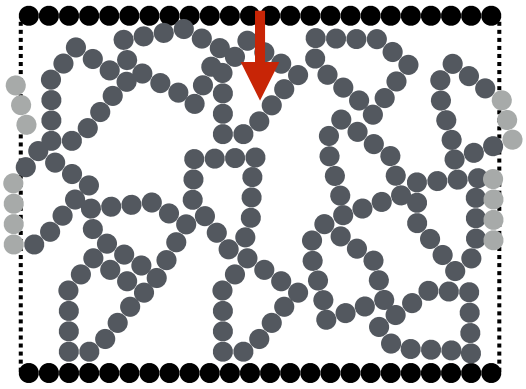

Figure 6.5: Boundary conditions used in the present study. The grains (medium gray) are compressed between two plates composed of spheres (black): the bottom plate is fixed and the top plate is moving down with a constant velocity V_{plate}. Periodic space was used in the horizontal directions. Elements (light gray) crossing the periodic cell limits (dotted lines) appear on the opposite side of the samples. Note that this figure represents a 2D simulation for clarity purpose but the performed simulations are 3D.

6.5, when a sphere crosses the cell boundary, it appears on the opposite side of the sample.

6.3 Results

First, a simulation is conducted on the sample of rounded grains (RG) to have an overview of the deformation mechanisms occurring during compression loading. Then, based on this first analysis, the sensitivity analysis of the model to the DEM parameters and microstructure representation is evaluated. Last the model is applied to all snow images described in 6.2.1 and the influence of the snow microstructure on the confined compressive behavior of snow is discussed.

6.3.1 First results

The model parameters used for this first simulation are summarized in Table 6.2 and are derived from typical ice properties [Schulson and Duval, 2009].

6.3.1.1 Observations

Because of the imposed velocity V_{plate} on the upper plate, the sample undergoes uniaxial compression with an overall vertical strain $\mathcal{E}_{zz}$ defined as the ratio of the displacement of the upper plate to the initial height L_0 of the sample. The sample produces a vertical reaction force F_z which defines a vertical overall stress $\Sigma_{zz} = F_z/L_0^2$ with L_0^2 the horizontal cross-section area of the sample. The relation between

Name	Symbol	Value
Material properties		
Young's modulus	E	10 MPa
Poisson's ratio	ν	0.3
Friction angle	φ	$\tan(\varphi) = 0.2$
Normal cohesion strength	$\sigma_n = \sigma_{ice}$	1 MPa
Shear cohesion strength	$\sigma_t = \sigma_{ice}$	1 MPa
Density of ice	ρ_{ice}	917 kg m^{-3}
Boundary condtions		
Side length of the cubic snow sample	L_0	4 mm
Compression velocity	V_{plate}	10 mm s^{-1}
Integration of motion's equation		
Time step	dt	5×10^{-7} s
Non-viscous damping coefficient	λ_a	0.2
Representation of the microstructure		
Segmentation parameter on curvature	$\widetilde{\kappa_t}$	1.0
Segmentation parameter on contiguity	c_t	0.25
Radius of the spherical members	r	25 μm

Table 6.2: Model parameters used for a first simulation presented in Figure 6.6.

macroscopic imposed strain $\mathcal{E}_{zz}$ and resulting macroscopic stress Σ_{zz} is shown in Figure 6.6a. The work of the imposed deformation adds mechanical energy to the snow sample which is stored as kinetic energy and elastic energy, and dissipated through plasticity (shear sliding), bond breaking and non-viscous damping (Figure 6.6b). During deformation, cohesive bonds are broken and new non cohesive contacts are created (Figure 6.6c). The distributions of overlap δ between spheres are shown for different strain states on Figure 6.6d. The observed mechanisms can be classified into three domains corresponding to different macroscopic strain intervals:

- *Elastic regime* for $\mathcal{E}_{zz} < 0.02$. During the uniaxial compression, the snow structure first undergoes elastic deformation. The work of the loading is completely stored as elastic energy at the bonds. No cohesive bonds are broken. No new bonds are created. If the upper plate is moved back to its initial position, the stress decreases to zero and the microstructure recovers fully its initial state without any residual deformation or stress. Because there are no new bonds and strains are small at the microstructural level, there is linear relation between stress Σ_{zz} strain $\mathcal{E}_{zz}$ in the elastic regime. The slope of the curve quantifies the elastic modulus E_s of the granular assembly. A significant number of bonds are in tension (existence of negative overlap on Figure 6.6d), even if the macroscopic loading is compression.

- *Brittle/frictional regime* for $0.02 < \mathcal{E}_{zz} < 0.4$. When the strain increases ($\mathcal{E}_{zz} > 0.1$), first bonds start to break and snow deforms with a resistance

of about 15 kPa. The stress-strain relation deviates from the elastic linear relation and if the upper plate is moved back to its initial position, permanent deformations is observed. The breaking of bonds leads to small "jumps" down of the stress which are balanced by friction on the broken bonds, the activation of other cohesive bonds or the creation of new bonds. The friction between grains yields plastic dissipation. Kinetic energy is negligible compared to total energy. The total number of interactions appears to decrease slightly. The structure tightens because fracture of the bonds permits grains to move in the pore space. Hardening of the structure is observed: Σ_{zz} increases from 10 kPa to 30 kPa when $\mathcal{E}_{zz}$ increases from 0.1 to 0.4.

- *Dense compaction regime* for $0.4 < \mathcal{E}_{zz}$. When density reaches about 500 kg m^{-3}, the increase of stress with strain becomes suddenly faster. This increase is accompanied by the creation of numerous contacts. Because most contacts are not cohesive in this regime, the distribution of overlaps shows a clear majority of bonds loaded in compression. Kinetic energy remains negligible compared to total energy.

Note that the stress-strain relationships predicted by the model are in good qualitative agreement with features observed during the experimental uniaxial compression of snow: large deformations with little resistance for low-density snow ($< 300 - 400$ kg m^{-3}); a gradual increase of stress with density until density reaches about 450 kg m^{-3} whereupon resistance increases dramatically with deformation [Abele and Gow, 1975, 1976, Johnson, 2011] (Figure 6.7).

6.3.1.2 Identification of potential model artefacts

The analysis of the model results is, here, used to identify potential artefacts introduced by the model in the simulation of the mechanical behavior of snow under compression. The same classification as in the previous section is used:

- *Elastic regime.* The model is composed of rigid grains which cannot deform. Only the contacts between members of different grains can deform to account for intergranular strain. Hagenmuller et al. [2014b] showed with FE simulations that even if the highest strains (or stress) are located on the bonds, the overall elastic strain is mainly due to the deformation of the grains themselves since they represent a very large majority of the ice volume. Therefore, in the present modeling approach, the computed Young's modulus is not expected to be realistic and is directly dependent on the modeling assumptions. Nevertheless, the aim of the model is not to reproduce the elastic properties of snow which can be accurately modeled by FEM simulations [Chandel et al., 2014, Hagenmuller et al., 2014b,c, Schneebeli, 2004] but to model large deformations. Note that the stiffness of ice is very high (about 1-10 GPa) and consequently the elastic strain of snow is very small and almost negligible compared to the strain due to particle re-arrangement. In the present study, the Young's

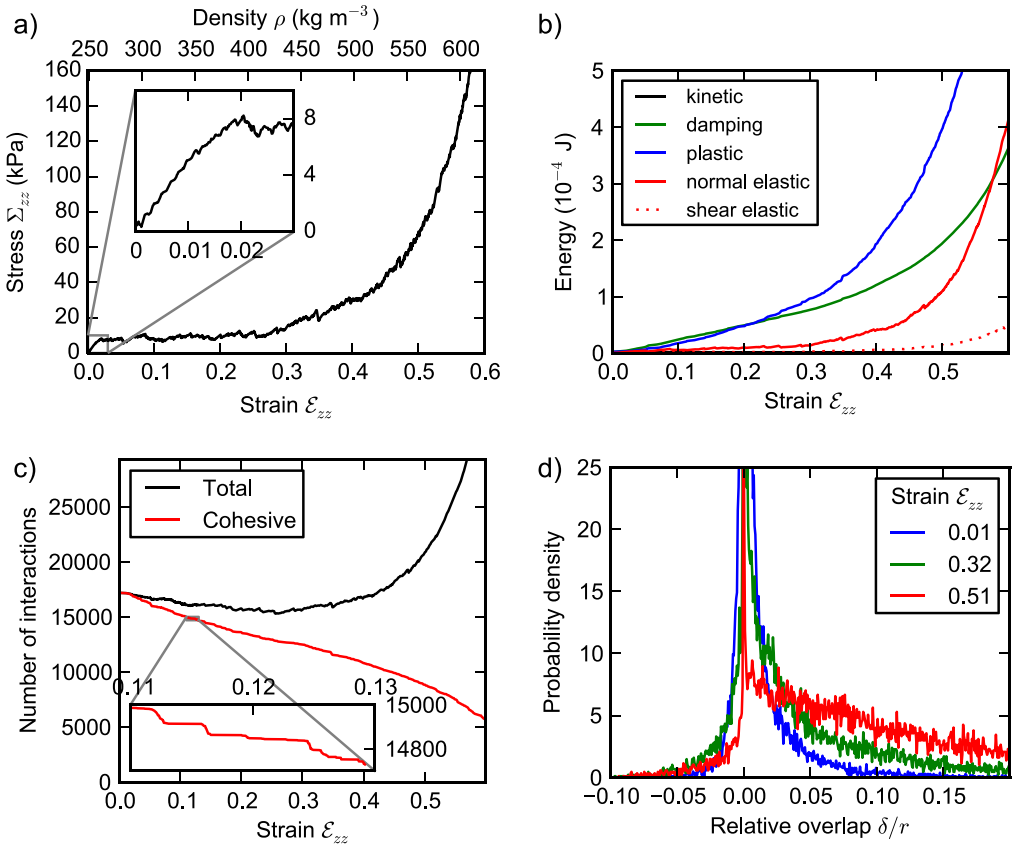

Figure 6.6: Results of the model applied on RG (sample I23) with the parameters described in Table 6.2.

modulus is just necessary to avoid particle interpenetration and was chosen relatively small compared to the stiffness of ice, to ensure numerical stability for relatively large time steps dt [e.g. Johnson and Hopkins, 2005]. Therefore, the strain interval for the elastic regime is here over-estimated. Indeed, in real snow, damage can occur for smaller strain of about 10^{-4} [Hagenmuller et al., 2014c]. In practice, for large strain, the elastic deformation is almost negligible.

- *Brittle/frictional regime.* This regime is controlled by the progressive failure of cohesive bonds and the friction between grains. Failures of intergranular bonds are determined by the force distribution on the sphere-sphere interactions between grains. This force distribution might depend on the number (or radius) of the spheres used to discretize the shape of the grains. Indeed, a larger number of smaller spheres are expected to better reproduce stress gradients on an intergranular bond. Besides, the friction between grains is determined by the roughness of the grain surfaces. The regular mesh used in the present study creates "bumpy" grain surfaces (Figures 6.1 and 6.5). Moreover, the mesh is aligned with the voxel grid, which might creates preferential sliding direction. Therefore, it is necessary to evaluate the sensitivity of the model to the meshing technique (radius of spheres and orientation of the grid) which might alter the modeled stress distribution and friction between grains.

- *Dense compaction regime.* In this regime, the rearrangement of grains cannot be accommodated within the pore space anymore. The grains form a dense packing whose compacity is determined by the shape of the grains. In this regime, the snow sample supports very high stresses. High tensile/shear intragranular stresses, which are not accounted for in the model, might thus develop and lead to the breaking of the grains into smaller parts. In this case, the assumption of "unbreakable" grains is no more valid. Besides, the high intergranular stresses might yield large overlaps between spheres compared to their radius. In this case, the assumption of rigid grains is no more valid and the modeled behavior becomes very sensitive to the Young's modulus. Therefore, it is necessary to evaluate the sensitivity of this deformation regime to the grain segmentation procedure and contact parameters.

In summary, the assumption of snow as a granular material ("unbreakable" grains) restricts the model validity to deformation regimes controlled by particle re-arrangement. The elastic regime is governed by intra-granular deformation and cannot be correctly reproduced by the model. The brittle/frictional regime is dependent on the stress distribution in the bonds and on the roughness of the grain surface, which might be sensitive to the meshing technique. The main focus of this study is on this regime. The compaction at very high strains might be altered by the assumption of unbreakable grains challenged by the high stresses occurring in this deformation regime. It might be sensitive to the grain segmentation procedure.

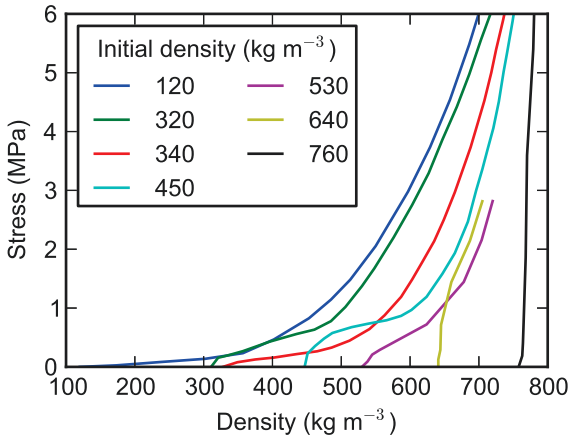

Figure 6.7: Uniaxial compression of snow. Adapted from [Johnson, 2011] with data from [Abele and Gow, 1975, 1976].

6.3.2 Sensitivity of the model to its parameters and modeling assumptions

Among the different model parameters, four different classes can be distinguished (Table 6.2).

- *The parameters linked to the integration of motion's equations.* The time step dt used for the numerical time integration scheme and the non-viscous coefficient λ_a used to dissipate energy in the model can lead to numerical artefacts. The sensitivity of the model to these parameters is investigated in section 6.3.2.1.

- *The parameters linked to the microstructure representation.* The microstructure representation used in the DEM depends on the number of grains used to discretize the microstructure (controlled by the parameters $\widetilde{\kappa}_t$ and c_t of the grain segmentation algorithm), the size of the spheres used to describe the grain shape (controlled by r). The sensitivity of the model to these parameters is investigated in section 6.3.2.2.

- *The parameters linked to the material properties.* These parameters control the relation between strain and stress at the contact interactions, and the inertia of the clumps. A priori, they depend on the ice properties. The values of cohesion σ_{ice} and microscopic friction coefficient $\tan(\varphi)$ are defined according to values reported from measurements on ice. However, as mentioned previously, the friction coefficient between grains also depends on the geometric roughness of the contact surface. The effects of the "physical" parameters such as cohesion and friction angle are investigated in section 6.3.2.3. The other constants (ρ_{ice}, E) appearing in the constitutive model of ice were chosen to reduce the

computing expense of the simulations. Here, the Young's modulus E and the density of ice ρ_{ice} are defined so that the time step dt is the largest, which decreases the overall computing time, while the overall mechanical behavior of snow in the brittle/frictional regime does not differ from the one observed with the material corresponding to ice. The relevance of this "numerical trick" is investigated at the same time as the sensitivity to dt in section 6.3.2.1.

- *The parameters L_0 and V_{plate} linked to boundary conditions.* The side-length of the sample L_0 is not really a model parameter since the model characterizes the mechanical behavior of the sample whatever its size. However, in order to characterize a mechanical behavior that is representative of a certain microstructural pattern, the sample needs to be large enough and at least larger than the representative elementary volume (REV). Investigations of the REV related to the compressive behavior of snow are presented in section 6.3.2.4. The velocity of the upper plate V_{plate} prescribes a certain compressive strain rate of the sample. The first simulation conducted on the RG sample showed that kinetic energy is negligible compared to the total energy. Therefore, the simulated mechanical behavior is quasi-static. The exact value prescribed velocity V_{plate} in the range $[0, 10^{-2}]$ m s^{-1} will thus not significantly affect the simulated mechanical behavior. However, let us recall that the assumption of brittle failure at bonds is valid only for relatively high strain rates ($\dot{\varepsilon} > 10^{-4}\ s^{-1}$, [Narita, 1983]). Therefore, the model is applicable only to reproduce the brittle regime of snow.

6.3.2.1 Time step dt

A sufficiently short time step is necessary for the stability of the simulated system and the physical relevance of the modeling. The mechanisms with the shortest timescales occurring in the DEM simulations arise from the propagation of elastic waves between the grains.The time step dt must be smaller than the timescales involved during the propagation elastic waves, to reproduce the elastic oscillations with sufficient precision. Usually the critical time step dt_c is estimated on the basis of the single degree-of-freedom system of a mass m connected to ground by a linear spring of stiffness k: $dt_c \approx \sqrt{m/k}$ [Radjai and Dubois, 2011]. In our case, m corresponds to the smallest grain mass, which is at least composed of one sphere, and k is the spring coefficient of a sphere-sphere interaction, so

$$dt_c \approx \sqrt{\rho_{ice} r^3/(Er)} = r\sqrt{\rho_{ice}/E}. \tag{6.7}$$

This critical time-step is estimated from a simplified case and there are no rigorous rules to derive a critical time step form the entire granular assembly of snow grains.

Equation 6.7 explicits the interplay between the critical time step dt_c on one hand, and the contact stiffness E, the ice density ρ_{ice} and the sphere radius r, on the other hand. To speed up the simulation, it is convenient to increase the critical time step by decreasing E and increasing ρ_{ice}. It is necessary to check if

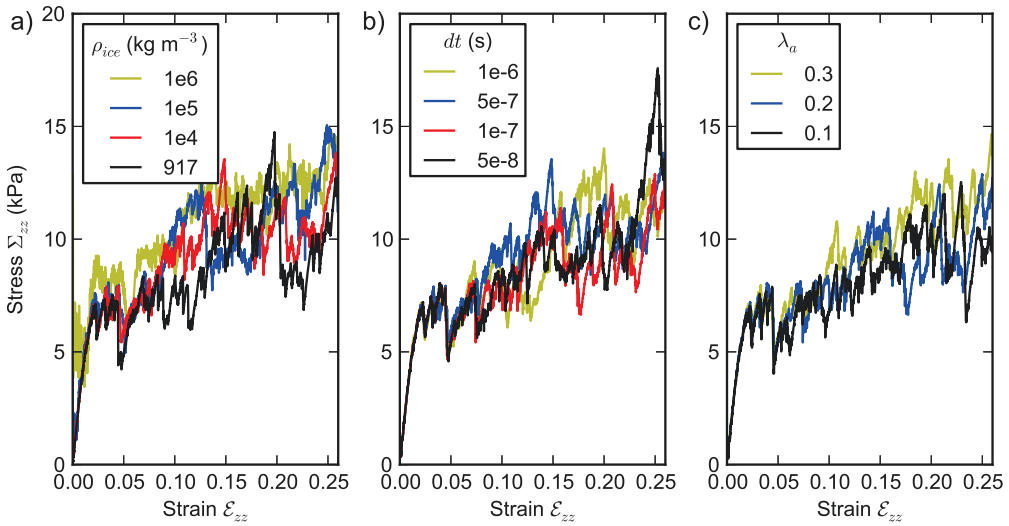

Figure 6.8: Stress-strain curve simulated by the model with the parameters described in Table 6.2 except various ice densities in subfigure a), various timed steps dt in subfigure b) and various damping coefficients in subfigure c).

the artificial adjustment of physical parameters does not affect the overall simulated mechanical behavior. As already mentioned, we do not expect to recover a realistic elastic behavior with this model. The presence of the elastic spring at the contacts is only motivated to ensure cohesion or non-interpenetration of grains but not to recover the elastic behavior of snow. Therefore, it possible to take a value for E much smaller than the real elastic modulus of ice (E_{ice}=1-10 GPa). However, it has to be recalled that when two grains touch, they overlap but do not deform and a force is computed as a function of the overlap. This simple contact model used is relevant if the overlap remains small (assumption of rigid grains). Therefore, the contact stiffness E must be chosen to ensure relatively small overlaps compared to the sphere radius. The maximum stress at the contact is expected to be on the order of the cohesion (σ_{ice}) of the contact, which yields an overlap of the order of $\delta = r \cdot (E/\sigma_{ice})$. We chose $E = 10 \cdot \sigma_{ice} = 10$ MPa to avoid large interpenetrations ($\delta/r > 0.1$) not correctly represented by the contact law.

Figure 6.8a shows the stress-strain curves of a sample of rounded grains subjected to uniaxial compression computed for different values of ice density, ρ_{ice}. The other model parameters were kept constant. Increasing ρ_{ice} increases the mass of the clumps and tends to diminish the elastic wave velocity and therefore increases the critical time step. However, it also leads to an additional force peak at the beginning of the simulation due to the high inertia of the grains that are suddenly moved by the upper plate. Using $\rho_{ice} = 10^4$ kg m^{-3} does not lead to a stress-strain curve significantly different from the ones computed with a realistic value of ice density

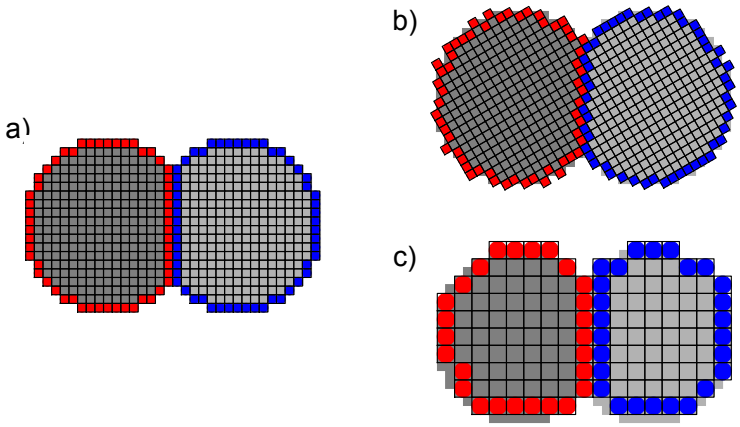

Figure 6.9: Example of the mesh of the same two grains but with a different orientation of the voxel grid (b) (turned by angle of 30°) or a different effective resolution (diameter of spheres) (c).

$\rho_{ice} = 917$ kg m^{-3}.

Figures 6.8b and 6.8c show the sensitivity of the modeled stress-strain curve to the time step dt and damping coefficient λ_a. The stress fluctuations depend on dt and λ_a but the mean behavior is not sensitive to λ_a and to dt, as long as $dt \lesssim dt_c = 10^{-6}$ s (dt_c calculated with $r = 25$ μm, $\rho_{ice} = 10^4$ kg m^{-3} and $E = 10$ MPa) . For the rest of the study we chose a relatively large time step $dt = 5 \times 10^{-7}$ s and $\lambda_a = 0.2$.

6.3.2.2 Microstructure representation

The total number of grains is not absolute but relative to the chosen grain segmentation parameters κ_t and c_t. The grains identified in the snow microstructure are described in discrete elements with spherical members 6.9a. This description depends on the effective resolution of the image (reduced compared to the initial resolution of the 3D image), which defines the diameter of the spheres (Figure 6.9c), and on the orientation of the voxel grid (Figure 6.9b).

Figures 6.10a shows the stress-strain curves obtained for different sphere sizes obtained by reducing the resolution of the 3D grain image. The mesh with the smallest spheres ($r = 15$ μm) shows the lowest mean resistance to strain during the brittle/frictional regime. This dependence is expected. Indeed, this mesh presents the largest number of spheres which can reproduce more finely the stress distribution, including the highest stress values. The maximum cohesion force is therefore reached at some sphere-sphere contacts for a smaller overall stress compared to the one observed for a rough mesh. When these sphere-sphere contacts break, the neighboring sphere-sphere cohesive contacts carry an additional load and then fail themselves, leading to the failure of the intergranular bond. For sphere radii in the range [25, 50] μm, the models mechanical behavior is very similar.

To evaluate the sensitivity of the mesh to the orientation of the voxel grid, the initial 3D image was rotated by a certain angle in the xy plane. As shown on Figure

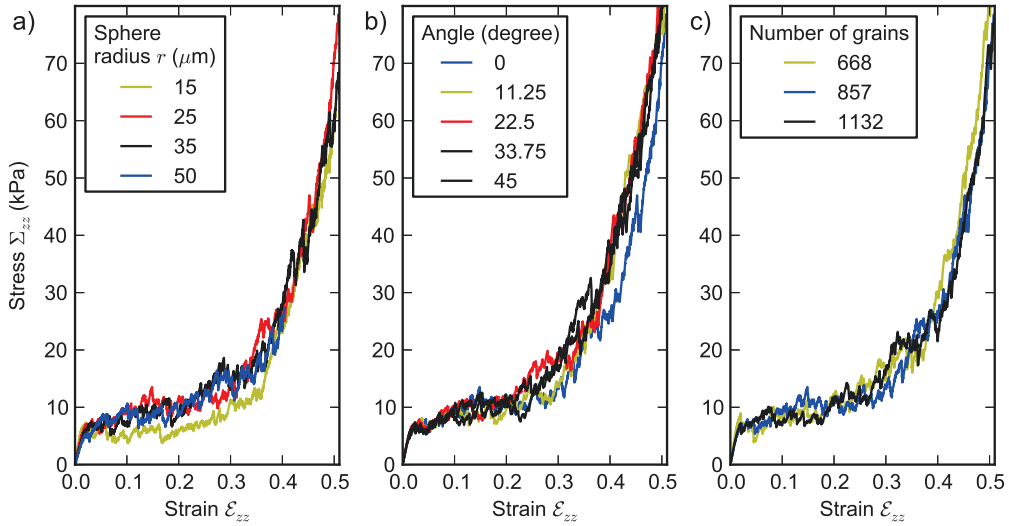

Figure 6.10: Stress-strain curve simulated by the model for different sphere sizes (a), initial grid orientation (b) and number of grains (c). In Figure b, the angle represents the rotation of the initial image in the xy plane. In Figure c, the grain images with 668, 857 and 1132 were obtained with the segmentation parameter (κ_t, c_t) set to $(1.3, 0.16)$, $(1.0, 0.25)$ and $(0.7, 0.5)$, respectively.

6.10b, the mean mechanical behavior is not very sensitive to the grid orientation. In the dense compaction regime ($0.4 < \mathcal{E}_{zz}$), the stress computed with the unrotated image (angle $= 0$) is systematically lower than the one computed with the rotated images. This difference may be explained by the fact that the edges of the grains located on the sides of the sample are "cut" and thus present horizontal and vertical surfaces. This creates an anisotropic distribution of the grain surface orientation with preferentially vertical and horizontal surface normals. The meshing of the horizontal and vertical surfaces is the smoothest (lowest apparent roughness) if the voxel grid is aligned with theses surfaces. Therefore, the roughness of the sample is slightly lower for the meshing with a zero-angle, which results in a lower overall stress.

The same image of RG was segmented into more or less grains with three different sets of segmentation parameters κ_t and c_t. As shown on Figure 6.10c, the modeled mechanical behavior is not very sensitive to the number of grains in the range [668, 1132]. It is required that the chosen decomposition into grains is sufficiently fine to describe correctly the mechanical behavior of snow and does not significantly constrain the degrees of freedom of the microstructure.

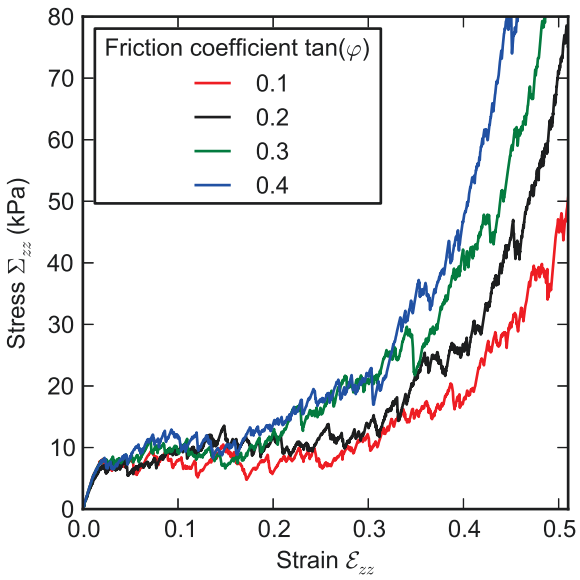

Figure 6.11: Stress-strain curve simulated by the model for different microscopic friction coefficients.

6.3.2.3 Friction and cohesion at intergranular contacts

The numerical values of the friction coefficient $\tan\varphi$ and the cohesion strength σ_{ice} are discussed in this section.

Serway and Jewett [2007] reported a static coefficient of the ice-ice friction equal to 0.1. It is unclear how this value applies to the micro-mechanics of snow in the context of our modeling approach. Indeed, the chosen meshing technique modifies the effective friction between grains. However, the failure processes in real snow bonds in snow have not been systematically studied. In particular, there is no evidence of a perfectly plane surface of failure at bonds. The reported values only guide into a relevant range of values for $\tan\varphi$. Figure 6.11 shows the models stress-strain curve for different values of the friction coefficient. The value of $\tan(\varphi)$ has little effect on the computed mechanical behavior for macroscopic strains in the range [0,0.2]. This observation indicates that microscopic friction is not the dominant deformation mechanism in the first phase of the so-called brittle/frictional regime. In contrast, for larger strains, the stress increases significantly with the value of $\tan(\varphi)$.

Petrovic [2003] reported tensile strength of ice in the range [0.7, 3.1] MPa. A large scatter exists because of temperature, strain rate, crystal size, etc. As shown on Figure 6.12a, the model macroscopic behavior of snow depends strongly on the microscopic cohesion at the contacts. As expected, macroscopic stress Σ_{zz} increases with σ_{ice}. There is an almost linear relation between Σ_{zz} and σ_{ice}. In the case of pure tension without the creation of new contacts, the linear relation between the

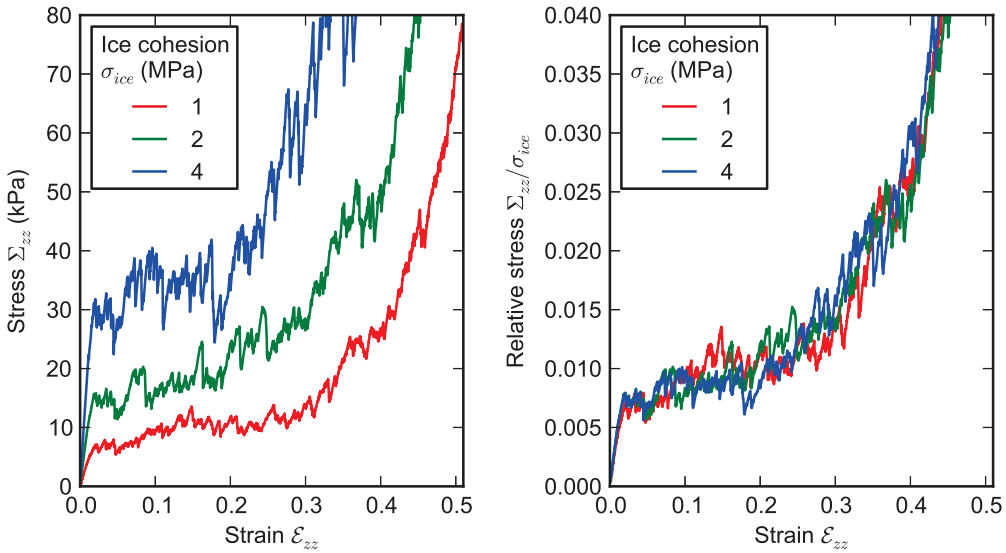

Figure 6.12: Stress-strain curve simulated by the model for different microscopic cohesion strengths.

microscopic and macroscopic strength is obvious. In the present case of compression, which involves the spatial re-arrangement of grains and creation of new contacts and friction, this linear relation was not necessarily expected a priori.

6.3.2.4 Representative elementary volume

The representative elementary volume (REV) is the smallest fraction of the sample volume over which the measurement or simulation of a given variable will yield a value representative of the whole. In this section, we investigated the REV related to the rapid confined compression of snow in order to assess the representativity of the simulations performed on volumes of about 5x5x5 mm^3. The macroscopic stress-strain relation was computed on snow volumes of increasing sizes for sample Ip04 and I23. In order to reduce the computing expense, the investigation of the REV size was limited to these two samples which span the tested range of snow density (Table 6.1). As shown on Figure 6.13, the modeled stress-strain relations converge with increasing volume. For volumes larger than 4x4x4 mm^3, the variations of stress-strain curve with the volume size are negligible compared to the variability of the model predictions due to the choice of the model parameters (see also Figures 6.8, 6.10 and 6.12). For smaller volumes, stress fluctuations due to the failure of single bonds are too large and it is not possible to define a homogeneous mechanical behavior. The sizes of the sample used in this study (see Table 6.1) are therefore large enough to be representative of the mechanical behavior of snow under compression. Note that the REV related to compression is much larger than the one related to density (1.5^3 mm^3, [Srivastava et al., 2010]) but is in good agreement

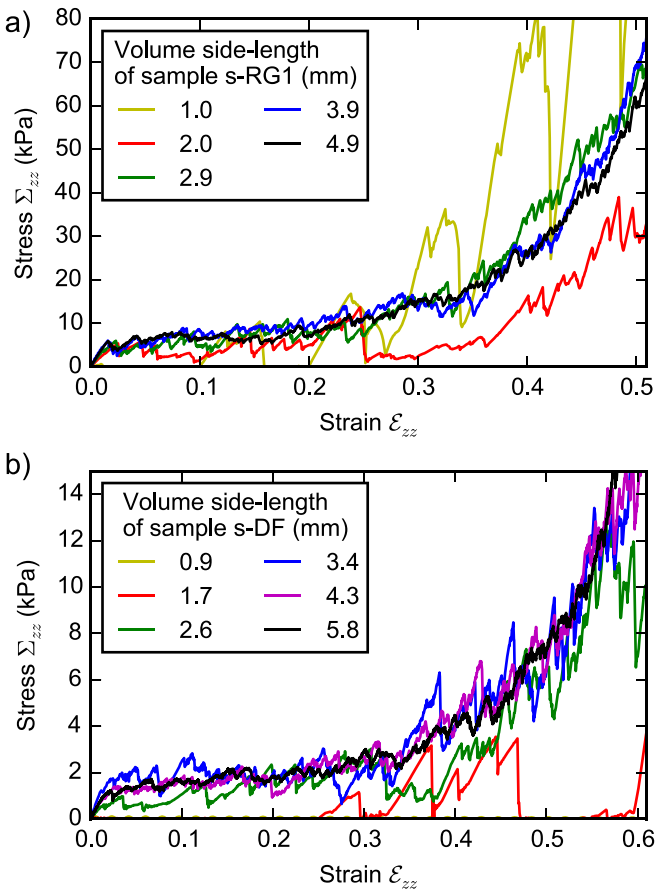

Figure 6.13: Stress-strain curve simulated by the model for different volume sizes on sample I23 (a) and sample Ip04 (b).

to the one related to a geometrical parameter characterizing the microstructural bonding system ($3^3 - 6^3$ mm^3, [Hagenmuller et al., 2014a]).

6.3.3 Application of the model to different snow microstructures

The discrete element model was applied to different snow samples spanning different snow types (see Table 6.1). The same model parameters, which are described in table 6.2, were used for all images. The size of the sample is indicated in Table 6.1. The only parameter differing between the samples is the size of the spheres (or effective resolution of the 3D image) in the mesh. Samples 4, 2A, 9 and I23 are characterized by a similar equivalent spherical radius r_{eq}, defined as $3V/S$ with V the volume of ice and S the area of the ice-air interface (Table 6.2). The equivalent spherical radius roughly characterizes the mean thickness of the ice matrix. The sensitivity analysis on sample I23 showed that the representation of the ice matrix with spheres of radius 25 μm, corresponding in practice to a reduction of the 3D image resolution by a

factor of 5, is satisfactory. This sphere radius was thus used for samples 4, 2A, 9 and I23. Samples Ip04, I08 and I15 present a finer ice matrix characterized by a smaller equivalent spherical radius (Table 6.2). These samples were thus decomposed in spheres with a smaller diameter of about 40 μm, corresponding to a reduction of the 3D image resolution by a factor of 4.

Figure 6.14a shows the modeled stress-strain curves for all samples. As already observed on sample I23 (Section 6.3.1.1), three regimes can be distinguished in all cases: elastic regime, brittle/frictional regime and dense compaction regime. The stress fluctuations due to individual bond breaking are limited compared to the mean stress-strain relationship, indicating that the size of the snow volume used for the simulation is large enough. After the elastic regime, first bonds start to break for a macroscopic stress Σ_{zz} between 1 kPa and 12 kPa, depending on the snow sample. Sample 2A exhibits hardening with an effective hardening modulus of 90 kPa. In contrast, samples Ip04, I08, 4, 9 and I15 present a plastic stress-strain curves with almost no hardening, up to strains of 0.3. These samples undergo very large deformations ($\mathcal{E}_{zz}$ in $[0, 0.4]$) with an almost constant stress. This apparent plastic behavior is caused by the geometrical re-arrangement of grains made possible by bond breakage and grain sliding. For sample I23, the strain interval without hardening is smaller $\mathcal{E}_{zz}$ in $[0, 0.3]$. After this almost perfect-plastic behavior, stress increases exponentially with strain. This point occurs when the grain packing has reached a certain compacity and cannot anymore accommodate the imposed displacement with little resistance. Note that the results obtained for samples Ip04 and I08, which both correspond to Decomposed and Fragmented snow with a density of 145 kg m^{-3} are consistent.

The tested samples characterized by different densities and snow types, show a large panel of stress-strain curves (Figure 6.14a). However, if plotted as stress-density relations, the same data appear to collapse onto a single trend with little variability (Figure 6.14b). This remarkable result shows that the resistance of snow to compression is mainly a function of density, even the tested microstructures span very different snow types.

However, some variability between the samples cannot be explained by density, especially during the brittle/frictional regime. For the same effective density and low compaction (density $<$ 300 kg m^{-3}), samples 4 and 9 composed of faceted crystals present a systematic lower resistance than samples Ip04, I08 and I15 composed of decomposed and fragmented snow or rounded grains. Sample I23, which results from the isothermal metamorphism of precipitation particles, is the sample with the highest resistance to compression in the range of density between 250 and 300 kg m^{-3}. Hence, the model predictions are consistent with the commonly accepted idea that snow types resulting from temperature-gradient metamorphism are less resistant to a mechanical load than snow types resulting from isothermal metamorphism. However, sample 2A composed of faceted crystals of initial density of 320 kg m^{-3} does not show a stress-density relation deviating from the general trend. It appears to be significantly more resistant than sample I23 of rounded grains with an initial density of 242 kg m^{-3}. Therefore, the characterization of the microstructure with a

snow type appears to be of "second order" compared to the importance of density.

When density reaches 300 kg m^{-3}, no significant trend between the different snow types can be recognized. The shape and size of the grains in the initial microstructure do not appear to be determinant during the high compaction of the sample. The microstructure is broken in grains so that the assembly of the individual grains reaches a certain compacity under certain load, independently of the initial microstructure.

6.4 Conclusion

We developed a new tool which enables to model the mechanical behavior of snow under large and rapid deformations with the full 3D microstructure as input. The geometry of the microstructure is directly translated into discrete elements by accounting for the shape of the grains and the initial bonding system of the ice matrix. The grains are rigid and the overall deformation is due to the geometric re-arrangement of grains made possible by bond failure. The sensitivity analysis of the model to its parameters and modeling assumptions showed that the effects of the microstructure geometry can be observed and are not shadowed by numerical artefacts.

In this study, the model was used to reproduce the mechanical behavior of snow under confined compression. The representative volume related to this type of loading conditions was estimated to be $4^3 - 5^3$ mm^3. For this type of loading conditions, it appears that the mechanical behavior of snow is mostly controlled by density. The stress-density relationships follow a single trend with little variability, even if the tested microstructures span very different snow types. Nevertheless, second order effects of the microstructure are observed during the first breaking of bonds. In particular, for a given density, snow samples resulting from temperature gradient metamorphism appear to be less resistant to compression than the one resulting from isothermal metamorphism. The model appears thus capable of accounting for the role of the microstructure on the mechanical properties. During the high compaction regime, the model did not reveal any clear influence of the shape and size of the grains.

To finish it is interesting to discuss the first-order role played by density in our results. As explained in introduction, density is often described as an insufficient mechanical indicator because of the large scatter observed in property-density plots [e.g. Mellor, 1975]. In contrast, density appears in this study to be a very good indicator of the resistance of snow under compression, with a little scatter attributed by the snow type. In other microstructure-based analysis of the mechanical and physical properties, the same strong dependence to density is also observed [e.g. Calonne et al., 2011, Hagenmuller et al., 2014c, Kochle and Schneebeli, 2014]. The main difference between the microstructure-based simulations and direct measurements is the size of the tested volume. Hence we argue that spatial variability of density in large samples used for measurements might be a reason for the scatter observed in property-density plots, especially for properties which do not depend linearly on

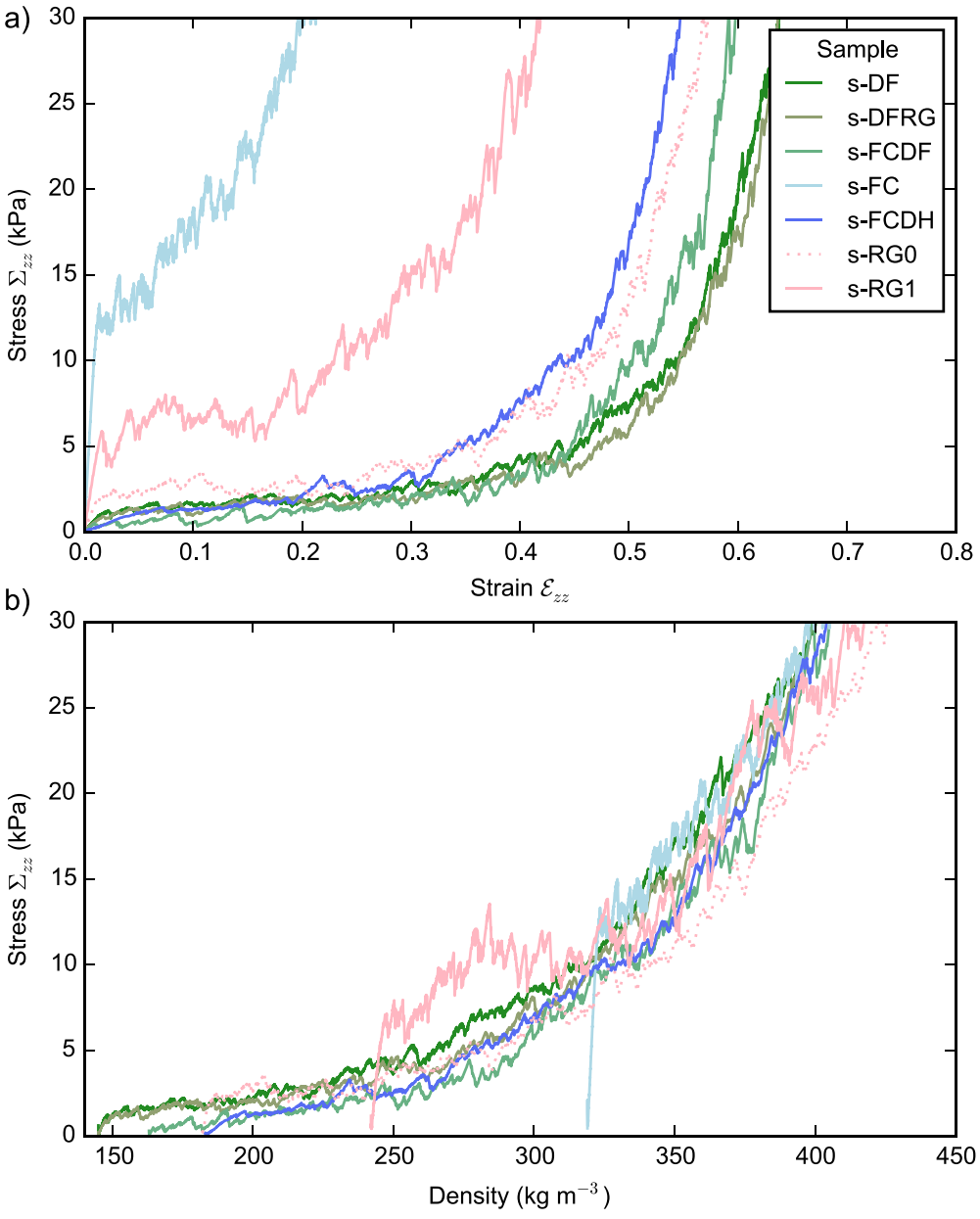

Figure 6.14: Modeled stress-strain relation (a) and stress-density relation (b) for different snow samples.

density. Besides, the dominant role of density of the observed mechanical behavior is relative to the given loading conditions. Shapiro et al. [1997] explained the apparent relationship between stress and density by the fact that both the mechanical properties and the density depend on the nature of the bonding/grain contacts, in this compression regime. The model appears thus capable of reproducing this feature and we expect the dependence to density to be lower in the case of different loading conditions, such as shear.

To further investigate the influence of microstructure on mechanical properties, the DEM model could be straightforwardly applied to other loading conditions. In particular, shear loading can be interesting in the context of slope stability and avalanche release. Besides, to better interpret the force/signal of snow indenter, such as the snow micro-penetrometer, simulations reproducing the penetration of an indenter in the snow microstructure can be performed. Lastly, mechanical experiments directly conducted in the μCT might be necessary to evaluate the model [Schleef et al., 2014]. However, since it is very difficult to follow rapid deformations of snow with a time consuming imaging procedure, measurements of mechanical properties of a snow sample after its microstructure was captured by μCT [Hagenmuller et al., 2014c] might be more realistic, as a first step.

Chapter 7

Characterization of the snow microstructural bonding system through the minimum cut density

Abstract Snow density is commonly used to phenomenologically parameterize other snow properties such as strength or thermal conductivity. However, density is insufficient to fully characterize the variety of microstructures, as revealed by the existing scatter in the parameterizations. This can be explained by the role of bonds which are almost as important as grains to describe the macroscopic properties of snow. A quantification of the narrow constrictions or bonds between snow grains is thus essential to accurately parameterize snow properties. In order to characterize the reduced thickness of the ice matrix at bonds, we introduce a new microstructural indicator, *the minimum cut density*, ρ_{mc}. This variable quantifies, on three-dimensional (3D) microtomographic images of snow, the minimal effective density of a surface that disconnects two opposite faces of the sample. The obtained minimum cut density values are surprisingly low, in the range $[0.2, 35]$ kg m^{-3} for the tested samples with density in the range $[100, 350]$ kg m^{-3}. This reveals the high variability and weak connectivity of the bonding system in snow. Structural anisotropy of faceted crystals and depth hoar is also well characterized by the minimum cut density. To evaluate the physical and mechanical relevance of this microstructural indicator, we estimate the thermal conductivity and the Young's modulus of the studied snow samples through microstructure-based simulations. An excellent correlation is found between the Young's modulus and the minimum cut density ($R^2 = 0.97$). In particular, the minimum cut density well accounts for the anisotropy of the Young's modulus in faceted snow types. The correlation of thermal conductivity and minimum cut density is also highly significant ($R^2 = 0.88$) but not better than the parameterization with density ($R^2 = 0.92$). We show that this difference is mainly due to the role played by thermal conduction of air.

Contents

7.1 Introduction

Snow properties, such as strength and thermal conductivity are critical for diverse applications like the forecasting of avalanche hazard [Schweizer et al., 2003] or the computation of the surface energy balance in snow-covered areas [Dadic et al., 2008]. The mechanical and physical properties of snow are tied to its microstructure, i.e. the three-dimensional (3D) configuration of ice and pores.

The snow density is commonly used as a microstructural indicator to parameterize snow properties. However, it is insufficient to fully characterize the snow microstructure, as shown by the important scatter of physical and mechanical properties corresponding to a given density, revealed for strength and Young's modulus by Mellor [1975], for thermal conductivity by Sturm et al. [1997], for permeability by Arakawa et al. [2009], etc. Therefore, it is necessary to better characterize the microstructure along with determining the density in order to derive indicators of the mechanical and physical properties of snow [Shapiro et al., 1997].

In the last decade, the specific surface area (SSA) has gained significant interest for the modeling of the physical and chemical properties of snow because it is an indicator of potential exchanges with the surrounding environment. For instance, SSA can be used to quantify the adsorption of chemical species [Albert et al., 2002] or light scattering and absorption [Warren, 1982]. However, certain properties, such as strength and thermal conductivity, are not controlled by SSA but are mainly sensitive to the narrow constrictions between grains, also called bonds [Colbeck, 1997]. In these bonds, stresses and heat fluxes are larger than in the other parts of the snow structure because the constriction between snow grains reduces the potential paths inside the ice matrix. Therefore, the bonding seems to be determinant to formulate an accurate parameterization of snow properties controlled by fluxes internal to the ice matrix [Colbeck, 1997].

In this paper, we want to geometrically characterize the microstructural bonding system of snow in order to provide a parameterization of snow properties that are mainly controlled by fluxes occurring inside the ice matrix. Different attempts of such a characterization can be found in the literature. They can be divided into two main groups:

1. *Characterizations based on a grain definition.* Most of the characterizations of the bonding system rely on the definition of a grain [e.g. Flin et al., 2011, Gubler, 1978, Kry, 1975a, Shertzer and Adams, 2011]. Kry [1975a] defined a grain bond geometrically "as the plane surface of minimum area situated in the neck region of two linked grains". In practice the identification of a neck is relative to a certain threshold of constriction. On two-dimensional (2D) images of snow, Kry [1975a] and Shertzer and Adams [2011] considered that a neck exists if the relative decrease of the hydraulic radius is of, at least, 30% in the neck region. On three-dimensional (3D) images of snow, Flin et al. [2011], Theile and Schneebeli [2011], Wang et al. [2012] and Hagenmuller et al. [2014b] used a threshold on curvature at the necks or on the contiguity of the grains. The main difficulty of these grain segmentation methods is to choose the right thresholds. This choice depends on the algorithm used but also on the type of snow and the property of interest. Once the snow microstructure is segmented into grains, the geometry of the grain assembly can be characterized with structural variables such as the mean grain size, the coordination number, the specific grain contact area, etc. However, the values of these variables are generally sensitive to the grain segmentation procedure. For instance, Kry [1975b] tried to link the specific grain contact area to the elastic modulus of a snow sample subjected to uniaxial compression. He pointed out that the grain definition is partly subjective and observed variations up to 40% in the number of bonds depending on whether the "non-obvious" bonds are taken into account or not [Kry, 1975a]. Moreover, he concluded that the specific contact area partially explains the stiffness of the ice matrix, because only a small fraction of the grain bonds support the load. More recently, Shertzer and Adams [2011] observed bonds on 2D slices of microtomographic (μCT) images of snow evolving with temperature gradient metamorphism and used the identified bond surfaces to compute the fabric tensor of the bonding system. Through this fabric tensor, these authors proposed an analytical conduction model that accounts for 43% of the observed increase in the heat transfer coefficient (EHC). However, the order of magnitude of the modeled EHC was relative to an arbitrary chosen bond radius, that was not derived from the grains obtained by the segmentation procedure. Generally, the interpretation of variables derived from the grain representation is challenging because grains are not absolute entities but are relative to the segmentation thresholds. The concept of grain is defined according to certain geometrical criteria and thus depends on both algorithm and microstructure [Hagenmuller et al., 2014b, 2013a].

2. *Characterizations based on correlation lengths.* The second approach used to characterize the geometry of the microstructure is based on correlation lengths, which quantify the 3D mean size of the material heterogeneity. Srivastava et al. [2010] used the mean interception length (MIL) fabric tensor along with density to explain the anisotropic stiffening of the snow microstructure with

temperature gradient metamorphism. More recently, Löwe et al. [2013] applied the rigorous formalism of second order bounds [Torquato and Sen, 1990] to snow and improved the parameterization of thermal conductivity by including a microstructural indicator of anisotropy Q. The computed lower bound for thermal conductivity is far lower than the values of thermal conductivity estimated through 3D microstructure-based simulations, but the computed bound appears to be highly correlated ($R^2 = 0.96$) to the estimated conductivity, especially in the direction of the thermal gradient for faceted snow types [Löwe et al., 2013]. However, the parameterization by Q shows greater scatter in the plane orthogonal to the temperature gradient. Löwe et al. [2013] attributed this scatter to the connectivity of the ice matrix which is "apparently more complex" in the plane orthogonal to the temperature gradient than along the direction of the temperature gradient. In general, the characterizations based on correlation lengths are well suited to quantify the microstructural anisotropy of pores and grains [Calonne et al., 2014] but, by definition, are unable to take into account the bonding for low connected snow types, since in this case the bonds represent a very small part of the entire snow image.

According to this brief review and in order to parameterize snow properties that are mainly controlled by fluxes occurring inside the ice matrix, we propose a microstructural indicator which:

1. takes into account the structural anisotropy of the ice matrix [Calonne et al., 2014, Löwe et al., 2013, Shertzer and Adams, 2011, Srivastava et al., 2010],

2. takes into account the fact that only a subset of the constrictions located in the ice matrix are determinant for the macroscopic behavior of the snow sample [Ballard and Feldt, 1965, Kry, 1975b].

3. is independent from a grain segmentation process but retains the concept of a bond as a "flow limiting valve" [Colbeck, 1997].

We developed an algorithm that computes the minimal connection surface between two parts of a snow sample imaged in 3D by μCT. We call this surface, the minimum cut surface. In the following, the two parts correspond to two opposite faces of a cube of snow. Thus, the minimum cut surface is the surface of minimal area among all the surfaces which disconnect two opposite faces of the snow sample (Figure 7.1). In other words, cutting the sample on this surface separates its two opposite faces while yielding the smallest amount of broken ice. The minimum cut density ρ_{mc} is defined as the effective density of the minimum cut surface (see section 7.3.1 for detailed definition and computation). This concept is directional since a value of ρ_{mc} can be computed in each direction normal to the sample faces (x, y, z) and is thus suited to quantify the anisotropy of the microstructure. Moreover, the minimum cut surface is composed of only a small fraction of the bonds, the ones that are expected to be the most significant for thermal and mechanical properties. Indeed, as shown in Figure 7.1, heat fluxes and elastic stresses are expected to be

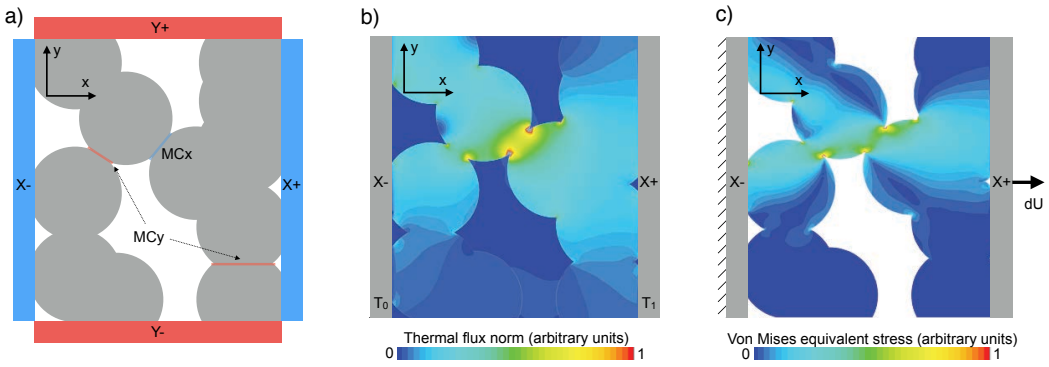

Figure 7.1: Minimum cut (a), thermal flux (b) and elastic stress (c) computed on a 2D schematic structure. (a) The minimum cut surface (MC) was computed between faces X-/X+ and Y-/Y+. The minimum cut surface between faces X-/X+ is constituted of one bond only (in blue), while the minimum cut surface between faces Y-/Y+ is the union of disjoint surfaces (in red). (b) Temperatures T_0 and $T_1 > T_0$ were imposed on faces X- and X+, respectively. Isotropic conduction properties were assumed for ice (conductivity $k_{ice} = 2.107$ W m^{-1} K^{-1}) and air (conductivity $k_{air} = 0.024$ W m^{-1} K^{-1}). (c) Displacement was blocked on face X- and an imposed displacement dU along x direction was imposed. Ice was assumed to be isotropic linear elastic with a Young's modulus of 9.5 GPa and a Poisson's ratio of 0.3.

the highest on the minimum cut surface. A small value of ρ_{mc} is thus expected to limit the overall potential thermal conductivity or to enhance the elasticity compliance. Lastly, computing the minimum cut density does not require the definition of a grain, this concept being independent from a grain segmentation procedure. Actually, the concept of minimum cut density was first theoretically introduced by Ballard and McGaw [1965] who defined the "effective porosity on the failure surface". Ballard and McGaw [1965] and Ballard and Feldt [1965] used this concept to reproduce the snow tensile strength assuming that the stress is homogeneous and maximal on the minimum cut surface. However, in the 1960's, no technique was available to efficiently measure this property.

In this paper, we compute the minimum cut density on a set of 3D images of snow obtained by microtomography. Then, as a proof of its physical and mechanical relevance, we relate ρ_{mc} to thermal conductivity and elasticity properties derived from numerical simulations based on the same microtomographic images [Calonne et al., 2011, Hagenmuller et al., 2014c].

7.2 Snow images

Numerical computations were performed on 12 microtomographic images of snow obtained from previous field sampling and controlled cold-room experiments. Detailed description of each image is provided in Table 1. The chosen images span most types of seasonal snow, i.e. precipitation particles (PP), decomposing and fragmented precipitation particles (DF), rounded grains (RG), faceted crystals (FC), depth hoar (DH) and melt forms (MF), according to the International Classification for Seasonal Snow on the Ground (ICSSG) [Fierz et al., 2009].

Samples I01, I03, I04 and I23 correspond to a time series taken during an isothermal experiment [Flin et al., 2004]. The series 2A, 5G, 7G was obtained during a temperature gradient experiment, as described in Calonne et al. [2011]. The temperature gradient was imposed along the vertical direction, i.e. the direction of gravity, here denoted z. The horizontal directions are denoted x and y. The samples Ip04 and Ip07 were collected in the field at Girose glacier (Ecrins, French Alps) [Flin et al., 2011]. The samples 4, 9 and F were collected at Col de Porte (Chartreuse, French Alps).

These samples were scanned with a X-ray microtomograph at a resolution between 4.91 μm and 10 μm. Then, the grayscale images were binary segmented with the method described by Hagenmuller et al. [2013b], ensuring that all noise artifacts were smoothed out. Eventually, the resolution was reduced by a factor of 2 and cubic sub-images of side-length ranging from 5 mm to 10 mm were extracted from the entire image.

Name	Type	Voxel size (μm)	Side length (mm)	Density (kg m^{-3})	SSA (m^2 kg^{-1})
I01	PP	9.82	4.9	95.7	59.3
I03	PP	9.82	4.9	120.4	42.5
I04	PP	9.82	4.9	109.6	43.1
Ip04	DF	17.18	8.6	145.5	25.4
Ip07	RG	17.22	8.6	261.5	18.1
I23	RG	9.82	4.9	242.1	17.2
2A	FC	16.75	8.4	311.4	18.1
5G	DH	19.31	9.6	310.6	13.4
7G	DH	19.34	9.6	320.2	12.3
F	MF/FC	19.24	9.6	303.6	5.8
4	FC/DF	19.29	9.6	153.8	17.5
9	FC/DH	19.32	9.6	179.5	18.2

Table 7.1: Description of the microtomographic images used in this study. All images were cubic, so only the side-length of the image is indicated.

7.3 Methods

7.3.1 Minimum cut density

In this section, we describe the algorithm used to calculate the minimum cut density on binary images of the snow microstructure.

To the best of our knowledge, Tabor [2007] made the first attempt to estimate the minimum cut surface on 3D images of material microstructures (trabecular bone). His algorithm is based on the skeletonization of the microstructure into a network, which is then segmented by spectral partitioning. The skeletonization procedure used is relevant for structures similar to a network of fibers, as bones. It is however not applicable, in general, to snow microstructures. We use an alternative and more efficient approach which calculates the exact minimum cut surface in a metric that approximates the euclidean metric. The main idea is that any surface that cuts the snow structure can be interpreted as a cut in a certain graph.

Let us define the graph $\mathcal{G}$ by a set of nodes corresponding to each ice voxel of the 3D image, and a set of edges that connect these nodes (Figure 7.2). We add two special nodes to the set of voxel nodes: the source s and the sink t, called terminal nodes. Each edge (p, q) between nodes p and q has a non negative weight ω_{pq}. A cut C between the source and the sink is a partitioning of the nodes into two disjoint subsets $\mathcal{S}$ and $\mathcal{T}$ such that $\mathcal{S}$ contains s and $\mathcal{T}$ contains t. The cost of a cut C, denoted $\mathcal{L}_{\mathcal{G}}(C)$, is the sum of the weights ω_{pq} of edges (p, q) where $p \in \mathcal{S}$ and $q \in \mathcal{T}$. The cut C directly defines a 3D surface of separation in the microstructure image (Figure 7.2). The edges weights ω_{pq} are chosen so that the minimal weight $\mathcal{L}^{min}_{\mathcal{G}}(C)$ of a cut in the graph is the minimum cut area of the 3D

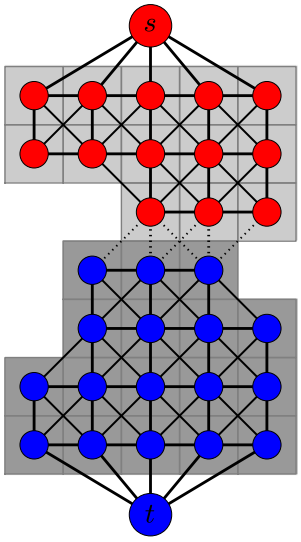

Figure 7.2: Graph cut approach to compute the minimum cut surface on binary images. Each voxel (or pixel in this 2D example) (dark and light gray squares) is associated to a node (small blue and red circles) in a graph. Each node is linked to its neighbors with edges so that the weight of a cut in the graph approximates the euclidean area of the associated surface. The nodes located at the bottom and top faces of the sample are linked to two extra nodes, the source s and the sink t. Eventually, the minimum cut between s and t in the graph is computed and the graph is partitioned into two parts (the red nodes and the blue nodes).

image [Boykov and Kolmogorov, 2003]. For that purpose, first, the voxels located on the two opposite faces of the samples are linked to the source and the sink with edges of infinite weight (Figure 7.2). This ensures that the cut between the source and the sink separates the two opposite faces of the sample. Second, the edge weights between the voxel nodes are defined so that $\mathcal{L}_{\mathcal{G}}(C)$ corresponds to the surface area of the corresponding 3D surface. Boykov and Kolmogorov [2003] first formalized the link between graph cut and length calculation using the Cauchy-Crofton formula which relates, in 2D, the euclidean length of a curve to the number of intersects with all straight lines in the plane. This formula can be generalized in 3D and discretized to provide an approximate surface measurement of 3D objects. For instance, in Figure 7.2, only four types of lines are considered: vertical, horizontal, first diagonal and second diagonal lines. In practice, we used the discrete formulation proposed by Danek and Matula [2011a] with 13 line directions on 3D images. With this method, the maximal deviation from the real surface area is about 10%. Details of the method can be found in Boykov and Kolmogorov [2003], Hagenmuller et al. [2013b].

Finding the minimal cut in the graph and, therefore the minimum cut surface, can then be solved by finding a maximum flow from the source to the sink, which is a problem solvable in polynomial time [Ford and Fulkerson, 1956]. The maximum flow between s and t can be imagined as the maximum flood of water that goes through the graph using the edges as pipes with a limited capacity (the weights). Finding the maximum flow of water is equivalent to finding the "limiting pipes". We performed the graph cut segmentation with the scalable graph-cut algorithm developed by Delong and Boykov [2008] which uses the grid structure of the graph to optimize the memory usage (freely available for research purposes on http://vision.csd.uwo.ca/code/). It enables the segmentation of massive grids up to 600^3 voxels-nodes on a personal computer (16 GB RAM).

The area of the minimum cut surface is an extensive variable which depends on the volume size. Therefore, we use the intensive variable $\rho_{mc,\alpha}$, the minimum cut density, as the effective density associated to the minimum cut surface in the α-direction ($\alpha = x, y, z$), i.e. as $\rho_{mc,\alpha} = \rho_{ice} S_\alpha / l^2$ where S_α is the area of the minimum cut surface computed in the α-direction, l the side-length of the cubic sample and ρ_{ice} is the density of ice. We refer to $\rho_{mc,z}$ as the vertical component and to $\rho_{mc,xy}$ as the average of the horizontal components. We refer to ρ_s as the traditional density of snow calculated by voxel counting. Note that a random plane cut orthogonal to the cut direction α presents, on average, an effective density equal to ρ_s.

7.3.2 Thermal and elastic properties

In order to evaluate the relevance of the parameterization of snow properties with the minimum cut density, we employ simulations based on tomographic images. We compute the effective thermal conductivity and the effective elastic modulus of snow.

7.3.2.1 Thermal conductivity

The effective thermal conductivity tensor $\mathbf{k_T}$ was estimated from 3D images of snow with the commercial software Geodict. Details of the method can be found in Calonne et al. [2011]. Only conduction in ice and air was considered, neglecting other heat transfer processes such as convection and phase change. Conduction in ice and air was supposed to be homogeneous and isotropic with the thermal properties of ice and air at 271 K (conductivity of air $k_{air} = 0.024$ W m^{-1} K^{-1} and conductivity of ice $k_{ice} = 2.107$ W m^{-1} K^{-1}). To investigate the relative importance of the heat flux in pores, computations were also carried out by neglecting air conduction, i.e. $k_{air} = 0$. We denote k_x, k_y and k_z the diagonal terms of the conductivity tensor $\mathbf{k_T}$ computed in the x-, y- and z-directions, respectively. In this study, we focus on k_z, i.e. the vertical component, and the average of the two horizontal components $k_{xy} = (k_x + k_y)/2$.

7.3.2.2 Elastic modulus

The effective elastic modulus E was estimated from the 3D images of snow with the commercial code Ansys. Ice was assumed to be isotropic and linear elastic with a Young's modulus of 9.5 GPa and a Poison's ratio of 0.3. The microstructure was meshed into quadratic tetrahedrons (SOLID92) of typical size on the order of a few voxels, to correctly model the structure geometry and the stress distribution. Simulations under uniaxial tension were performed for each cartesian direction (x, y, z). One side of the sample was fixed and a uniform displacement dU was imposed to the opposite side (example in Figure 7.1c). The apparent Young's modulus E_α in the α-direction, for the specimen as a whole, was calculated from the formula $E_\alpha = \Sigma_{\alpha\alpha}/\mathcal{E}_{\alpha\alpha}$, where $\Sigma_{\alpha\alpha}$ is the apparent stress and $\mathcal{E}_{\alpha\alpha}$ the apparent strain in the α-direction. The apparent stress and apparent strain were calculated from $\Sigma_{\alpha\alpha} = F_\alpha/l^2$ and $\mathcal{E}_{\alpha\alpha} = dU/l$, where F_α is the total reaction force at the face where the displacement dU was prescribed, and l the sample side-length. We refer to E_{xy} as the average of the two horizontal Young's moduli. Details of the method can be found in Hagenmuller et al. [2014c]. Note that the boundary conditions used for the calculation of the Young's modulus are similar to the one prescribed in the study of Schneebeli [2004] and Chandel et al. [2014]. However, different boundary conditions could lead to different Young's moduli since the size of the simulated snow volume is expected to be close to the size of the mechanical representative elementary volume [Kanit et al., 2006].

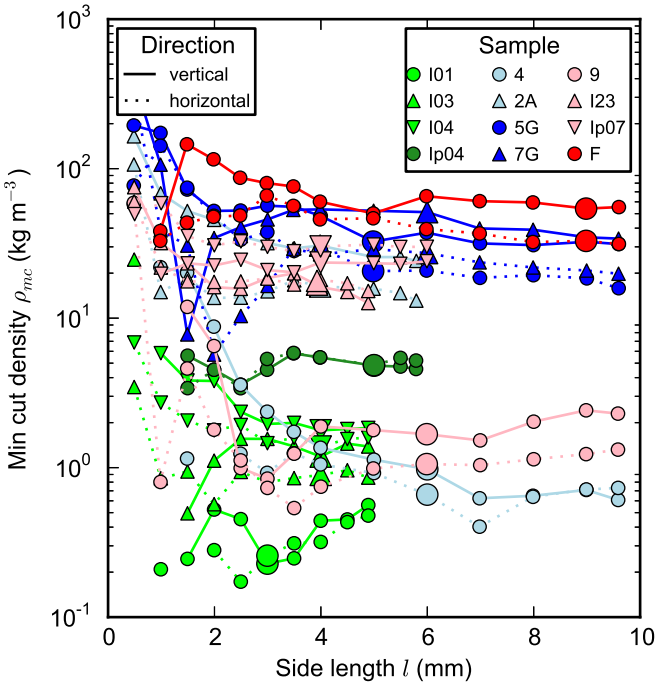

Figure 7.3: Representative elementary volume of the minimum cut density ρ_{mc}. The minimum cut density ρ_{mc} was computed on cubic concentric images of increasing side-length. Markers are colored according to the snow type and the ICSSG [Fierz et al., 2009]. The larger markers indicate the volumes used in the following for thermal and elastic simulations.

7.4 Results

7.4.1 Minimum cut density

7.4.1.1 Representative elementary volume

The representative elementary volume (REV) is the smallest fraction of the sample volume over which the measurement of a given variable will yield a value representative of the whole. It depends on the considered variable and the snow type. To investigate the existence and the size of the REV related to the minimum cut density, numerical computations were performed on snow volumes of increasing sizes. The volumes used were concentric and cubic with a side-length varying between 0.5 mm and the maximal image size provided by the tomograph.

The evolution of ρ_{mc} with the size of the volume used for calculations is shown in Figure 7.3. For all samples, ρ_{mc} is observed to progressively reach a convergence value when the side-length l of the volume increases. We consider that the REV size is reached when the relative variations of ρ_{mc} with the volume size l become neg-

ligible compared to differences observed between snow samples. Overall, the REV size increases when the convergence value of ρ_{mc} decreases, and can be estimated in the range [3^3 mm^3, 6^3 mm^3]. For sample I01(PP), characterized by a very low value of ρ_{mc}, the REV appears to be larger than the size of the sample scanned by tomography.

In the following, computations of the minimum cut density, thermal conductivity and elastic modulus were carried out on volumes of the size of the REV related to the minimum cut density (Figure 7.3). The representativity of the chosen volume sizes for thermal conductivity and elastic modulus was not evaluated in this study and is discussed in section 7.5.2. A good compromise between reasonable processing times and a sufficiently large volume was not found for sample I01. Hence, the minimum cut density computed on this sample might be not fully representative of the corresponding snow type, but the comparison of the computed thermal conductivity and Young's modulus versus ρ_{mc} is still possible, since these values characterize the exact same microstructure.

7.4.1.2 Geometrical characteristics of the snow bonding system

An example of a minimum cut surface on a sample of rounded grains is presented in Figure 7.4. The overall minimum cut surface is composed of a small number n_α of bonds.

The minimum cut density ρ_{mc} is shown for the complete set of snow images in Figure 7.5. The values of ρ_{mc} range between 0.2 and 35 kg m^{-3} for a density ρ_s between 100 and 350 kg m^{-3}. Hence, ρ_{mc}, which quantifies the density along the minimum cut surface, is significantly smaller (up to two orders of magnitude) than the density ρ_s calculated from voxel counting on the entire volume. We note that ρ_{mc} tends to increase with density ρ_s but with a large scatter. In particular, faceted crystals (sample 2A) and depth hoar (samples 5G, 7G) present values of $\rho_{mc,xy}$ similar to those observed for rounded grains (samples Ip07, I23) even if the density ρ_s of the latter samples is significantly smaller. On the samples obtained from temperature gradient metamorphism (samples F, 5G, 7G, 2A), $\rho_{mc,z}$ is larger than $\rho_{mc,xy}$, indicating an anisotropy of the bonding system. On the other samples, the anisotropy is less pronounced.

The mean contact area of each individual bond that constitutes the overall minimum cut surface is shown in Figure 7.6, as a function of the number of cut bonds per unit area (n_α/l^2). The number of cut bonds per unit area varies in the range $[0.2, 3]$ mm^{-2} and the mean contact area in the range $[2.10^{-4}, 10^{-1}]$ mm^2. The variability of the minimum cut density observed in Figure 7.5 is therefore mainly due to the variations of the mean contact area of the cut bonds. Except for sample I01 whose mean contact area is about the size of one voxel, the resolution used to image the samples is sufficient to correctly reproduce the bonds whose area is, at least, on the order of tenths of voxels.

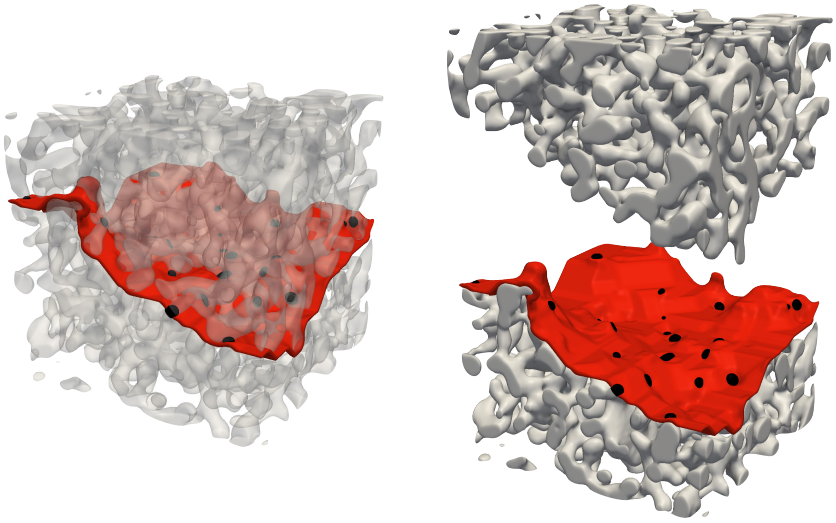

Figure 7.4: Example of a vertical minimal cut on a 3D sample of RG (sample I23). The side-length l of the volume is 3 mm. The minimum cut surface is the union of numerous disjoint small surfaces (black). The red surface joints these small surfaces in the air and shows that the minimum cut surface separates the sample in two parts. Note that only the area of the minimum cut surface in the ice is taken into account for the calculation of ρ_{mc}. In the right image, the two parts disconnected by the minimum cut surface were separated by a vertical translation to better visualize the minimum cut surface.

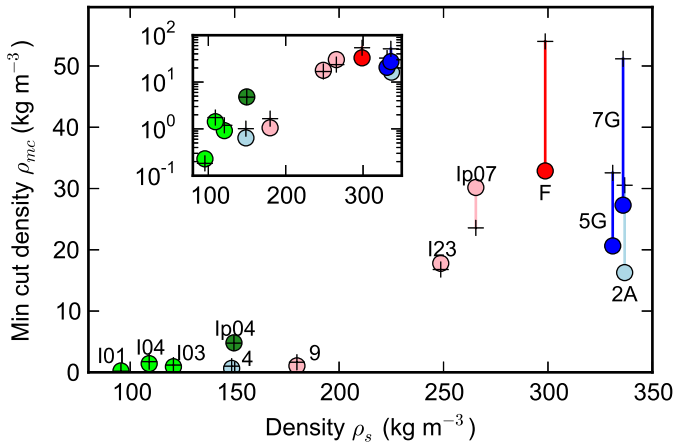

Figure 7.5: Minimum cut density ρ_{mc} as a function of the snow density ρ_s. The vertical component is denoted with ◯ and the horizontal component with +. Both components are linked with a segment to indicate that they characterize the same sample. Markers are colored according to the snow type [Fierz et al., 2009]. The same data are shown in a semilog plot in inset.

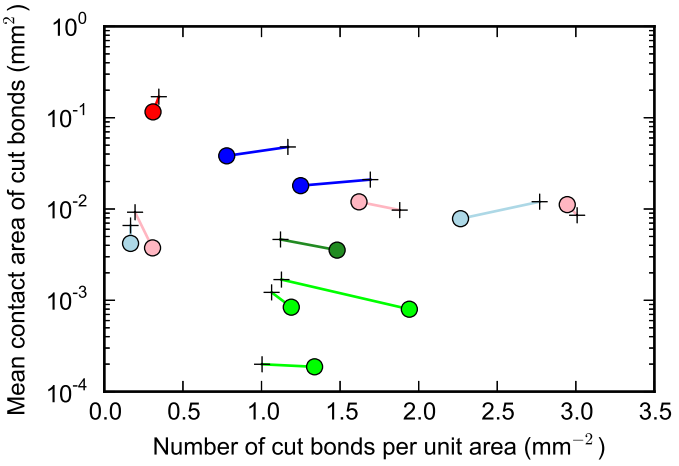

Figure 7.6: Mean contact area of the cut bonds as a function of the number of cut bonds per unit area (n_α/l^2). Same notations as in Figure 7.5.

7.4.2 Thermal conduction and elasticity

The thermal conductivity k is shown for the complete set of snow images in Figure 7.7a. This quantity ranges between 0.05 W m^{-1} K^{-1} and 0.30 W m^{-1} K^{-1}, depending on the snow sample. Figure 7.7a also illustrates that the heat flux through pores cannot be neglected, especially for low density snow where air contributes up to 80% of the overall heat conduction. The conductivity k increases almost linearly with density for the density range investigated. An anisotropy between vertical and horizontal conductivity is also observed, especially for the FC and DH samples. This anisotropy cannot be taken into account by density, which is, by definition an isotropic characterization of the microstructure. This results in an apparent scatter in the conductivity-density plot (Figure 7.7a).

The elastic modulus E is shown for the complete set of snow images in Figure 7.7b. The differences in snow type and density are emphasized by the Young's modulus values which range between 0.01 MPa and 400 MPa. However, the extremely low Young's modulus value ($E \sim 10$ kPa) obtained for sample I01 might not be fully representative of precipitation particles, because of volume size issues. The Young's modulus E tends to increase with density but with a large scatter. Faceted crystals (samples 2A, 4) and depth hoar (samples 5G, 7G) appear to be significantly stiffer vertically than horizontally.

7.4.3 Correlation with minimum cut density

As illustrated qualitatively in Figure 7.1, the minimum cut surface is expected to concentrate heat fluxes and elastic stresses and thus to be a good predictor of thermal conductivity and Young's modulus. This idea is evaluated in Figures 7.8a and 7.8b. Globally, the value of k and E is highly correlated to ρ_{mc}. Except for a sample of DF (sample Ip04), the anisotropy detected by ρ_{mc} shows good consistence with anisotropy observed for k and E. The microstructural indicator ρ_{mc} appears to account for the anisotropy observed for thermal conductivity and Young's modulus. Results of linear regressions between thermal conductivity, Young's modulus and, minimum cut density, density are indicated on Table 2. We find an excellent correlation between the Young' modulus and the minimum cut density ($R^2 = 0.97$). The correlation of thermal conductivity and minimum cut density is also highly significant but is not better than the parameterization with density ($R^2 = 0.92$).

7.5 Discussion and conclusion

7.5.1 Low connectivity of the ice matrix

In this paper, we propose to characterize the bonding system of the snow microstructure with the minimum cut density. The first notable result is the weak connectivity of the snow microstructure as revealed by the low values obtained for ρ_{mc} (Figure 7.5). The minimum cut density is at least one order of magnitude smaller than the snow density. This very low connectivity is not revealed by other indicators. For

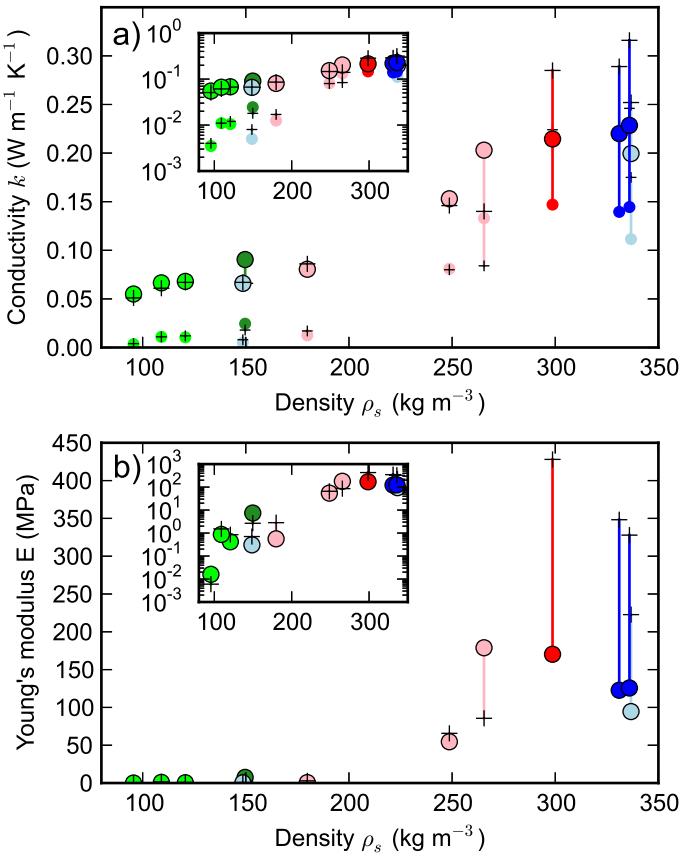

Figure 7.7: Thermal conductivity (a) and elastic modulus (b) as a function of snow density. The vertical component is denoted with ◯ and the horizontal component with +. Both components are linked with a segment to indicate that they characterize the same sample. Markers are colored according to the snow type [Fierz et al., 2009]. The same data are shown in semilog plot in inset. The thermal conductivity (a) was computed either with $k_{air} = 0.024$ W m^{-1} K^{-1} (large markers contoured in black) or with $k_{air} = 0$ (small markers without black contour).

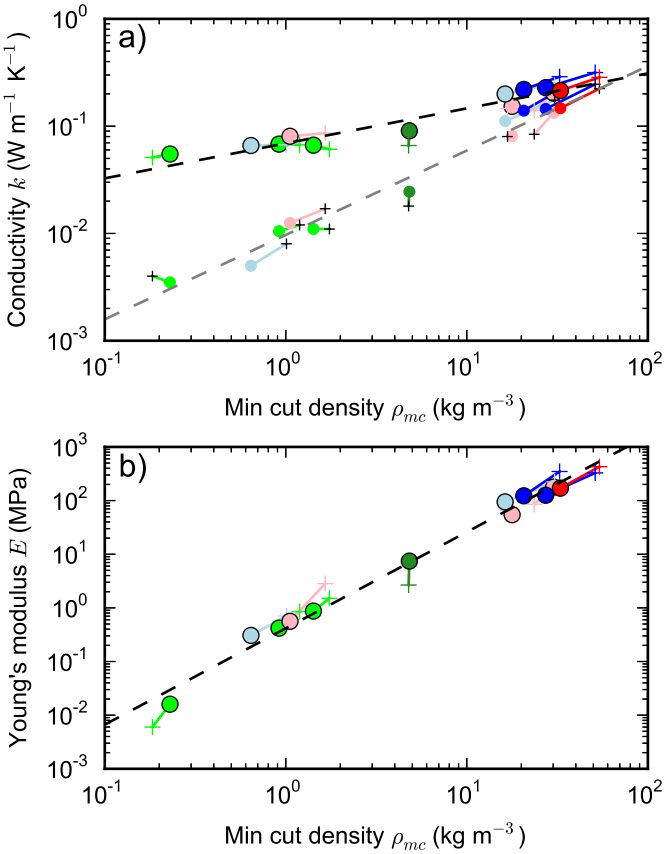

Figure 7.8: Thermal conductivity (a) and elastic modulus (b) as a function of the minimum cut density. The vertical component is denoted with ◯ and the horizontal component with +. Both components are linked with a segment to indicate that they characterize the same sample. Markers are colored according to the snow type [Fierz et al., 2009]. The thermal conductivity (a) was computed either with $k_{air} = 0.024$ W m^{-1} K^{-1} (large markers contoured in black) or with $k_{air} = 0$ (small markers without black contour). The dashed lines correspond to the linear regression models described in Table 2.

x	y	a	b	R^2
k	ρ_s	1.30	-0.12	0.92
$k\,(k_{air}=0)$	ρ_s	2.97	1.23	0.90
E	ρ_s	6.62	12.3	0.86
k	ρ_{mc}	0.32	-0.44	0.88
$k\,(k_{air}=0)$	ρ_{mc}	0.78	0.73	0.97
E	ρ_{mc}	1.80	11.4	0.98

Table 7.2: Linear regressions of the form $\log(y) = a\log(x/\rho_{ice}) + b$, with x being ρ_s or ρ_{mc} and y being k or E. The sign log represents the natural logarithm.

instance, Flin et al. [2011] reported rather large values of the mean grain contact area in snow, between 10% and 50% of the mean surface area of the grains. The extreme case is represented by the precipitations particles (samples I03 and I04), which exhibit a direction-averaged value for ρ_{mc} of 1 kg m^{-3}. Such a value means that two opposite faces of a cubic snow sample of side-length 10 cm are connected by a surface area of only 3.5 mm x 3.5 mm. Löwe et al. [2011] pointed out the bi-continuity of the snow microstructure. We see here that the connectivity of the ice matrix is not null, which is impossible because of gravity, but is very low, especially for the precipitation particles.

The study on the representative volume related to the minimum cut density shows that the variations of ρ_{mc} with the volume size are negligible compared to the difference between snow samples, as soon as volumes larger than about 5^3 mm^3 are considered (except for sample I01). The minimum cut is an extreme variable since it measures the minimal effective density of a cut in the microstructure. Therefore, convergence with the volume size is far from being obvious. Our study shows that a REV related to the minimum cut density exists and is on the order of about 5^3 mm^3, for non dendritic snow types (RG, FC, DH, MF). For precipitation particles, investigations on larger samples should be conducted. The existence of this REV indicates that the minimum cut density characterizes bonding structures which repeat themselves throughout the entire microstructure. The REV related to the bonding system is consistent with REV previously estimated for other quantities. It is larger than the one previously observed for density [Coléou et al., 2001] and SSA [Flin et al., 2011] and on the order of those obtained for thermal conductivity [Calonne et al., 2011] and mechanical properties [Hagenmuller et al., 2014c]. This supports the idea that only few snow grains might be representative for "local" variables such as density and SSA, but that "network" variables such as thermal conductivity, mechanical properties and minimum cut density need to be estimated on at least a collection of connected grain clusters. The difference between the size of the REVs related to "local" and to "network" variables is emphasized for snow types with a low minimum cut density.

7.5.2 The minimum cut density as a microstructural indicator

The development of the minimum cut density concept was motivated by the fact that, for certain properties, only a small part of the structure contributes to the overall macroscopic behavior. We showed that the minimum cut density is indeed a good indicator of potential fluxes inside the ice matrix. Excellent correlation between the minimum cut density and thermal conductivity ($R^2 = 0.88$) or Young's modulus ($R^2 = 0.98$) were found (Table 2). However, the correlation obtained for thermal conductivity is not better than the correlation obtained with density ($R^2 = 0.92$). This scatter is explained by the fact that the minimum cut density quantifies potential fluxes in ice but does not consider the conduction of air. Two grains very close to each other but not connected by an ice bond might exchange heat through air, which significantly contributes to the overall heat conduction. This phenomenon is illustrated in Figure 7.1b and confirmed by the large difference observed on thermal conductivity whether conduction through air is neglected or not (Figure 7.7a). Moreover, if air conduction is neglected the correlation between k and ρ_{MC} is significantly enhanced ($R^2 = 0.97$).

The sensitivity of the Young's modulus to density is extreme. A power law fit of the form $E \sim \rho_s^a$ yields an exponent $a = 6.6$ from our data. As a comparison, Sigrist [2006] obtained an exponent value of 2.94 based on experimental data obtained via high frequency cyclic loading of snow. Even if the exponents of the power law fit are different (attributed in general to the effect of strain rate on the elasto-viscoplastic properties of ice [Schneebeli, 2004]), both approaches reveal the high non linearity between Young's modulus and density. More generally, a power law fit with an exponent much larger than 1 is generally observed between mechanical properties (Young's modulus, strength, toughness) and density. Here, we show that the non linear relationship between the minimum cut density and density explains a large part of this non linear relation. Indeed, the fit between E and ρ_{mc} exhibits a exponent $a = 1.80$ (Table 2).

Furthermore, the anisotropy of the minimum cut density appears to account for the anisotropy of the thermal conductivity and Young's modulus. Microstructures resulting from temperature gradient metamorphism exhibit a minimum cut density larger in the vertical direction than in the horizontal plane. In contrast, density ρ_s is inherently an isotropic characteristics of the microstructure. The presence of anisotropy thus inevitably introduces scatter in the parameterization of thermal conductivity and Young's modulus by density. In our data, temperature gradient seems to be the main reason for the occurrence of anisotropy. Comparatively, effects of gravity appear to be much smaller (Figure 7.7).

The minimum cut density was, here, related only to thermal conductivity and Young's modulus. However, the significant linear correlation between the Young's modulus and the tensile strength of snow simulated by Hagenmuller et al. [2014c], indicates that the strength of snow might as well be predicted by the minimum cut density. Moreover, Domine et al. [2011] investigated the link between the shear strength τ of snow, measured by a shear vane and its thermal conductivity k_{exp},

measured with the heated needle probe technique. The correlation between k_{exp} and τ obtained in this study at a macroscopic level (scale of tenth of cm) also supports the same intuition that both conduction and strength are limited by the narrow constrictions at the bonds between the ice grains [Domine et al., 2011].

In the present study, only a small number of μCT samples were considered. A systematic study on a larger set of samples including complete time series of isothermal and temperature gradient metamorphisms could provide quantitative relationships to link conduction and mechanical properties and to quantify the evolution of ρ_{mc} with time and temperature. The microstructure-based model of Hagenmuller et al. [2014c], which simulates the tensile strength of snow, might further help to investigate such structure-property relationships.

Acknowledgments Funding by the VOR research network (Tomo_FL project) is acknowledged. We thank the scientists of 3SR laboratory and ESRF ID19 beamline, where the 3D images have been obtained. We also acknowledge the CEN staff, especially B. Lesaffre, for their significant contribution to the data acquisition. Irstea and CNRM-GAME/CEN are part of Labex OSUG@2020 (Investissements d'Avenir - Grant Agreement ANR-10-LABX-0056) and Irstea is member of Labex TEC21 (Investissements d'Avenir - Grant Agreement ANR-11-LABX-0030). The authors thank C. Fierz and an anonymous reviewer for their constructive feedback on the manuscript.

7.A Appendix

This appendix was not submitted for publication with chapter 7 in Cold Regions Science and Technology. Different issues raised in previous sections of chapter 7 are discussed in this appendix:

- the evolution of the minimum cut density with metamorphism,
- the relevance of the specific grain contact area as a microstructural indicator,
- the computation of the minimum cut density limited to volumes of size 600^3 voxels.

These issues are discussed on 3D snow images corresponding to two time series previously obtained during an isothermal experiment (images I01, I03, I04, I05, I08, I11, I15, I19, I21 and I23; details in [Flin et al., 2004]; Figure 7.9) and a temperature gradient experiment (images 0A, 1A, 2A, 3A, 4A, 5G and 6G; details in [Calonne et al., 2011]; Figure 7.9). The isothermal experiment was conducted at a constant temperature of 271 K. The temperature gradient experiment was conducted with a temperature gradient of 43 K m^{-1} and a mean temperature of 269 K. The images are composed of $600 \times 600 \times 600$ voxels with a resolution of 4.91 μm, and between 7 μm and 9 μm for the isothermal and temperature gradient images, respectively.

7.A.1 Evolution of the minimum cut density with metamorphism

The evolution of the minimum cut density ρ_{mc} and density ρ_s is shown in figure 7.10.

The value of ρ_{mc} increases with time during the isothermal metamorphism of Precipitation Particles (PP) into Rounded Grains (RG). This increase is observed for all directions, indicating an isotropic evolution of the bonding system. The small differences observed between the different directions may be explained by spatial variability of the bonding system emphasized by the small volume (3^3 mm^3) used for the computation. Note that the value of ρ_{mc} increases by an order of magnitude during the experiment while the density only doubles.

During the temperature gradient metamorphism of Rounded Grains (RG) into depth hoar (DH), the variations of ρ_{mc} depends on the direction. In the vertical direction, ρ_{mc} first decreases when the Rounded Grains transforms into Faceted Crystals, then it increases and exceeds the value obtained at the beginning of the experiment. In the horizontal plane, ρ_{mc} globally decreases. It reaches a value close to the one obtained for rounded grains at a density of only 150 kg m^{-3}, while the density is almost constant about 300 kg m^{-3}. This observation indicates the creation of long vertical chains in the ice matrix, which are not "well connected laterally". The minimum cut density thus well captures the anisotropy created by the temperature gradient.

These first observations support the idea that the minimum cut density well characterizes the bonding system and its evolution with metamorphism. However,

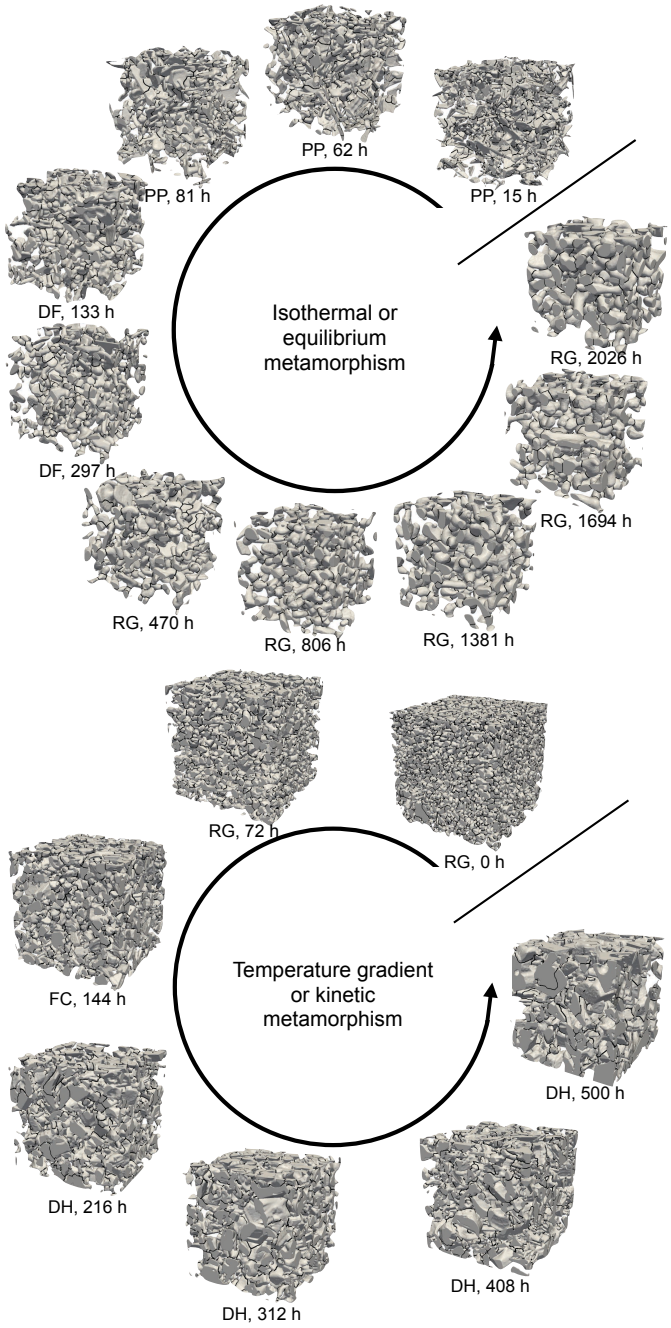

Figure 7.9: Time series images taken during an isothermal (top) and temperature gradient experiment (bottom). The side-length of the cubic snow images is about 3 mm for the isothermal experiment images and about 5 mm for the temperature gradient experiment images. The labels below the 3D images indicate the snow type and the time from the beginning of the experiment. The boundaries between grains are shown in black.

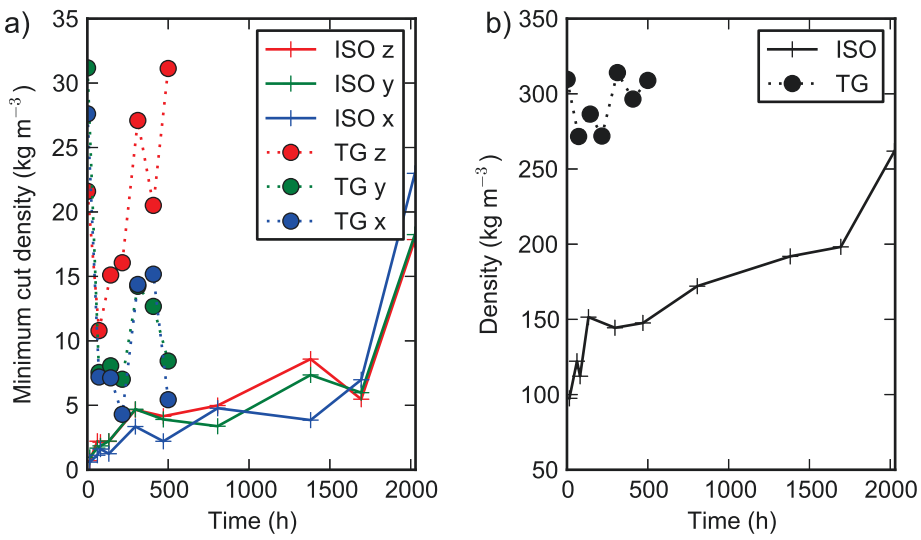

Figure 7.10: Evolution of the minimum cut density ρ_{mc} (a) and density ρ_s (b) with metamorphism. The labels "ISO" and "TG" refer to isothermal metamorphism and temperature gradient metamorphism, respectively. The labels x, y, and z correspond to the computation direction of ρ_{mc}. The direction z is the direction of gravity and temperature gradient. The directions x and y are in the horizontal plane.

the tested image data set is too small to provide quantitative relationships at this stage.

7.A.2 Specific grain contact area

It is difficult to determine characteristics of the bonding system from the results of a grain segmentation procedure. This difficulty motivated the development of the minimum cut density ρ_{mc}, which is independent from a grain segmentation procedure.

To evaluate nevertheless the relevance of the specific grain contact area, a variable often proposed to quantify the bonding of the ice matrix [e.g. Flin et al., 2011, Voitkovsky et al., 1975], the images of the two times series were segmented into grains with the algorithm of Hagenmuller et al. [2014b] (Chapter 5) and the specific grain contact area (SGCA), i.e. the intergranular contact area per unit mass, was calculated from the grain-segmented images.

The evolution of SGCA with time is shown in Figure 7.11. For both types of metamorphisms, the SGCA decreases with time. The values of the SGCA strongly depend on the contiguity threshold c_t used in the grain segmentation. However, the same SGCA-time trend is observed for all values of c_t. The strengthening of the microstructure during isothermal metamorphism and the development of a weak connectivity in the horizontal plane during temperature gradient metamorphism

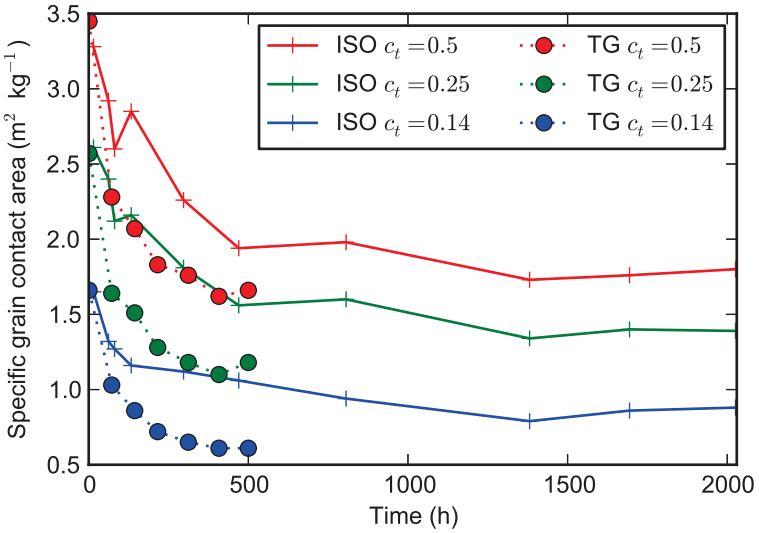

Figure 7.11: Evolution of the specific grain contact area with metamorphism. The labels "ISO" and "TG" refer to isothermal metamorphism and temperature gradient metamorphism, respectively. The grains were segmented with a threshold on curvature $\widetilde{\kappa}_t = 1.0$ and a threshold on contiguity $c_t \in [0.14, 0.5]$. See [Hagenmuller et al., 2014b] for details on the grain segmentation algorithm.

are not revealed by the value of the SGCA. A possible explanation is that only a few contacts among those determined by the grain segmentation algorithm are mechanically relevant. The evolution of the contact area of these bonds is therefore not visible in the evolution of the SGCA which embraces the entire set of detected bonds. Note that the sensitivity of SGCA to the grain segmentation parameter on curvature $\widetilde{\kappa}_t$ was not evaluated here. In [Hagenmuller et al., 2013a], we reported a different evolution of the SGCA with isothermal metamorphism because we used a previous version of the grain segmentation algorithm where the threshold on curvature was set differently. This further illustrates the strong sensitivity of the SGCA values to the segmentation procedure.

7.A.3 Computation on limited volume sizes

As stated in chapter 7, the computation of the minimum cut density is memory consuming. For instance, computing ρ_{mc} on image I23, a 600^3 voxels image of density 250 kg m^{-3}, requires 10 GB RAM memory to store a graph composed of 5.4×10^7 nodes and 7×10^8 edges. The algorithm presented in chapter 7 works on a binary image. There are no restrictions on the topology of the minimum cut surface. If we restrict the minimum cut surface to be composed of a subset of bonds detected by a grain segmentation algorithm, the memory usage of the minimum cut algorithm is tremendously decreased. Indeed, the basic unit of the algorithm is

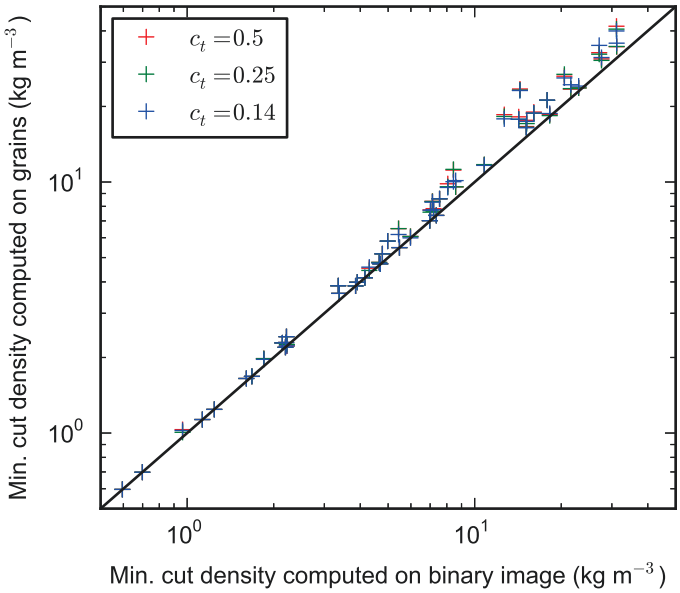

Figure 7.12: Minimum cut density computed with two different methods: on the binary image composed of numerous voxels or on a representation of the microstructure as a set of interconnected grains.

then the grain (composed of numerous voxels) instead of the voxels themselves. For instance on image I23, the corresponding graph is reduced to about 1000 nodes (or grains) and 2000 edges (or intergranular contacts). Segmenting the binary image into grains might be time consuming but is not restricted to a certain image size since the grain segmentation can be computed locally.

Figure 7.12 shows the minimum cut density computed with the two methods (with binary image or grain representation). The minimum cut density is slightly over-estimated when computed on the grains. This is expected since the minimum cut surface computed on the grains is included in the potential cut surfaces that can be represented with voxels. However, the agreement between both methods is very good, especially on images with a low value of ρ_{mc}. Therefore, it is possible to compute the minimum cut density with a reasonable accuracy without any limitation of the size of the image. Moreover, it further validates the developed grain segmentation algorithm which preserves this connectivity characteristic of the ice matrix.

Chapter 8

Conclusion and perspectives

Contents

8.1 Conclusion

The principal objective of this PhD thesis was to explore the link between snow microstructure and snow mechanical properties with microtomographic data. New numerical tools and methods were developed. New insights into the mechanisms active during the brittle behavior of snow were obtained.

8.1.1 New modeling tools for snow mechanics

Binary segmentation An algorithm to segment the 3D grayscale images, obtained by microtomography, into binary ice-air images was proposed. The algorithm is based on the minimization of a segmentation energy. The parameterization of the algorithm is automatically derived from the analysis of the grayscale histogram, which takes advantage of the Gaussian distribution of noise. The algorithm also benefits from the knowledge that the segmented material is snow and not some arbitrary porous material: it mimics the natural tendency of snow to reduce its surface energy. The binary segmentation algorithm was evaluated on images of snow impregnated with 1-chloronaphtalene and non-impregnated snow. On the images of non-impregnated snow, the proposed algorithm performs very similarly to the commonly-used approach based on a the sequence of filters (low-pass filter, global thresholding and morphological filters). In this case, the proposed analysis of the grayscale histogram can be used to automatically and accurately determine the global threshold, which reduces possible bias introduced by the manual choice of the threshold. The formalism provided by the minimization of a segmentation energy is of particular interest for the images of impregnated snow which corresponds

to a three phases material (air, ice and 1-chloronapthalene) and which cannot be easily segmented with a classical sequence of filters.

Finite element model A finite element model was developed to reproduce the brittle behavior of snow in tension. The microstructure geometry is meshed with tetrahedral elements. The constitutive material of the elements, ice, is supposed to be elastic fragile, homogeneous and isotropic. To reduce the computation time and to enable simulations on sufficiently large volumes representative of the microstructure, potential crack paths were pre-determined at the beginning of the simulation. A distance-based watershed algorithm was used to detect the bonds in the ice matrix, here composed of rounded grains. If the stress in one element located next to a certain bond reaches the strength of ice, the bond is deleted. The tensile strength predicted by the model is in good agreement with the measurements conducted on the same samples of rounded grains.

Modeling snow as granular material Efforts were made to model snow as a granular material, which appears as a reasonable assumption in case of rapid and large deformations mainly controlled by particle rearrangements and contact interactions. This approach requires to detect grains in the ice matrix geometry captured by tomography and to develop a discrete element model accounting for the grain geometry and bonding.

We developed a new grain segmentation algorithm based on criteria on curvature and contiguity. First, bond candidates are identified with the value of the minimal principal curvature. Then the bonds candidates are modified so that their area is minimized and highly contiguous grains are merged. The results of the grain segmentation algorithm were evaluated against grains directly inferred from elastic stress distributions computed with finite elements. We showed that the developed algorithm is effectively able to detect bonds supporting locally the highest stresses. Assuming that the strength of ice is homogeneous, the algorithm thus detects potential failure paths in the microstructure which are required for DEM modeling. Unlike a simple distance-based watershed segmentation, this algorithm can be applied on different types of snow such as precipitation particles, faceted crystals, depth hoar and not only rounded grains.

We then used the grains detected in the 3D microstructure to develop a discrete element model of snow. The complex shapes of the grains are described with rigid clumps of spheres. The bonding system is reproduced by connecting the clumps through cohesive contacts. The contact law used in the simulation accounts for the failure of cohesive bonds and the creation of new frictional bonds. The sensitivity analysis of the model to its parameters showed that the effects of potential artefacts introduced by the modeling approach are limited compared to the variability due to different microstructures. The DEM model is generic and was, here applied to simulate the confined compression of snow.

Measure of connectivity The bonds between grains are as important as the grains themselves (if not more important) to describe the macroscopic behavior of snow. In theses bonds, stresses or heat fluxes are larger than in other parts of the snow microstructure because of a "neck effect" induced by the reduced ice thickness. However, a grain is not an "absolute" entity but inevitably depends on a certain definition or a given "threshold". Indeed, we observed that the thresholds on contiguity or curvature in the developed grain segmentation algorithm have a large effect on the segmented grains and therefore on the subsequent characterization of the bonding system. We developed a new indicator of the bonding between grains, the minimum cut density. This microstructural indicator accounts for the anisotropy of bonding, while being independent from a grain segmentation process. It characterizes the weakest connectivity of the ice matrix.

General remarks The main difficulty encountered during the development of these tools was the large amount of data contained in a 3D image of the microstructure, typically $500 \times 500 \times 500 = 125 \times 10^6$ voxels. Therefore minor constraints or assumptions have been used to reduce the computing time:

- The binary and grain segmentation algorithms and the minimum cut density algorithm are all based on the optimization of a certain energy. These energy functions depend on millions of variables (one variable per voxel). Their optimization seems therefore very difficult. But we know that these variables can take only a small number of values (0/1 for binary segmentation or minimum cut calculation; a few grain labels for grain segmentation) and that the energy function involves only "pair" interactions. This enables to minimize very efficiently the energy function with the graph-cut approach, with a number of operations polynomially dependent on the number of voxels.

- The toughness of ice is small (50-150 kPa $m^{1/2}$), indicating a relatively easy propagation of cracks. Therefore it is reasonable to assume that when a bond in snow starts to fail, a cracks propagates instantaneously in the bond. We used this assumption in the modeling of tensile strength to keep calculations of crack propagation very simple and to expedite the simulation.

- Rapid and large deformations in snow are mainly due to the re-arrangement of grains. Assuming that the grains behave as rigid bodies significantly reduces the number of degrees of freedom of the whole structure. This made our DEM model computable in reasonable time on representative volumes of snow.

8.1.2 An insight into the brittle behavior of snow

The developed modeling tools were applied to different microtomographic images of snow measured in the framework of this PhD thesis (microtomograph of laboratory 3S-R, Grenoble, France), of my master thesis (microtomograph of SLF, Davos, Swiss), and previously measured by other researchers (CEN-CNRM team, Margret

Matzl, SLF). The conducted numerical tests provide novel information about the brittle behavior of snow.

Initiation of failure in tension The finite element model revealed a very heterogeneous stress distribution in the ice matrix subjected to tension. On the tested snow, rounded grains, the maximal stress appears to exceed the mean value by a factor of 100. About 30% of the microstructure experiences local compression in response to macroscopic tension. These observations illustrate the complex relation between macroscopic and microscopic stresses, induced by the microstructure.

The simulations also showed that the first breaking of bonds does not immediately lead to the global failure of the sample under force-controlled tests. Damage (failure of individual bonds) first occurs in a spatially distributed manner, which results in a pseudo-plastic macroscopic stress-strain curve. Toward the end of the simulations, the broken bonds form a unique failure surface. Only 25% of the broken bonds do not contribute to the final failure surface, indicating that the macroscopic tensile failure is due to the breaking of a few bonds throughout the sample.

Damage is shown to occur for very small macroscopic strain as low as 10^{-4}, because ice is very stiff ($E = 10$ GPa) and stress highly localized in the microstructure. Besides, the calculated Young's modulus is about 10 times higher than existing measurements on rounded grains with a similar density.

Confined compression of snow The discrete element model showed that the resistance of snow to confined compression is mainly a function of density. Indeed, even if tests were conducted on very different snow types, the stress-density relations fit a unique trend with little variability.

For samples of similar density but different microstructural patterns, the stress-strain relationship appears to be different in the first stage of the compression when the first bonds break. The model predicts a weakening effect of temperature gradient metamorphism compared to isothermal metamorphism.

For the tested range of strain, friction is shown to have little effect on the overall mechanical behavior. In contrast, a linear relation between simulated macroscopic compression stress and microscopic cohesion strength of ice is found.

Connectivity of the ice matrix The minimum cut density values are in the range [0.2,35] kg m^{-3} for the tested samples with density in the range [100,350] kg m^{-3}. The factor 10-50 between minimum cut density and density reveals the very weak connectivity of the snow microstructure. This weak connectivity is a possible explanation for the high stress localization in the ice matrix: only a few bonds support the entire load.

The minimum cut density properly accounts for the anisotropy of the thermal conductivity and Young's modulus. In particular, the minimum cut density appears to be larger along the temperature gradient than in its orthogonal plane. This anisotropy cannot be captured by density.

General remarks The main motivation for the study of the link between microstructure and snow mechanical properties was the well-known scatter in the density parameterization of these properties [e.g. Mellor, 1975]. In the light of the obtained results, some remarks on the possible origins of the observed scatter can be formulated:

- We showed that the elastic regime of snow is limited to very small strain (e.g. $\varepsilon < 10^{-4}$, for rounded grains with a density of about 350 kg m^{-3}). Therefore, it is very difficult to measure the Young's modulus of snow without damaging the sample. Ice viscosity is often considered as the main reason for the scatter in density-Young's modulus plot and the systematic higher values of the elastic modulus estimated with tomography-based models compared to experiments. We suggest to also account for the potential damage on the microstructure induced by measurements.

- We showed that a snow sample can hold in one connected block just through a few bonds. If these bonds fail, the resistance to tension of the sample is null, regardless of the mean density of the sample. Therefore, tensile strength properties of snow might be not so sensitive to density but is mainly controlled by the effective density of the "weakest" surface crossing the sample. This local heterogeneity of density can be one reason for the observed scatter. In contrast, we found a good correlation between density and compression resistance. In compression, the failure of the weakest part of the microstructure does not lead to the failure of the whole sample because of the creation of new bonds. Compression tends to homogenize the density of the sample.

- Density is by definition an isotropic characteristic of snow. However, temperature gradient metamorphism introduces a significant anisotropy of the microstructure which mirrors in the physical and mechanical properties of snow. This anisotropy thus appears as scatter in density parameterizations.

- In this PhD thesis, we assume ice to be elastic fragile and considered constant values for the Young's modulus and cohesion. We observed a linear relation between microscopic cohesion and macroscopic strength in tension or compression. Therefore variations of the microscopic properties of ice induced, for instance by temperature or by preferential crystalline orientation of the grains, are directly reflected in the macroscopic properties of snow. More generally, the activation of different deformations mechanism at the microscopic level can completely change the observed macroscopic behavior.

8.2 Perspectives

In this section, I describe possible outlooks and research perspectives based on the work done during my PhD.

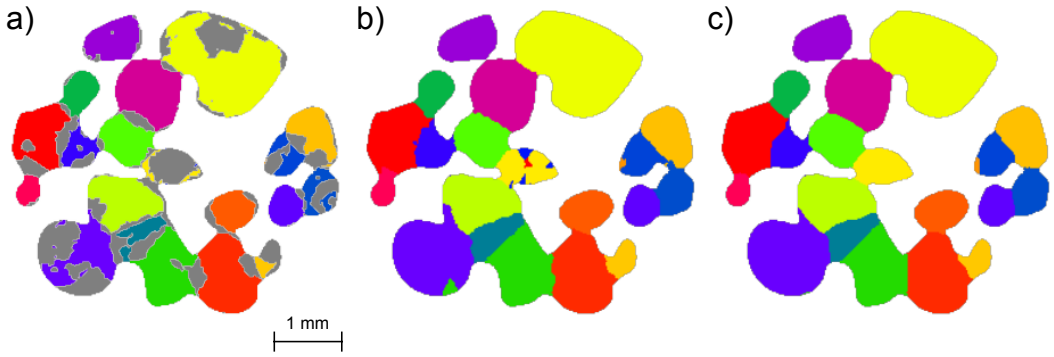

Figure 8.1: Diffraction contrast tomography (DCT). The result of the DCT measurements presents zones with undetermined crystallographic orientation (gray) (a), which can be determined with an extrapolation of the determined grains with a Voronoi diagram (b) or a contact area minimization criterion (c). The DCT data are 3D but only 2D slices are shown on the figures.

8.2.1 Microtomography of snow

Effects of impregnation The effects of numerical processing on the snow characteristics derived from microtomographic data was evaluated in this work. But the effects of the sample impregnation on the microstructure remain to be estimated. Indeed, capillary forces due to the liquid impregnation product might damage very fragile snow types as precipitation particles. Chemical reactions between ice and chlorine (e.g. in 1-chloronaphtalene) might also modify the ice matrix.

Multi-material segmentation applied to diffraction contrast tomography The energy-based formalism used for binary and grain segmentation could be applied to images of snow obtained by diffraction contrast tomography (DCT). In addition to the measurement of the attenuation coefficient to X-rays, DCT also reveals the crystallographic orientation of individual grains. However, some ice zones are not associated to any crystallographic orientation because of the distortion of the distraction spots caused by imperfections in the ice crystals (Figure 8.1a). Roscoat et al. [2011b] used successive dilations of the determined grains to fill the missing orientation information in the ice matrix (Figure 8.1b). With our energy-based approach, the extrapolation of the orientation information can be also done with a intergranular contact area minimization criterion to mimic the surface energy reduction induced by metamorphism (Figure 8.1c). An efficient image processing method of DCT data could further help to identify the deformation mechanisms occurring at the microstructural level and to assess the role of the crystallographic fabric of ice on the overall behavior.

Model evaluation with in situ microtomography experiments The developed finite element model was evaluated against measurement of the tensile strength. The discrete element model was not evaluated against experiments. In situ microtomography measurements may help to assess the assumptions made at the microstructural level and the accuracy of the models. Schleef et al. [2014] conducted such tests to investigate the creep behavior of snow. In case of rapid deformations of snow (brittle regime), the acquisition time of X-ray tomography will need however to be reduced to follow high strain rates.

8.2.2 Snow mechanics

Model improvements Simple and straightforward improvements of the developed finite and discrete element models could further expand their range of applicability. The finite element model of tensile strength works only on rounded grains since it is based on bond detection with a simple distance-based watershed segmentation. The advanced grain segmentation algorithm, that we developed, appears to be accurate on several snow types and not only rounded grains. New tests combining both approaches will enable to characterize the brittle behavior of different snow types in tension. The discrete element model was evaluated under loading conditions reproducing confined compression. Simulating a generic tri-axial test (including shear loading under normal pressure, Figure 8.2) will further help elucidating the relation between microstructure and mechanical properties. Besides, Szabo and Schneebeli [2007] showed that two ice grains in contact can sinter in a very short time. Accounting for this feature in the contact law will provide a new insight into the temperature and strain-rate dependence of rapid and large deformations.

Tests on a large set of snow images In future work, the systematic application of the developed models on a large set of snow images will constitute a new step to define quantitative relations between snow microstructure and mechanical properties. Especially, modeling the strength and softening behavior of weak layers (composed of faceted crystals and depth hoar) is of great interest for modeling avalanche release at the slab scale [e.g. Gaume, 2013].

Interpretation of the penetration resistance tests In the field, the vertical profile of snow strength is usually estimated with an indenter which measures the penetration resistance of snow (e.g. SnowMicroPen SMP, [Johnson and Schneebeli, 1999]). The force signal of the indenter is used to deduce microstructural parameters of the snowpack. However, the force signal interpretation remains unclear [e.g. Löwe and van Herwijnen, 2012]. The explicit modeling of the penetration of the SMP in a snow sample could help to further decipher this issue. See an example on figure 8.3.

Coupling with thermodynamics Flin and Brzoska [2008], Flin et al. [2003] developed numerical models describing the evolution of 3D snow structures with

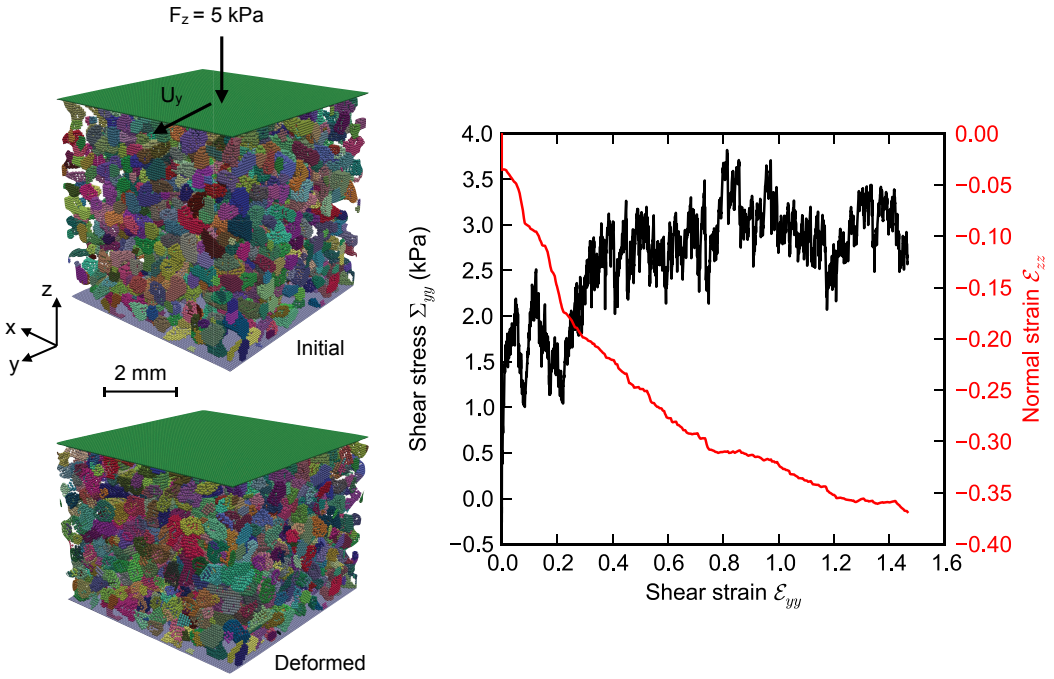

Figure 8.2: Preliminary simulation of the mechanical behavior of rounded grains under imposed shear velocity and normal pressure. Lateral periodic boundary conditions are used.

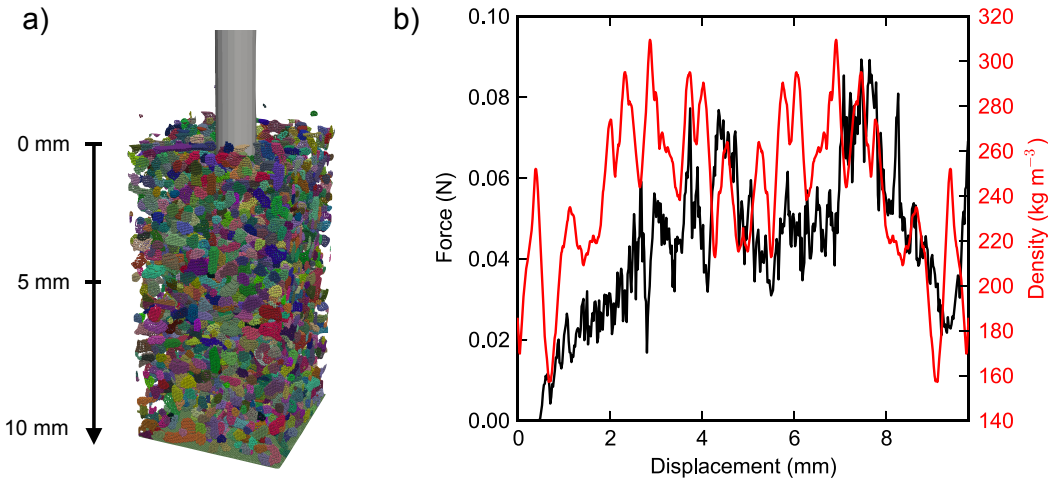

Figure 8.3: Preliminary numerical micro-penetration test. (a) 3D configuration. (b) Force-displacement signal. The density value also shown on figure b) was calculated on horizontal slices of the snow image. Note that the diameter of the indenter tip is, here, 1.125 mm. The commonly-used snow micro-penetrometer (SMP) has a tip diameter of 5 mm.

isothermal and temperature gradient metamorphism. To assess the relative importance of possible metamorphism mechanisms, such as curvature-driven vapor transport or surface diffusion, the model results must be confronted to experiments. In experiments, metamorphism leads to a densification of the snow structure (for snow density < 300 kg m^{-3}) due to the inevitable presence of gravity [Schleef and Löwe, 2013]. At present, gravity is not considered or poorly represented in these metamorphism models. Coupling these models with the mechanical model developed in this thesis will enable to conduct realistic simulations of the evolution of the microstructure with metamorphism, which are comparable to experimental tests.

Physical parameterization of empirical models used in the operational forecasting and prevention of the avalanche risk In the present modeling work, the microstructure of snow is known with a micrometer resolution and the properties of ice are supposed to be completely known. The perfectly controlled environment of the mechanical model enables to theoretically distinguish the different factors contributing to the overall mechanical behavior. In contrast, the operational forecasting services rely on models working at the resolution of km, with scarce measurements. The gap between both approaches is huge. Especially, a lot of work is still required to transfer the results of snow mechanics deduced from fundamental microstructural studies, to operational models. As a first step, the empirical parameterization of snow mechanical properties used in models such as MEPRA could incorporate the physically-based parameterization of the bonding system with the minimum cut density.

Bibliography

Abele, G. and Gow, A. J. (1975). Compressibility characteristics of undisturbed snow. Technical Report May, U.S. Army Cold Regions Research and Engineering Laboratory, Hanover, NH, USA. (Cited on pages 143 and 146.)

Abele, G. and Gow, A. J. (1976). Compressibility characteristics of compacted snow. Technical report, U.S. Army Cold Regions Research and Engineering Laboratory, Hanover, NH, USA. (Cited on pages 143 and 146.)

Albert, M. R., Grannas, A. M., Bottenheim, J., Shepson, P. B., and Perron, F. E. (2002). Processes and properties of snow-air transfer in the high Arctic with application to interstitial ozone at Alert, Canada. *Atmospheric Environment*, 36(15-16):2779–2787. (Cited on page 160.)

Alley, R. B. (1986). Three-dimensional coordination number from two-dimensional measurements: a new method. *Journal of Glaciology*, 32(112):391–396. (Cited on pages 25 and 133.)

Alley, R. B. (1987). Firn densification by grain-boundary sliding: a first model. *Journal de Physique*, 48:249–256. (Cited on page 30.)

Ancey, C. (1998). *Guide neige et avalanches: connaissances, pratiques et sécurité.* Edisud (Aix-en-Provence, France). (Cited on page 6.)

Arakawa, H., Izumi, K., Kawashima, K., and Kawamura, T. (2009). Study on quantitative classification of seasonal snow using specific surface area and intrinsic permeability. *Cold Regions Science and Technology*, 59:163–168. (Cited on page 160.)

Arnaud, L., Gay, M., Barnola, J.-M., and Duval, P. (1998). Imaging of firn and bubbly ice in coaxial reflected light : a new technique for the characterization of these porous media. *Journal of Glaciology*, 44(147):326–332. (Cited on pages 25 and 111.)

Arnaud, L., Picard, G., Champollion, N., Domine, F., Gallet, J. C., Lefebvre, E., Fily, M., and Barnola, J.-M. (2011). Measurement of vertical profiles of snow specific surface area with a 1 cm resolution using infrared reflectance: instrument description and validation. *Journal of Glaciology*, 57(201):17–29. (Cited on page 43.)

Bader, H. and Niggli, P. (1939). *Der Schnee und seine Metamorphose: Erste Ergebnisse und Anwendungen einer systematischen Untersuchung der alpinen Winterschneedecke. Durchgeführt von der Station Weissfluhjoch-Davos der Schweiz. Schnee- und Lawinenforschungskommission 1934-1938.* Kümmerly and Frey. (Cited on pages 6, 18, 24, 26 and 133.)

Ballard, G. and Feldt, E. (1965). A theoretical consideration of the strength of snow. *Journal of Glaciology*, 6(43):159–170. (Cited on pages 162 and 164.)

Ballard, G. and McGaw, R. W. (1965). A theory of snow failure. Technical report, U.S. Cold Regions Research and Engineering Laboratory., Hanover, NH, USA. (Cited on page 164.)

Barbero, M., Barpi, F., Borri-Brunetto, M., and Pallara, O. (2013). An Apparatus for In Situ Direct Shear Tests on Snow. *Experimental Techniques*. (Cited on page 26.)

Bartelt, P. and von Moos, M. (2000). Triaxial tests to determine a microstructure-based snow viscosity law. *Annals of Glaciology*, 31(1):457–462. (Cited on pages 29 and 30.)

Bartlett, S. J., Rüedi, J.-D., Craig, A., and Fierz, C. (2008). Assessment of techniques for analyzing snow crystals in two dimensions. *Annals of Glaciology*, 48:103–112. (Cited on page 20.)

Bentley, W. A. and Humphreys, W. J. (1931). *Snow Crystals*. McGraw-Hill, New York, NY, USA. (Cited on page 132.)

Berthod, M., Kato, Z., Yu, S., and Zerubia, J. (1996). Bayesian image classification using Markov random field. *Image and Vision Computing*, 14:285–295. (Cited on page 73.)

Bessinger, B. A., Liu, Z., Cook, N. G. W., and Myer, L. R. (1997). A new fracturing mechanism for granular media. *Geophysical Research Letters*, 24(21):2605–2608. (Cited on page 102.)

Blackford, J. R. (2007). Sintering and microstructure of ice: a review. *Journal of Physics D: Applied Physics*, 40(21):R355. (Cited on page 110.)

Borstad, C. (2011). *Tensile strength and fracture mechanics of cohesive dry snow related to slab avalanches*. PhD thesis, The University of British Columbia. (Cited on pages 16, 26, 27 and 110.)

Boykov, Y. and Funka-Lea, G. (2006). Graph cuts and efficient ND image segmentation. *International Journal of Computer Vision*, 70(2):109–131. (Cited on pages 43, 47 and 50.)

Boykov, Y. and Kolmogorov, V. (2003). Computing geodesics and minimal surfaces via graph cuts. In *Proceedings. Ninth IEEE International Conference on Computer Vision, 2003*, volume 1, pages 26–33, Nice, France. Ieee. (Cited on pages 43, 54, 67, 83 and 167.)

Boykov, Y. and Kolmogorov, V. (2004). An experimental comparison of min-cut/max-flow algorithms for energy minimization in vision. *IEEE Transactions on*

Pattern Analysis and Machine Intelligence, 26(9):1124–1137. (Cited on pages 68, 69 and 115.)

Boykov, Y., Veksler, O., and Zabih, R. (2001). Fast approximate energy minimization via graph cuts. *IEEE Transactions on Pattern Analysis and Machine Intelligence*, 23(11):1222–1239. (Cited on pages 43, 51, 54 and 115.)

Brown, R. L. (1989). Perspective on mechanical properties of snow. In *Proceedings of the 1st International Conference on Snow Engineering*, pages 502–503, California, USA. (Cited on page 132.)

Brucker, L., Picard, G., Arnaud, L., Barnola, J.-M., Schneebeli, M., Brunjail, H., Lefebvre, E., and Fily, M. (2011). Modeling time series of microwave brightness temperature at Dome C, Antarctica, using vertically resolved snow temperature and microstructure measurements. *Journal of Glaciology*, 57(201):171–182. (Cited on page 72.)

Brun, E., David, P., and Sudul, M. (1992). A numerical model to simulate snow-cover stratigraphy for operational avalanche forecasting. *Journal of Glaciology*, 38(128):13–22. (Cited on page 20.)

Brzoska, J.-B., Coléou, C., Lesaffre, B., Borel, S., Brissaud, O., Ludwig, W., Boller, E., and Baruchel, J. (1999). 3D visualization of snow samples by microtomography at low temperature. *ESRF Newsletter*, 32(22-23):112. (Cited on pages 25, 42 and 133.)

Brzoska, J.-B., Flin, F., and Barckicke, J. (2008). Explicit iterative computation of diffusive vapour field in the 3-D snow matrix: preliminary results for low flux metamorphism. *Annals of Glaciology*, 48(1):13–18. (Cited on page 42.)

Brzoska, J.-B., Flin, F., and Ogawa, N. (2007). Using gaussian curvature for the 3D segmentation of snow grains from microtomographic data. In Kuhs, W., editor, *Physics and Chemistry of Ice*, volume 1, pages 125–132. The Royal Society of Chemistry. (Cited on pages 90 and 112.)

Calonne, N., Flin, F., Geindreau, C., Lesaffre, B., and Roscoat, S. R. D. (2014). Study of a temperature gradient metamorphism of snow from 3-D images: time evolution of microstructures, physical properties and their associated anisotropy. *The Cryosphere Discussions*, 8(1):1407–1451. (Cited on pages 11, 79 and 162.)

Calonne, N., Flin, F., Lesaffre, B., Dufour, A., Roulle, J., Pugliese, P., and Geindreau, C. (2013). A room temperature operating cryogenic cell for in vivo monitoring of dry snow metamorphism by X-ray microtomography. In *AGU Fall Meeting Abstracts*, page 667. (Cited on page 25.)

Calonne, N., Flin, F., Morin, S., Lesaffre, B., Roscoat, S. R. D., and Geindreau, C. (2011). Numerical and experimental investigations of the effective thermal

conductivity of snow. *Geophysical Research Letters*, 38(23):L23501. (Cited on pages 42, 110, 134, 155, 164, 168, 176 and 179.)

Calonne, N., Geindreau, C., Flin, F., Morin, S., Lesaffre, B., Roscoat, S. R. D., and Charrier, P. (2012). 3-D image-based numerical computations of snow permeability: links to specific surface area, density, and microstructural anisotropy. *The Cryosphere*, 6(5):939–951. (Cited on page 110.)

Camponovo, C. and Schweizer, J. (2001). Rheological measurements of the viscoelastic properties of snow. *Annals of Glaciology*, 32:44–50. (Cited on page 26.)

Carmagnola, C. M., Morin, S., Lafaysse, M., Domine, F., Lesaffre, B., Lejeune, Y., Picard, G., and Arnaud, L. (2014). Implementation and evaluation of prognostic representations of the optical diameter of snow in the SURFEX/ISBA-Crocus detailed snowpack model. *The Cryosphere*, 8(2):417–437. (Cited on page 21.)

Casassa, G., Narita, H., and Maeno, N. (1989). Measurements of friction coefficients of snow blocks. *Annals of Glaciology*, 13(40):40–44. (Cited on page 110.)

Chandel, C., Srivastava, P. K., and Mahajan, P. (2014). Micromechanical analysis of deformation of snow using X-ray tomography. *Cold Regions Science and Technology*, 101:14–23. (Cited on pages 133, 143 and 168.)

Chandel, C., Srivastava, P. K., and Upadhyay, A. (2007). Estimation of Rheological Properties of Snow Subjected to Creep. *Defence Science Journal*, 57(4):393–401. (Cited on pages 11 and 27.)

Chen, S. and Baker, I. (2010). Evolution of individual snowflakes during metamorphism. *Journal of Geophysical Research*, 115(D21):1–9. (Cited on pages 42 and 98.)

Colbeck, S. (1975). Grain and bond growth in wet snow. In *Snow Mechanics Symposium*, pages 51–61, Grindelwald. (Cited on page 11.)

Colbeck, S. (1997). A Review of Sintering in Seasonal Snow. Technical Report December, U.S. Army Cold Regions Research and Engineering Laboratory, Hanover. (Cited on pages 22, 111, 160 and 162.)

Colbeck, S. (2001). Sintering of unequal grains. *Journal of Applied Physics*, 89(8):4612. (Cited on page 110.)

Coléou, C., Lesaffre, B., Brzoska, J.-B., Ludwig, W., and Boller, E. (2001). Three-dimensional snow images by X-ray microtomography. *Annals of Glaciology*, 32(1):75–81. (Cited on pages 42, 48, 110, 133 and 176.)

Cundall, P. A. and Strack, O. D. L. (1979). A discrete numerical model for granular assemblies. *Geotechnique*, 29(1):47–65. (Cited on pages 111 and 137.)

Dadic, R., Schneebeli, M., Lehning, M., Hutterli, M. a., and Ohmura, A. (2008). Impact of the microstructure of snow on its temperature: A model validation with measurements from Summit, Greenland. *Journal of Geophysical Research*, 113(D14):1–11. (Cited on page 160.)

Danek, O. and Matula, P. (2011a). An improved riemannian metric approximation for graph cuts. In Debled-Rennesson, I., Domenjoud, E., Kerautret, B., and Even, P., editors, *Discrete Geometry for Computer Imagery*, pages 71–82. Springer Berlin Heidelberg. (Cited on pages 68 and 167.)

Danek, O. and Matula, P. (2011b). On Euclidean Metric Approximation via Graph Cuts. In Richard, P. and Braz, J., editors, *Computer Vision, Imaging and Computer Graphics. Theory and Applications*, volume 229 of *Communications in Computer and Information Science*, pages 125–134. Springer Berlin Heidelberg. (Cited on pages 68 and 83.)

de Crécy, L. (1965). Cadastre et statistique d'avalanches. *Revue Forestière Française*, 1:24–33. (Cited on page 6.)

de Crécy, L. (1980). Avalanche zoning in France - Regulations and technical bases. *Journal of Glaciology*, 26(94):325–330. (Cited on page 8.)

Delong, A. and Boykov, Y. (2008). A scalable graph-cut algorithm for N-D grids. In *IEEE Conference on Computer Vision and Pattern Recognition*, pages 1–8. (Cited on pages 54, 69 and 167.)

Desrues, J., Darve, F., Flavigny, E., Navarre, J. P., and Taillefer, A. (1980). An incremental formulation of constitutive equations for deposited snow. *Journal of Glaciology*, 25(92):289–307. (Cited on page 27.)

Domine, F., Bock, J., Morin, S., and Giraud, G. (2011). Linking the effective thermal conductivity of snow to its shear strength and density. *Journal of Geophysical Research*, 116(F4):F04027. (Cited on pages 177 and 178.)

Domine, F., Taillandier, A.-S., and Simpson, W. R. (2007). A parameterization of the specific surface area of seasonal snow for field use and for models of snowpack evolution. *Journal of Geophysical Research*, 112(F2):1–13. (Cited on page 72.)

Duclos, A. (1998). Slab avalanches and "new" snow. In *International Snow Science Workshop*, pages 478–488, Sunriver, Oregon, USA. (Cited on page 11.)

Durand, Y., Giraud, G., Brun, E., Merindol, L., and Martin, E. (1999). A computer-based system simulating snowpack structures as a tool for regional avalanche forecasting. *Journal of Glaciology*, 45(151):469–484. (Cited on pages 7, 8 and 20.)

Edens, M. and Brown, R. L. (1995). Measurement of microstructure of snow from surface sections. *Defence Science Journal*, 45(2):107–116. (Cited on page 132.)

El-Zehiry, N. and Grady, L. (2010). Fast global optimization of curvature. *IEEE Conference on Computer Vision and Pattern Recognition*, pages 3257–3264. (Cited on page 43.)

Fassnacht, S. (2011). Snow density. In Singh, V. P., Singh, P., and Haritashya, U. K., editors, *Encyclopedia of Snow, Ice and Glaciers*, page 1045. Springer, Dordrecht, the Netherlands. (Cited on page 110.)

Ferellec, J.-F. and McDowell, G. R. (2010). A method to model realistic particle shape and inertia in DEM. *Granular Matter*, 12(5):459–467. (Cited on page 136.)

Fierz, C., Durand, R., Etchevers, Y., Greene, P., McClung, D. M., Nishimura K, Satyawali, P. K., and Sokratov, S. A. (2009). The international classification for seasonal snow on the ground. Technical report, IHP-VII Technical Documents in Hydrology N83, IACS Contribution N1, UNESCO-IHP, Paris. (Cited on pages 10, 11, 18, 21, 24, 43, 44, 72, 110, 111, 112, 122, 132, 134, 164, 169, 172, 174 and 175.)

Flanner, M. G. and Zender, C. S. (2006). Linking snowpack microphysics and albedo evolution. *Journal of Geophysical Research*, 111(D12):D12208. (Cited on page 72.)

Flin, F. (2004). *Snow metamorphism description from 3D images obtained by X-ray microtomography*. PhD thesis, Université de Grenoble 1. (Cited on pages 25, 44, 49, 78 and 132.)

Flin, F. and Brzoska, J.-B. (2008). The temperature-gradient metamorphism of snow: vapour diffusion model and application to tomographic images. *Annals of Glaciology*, 49(1):17–21. (Cited on pages 42 and 191.)

Flin, F., Brzoska, J.-B., Lesaffre, B., Coléou, C., and Pieritz, R. A. (2003). Full three-dimensional modelling of curvature-dependent snow metamorphism: first results and comparison with experimental tomographic data. *Journal of Physics D: Applied Physics*, 36(10A):A49–A54. (Cited on pages 42, 43, 44, 48, 49, 73, 79, 110 and 191.)

Flin, F., Brzoska, J.-B., Lesaffre, B., Coléou, C., and Pieritz, R. A. (2004). Three-dimensional geometric measurements of snow microstructural evolution under isothermal conditions. *Annals of Glaciology*, 38(1):39–44. (Cited on pages 11, 72, 112, 134, 164 and 179.)

Flin, F., Budd, W. F., Coeurjolly, D., Pieritz, R. A., Lesaffre, B., Coléou, C., Lamboley, P., Teytaud, F., Vignoles, G. L., and Delesse, J.-F. (2005). Adaptive estimation of normals and surface area for discrete 3-D objects: application to snow binary data from X-ray tomography. *Image Processing, IEEE Transactions on*, 14(5):585–596. (Cited on page 82.)

Flin, F., Lesaffre, B., Dufour, A., Gillibert, L., Hasan, A., Roscoat, S. R. D., Cabanes, S., and Pugliese, P. (2011). On the Computations of Specific Surface Area

and Specific Grain Contact Area from Snow 3D Images. In *Physics and Chemistry of Ice*, pages 321–328. (Cited on pages 43, 68, 82, 84, 134, 161, 164, 176 and 181.)

Ford, L. R. and Fulkerson, D. R. (1956). Maximum flow through a network. *Canadian Journal of Mathematics*, 8(3):399–404. (Cited on pages 54, 68 and 167.)

Freedman, D. (2005). Interactive Graph Cut Based Segmentation with Shape Priors. *IEEE Computer Society Conference on Computer Vision and Pattern Recognition*, 1:755–762. (Cited on page 43.)

Freitag, J., Wilhelms, F., and Kipfstuhl, S. (2004). Microstructure-dependent densification of polar firn derived from X-ray microtomography. *Journal of Glaciology*, 50(169):243–250. (Cited on page 42.)

Gallet, J. C., Domine, F., Zender, C., and Picard, G. (2009). Measurement of the specific surface area of snow using infrared reflectance in an integrating sphere at 1310 and 1550 nm. *The Cryosphere*, 3:167–182. (Cited on page 43.)

Garboczi, E. (1998). Finite element and finite difference programs for computing the linear electric and elastic properties of digital images of random materials. Rep 6269. Technical report, National Institute of Standards and Technology, Gaithersburg, Marylans. (Cited on page 31.)

Gaume, J. (2013). *Prédétermination des hauteurs de départ d'avalanches.* PhD thesis, Université de Grenoble. (Cited on pages 8, 28 and 191.)

Giraud, G. (1992). MEPRA an expert system for avalanche risk forecasting. In *International Snow Science Workshop*, pages 97–104, Breckenridge, Colorado, USA. (Cited on page 21.)

Glass, B., Huet, P., Rat, M., and Tordjeman, R. (2000). Retour d'expérience sur l'avalanche du 9 février 1999 à Montroc. Technical report, Inspection générale de l'environnement. (Cited on page 7.)

Goetz, D. (2010). Rappels de nivologie. (Cited on page 8.)

Good, W. (1987). Thin sections, serial cuts and 3D analysis of snow. *IAHS Publication*, 162(Symposium on avalanche formation, movement and effects):35–47. (Cited on pages 24, 25 and 42.)

Gubler, H. (1978). Determination of the mean number of bonds per snow grain and of the dependence of tensile strength of snow on stereological parameters. *Journal of Glaciology*, 20(83):329–341. (Cited on page 161.)

Habermann, M., Schweizer, J., and Jamieson, J. B. (2008). Influence of snowpack layering on human-triggered snow slab avalanche release. *Cold Regions Science and Technology*, 54(3):176–182. (Cited on page 27.)

Hagenmuller, P., Calonne, N., Chambon, G., Flin, F., Geindreau, C., and Naaim, M. (2014a). Characterization of the snow microstructural bonding system through the minimum cut density. *Cold Regions Science and Technology*, 108:72–79. (Cited on pages 16 and 153.)

Hagenmuller, P., Chambon, G., Flin, F., Morin, S., and Naaim, M. (2014b). Snow as a granular material: assessment of a new grain segmentation algorithm. *Granular Matter*, 16(4):421–432. (Cited on pages 134, 135, 143, 161, 181 and 182.)

Hagenmuller, P., Chambon, G., Flin, F., Wang, X., Lesaffre, B., and Naaim, M. (2013a). Description of the snow microstructure as a 3D assembly of grains. In *International Snow Science Workshop*, page 5, Grenoble - Chamonix Mont-Blanc. (Cited on pages 161 and 182.)

Hagenmuller, P., Chambon, G., Lesaffre, B., Flin, F., and Naaim, M. (2013b). Energy-based binary segmentation of snow microtomographic images. *Journal of Glaciology*, 59(217):859–873. (Cited on pages 73, 79, 81, 86, 87, 91, 112, 134, 164 and 167.)

Hagenmuller, P., Theile, T., and Schneebeli, M. (2014c). Numerical simulation of microstructural damage and tensile strength of snow. *Geophysical Research Letters*, 41(1):86–89. (Cited on pages 110, 111, 122, 133, 143, 145, 155, 157, 164, 168, 176, 177 and 178.)

Hansen, A. C. and Brown, R. L. (1986). The granular structure of snow: an internal-state variable approach. *Journal of Glaciology*, 32(112):434–438. (Cited on page 132.)

Hansen, A. C. and Brown, R. L. (1988). An internal state variable approach to constitutive theories for granular materials with snow as an example. *Mech. Mater.*, 7(2):109–119. (Cited on pages 29, 30 and 133.)

Heggli, M., Frei, E., and Schneebeli, M. (2009). Snow replica method for three-dimensional X-ray microtomographic imaging. *Journal of Glaciology*, 55(192):631–639. (Cited on pages 25, 42, 46, 48 and 78.)

Heggli, M., Kochle, B., Matzl, M., Pinzer, B. R., Riche, F., Steiner, S., Steinfeld, D., and Schneebeli, M. (2011). Measuring snow in 3-D using X-ray tomography: assessment of visualization techniques. *Annals of Glaciology*, 52(58):231–236. (Cited on page 98.)

Herwijnen, A. V. (2013). Experimental analysis of snow micropenetrometer (SMP) cone penetration in homogeneous snow layers. *Canadian Geotechnical Journal*, 1054(August):1044–1054. (Cited on page 26.)

Hildebrand, T., Laib, A., Müller, R., Dequeker, J., and Rüegsegger, P. (1999). Direct three-dimensional morphometric analysis of human cancellous bone: microstructural data from spine, femur, iliac crest, and calcaneus. *Journal of bone and mineral research*, 14(7):1167–1174. (Cited on page 82.)

Iassonov, P., Gebrenegus, T., and Tuller, M. (2009). Segmentation of X-ray computed tomography images of porous materials: A crucial step for characterization and quantitative analysis of pore structures. *Water Resources Research*, 45(9):W09415. (Cited on pages 43, 47 and 73.)

Jamieson, J. B. (1988). *In situ tensile strength of snow in relation to slab avalanches*. PhD thesis, The University of Calgary. (Cited on page 16.)

Jamieson, J. B. and Johnston, C. (1990). In-situ tensile tests of snow-pack layers. *Journal of Glaciology*, 36(122):102–106. (Cited on page 27.)

Jenkins, M. K. (2000). *The White Death: Tragedy and Heroism in an Avalanche Zone*. Random House. (Cited on page 5.)

Johnson, J. B. (2011). Snow deformation. In Singh, V. P., Singh, P., and Haritashya, U. K., editors, *Encyclopedia of Snow, Ice and Glaciers*, pages 1041–1045. Springer, Dordrecht, the Netherlands. (Cited on pages 122, 143 and 146.)

Johnson, J. B. and Hopkins, M. A. (2005). Identifying microstructural deformation mechanisms in snow using discrete-element modeling. *Journal of Glaciology*, 51(174):432–442. (Cited on pages 30, 111, 133 and 145.)

Johnson, J. B. and Schneebeli, M. (1999). Characterizing the microstructural and micromechanical properties of snow. *Cold Regions Science and Technology*, 30(1-3):91–100. (Cited on page 191.)

Kaempfer, T. U., Schneebeli, M., and Sokratov, S. A. (2005). A microstructural approach to model heat transfer in snow. *Geophysical Research Letters*, 32(21):1–5. (Cited on pages 42 and 110.)

Kaestner, A., Lehmann, E., and Stampanoni, M. (2008). Imaging and image processing in porous media research. *Advances in Water Resources*, 31(9):1174–1187. (Cited on pages 46, 48 and 73.)

Kanit, T., Forest, S., Galliet, I., Mounoury, V., and Jeulin, D. (2003). Determination of the size of the representative volume element for random composites: statistical and numerical approach. *International Journal of Solids and Structures*, 40(13-14):3647–3679. (Cited on page 33.)

Kanit, T., N'Guyen, F., Forest, S., Jeulin, D., Reed, M., and Singleton, S. (2006). Apparent and effective physical properties of heterogeneous materials: Representativity of samples of two materials from food industry. *Computer Methods in Applied Mechanics and Engineering*, 195(33-36):3960–3982. (Cited on page 168.)

Keeler, C. M. (1969). The growth of bonds and the increase of mechanical strength in a dry seasonal snow-pack. *Journal of Glaciology*, 8(54):441–450. (Cited on page 132.)

Keeler, C. M. and Weeks, W. F. (1968). Investigations into the mechanical properties of alpine snow-packs. *Journal of Glaciology*, 7(50):253–271. (Cited on pages 15, 110 and 132.)

Kerbrat, M., Pinzer, B. R., Huthwelker, T., Gäggeler, H. W., Ammann, M., and Schneebeli, M. (2008). Measuring the specific surface area of snow with X-ray tomography and gas adsorption: comparison and implications for surface smoothness. *Atmospheric Chemistry and Physics*, 8(5):1261–1275. (Cited on pages 42, 43, 46, 48, 77, 78, 79 and 87.)

Kirchner, H. O. K., Michot, G., Narita, H., and Suzuki, T. (2001). Snow as a foam of ice: Plasticity, fracture and the brittle-to-ductile transition. *Philosophical Magazine A*, 81(9):2161–2181. (Cited on page 27.)

Kirchner, H. O. K., Peterlik, H., and Michot, G. (2004). Size independence of the strength of snow. *Physical Review E*, 69(1):011306. (Cited on pages 26 and 104.)

Kochle, B. and Schneebeli, M. (2014). Three-dimensional microstructure and numerical calculation of elastic properties of alpine snow with a focus on weak layers. *Journal of Glaciology*, 60(222):1–9. (Cited on page 155.)

Kolmogorov, V. and Zabih, R. (2004). What energy functions can be minimized via graph cuts? *IEEE Transactions on Pattern Analysis and Machine Intelligence*, 26(2):147–59. (Cited on pages 81 and 115.)

Kry, P. (1975a). Quantitative stereological analysis of grain bonds in snow. *Journal of Glaciology*, 14(72):467–477. (Cited on pages 24, 25, 29, 132 and 161.)

Kry, P. (1975b). The relationship between the visco-elastic and structural properties of fine-grained snow. *Journal of Glaciology*, 14(72):479–500. (Cited on pages 16, 28, 29, 30, 121, 133, 161 and 162.)

Kubo, M., Seto, K., Muramoto, K., Fujiyoshi, Y., Shinoda, T., and Ohigashi, T. (2009). Shape classification of snow particle into snowflake and graupel using image processing. In *ICCAS-SICE*, pages 5451–5456. (Cited on page 111.)

Lecorps, D. and Sudul, M. (1991). Mesure automatique de hauteur de neige. In *Symposium de Chamonix CISA-IKAR, Anena*, pages 33–39, Chamonix. (Cited on page 18.)

Lee, Y., Fang, C., Tsou, Y.-R., Lu, L.-S., and Yang, C.-T. (2009). A packing algorithm for three-dimensional convex particles. *Granular Matter*, 11(5):307–315. (Cited on page 136.)

Legagneux, L. and Domine, F. (2005). A mean field model of the decrease of the specific surface area of dry snow during isothermal metamorphism. *Journal of Geophysical Research*, 110(F4):F04011. (Cited on page 110.)

Lehmann, G., Legland, D., and Génie, U. M. R. (2012). Efficient N-Dimensional surface estimation using Crofton formula and run-length encoding. *The Insight Journal*, pages 1–11. (Cited on pages 54 and 68.)

Lesaffre, B., Pougatch, E., and Martin, E. (1998). Objective determination of snow grain characteristics from images. *Annals of Glaciology*, 26:112–118. (Cited on pages 20 and 24.)

Liang, Z., Ioannidis, M. A., and Chatzis, I. (2000). Geometric and topological analysis of three-dimensional porous media: Pore space partitioning based on morphological skeletonization. *Journal of colloid and interface science*, 221(1):13–24. (Cited on page 111.)

Liu, Y.-S., Yi, J., Zhang, H., Zheng, G.-Q., and Paul, J.-C. (2010). Surface area estimation of digitized 3D objects using quasi-Monte Carlo methods. *Pattern Recognition*, 43(11):3900–3909. (Cited on page 68.)

Lomonaco, R., Albert, M., and Baker, I. (2011). Microstructural evolution of fine-grained layers through the firn column at Summit, Greenland. *Journal of Glaciology*, 57(204):755–762. (Cited on page 77.)

Lorensen, W. E. and Cline, H. E. (1987). Marching Cubes: A High Resolution 3D Surface Construction Algorithm. *SIGGRAPH Comput. Graph.*, 21(4):163–169. (Cited on page 83.)

Löwe, H., Riche, F., and Schneebeli, M. (2013). A general treatment of snow microstructure exemplified by an improved relation for thermal conductivity. *The Cryosphere*, 7(5):1473–1480. (Cited on pages 110 and 162.)

Löwe, H., Spiegel, J., and Schneebeli, M. (2011). Interfacial and structural relaxations of snow under isothermal conditions. *Journal of Glaciology*, 57(203):499–510. (Cited on page 176.)

Löwe, H. and van Herwijnen, A. (2012). A Poisson shot noise model for micro-penetration of snow. *Cold Regions Science and Technology*, 70:62–70. (Cited on page 191.)

Maeno, N., Narita, H., and Araoka, K. (1978). Measurements of aire permeablity and elastic modulus of snow and firn drilled at Mizuho station east antarctica. *Memoirs of National Institute of Polar Research*, 10:62–76. (Cited on page 16.)

Mahajan, P. and Brown, R. L. (1993). A microstructure-based constitutive law for snow. *Annals of Glaciology*, 18:287–294. (Cited on pages 29, 30 and 132.)

Mandelbrot, B. B. (1982). *The fractal geometry of nature*. Times Books. (Cited on page 54.)

Marshall, H.-P. and Johnson, J. B. (2009). Accurate inversion of high-resolution snow penetrometer signals for microstructural and micromechanical properties. *Journal of Geophysical Research*, 114(F4):F04016. (Cited on page 16.)

Matsushima, T., Katagiri, J., Uesugi, K., Tsuchiyama, A., and Nakano, T. (2009). 3D Shape Characterization and Image-Based DEM Simulation of the Lunar Soil Simulant FJS-1. *J. Aerospace Eng.*, 15(January):15–23. (Cited on page 136.)

Matzl, M. (2006). Measuring specific surface area of snow by near-infrared photography. *Journal of Glaciology*, 52(179):558–564. (Cited on page 43.)

Maurer Jr., C. R., Qi, R., and Raghavan, V. (2003). A Linear Time Algorithm for Computing Exact Euclidean Distance Transforms of Binary Images in Arbitrary Dimensions. *IEEE Transactions on Pattern Analysis and Machine Intelligence*, 25(2):265–270. (Cited on page 112.)

McClung, D. M. (1977). Direct simple shear tests on snow and their relation to slab avalanche. *Journal of Glaciology*, 19(81):101–109. (Cited on page 27.)

McClung, D. M. (1979). In-situ estimates of the tensile strength of snow utilizing large sample sizes. *Journal of Glaciology*, 22(87):321–329. (Cited on page 16.)

McClung, D. M. (2011). Analysis of critical length measurements for dry snow slab weak-layer shear fracture. *Journal of Glaciology*, 57(203):557–566. (Cited on page 98.)

Mellor, M. (1975). A review of basic snow mechanics. In *IAHS Publication*, volume 114, pages 251–291. International Association of Scientific Hydrology. (Cited on pages 13, 15, 16, 24, 26, 27, 31, 42, 103, 110, 132, 155, 160 and 189.)

Meyssonnier, J., Philip, A., Capolo, L., and Mansuy, P. (2009). Experimental studies of the viscoplasticity of ice and snow. In Kolymbas, D. and Viggiani, G., editors, *Mechanics of Natural Solids*, pages 203–221. Springer Berlin Heidelberg. (Cited on page 30.)

Nakaya, U. (1954). *Snow crystals: natural and artificial*. Harvard University Press, 1954. (Cited on page 132.)

Nakaya, U. (1959). Visco-elastic Properties of Snow and Ice in Greenland Ice cap. *Journal of the Faculty of Science, Hokkaido University. Ser. 2, Physics*, 5(3):119–164. (Cited on page 26.)

Narita, H. (1980). Mechanical behaviour and structure of snow under uniaxial tensile stress. *Journal of Glaciology*, 26(94):275–282. (Cited on pages 27, 98, 102 and 103.)

Narita, H. (1983). An experimental study on tensile fracture of snow. *Contributions from the Institute of low temperature science*, 32:1–37. (Cited on pages 14, 15, 16 and 147.)

Nicot, F. (2004). Constitutive modelling of snow as a cohesive-granular material. *Granular Matter*, 6:47–60. (Cited on pages 29, 30 and 132.)

Ogawa, N., Flin, F., and Brzoska, J.-B. (2006). Representation of two curvatures of surface and its application to snow physics. *Memoirs of the Hokkaido Institute of Technology*, 34:81–87. (Cited on page 112.)

Otsu, N. (1975). A threshold selection method from gray-level histograms. *Automatica*, 20(1):62–66. (Cited on page 78.)

Pahaut, E. and Giraud, G. (1995). La prévision du risque d'avalanche en France. *La Météorologie*, 8(12):46–57. (Cited on pages 18 and 20.)

Perla, R. (1969). Strength tests on newly fallen snow. *Journal of Glaciology*, 8(54):427–440. (Cited on page 26.)

Perla, R. (1977). Slab avalanche measurements. *Canadian Geotechnical Journal*, 14(2):206–213. (Cited on page 10.)

Perla, R., Beck, T., and Cheng, T. (1982). The shear strength index of alpine snow. *Cold Regions Science and Technology*, 6(1):11–20. (Cited on page 26.)

Perla, R., Dozier, J., and Davis, R. E. (1986). Preparation of serial sections in dry snow specimens. *Journal of Microscopy*, 142(1):111–114. (Cited on page 42.)

Petrovic, J. J. (2003). Mechanical properties of ice and snow. *J. Mat. Sci.*, 38:1–6. (Cited on pages 132 and 151.)

Pieritz, R. A., Brzoska, J.-B., Flin, F., Lesaffre, B., and Coléou, C. (2004). From snow X-ray microtomograph raw volume data to micromechanics modeling: first results. *Annals of Glaciology*, 38:52–58. (Cited on pages 31, 34 and 42.)

Pinzer, B. R., Schneebeli, M., and Kaempfer, T. U. (2012). Vapor flux and recrystallization during dry snow metamorphism under a steady temperature gradient as observed by time-lapse micro-tomography. *The Cryosphere*, 6(5):1141–1155. (Cited on pages 78 and 98.)

Podolskiy, E. a., Barbero, M., Barpi, F., Chambon, G., Borri-Brunetto, M., Pallara, O., Frigo, B., Chiaia, B. M., and Naaim, M. (2014). Healing of snow surface-to-surface contacts by isothermal sintering. *The Cryosphere Discussions*, 8(3):2465–2490. (Cited on page 26.)

Podolskiy, E. a., Chambon, G., Naaim, M., and Gaume, J. (2013). A review of finite-element modelling in snow mechanics. *Journal of Glaciology*, 59(218):1189–1201. (Cited on page 28.)

Prinet, V., Monga, O., Cong, G., Loa, X. S., and Ma, S. (1996). Thin network extraction in 3D images: application to medical angiograms. In *Proceedings of the International Conference on Pattern Recognition (ICPR '96)*, volume 3, pages 386–390. (Cited on page 115.)

Quervain, M. R. D. (1983). The institute for snow and avalanche research at weissfluhjoch/davos: the first five years (1943 to 1948). *Annals of Glaciology*, 4:307–314. (Cited on page 25.)

Radjai, F. and Dubois, F. (2011). *Discrete Numerical Modeling of Granular Materials*. Wiley-ISTE. (Cited on pages 111 and 147.)

Reiweger, I. (2009). Modelling snow failure with a fibre bundle model. *Journal of Glaciology*, 55(194):997–1002. (Cited on pages 29 and 102.)

Reiweger, I., Schweizer, J., Ernst, R., and Dual, J. (2010). Load-controlled test apparatus for snow. *Cold Regions Science and Technology*, 62:119–125. (Cited on pages 25 and 98.)

Riche, F., Montagnat, M., and Schneebeli, M. (2013). Evolution of crystal orientation in snow during temperature gradient metamorphism. *Journal of Glaciology*, 59(213):47–55. (Cited on page 111.)

Riche, F. and Schneebeli, M. (2013). Thermal conductivity of snow measured by three independent methods and anisotropy considerations. *The Cryosphere*, 7(1):217–227. (Cited on page 98.)

Riche, F., Schreiber, S., and Tschanz, S. (2012). Design-based stereology to quantify structural properties of artificial and natural snow using thin sections. *Cold Regions Science and Technology*, 79-80:67–74. (Cited on page 72.)

Rietbergen, B. and Weinans, H. (1996). Computational strategies for iterative solutions of large FEM applications employing voxel data. *International Journal for Numerical Methods in Engineering*, 39(April 1994):2743–2767. (Cited on pages 31 and 33.)

Roscoat, S. R. D., King, A., Philip, A., Reischig, P., Ludwig, W., Flin, F., and Meyssonnier, J. (2011a). Analysis of Snow Microstructure by Means of X-Ray Diffraction Contrast Tomography. *Advanced Engineering Materials*, 13(3):128–135. (Cited on page 25.)

Roscoat, S. R. D., King, A., Philip, A., Reischig, P., Ludwig, W., Flin, F., and Meyssonnier, J. (2011b). Analysis of Snow Microstructure by Means of X-Ray Diffraction Contrast Tomography. *Advanced Engineering Materials*, 13(3):128–135. (Cited on page 190.)

Salm, B. (1982). Mechanical properties of snow. *Rev. Geophys.*, 20(1):1–19. (Cited on pages 24, 28 and 132.)

Saunier, J. (1970). Mission interministerielle d'étude sur la sécurité des stations de montagne. Technical report, Administration française. (Cited on page 6.)

Scapozza, C. (2004). *Entwicklung eines dichte-und temperaturabhängigen Stoffgesetzes zur Beschreibung des visko-elastischen Verhaltens von Schnee*. PhD thesis, Eidgenössischen Technischen Hochschule Zürich. (Cited on pages 16 and 27.)

Schleef, S. and Löwe, H. (2013). X-ray microtomography analysis of isothermal densification of new snow under external mechanical stress. *Journal of Glaciology*, 59(214):233–243. (Cited on pages 77 and 193.)

Schleef, S., Löwe, H., and Schneebeli, M. (2014). Hot-pressure sintering of low-density snow analyzed by X-ray microtomography and in situ microcompression. *Acta Materialia*, 71:185–194. (Cited on pages 27, 79, 133, 157 and 191.)

Schlüter, S. and Sheppard, A. (2014). Image processing of multiphase images obtained via X-ray microtomography: A review Steffen. *Water Resources Research*, pages 3615–3639. (Cited on pages 73 and 76.)

Schneebeli, M. (2000). Three-dimensional snow: what snow really looks like. In Bozeman, M., editor, *International Snow Science Workshop*, pages 407–408, Big Sky, Montana, USA. (Cited on page 42.)

Schneebeli, M. (2002). The importance of the microstructure of snow in nature and engineering. *Design and nature*, pages 87–93. (Cited on pages 42 and 110.)

Schneebeli, M. (2004). Numerical simulation of elastic stress in the microstructure of snow. *Annals of Glaciology*, 38:339–342. (Cited on pages 31, 32, 33, 34, 42, 98, 110, 111, 133, 143, 168 and 177.)

Schneebeli, M. and Johnson, J. B. (1998). A constant-speed penetrometer for high resolution snow stratigraphy. *Annals of Glaciology*, 26:107–111. (Cited on pages 26 and 133.)

Schneebeli, M. and Sokratov, S. A. (2004). Tomography of temperature gradient metamorphism of snow and associated changes in heat conductivity. *Hydrological Processes*, 18(18):3655–3665. (Cited on pages 11, 25, 42, 48, 132 and 133.)

Schulson, E. M. and Duval, P. (2009). *Creep and Fracture of ice*. Cambridge University Press. (Cited on pages 98, 100, 103, 116 and 141.)

Schweizer, J. (1998). Laboratory experiments on shear failure of snow. *Annals of Glaciology*, 26:97–102. (Cited on page 27.)

Schweizer, J. and Camponovo, C. (2002). The temperature dependence of the effective elastic shear modulus of snow. *Cold Regions Science and Technology*, 35:55–64. (Cited on page 16.)

Schweizer, J., Jamieson, J. B., and Schneebeli, M. (2003). Snow avalanche formation. *Rev. Geophys.*, 41(4):1016–1041. (Cited on pages 8, 9, 10, 17, 98, 110, 133 and 160.)

Schweizer, J. and Lütschg, M. (2000). Measurements of human-triggered avalanches from the swiss alps. In *International Snow Science Workshop*, pages 200–207, Big Sky, Montana, USA. (Cited on page 9.)

Serway, R. and Jewett, J. (2007). *Physics for Scientists and Engineers, Volume 2, Chapters 23-46*. Physics for Scientists and Engineers. Cengage Learning. (Cited on page 151.)

Seta, E., Kamegawa, T., and Nakajima, Y. (2003). Prediction of snow/tire interaction using explicit FEM and FVM. *Tire Science and Technology*, 31(3):173–188. (Cited on page 110.)

Sezgin, M. and Sankur, B. (2004). Survey over image thresholding techniques and quantitative performance evaluation. *Journal of Electronic imaging*, 13(1):220. (Cited on page 78.)

Shapiro, L. H., Johnson, J. B., Sturm, M., and Blaisdell, G. L. (1997). Snow mechanics - Review of the state of knowledge and applications. *CRREL Report*, 97(3). (Cited on pages 10, 15, 16, 26, 27, 42, 110, 132, 157 and 160.)

Shekhawat, A., Zapperi, S., and Sethna, J. P. (2013). From Damage Percolation to Crack Nucleation Through Finite Size Criticality. *Physical Review Letters*, 110(18):185505. (Cited on page 103.)

Shertzer, R. H. (2011). *Fabric tensors and effective properties of granular materials with application to snow*. PhD thesis, Montana State University. (Cited on pages 24, 29 and 30.)

Shertzer, R. H. and Adams, E. E. (2011). Anisotropic Thermal Conductivity Model for Dry Snow. *Cold Regions Science and Technology*, 69:122–128. (Cited on pages 161 and 162.)

Sigrist, C. (2006). *Measurement of fracture mechanical properties of snow and application to dry snow slab avalanche release*. PhD thesis, Swiss Federal Institute of Technology, Zurich. (Cited on pages 10, 16, 26, 27 and 177.)

Soille, P. (2003). *Morphological Image Analysis: Principles and Applications*. Springer-Verlag New York, Inc., Secaucus, NJ, USA, 2 edition. (Cited on pages 111 and 115.)

Srivastava, P. K., Mahajan, P., Satyawali, P. K., and Kumar, V. (2010). Observation of temperature gradient metamorphism in snow by X-ray computed microtomography: measurement of microstructure parameters and simulation of linear elastic properties. *Annals of Glaciology*, 50(54):73–82. (Cited on pages 31, 32, 33, 34, 42, 110, 133, 152, 161 and 162.)

St. Lawrence, W. (1980). The acoustic emission response of snow. *Journal of Glaciology*, 26(94):209–216. (Cited on page 110.)

St. Lawrence, W., Lang, T. E., Brown, R. L., and Bradley, C. C. (1973). Acoustic emission in snow at constant rates of deformation. *Journal of Glaciology*, 12(64):144–146. (Cited on page 102.)

Sturm, M., Holmgren, J., König, M., and Morris, K. (1997). The thermal conductivity of seasonal snow. *Journal of Glaciology*, 43(143):26–41. (Cited on page 160.)

Szabo, D. and Schneebeli, M. (2007). Subsecond sintering of ice. *Applied Physics Letters*, 90(151916). (Cited on page 191.)

Tabor, Z. (2007). Optimal cut of trabecular network. *Medical engineering & physics*, 29(3):298–306. (Cited on page 165.)

Theile, T. (2010). *Three-dimensional structural images analysis and micromechanics of snow*. PhD thesis, Technischen Universität Dortmund. (Cited on pages 24, 30, 32 and 34.)

Theile, T., Löwe, H., and Schneebeli, M. (2011). Simulating creep of snow based on microstructure and the anisotropic deformation of ice. *Acta Materialia*, 59(18):7104–7113. (Cited on pages 30, 31, 32, 33, 42, 110 and 122.)

Theile, T. and Schneebeli, M. (2011). Algorithm to decompose three-dimensional complex structures at the necks: tested on snow structures. *Image Processing, IET*, 5(2):132–140. (Cited on pages 25, 90, 100, 111, 121 and 161.)

Theile, T., Szabo, D., Luthi, A., Rhyner, H., and Schneebeli, M. (2009). Mechanics of the Ski-Snow Contact. *Tribology letters*, 36(3):223–231. (Cited on page 77.)

Torquato, S. (2002). *Random heterogeneous materials: microstructure and macroscopic properties*, volume 16. Springer. (Cited on page 82.)

Torquato, S. and Sen, A. K. (1990). Conductivity tensor of anisotropic composite media from the microstructure. *Journal of Applied Physics*, 67(3):1145–1155. (Cited on page 162.)

Upadhyay, A., Joshi, S. K., and Chandel, C. (2007). Tensile strength of snow using centrifugal technique. *Defence Science Journal*, 57(6):787–795. (Cited on pages 16 and 26.)

Van den Boomgaard, R. and Van der Weij, R. (2001). Gaussian convolutions numerical approximations based on interpolation. In Kerckhove, M., editor, *Scale-Space and Morphology in Computer Vision: Third International Conference*, pages 205–214, Vancouver. Springer Berlin Heidelberg. (Cited on page 112.)

van Herwijnen, A., Schweizer, J., and Heierli, J. (2010). Measurement of the deformation field associated with fracture propagation in weak snowpack layers. *Journal of Geophysical Research: Earth Surface*, 115(F3). (Cited on page 103.)

Vetter, R., Sigg, S., Singer, H. M., Kadau, D., Herrmann, H. J., and Schneebeli, M. (2010). Simulating isothermal aging of snow. *Europhys. Lett.*, 89(2):26001. (Cited on pages 11, 43, 73, 110 and 132.)

Vionnet, V., Brun, E., Morin, S., Boone, A., Faroux, S., Le Moigne, P., Martin, E., and Willemet, J.-M. (2012). Model Development The detailed snowpack scheme Crocus and its implementation in SURFEX v7 . 2. *Geoscientific Model Development*, 5:773–791. (Cited on page 20.)

Voitkovsky, K. F., Boshinsky, A. N., Golubev, V. N., and Laptev, M. N. (1975). Creep induced changes in structure and density of snow. *Symposium at Grindelwald 1974 - Snow mechanics*, pages 171–179. (Cited on pages 28, 132 and 181.)

Šmilauer, V., Catalano, E., Chareyre, B., Dorofenko, S., Duriez, J., Gladky, A., Kozicki, J., Modenese, C., Scholtès, L., Sibille, L., Stránsky, J., and Thoeni, K. (2010). *Yade Documentation*. The Yade Project, 1st edition. (Cited on pages 137 and 138.)

Wang, X., Coeurjolly, D., and Flin, F. (2014). Digital Flow for Shape Decomposition: Application to 3-D Microtomographic Images of Snow. *Pattern Recognition Letters*, 45(1):181–188. (Cited on page 121.)

Wang, X., Gillibert, L., Flin, F., and Coeurjolly, D. (2012). Curvature-driven volumetric segmentation of binary shapes: an application to snow microstructure analysis. In *International Conference on Pattern Recognition*, pages 742–745. IEEE Computer Society. (Cited on pages 111, 115, 121 and 161.)

Warren, S. (1982). Optical properties of snow. *Rev. Geophys.*, 20(1):67–89. (Cited on pages 21, 72, 111 and 160.)

Yamanoi, K. and Endo, Y. (2002). Dependence of shear strength of snow cover on density and water content. *Journal of the Japanese Society of Snow and Ice*, 64(4):443–451. (Cited on page 27.)

Yong, R. and Fukue, M. (1977). Performance of snow in confined compression. *J. Terramechanics*, 14(2):59–82. (Cited on page 133.)